

ISTANBUL TECHNICAL UNIVERSITY ★ GRADUATE SCHOOL OF SCIENCE
ENGINEERING AND TECHNOLOGY

**CFD ANALYSIS OF HELICOPTER ROTOR-FUSELAGE FLOW
INTERACTION IN HOVERING AND FORWARD FLIGHT CONDITIONS**

Ph.D. THESIS

Mustafa Berkay AÇIKGÖZ

Department of Aeronautics and Astronautics Engineering

Aeronautics and Astronautics Engineering Programme

JUNE 2016

ISTANBUL TECHNICAL UNIVERSITY ★ GRADUATE SCHOOL OF SCIENCE
ENGINEERING AND TECHNOLOGY

**CFD ANALYSIS OF HELICOPTER ROTOR-FUSELAGE FLOW
INTERACTION IN HOVERING AND FORWARD FLIGHT CONDITIONS**

Ph.D. THESIS

Mustafa Berkay AÇIKGÖZ
(521092105)

Department of Aeronautics and Astronautics Engineering

Aeronautics and Astronautics Engineering Programme

Thesis Advisor: Prof. Dr. A. Rüstem ASLAN

JUNE 2016

İSTANBUL TEKNİK ÜNİVERSİTESİ ★ FEN BİLİMLERİ ENSTİTÜSÜ

**ASKI VE İLERİ UÇUŞ ŞARTLARINDAKİ HELİKOPTER ROTOR-GÖVDE
AKIŞ ETKİLEŞİMİNİN HAD ANALİZİ**

DOKTORA TEZİ

**Mustafa Berkay AÇIKGÖZ
(521092105)**

Uçak ve Uzay Mühendisliği Anabilim Dalı

Uçak ve Uzay Mühendisliği Programı

Tez Danışmanı: Prof. Dr. A. Rüstem ASLAN

HAZİRAN 2016

Mustafa Berkay AÇIKGÖZ, a Ph.D. student of ITU Graduate School of Science Engineering and Technology student ID **521092105**, successfully defended the thesis entitled “**CFD ANALYSIS OF HELICOPTER ROTOR-FUSELAGE FLOW INTERACTION IN HOVERING AND FORWARD FLIGHT CONDITIONS**”, which he prepared after fulfilling the requirements specified in the associated legislations, before the jury whose signatures are below.

Thesis Advisor : **Prof. Dr. A. Rüstem ASLAN**

Istanbul Technical University

Jury Members : **Assist. Prof. Dr. Ayşe Gül GÜNGÖR**

Istanbul Technical University

Prof. Dr. İlyas Bedii ÖZDEMİR

Istanbul Technical University

Prof. Dr. Oktay ÖZCAN

Kemerburgaz University

Prof. Dr. Abdurrahman HACIOĞLU

Turkish Air Force Academy /

Aeronautics and Space Technologies Institute

Date of Submission : 16 May 2016

Date of Defense : 07 June 2016

To my family,

FOREWORD

I would like to express my heartfelt gratitude and appreciation to my advisor, Prof. Dr. A. Rüstem ASLAN, for his invaluable support, and encouragement. This Thesis would not have been possible without his guidance.

I would also like to thank my committee members, Prof. Dr. İ. Bedii ÖZDEMİR and Prof. Dr. Oktay ÖZCAN, for their brilliant comments and suggestions provided during the term presentations.

I would like to express my deepest and sincere gratitude to Assoc. Prof. Dr. Mehmet ŞAHİN, for providing me with excellent feedback on my manuscript, and for his enlightening suggestions and friendship.

I would like to extend my thanks to Assist. Prof. Dr. Ayşe Gül GÜNGÖR for her helpful suggestions and useful comments.

A special thanks goes to my family. You have been very supportive in my decision to receive a higher education. Today, I receive this accomplishment because you told me to never give up. You have been always there to listen and encourage me during my hopeless times. You were the only one who spent long sleepless nights with and were always my support in the moments when I needed it most. Words may not suffice to express my gratitude for all of the sacrifices that you've made on my behalf. Your unconditional love and support have sustained me thus far and helped me succeed. I couldn't have done it without you. I thank God that I'm blessed to have you in my life. I love each and every one of you.

June 2016

Mustafa Berkay AÇIKGÖZ

TABLE OF CONTENTS

	<u>Page</u>
FOREWORD	ix
TABLE OF CONTENTS	xi
ABBREVIATIONS	xiii
SYMBOLS	xv
LIST OF TABLES	xix
LIST OF FIGURES	xxi
SUMMARY	xxiii
ÖZET	xxvii
1. INTRODUCTION	1
1.1 Purpose of Thesis	2
1.2 Literature Review	4
2. ROTOR AERODYNAMICS	13
2.1 Simplified methods	17
2.2 Navier-Stokes solvers.....	20
3. MATHEMATICAL FORMULATION	21
3.1 Navier-Stokes Equations	21
3.2 ALE Navier-Stokes Equations	22
4. NUMERICAL METHOD	23
4.1 Finite Volume Approach	24
4.2 Pressure-Velocity Coupling	25
4.3 Spatial Discretization	27
4.4 Temporal Discretization	28
4.5 Boundary and Initial Conditions	34
4.6 Methods for Modeling Rotating Bodies.....	38
4.6.1 Moving reference frame.....	38
4.6.2 Sliding mesh technique	39
4.6.3 Dynamic mesh technique	39
5. TURBULENCE	43
5.1 Introduction	43
5.2 Typical Features of Turbulence.....	45
5.3 Turbulent Length Scales.....	46
5.4 Direct Numerical Simulation (DNS).....	47
5.5 Large Eddy Simulation (LES).....	47
5.6 Detached Eddy Simulation (DES).....	48
5.7 Reynolds Averaged Navier-Stokes (RANS) Models	50
5.7.1 Zero equation (Algebraic) models	54
5.7.2 One equation models.....	55
5.7.3 Two equation models	55
5.7.3.1 The realizable k- ϵ model	56
5.7.3.2 The renormalization group (RNG) k- ϵ model.....	57
5.7.3.3 The shear-stress transport (SST) k- ω model	58
5.7.4 Near wall behavior of RANS turbulence models.....	61

6. RESULTS AND DISCUSSION.....	63
6.1 Isolated Fuselage Analyses.....	63
6.1.1 The Robin geometry.....	64
6.1.2 Numerical solution procedure.....	65
6.1.2.1 Mesh dependency framework.....	67
6.1.2.2 Examination of spatial discretization schemes.....	69
6.1.2.3 The effect of turbulence models on the results.....	71
6.1.3 Drag and lift predictions at various angles of attack.....	73
6.2 Isolated Rotor Analyses.....	80
6.2.1 Hover performance prediction of UH60-black hawk rotor.....	80
6.2.1.1 Geometry.....	80
6.2.1.2 Computational mesh details.....	82
6.2.1.3 Numerical methods.....	83
6.2.1.4 Results and discussion.....	84
6.2.1.5 Concluding remarks.....	89
6.2.2 Four-bladed rotor analyses in forward flight.....	90
6.2.2.1 Geometry.....	90
6.2.2.2 Rotating blade motion.....	91
6.2.2.3 Practical difficulties and aspects open to improvement.....	94
6.2.2.4 Computational mesh details.....	94
6.2.2.5 Numerical methods.....	99
6.2.2.6 Results and discussion.....	103
6.3 Rotor and Fuselage Analyses.....	108
6.3.1 Computational mesh details.....	108
6.3.2 Numerical methods.....	110
6.3.3 Results and discussion.....	111
7. CONCLUSION AND RECOMMENDATIONS.....	121
REFERENCES.....	125
APPENDICES.....	139
CURRICULUM VITAE.....	151

ABBREVIATIONS

2D	: Two-Dimensional
3D	: Three-Dimensional
ALE	: Arbitrary Lagrangian-Eulerian
AMR	: Adaptive Mesh Refinement
AoA	: Angle of Attack
ARSM	: Algebraic Reynolds Stress Models
BC	: Boundary Condition
BEM	: Blade-Element Momentum
B-L	: Baldwin-Lomax
BVI	: Blade-Vortex Interaction
CAD	: Computer-Aided Design
CFD	: Computational Fluid Dynamics
CPU	: Central Processing Unit
CSD	: Computational Structural Dynamics
DES	: Detached Eddy Simulation
DGCL	: Discrete Geometric Conservation Law
DNS	: Direct Numerical Simulation
EU	: European Union
FDS	: Flux Difference Splitting
FM	: Figure of Merit
FSI	: Fluid Structure Interaction
FSM	: Fractional Step Method
FVM	: Finite Volume Method
GCL	: Geometric Conservation Law
HPC	: High Performance Computing
IRTS	: Independent Rotor Test System
ITA	: Iterative Time Advancement
JAXA	: Japan Aerospace Exploration Agency
KES	: Kinetic Eddy Simulation
KET	: Kinetic Energy Transport
LES	: Large Eddy Simulation
LEVM	: Linear Eddy Viscosity Models
MP	: Mixing Plane
MRF	: Moving Reference Frame
MUSCL	: Monotonic Upstream-Centered Scheme for Conservation Laws
NACA	: National Advisory Committee for Aeronautics
NASA	: National Aeronautics and Space Administration
NITA	: Non-Iterative Time Advancement
NLEVM	: Nonlinear Eddy Viscosity Models
N-S	: Navier-Stokes
PDEs	: Partial Differential Equations
PISO	: Pressure-Implicit with Splitting of Operators
QUICK	: Quadratic Upwind Interpolation for Convective Kinetics
RAM	: Random Access Memory

RANS : Reynolds Averaged Navier-Stokes
RBF : Radial Basis Function
RKE : Realizable k- ϵ
RMS : Root Mean Square
RNG : Renormalization Group
ROBIN : Rotor-Body Interaction
RPM : Revolution per Minute
RSM : Reynolds Stress Models
RST : Reynolds Stress Transport
SA : Spalart-Allmaras
SIMPLE : Semi-Implicit Method for Pressure Linked Equations
SIMPLEC : Semi-Implicit Method for Pressure Linked Equations-Consistent
SKE : Standard k- ϵ
SLAU : Simple Low-dissipative Advection Upstream Splitting Method
SST : Shear Stress Transport
UDF : User Defined Functions
URANS : Unsteady Reynolds Averaged Navier-Stokes
VTM : Vorticity Transport Method
WALE : Wall-Adapting Local Eddy-Viscosity
WENO : Weighted-Essentially-Non-Oscillatory
WENO-M : Mapped Weighted-Essentially-Non-Oscillatory
WMLES : Wall-Modeled LES

SYMBOLS

'	: Fluctuating component
—	: Mean component
∂	: Partial derivative operator
∇	: Gradient operator
∇^2	: Laplace operator
$\nabla \cdot$: Divergence operator
$\nabla \times$: Curl operator
$^{\circ}$: Degree sign
∞	: Quantity at infinity (freestream flow parameter)
A	: Area (m ²)
a_{∞}	: Free-stream speed of sound (m/s)
b	: Number of rotor blades
c	: Blade chord length (m)
C_D	: Drag force coefficient
C_{DES}	: DES calibration constant
C_L	: Lift force coefficient
C_P	: Pressure coefficient, $2(P - P_{\infty})/(\rho_{\infty}U_{\infty}^2)$
$C_P M^2$: Blade sectional pressure coefficient, $2(P - P_{\infty})/(\rho_{\infty}(\Omega r)^2)(\Omega r/a_{\infty})^2$
C_T	: Rotor thrust coefficient, $T/\pi\rho_{\infty}R^2(\Omega R)^2$
C_{μ}	: Model constant for eddy viscosity
d	: Distance to the nearest wall (m)
e	: Internal energy
f_{ϕ}	: Damping functions for variable ϕ , (i.e. 1, 2, d , μ)
F_{ϕ}	: Blending functions for $\phi = 1, 2$
h	: Enthalpy
\mathbf{I}	: Unit tensor
i, j, k	: Computational grid indices, or cartesian tensor indices
J	: Jacobian of transformation
k	: Turbulent kinetic energy, or Thermal conductivity
ℓ	: Integral length scale
L	: Fuselage length (m), or Lift force
l_m	: Mixing length
M_{tip}	: Rotor tip Mach number, $\Omega R/a_{\infty}$
$n, n + 1$: Physical time level
p	: Instantaneous pressure
P	: Mean pressure
Pr	: Prandtl number
Pr_T	: Turbulent Prandtl number
r	: Radial position from rotor hub (m)
R	: Rotor radius (m)
R	: Specific gas constant
Re	: Reynolds number

S	: Modulus of the mean strain-rate tensor
S_{ij}	: Mean strain-rate tensor
S_m	: Mass source
T	: Rotor thrust (N), or Temperature (K)
\vec{u}_g	: Grid velocity
u, v, w	: Cartesian components of velocity
U_∞	: Free-stream velocity (m/s)
u_i	: Instantaneous velocity component
U_i	: Mean velocity component
U_{tip}	: Rotor tip velocity (m/s), ΩR
u_η	: Turbulent velocity scale
x, y, z	: Cartesian coordinate directions
y^+	: Viscous sublayer length scale, $y(\tau_w/\rho)^{1/2}/\nu$
α_s	: Shaft tilting angle ($^\circ$)
β	: Artificial compressibility, or Thermal expansion coefficient
$\beta(t)$: Flap angle ($^\circ$)
β_0	: Cone angle ($^\circ$)
γ	: Ratio of specific heats
Γ	: Diffusion coefficient, or Circulation
Γ_t	: Turbulent diffusivity
δ	: Boundary layer thickness
Δ	: Maximum local length of the mesh element, or difference operator
δ^*	: Boundary layer displacement thickness
δ_{ij}	: Kronecker delta function
ε	: Turbulent dissipation rate
ε_{ij}	: Strain rate tensor
η	: Kolmogorov length scale
$\theta(t)$: Pitch angle ($^\circ$)
θ_0	: Collective pitch of the rotor blade ($^\circ$)
θ_c	: Lateral cyclic pitch angle ($^\circ$)
θ_s	: Longitudinal cyclic pitch angle ($^\circ$)
κ	: von Karman constant, (=0.41)
λ	: Bulk viscosity
μ	: Advance ratio, (U_∞/U_{tip})
μ_{eff}	: Effective viscosity
μ_m	: Dynamic molecular viscosity
μ_t	: Turbulent dynamic viscosity
ν	: Kinematic molecular viscosity
ν_∞	: Kinematic viscosity of fluid at freestream, (m^2/s)
ν_t	: Turbulent kinematic viscosity
ξ, η, ζ	: Spatial directions in computational space
ρ_∞	: Free-stream fluid density (kg/m^3)
σ	: Turbulent Prandtl-Schmidt number, or rotor solidity: $bc/\pi R$
σ_{ij}	: Stress tensor
σ_ϕ	: Turbulent Prandtl number for variable ϕ , (i.e. k, ε, ω)
τ	: Time scale
τ_{ij}	: Reynolds stress tensor
τ_w	: Wall shear stress

$\psi(t)$: Rotor azimuth angle (°)
Ω	: Rotational frequency of the rotor (rpm)
Ω_{ij}	: Mean rate of rotation tensor
ω	: Specific dissipation rate
ω_k	: Angular velocity

LIST OF TABLES

	<u>Page</u>
Table 2.1 : An overview for the multi-purpose flow solvers	20
Table 6.1 : Details of the medium mesh resolution	65
Table 6.2 : Mesh resolution specifications.....	68
Table 6.3 : Non-dimensional positions of the sections	73
Table 6.4 : Simulation details for the different angle of attack conditions	74
Table 6.5 : Section characteristics, [158].	81
Table 6.6 : Comparison of the CFD results with the experimental data.	85
Table 6.7 : ROBIN IRTS geometric features.	90
Table 6.8 : Blade control variables obtained by experiments, [31].....	92
Table 6.9 : Blade control variables obtained by other simulations, [28].	92
Table 6.10 : Blade control variables obtained by other simulations, [82].	92
Table 6.11 : Flow conditions and blade control variables.....	92
Table 6.12 : Computational parameters.	102
Table 6.13 : Predicted thrust coefficients for the isolated rotor configuration.	106
Table 6.14 : Predicted thrust coefficients for the rotor-fuselage configuration.	119

LIST OF FIGURES

	<u>Page</u>
Figure 1.1 : DES analysis of the UH-60 helicopter rotor, [49].....	8
Figure 1.2 : Effect of the AMR technique on the wake predictions, [51].....	9
Figure 2.1 : Incident velocities occurred in hover and forward flight, [105].....	14
Figure 2.2 : Flow structure around a helicopter in forward flight, [105].....	15
Figure 2.3 : View of a fully articulated rotor hinge system, [106].....	16
Figure 4.1 : Change in the blade's position: (a) actual, (b) imaginary.....	31
Figure 4.2 : Time-step sensitivity study for rotor only case ($\mu=0.231$).....	32
Figure 4.3 : Convergence history for rotor only case ($\mu=0.231$).....	33
Figure 5.1 : A schematic view of the transition region in DES Method.....	49
Figure 5.2 : Subdivisions of the near-wall region, [123].....	61
Figure 6.1 : Cross-sections of the (a) pylon and (b) body shapes.....	64
Figure 6.2 : Mesh details for the ROBIN fuselage.....	66
Figure 6.3 : Surface element length distribution [mm].....	66
Figure 6.4 : Size-box usage.....	67
Figure 6.5 : Effect of the number of layers on the results.....	68
Figure 6.6 : Equiangle skewness of the surface elements.....	69
Figure 6.7 : Prediction of drag coefficient at different mesh resolutions.....	69
Figure 6.8 : Effect of the discretization schemes on the results.....	70
Figure 6.9 : Comparison of the Cell Based and Node Based discretizations.....	71
Figure 6.10 : Comparison of the turbulence models at selected sections.....	72
Figure 6.11 : Reference pressure sections of numerical solution.....	73
Figure 6.12 : Prediction of drag coefficients at different angles of attack.....	75
Figure 6.13 : Prediction of lift coefficients at different angles of attack.....	75
Figure 6.14 : Fuselage surface streamlines.....	77
Figure 6.15 : Fuselage surface streamlines of reference studies.....	77
Figure 6.16 : X-velocity contours at symmetry plane, $\alpha_f = 0^\circ$	78
Figure 6.17 : The C_p contours at symmetry plane, $\alpha_f = 0^\circ$	78
Figure 6.18 : Flow patterns obtained at $\alpha_f = 0^\circ$	79
Figure 6.19 : Airfoils used in the blade geometry, [170].....	80
Figure 6.20 : Blade planform view and position of the airfoils, [170].....	81
Figure 6.21 : Twist angle distributions used in: (a) [169] and (b) [170].....	81
Figure 6.22 : UH60 Black Hawk blade geometry.....	82
Figure 6.23 : View for the boundary conditions and grid structure.....	83
Figure 6.24 : (a) The surface grid structure, (b) the applied grid stretching.....	83
Figure 6.25 : Convergence of the thrust and torque coefficients.....	84
Figure 6.26 : (a) CT/σ vs. θ , (b) CQ/σ vs. CT/σ , (c) FM vs. CT/σ , [169].....	85
Figure 6.27 : The y^+ distribution over the blade : (a) coarse grid, (b) fine grid.....	85
Figure 6.28 : (a) z-velocity distribution [m/s], (b) the vorticity distributions.....	86
Figure 6.29 : Comparison of C_p distributions with [169].....	87
Figure 6.30 : Inflow ratio at $\psi = -10^\circ$: (a) [169], (b) present study.....	88
Figure 6.31 : Axial velocity and tip vortices: (a) [169], (b) present study.....	88
Figure 6.32 : Computed vorticity magnitudes: (a) [169], (b) present study.....	88

Figure 6.33 : The path of the blade tip vortex.....	89
Figure 6.34 : Normalized vorticity contours of the blade tip vortex.....	89
Figure 6.35 : Surface model of the ROBIN fuselage and its four-bladed rotor.....	91
Figure 6.36 : Mesh details around the blade	95
Figure 6.37 : Structure of the blocks: (a) top view, (b) side view.....	96
Figure 6.38 : Uniformly generated elements in the deforming block.....	97
Figure 6.39 : View of the volume mesh for isolated rotor cases at $\mu = 0.012$	98
Figure 6.40 : View of the volume mesh for isolated rotor cases at $\mu = 0.151$	98
Figure 6.41 : View of the volume mesh for isolated rotor cases at $\mu = 0.231$	98
Figure 6.42 : Dynamic mesh and time advancement algorithms	100
Figure 6.43 : Change in pitch and flap angles with azimuth for $\mu = 0.012$	103
Figure 6.44 : Change in pitch and flap angles with azimuth for $\mu = 0.151$	103
Figure 6.45 : Change in pitch and flap angles with azimuth for $\mu = 0.231$	103
Figure 6.46 : Positions of deformed and undeformed blades.....	104
Figure 6.47 : Comparison of the blade positions at different advance ratios.....	104
Figure 6.48 : Instantaneous thrust coefficients for individual rotor blades.....	105
Figure 6.49 : Comparison of $-C_{PM^2}_{\Gamma=0.75R}$	107
Figure 6.50 : Locations of the static pressure orifices	108
Figure 6.51 : Boundary layer mesh around fuselage.....	109
Figure 6.52 : Volume mesh views: (a) $\mu=0.012$, (b) $\mu=0.151$, (c) $\mu=0.231$	110
Figure 6.53 : Comparison of $-C_{PM^2}_{\Gamma=0.75R}$ at $\mu=0.012$	111
Figure 6.54 : Comparison of $-C_{PM^2}_{\Gamma=0.75R}$ at $\mu=0.151$	112
Figure 6.55 : Comparison of $-C_{PM^2}_{\Gamma=0.75R}$ at $\mu=0.231$	112
Figure 6.56 : Comparison of C_p fluctuations with other RANS results, [30].....	114
Figure 6.57 : Comparison of averaged periodical C_p values	115
Figure 6.58 : Iso-surface plots of vorticity ranges between 10-50 (1/s)	117
Figure 6.59 : Iso-surface plots of λ_2 -criterion.....	118
Figure 6.60 : Surface streaklines, $\mu=0.012$: (a) starboard, (b) port, (c) top views..	120
Figure 6.61 : Surface streaklines, $\mu=0.151$: (a) starboard, (b) port, (c) top views..	120
Figure 6.62 : Surface streaklines, $\mu=0.231$: (a) starboard, (b) port, (c) top views..	120
Figure A.1 : C_p distributions obtained at $\alpha_f = -10^\circ$	140
Figure A.2 : C_p distributions obtained at $\alpha_f = -5^\circ$	141
Figure A.3 : C_p distributions obtained at $\alpha_f = 0^\circ$	142
Figure A.4 : C_p distributions obtained at $\alpha_f = 5^\circ$	143
Figure B.1 : Flow patterns of different AoA conditions, top view	144
Figure B.2 : Flow patterns of different AoA conditions, side view	145
Figure B.3 : Flow patterns of different AoA conditions, isometric view	146
Figure C.1 : Comparison of C_p fluctuations ($\mu=0.012$).....	147
Figure C.2 : Comparison of C_p fluctuations ($\mu=0.151$).....	148
Figure C.3 : Comparison of C_p fluctuations ($\mu=0.231$).....	149

CFD ANALYSIS OF HELICOPTER ROTOR-FUSELAGE FLOW INTERACTION IN HOVERING AND FORWARD FLIGHT CONDITIONS

SUMMARY

Academic studies carried out by industry and university collaboration constitute the basis for all of these projects aiming to locate helicopters to a higher level. The development of an effective methodology to predict the flow structure around the helicopter is one of the most significant research topics. CFD is an important discipline that may provide improvements to the helicopter performance analysis. Aerodynamic forces on the helicopter rotor blades and fuselage can be determined by accurate modeling of flow field with the implementation of advanced CFD techniques, which contribute significantly to the design of helicopters to meet the mission requirements. A helicopter rotor wake is dominated by highly unsteady and three-dimensional vortex structures. Particularly in forward flight, a challenging flow phenomenon occurs and thus, the blades are exposed to asymmetric aerodynamic loads. The motion of the blades varies arbitrarily within the azimuthal direction due to these cyclically varying air-loads. Flow characteristics can be transonic or locally supersonic which could be resulted with a shock wave formation around the advancing blade side. On the other hand, the angle of attack of the blade on the retreating side can become quite large to meet the stability requirements. However, excessive increase in the angle of attack can cause dynamic stall. In such situation, the total thrust and lift provided by the rotor are lost. Rotor wake remains near the vehicle almost all of its flight conditions. Helicopter thrust can be modified by the proximity of the wake since it alters the inflow distribution in the region surrounding the rotor blades. Therefore, accurate prediction of the strength and the position of the blade tip vortex is of crucial importance in order to determine the performance characteristics of the helicopter, realistically. Moreover, undesirable unsteady impulsive loads may occur due to the impingement of the main rotor wake on the fuselage. This situation brings vibrational problems, which negatively affect the crew and passenger flight experience. Another substantial point, especially at high rotational speeds of the rotor, is the existence of high dynamic pressure at blade tips, which may result in strong tip vortices. The performance, the vibration problems and the operating characteristics are in a strong relationship with the wake structures generated by helicopter rotor blades. The wake itself is also responsible for the noise generated. In some flight conditions, the tip vortex of the preceding blade may interact with the subsequent blade, where this interaction occurring between the rotor blades and the tip vortices is known as the blade-vortex interaction (BVI). Revealing the physical mechanism of the interactions (solid-fluid, fluid-fluid) that are highly responsible for both the noise and vibration is one of the most fundamental research topics in the field of helicopter aerodynamics, which is needed in order to overcome BVI problems. The rotorcraft industry demands an improved blade design in order to enhance performance, such as increasing the forward flight speed and reducing noise and vibration. The parameters such as sweep, taper and airfoil section, which mainly identify the aerodynamic and aeroacoustics characteristics of the blade, are being examined intensively to improve blade design.

Moreover, the interactions of rotor with fuselage and other rotorcraft components shall be taken into account for more realistic description of the flow field. The more accurate practical performance predictions shall be able to be achieved by the development of a robust and cost effective methodology.

Unsteady compressible flow analyses are carried out to investigate the challenging helicopter rotor–fuselage interaction problem in hover and forward flight conditions. First, the isolated fuselage and the isolated rotor configurations are analyzed to examine the individual effects of each component on the flow field. Then, the rotor–fuselage interaction problem is considered. The isolated fuselage analyses are based on the steady RANS computations. URANS simulations are carried out for the cases with rotor blades. The Realizable k - ϵ turbulence model is found to perform best for the predictions. The time-dependent rotor analyses are simulated at three different advance ratios. The blade dynamic motions excited by the air loads, which vary periodically in the azimuth direction and also differ based on the advance ratio, have been prescribed by a UDF code embedded into the solver, since these motions cannot be directly represented with the existing commercial code capabilities. Azimuthal variations of the flap and pitch motions of the blades are prescribed a priori as a first order Fourier series through User Defined Function feature of the code. The computational domain was modeled by unstructured hybrid mesh elements. Commonly seen dynamic mesh problems are alleviated by appropriately formed dynamic grids using the spring based smoothing and cell re-meshing methods. The accuracy of the present numerical predictions has been demonstrated by the comparison of obtained results with the experiments and other numerical results available in the open literature. The present single grid methodology has given similar successful results with much lower number of grid elements, thus resulting in much shorter computing times, using modest computational power.

In Chapter 1, the purpose of the thesis is stated, and the literature review is given. All the main areas related to the helicopter interactional aerodynamics have been examined in the literature review section. The investigation performed is mainly focused on the numerical simulation techniques used for rotor analysis in literature.

Chapter 2 provides insights for the challenging flow field around helicopters and a summary of information associated with the methods of rotor aerodynamic analysis that have been used from past to present. This section also provides information on the advantages and disadvantages of the used analysis methods, as well as their usage, applicability and historical development.

In Chapter 3, the mathematical formulation of the Navier-Stokes equations are given.

In Chapter 4, a brief information is given for the frequently used fluid flow analysis methods. Numerical models developed specifically for the analysis of rotor flow field are introduced. Moreover, their capabilities: advantages and disadvantages are discussed. Furthermore, some details of the present numerical simulations are given.

In Chapter 5, a brief description of the turbulence is given. Turbulence modeling is a necessity, especially for high Reynolds number flows. Indeed, in most cases of real engineering applications, the fluid flow is turbulent. Simulations of turbulent flows can be performed using turbulence models. However, the results to be obtained may have some discrepancy due to the chosen turbulence models of varying complexity. Therefore, turbulence and its reasons should be well understood in order to reach accurate solutions efficiently. Some examined eddy viscosity models in the context of this study are given with their formulations.

Chapter 6 includes several simulation cases that are carried out in order to examine rotor fuselage flow interaction phenomena. In Section 6.1, isolated fuselage analyses have been performed for the well-known ROBIN fuselage geometry. The pressure coefficients of predefined measurement locations are obtained for the various angle of attack conditions to validate the present CFD simulation by comparison with both experimental and numerical results. The steady RANS analyses are carried out for the isolated fuselage configuration. At the beginning, the mesh dependency work is pursued to obtain a mesh independent result. For this purpose, the drag force generated due to the presence of the fuselage is chosen as a variable to be investigated. The viscous and pressure components of the drag force are predicted whether to determine the most dominant one. Then, the mesh generation is performed with an increased resolution at the necessary regions. Furthermore, the effect of the spatial discretization schemes on the results is investigated. The second order upwind and the third order MUSCL schemes are compared. In addition, the results of the cell-based and node-based solvers on the tetrahedral volume elements are studied. Moreover, the turbulence nature of the flow is simulated by using a variety of turbulence models that are available in the solver. A comprehensive numerical study has been conducted in order to find the best available numerical approach that achieves the most consistent results with both previously performed experimental measurements and numerical studies. After determining the ideal configuration of the numerical approach for the examined problem, the drag and the lift predictions have been obtained at various angle of attack conditions. In Section 6.2, two types of numerical approaches have been used to simulate the flow fields around rotor blades. In sub-section 6.2.1, the isolated rotor analyses are carried out using moving reference frame approach by considering the effects of different grid resolutions and turbulence models. The grid structure consists of all hexahedral elements for hover performance prediction of UH60-Black Hawk rotor. The predicted tip vortex position is well correlated with experimental measurement. The presented numerical methodology can be said reliable enough to simulate a helicopter rotor analysis in hover condition. However, it is noteworthy to mention that the MRF approach is not very convenient for forward flight condition, especially when the unsteady flow field data is needed. Therefore, in sub-section 6.2.2, a more accurate numerical approach, the so-called "dynamic mesh technique", is introduced to evaluate the unsteady flow characteristics of forward flight condition. In this section, the four-bladed IRTS rotor is analyzed. All of the details needed to simulate a rotating blade motion are given with mathematical formulations. A non-overset dynamic mesh motion method that applies volume mesh deformation and cell re-meshing within a priori organized block mesh structure has been used to accommodate the prescribed rigid blade motion. The application of the technique is presented and the obtained results are discussed in detail. It is observed that the deviation in pitch and flap angles becomes larger as the advance ratio increases. The obtained results emphasize a rise in the level of asymmetry with respect to longitudinal axis by the increased advance ratio. In Section 6.3, the interference effects between rotor and fuselage are analyzed. Computations are carried out for the previously defined three advance ratios. The effect of rotor wake on the fuselage is studied by analyzing of recorded transient pressure data at measurement points. It is observed that the effect of rotor wake on the fuselage is gradually reduced by the increase in advance ratio since the wake bends downstream and flows above the body at higher forward flight speeds.

Chapter 7 includes concluding remarks and provides some possible directions for future research.

ASKI VE İLERİ UÇUŞ ŞARTLARINDAKİ HELİKOPTER ROTOR-GÖVDE AKIŞ ETKİLEŞİMİNİN HAD ANALİZİ

ÖZET

Helikopterlerin geliştirilerek daha üst seviyelere ulaştırılmasını hedefleyen projelerin temelinde sanayi ve üniversite işbirliği ile yürütülen akademik çalışmalar yer almaktadır. Helikopter etrafındaki akış yapısını doğru tahmin etmek için etkili bir yöntem geliştirilmesi başlıca önemli araştırma konularındandır. HAD, helikopter performansının geliştirilmesi açısından önemli bir disiplindir. Helikopter rotor palaları ve gövde üzerindeki aerodinamik kuvvetler, akış alanının doğru bir biçimde modellenmesini mümkün kılacak ileri seviye HAD teknikleri ile tespit edilebilir ve böylece görev isterlerini karşılayan helikopter tasarımına önemli ölçüde katkı sağlanmış olur. İz bölgesi yapısı zamana bağlıdır ve 3-boyutluluk etkileri oldukça belirgin olup kararsız bir davranış sergiler. Özellikle ileri uçuş esnasında, rotor diski etrafındaki asimetrik akış nedeniyle zorlu bir akış problemi meydana gelmektedir. Pala etkisi eden hava yükleri, palanın salt dönüş hareketinden başkaca bir takım keyfi hareketlere sebebiyet vermektedir. İlerleyen taraftaki pala ucunda akış yapısı geçişli veya bölgesel sesüstü olabilir, bu durumda şok dalgaları oluşabilir. Öte yandan, geri çekilen pala tarafında denge gereksinimi nedeniyle hücum açısında aşırı bir artış gerçekleşebilir. Zamana bağlı ve oldukça kararsız akış yapısı nedeniyle oluşan bu durum dinamik tutunma kaybı olarak adlandırılmaktadır. Böyle bir durumda rotorun sağladığı toplam itki ve taşımada kayıp meydana gelmektedir. Performans, titreşim problemleri ve uçuş kalitesi, helikopter palalarının oluşturduğu iz yapısı ile doğrudan ilişkilidir. Rotor izi, neredeyse tüm uçuş durumlarında taşıtın yakın civarında kalmaktadır. Rotor girdaplarının yakınlığı rotor düzleminde çekiş dağılımını etkileyerek helikopter itkisinin değişmesine neden olabilir. Bu bakımdan, pala uç girdaplarının şiddet ve konumlarının doğru tahmini helikopter performans niteliklerinin belirlenmesinde oldukça önemlidir. Ayrıca, ana rotor girdaplarının gövdeye çarpmasından dolayı kararsız yapıda ve tahrik edici nitelikte yükler oluşabilir. Bu durum, mürettebat ve yolcu uçuş deneyimini olumsuz bir şekilde etkileyen titreşim sorunlarını beraberinde getirmektedir. Bir diğer önemli husus, özellikle rotorun yüksek devir hızlarında pala uçlarında oluşan yüksek dinamik basınçtır ki bu durum oldukça şiddetli uç girdaplarına neden olabilmektedir. Bu uç girdapları rotor devri esnasında palalara yakın kalabilmektedir. Hatta bazı durumlarda pala ucundan ayrılan girdabın diğer palayla etkileşimi söz konusudur. Pala-girdap etkileşimi olarak adlandırılan bu olgu rotor performansını etkilediği gibi helikopter rotor gürültüsünün de en temel kaynağıdır. Gürültü ve titreşim problemlerinin esas nedeni olan duvar-akışkan, akışkan-akışkan gibi etkileşimlerin fiziksel mekanizmasını ortaya çıkarmak üzere yapılacak araştırmalar, mevcut problemlerinin aşılmasında etkili olacaktır. Helikopter sanayisi, gürültü ve titreşim seviyelerinin iyileştirilmesi vasıtasıyla daha yüksek performanslı tasarımlara ulaşmayı hedeflemektedir. Bu bakımdan geliştirilmiş pala tasarımlarına ihtiyaç duymaktadır. Pala tasarımını iyileştirmek için palanın aerodinamik ve aeroakustik karakterini belirleyen ok açısı, kanat sivrilik oranı ve kesit profili gibi başlıca parametreler üzerinde yoğun olarak çalışılmaktadır. Ayrıca, akış

alanının daha gerçekçi tasviri için rotor-gövde ve diğer helikopter bileşenleri arasındaki etkileşimler de dikkate alınmalıdır. Oldukça zorlu bir problem olan etkileşimsel helikopter aerodinamiğinin daha doğru hesaplanmasını sağlamaya yönelik çalışmalar hızla devam etmektedir. Daha doğru ve pratik performans tahminlerinin elde edilmesi, ancak güçlü ve etkili bir analiz metodolojisinin geliştirilmesi ile mümkün olacaktır.

Askı ve ileri uçuş durumunda zorlu rotor-gövde akış etkileşim problemini incelemek için zamana bağlı sıkıştırılabilir akış analizleri gerçekleştirilmiştir. Sistemi oluşturan her bir bileşenin akış yapısı üzerindeki etkilerini irdelemek için izole gövde ve izole rotor konfigürasyonları ele alınmıştır. Daha sonra, bileşenlerin birbirlerine olan etkilerini incelemek amacıyla sistemin tamamı analize tabi tutulmuştur. İzole gövde analizleri RANS tabanlı daimi hesaplamalara dayanmaktadır. Rotor palalarını içeren durumlar için ise URANS çözümleri gerçekleştirilmiştir. Akışın türbülanslı doğasını modellemek için daha güvenilir sonuç ürettiği analizler ile tespit edilmiş olan Realizable k- ϵ türbülans modeli kullanılmıştır. Zamana bağlı rotor analizleri üç farklı ilerleme oranı için gerçekleştirilmiştir. Hava yükleri nedeniyle palada gözlemlenen dinamik hareketler azimut açısı ile periyodik bir şekilde değişim gösterirken, aynı zamanda ilerleme oranına bağlı olarak da değişim göstermektedir. Palanın tanımlı hareketleri, mevcut kod yetenekleri ile temsil edilememektedir. Fakat, bu dinamik hareketler ticari HAD yazılımı içerisinde kullanıcı tarafından yazılan bir kod vasıtasıyla simülasyon modeline dahil edilebilmektedir. Bilhassa ileri uçuş şartlarında daha belirgin olan çırpma ve yunuslama hareketlerini modellemek için birinci mertebe Fourier serilerinden yararlanılarak bir UDF kodu yazılmıştır. Hesaplama hacmi düzensiz yapıda olup karma elemanlardan oluşmaktadır. Dinamik çözüm ağı yaklaşımlarında sıklıkla görülen problemler çözüm ağı deformasyonu ve çözüm ağı oluşturma yöntemlerinin kullanıldığı dinamik ağlar ile aşılmıştır. Mevcut sayısal çalışmanın doğruluğu deneyler ve diğer sayısal çalışmaların sonuçları ile karşılaştırılarak ortaya konmuştur. Benzer başarılı sonuçlar, daha az sayıda çözüm ağı kullanılarak elde edilmiştir. Bu nedenle, mevcut yöntem hesaplama süresinde azalma sağlamak ve makul hesaplama kaynağı kullanımını mümkün kılmaktadır.

Bölüm 1'de, tezin amacı ifade edilmiş ve kaynak çalışmalara yer verilmiştir. Helikopter etkileşimsel aerodinamiği ile ilgili tüm ana araştırma alanları kaynak taraması bölümünde incelenmiş olup genellikle pala analizleri için kullanılan sayısal benzetim tekniklerine odaklanılmıştır.

Bölüm 2, helikopterler etrafındaki zorlu akış yapısının çözümüne yönelik geliştirilmiş olan aerodinamik analiz yöntemleri ile ilgili özet bilgiler sağlamaktadır. Ayrıca, mevcut analiz yöntemlerinin avantaj ve dezavantajlarının yanı sıra kullanım alanları, uygulanabilirlikleri ve tarihsel gelişimlerine yönelik bilgilere de yer verilmiştir.

Bölüm 3'te, Navier-Stokes denklemlerinin matematiksel formülasyonu verilmiştir.

Bölüm 4'te, akış analizlerinde sıklıkla kullanılan sayısal yöntemler hakkında özet bilgiler verilmiştir. Özellikle rotor akış yapısının analizine yönelik geliştirilmiş sayısal teknikler tanıtılmıştır. Tekniklerin yetenekleri, avantaj ve dezavantajları tartışılmıştır. Çalışma kapsamındaki sayısal benzetimler ile ilgili bazı detaylar da yer almaktadır.

Bölüm 5'te, türbülans ile ilgili özet bir açıklama bulunmaktadır. Türbülans modellemesi, özellikle yüksek Reynolds sayılı akışlar için bir zorunluluktur. Gerçekten de, çoğu mühendislik uygulaması türbülanslı akış yapısına sahiptir. Türbülans ihtiva eden akışlarda alan değişkenlerinin hesaplanması türbülans modelleri kullanılarak yapılabilir. Ancak, seçilen türbülans modelinin karmaşıklık derecesine

bağlı olarak elde edilecek sonuçlarda bazı farklar gözlemlenebilir. Bu nedenle, doğru çözümlere etkili bir biçimde ulaşılabilmesi için türbülans ve ardındaki nedenler oldukça iyi anlaşılmalıdır. Bu çalışma kapsamında incelen bazı türbülans modelleri formülasyonları ile birlikte verilmiştir.

Bölüm 6, rotor-gövde akış etkileşim problemini incelemek amacıyla yürütülmüş farklı benzetim durumlarını kapsamaktadır. Kısım 6.1’de literatürde sıklıkla test edilmiş ROBIN gövde geometrisi kullanılarak izole gövde analizleri gerçekleştirilmiştir. Gövde üzerinde tanımlanmış ölçüm kesitlerinde çeşitli hücum açıları için elde edilen basınç katsayıları, mevcut HAD analizlerini doğrulamak amacıyla deneysel ve diğer sayısal sonuçlarla kıyaslanmıştır. İzole gövde konfigürasyonu için daimi RANS analizleri gerçekleştirilmiştir. Başlangıçta, sonuçların sayısal çözüm ağına olan bağımlılığı giderilmiştir. Bunu sağlamak için, gövdeye etki eden sürüklenme kuvveti incelenecek parametre olarak belirlenmiştir. Sürüklenme kuvvetinin viskoz ve basınç bileşenleri ayrıştırılıp hangi bileşenin daha baskın olduğu saptanmıştır. Buna müteakiben, sayısal çözüm ağı çözünürlüğü gerekli bölgelerde arttırılmıştır. Ayrıca, ikinci ve üçüncü mertebeye mekansal ayrıştırma şemalarının sonuçlar üzerindeki etkisi araştırılmıştır. Düzgün dört yüzlü hacim elemanları özelinde, hücre ve düğüm merkezli çözümlerin davranışı tespit edilmiştir. Akışın türbülanslı yapısı çözümlerin sağladığı farklı türbülans modelleri ile analiz edilmiştir. Deneysel ve diğer sayısal sonuçlar ile tam uyum sağlayacak mümkün olan en iyi sayısal yaklaşımının belirlenmesine yönelik kapsamlı bir çalışma yürütülmüştür. Çözüm yönteminin belirlenmesinin ardından gövdenin farklı hücum açısı şartlarındaki sürüklenme ve taşıma kuvveti hesabı yapılmıştır. Kısım 6.2’de, rotor palaları etrafındaki akış alanını hesaplamak için iki farklı sayısal yaklaşım kullanılmıştır. Alt-kısım 6.2.1’de, farklı sayısal çözüm ağı çözünürlükleri ve türbülans modellerinin etkileri dikkate alınmış olup, hareketli referans çerçeve yaklaşımıyla izole rotor analizleri gerçekleştirilmiştir. Askı durumundaki UH60-Kara Şahin rotorunun performans tahminlerinde kullanılan çözüm ağı yapısı tümüyle düzgün altı yüzlü elemanlardan oluşmaktadır. Pala ucu girdabının konum hesabı deneysel ölçümler ile yüksek uyum göstermiştir. Sunulan sayısal metodolojinin askı durumundaki bir helikopter rotoru etrafındaki akış alanını yeterince güvenilir bir biçimde tahmin ettiği söylenebilir. Ancak, ileri uçuş durumu için bilhassa zamana bağlı akış alanı verilerine ihtiyaç duyulduğunda, hareketli referans çerçeve yaklaşımının pek uygun olmayacağını belirtmekte fayda vardır. Bu nedenle alt-kısım 6.2.2’de, ileri uçuş durumunun kararsız akış özelliklerini değerlendirebilmek için “dinamik çözüm ağı tekniği” olarak adlandırılan daha doğru bir sayısal çözüm tekniği tanıtılmıştır. Bu teknik, dört paladan oluşan IRTS rotoruna uygulanmıştır. Dinamik pala hareketini modellemek için gerekli tüm detaylar matematiksel formülasyonları ile verilmiştir. Çözüm öncesi belirlenmiş bir blok çözüm ağı yapısı içerisinde, çözüm ağı deformasyonu ve yeniden çözüm ağı oluşturma ilkesine dayalı bu yöntem sayesinde tanımlı pala hareketi gerçekleştirilmiştir. Palanın çırpma ve yunuslama hareketlerindeki sapma miktarının, ilerleme oranının artması ile daha da belirginleştiği gözlenmiştir. Dolayısıyla, ilerleme oranının artması, boylamasına eksene göre asimetri seviyesinde artış meydana getirmektedir. Kısım 6.3’te, rotor-gövde arasındaki etkileşim üç farklı ilerleme oranı için analiz edilmiştir. Rotor iz bölgesinin gövde üzerindeki etkisi, ölçüm noktalarında zamana bağlı basınç verileri toplanarak değerlendirilmiştir. İlerleme oranının artan değerlerinde, rotorun gövde üzerindeki etkisinin giderek azaldığı tespit edilmiştir.

Bölüm 7 son yorumları içermektedir ve gelecekteki araştırmalar için bazı olası yönlendirmeler sağlamaktadır.

1. INTRODUCTION

The objective of the present research is to study and obtain aerodynamic loading on the rotor blades and rotor-fuselage flow interaction both in hovering and forward flight. Aerodynamic forces on the helicopter rotor blades and fuselage can be determined by accurate modeling of flow field, which leads to a proper design of desired helicopter.

The research topics are determined as,

- Isolated fuselage in forward flight,
- Isolated rotor blade during hovering and forward flight,
- Rotor with fuselage during hovering and forward flight.

Detailed examination of the previous studies made to solve similar problem is of great importance to identify the right target and to reach reliable results. Thus, publications covering all the main areas related to the subject of the present study have been examined in the literature review section.

A comprehensive study is needed to get a better understanding of the complex flow structure around the helicopter. Hence, the individual effects of each component on the flow are investigated by simulating the isolated fuselage and the isolated rotor configurations. Then, the aerodynamic interaction between main rotor and fuselage is analyzed in order to reveal the influences reciprocally.

The study presents Reynolds Averaged Navier-Stokes (RANS) simulations of a rotor-fuselage configuration using the commercial software ANSYS FLUENT, with particular emphasis on the interactional effects. However, blade pitch and flap motions cannot be directly represented with the existing code capabilities. Therefore, a User Defined Function (UDF) code shall be prepared and embedded into the solver. In this study, a user-defined function is prepared to define the rigid-body motion of the blades. Thus, azimuthal variations of the flap and pitch motions of the blades are prescribed a priori as a first order Fourier series through User Defined Function feature of the code.

The prescribed blade motion may result in meshes with undesirable grid qualities, which may lead to unphysical solutions. A non-overset dynamic mesh motion method that applies volume mesh deformation and cell re-meshing within a priori organized block mesh structure is used to avoid the above mentioned common problem and thus to accommodate the rigid blade motion. The re-meshing is performed only when the grid deformation is more than a pre-defined skewness value. The results of the present study have been compared with the experiments and other available numerical results found in literature. The numerical technique presented in this study is capable of accurately simulating the rotor-fuselage interactions in order to provide better insights into understanding the flow behaviors around the helicopters and thus, achieve better design. The present single grid methodology has given similar successful results with much lower number of grid elements, thus resulting in much shorter computing times, using modest computational power.

1.1 Purpose of Thesis

Industry demands for the improved blade design in order to get enhanced performance, reduced noise and vibration. Accurate prediction of the flow field around rotor blades is necessary for rotor performance analyses and aeroacoustics predictions. The parameters such as sweep, taper and airfoil section which mainly identify the aerodynamic and aeroacoustics' characteristics of the blade are being examined intensively to improve blade design. However, these parameters are needed to be analyzed with reliable tools in order to understand and to evaluate their functionality. This can be done by conducting experiments or utilizing numerical techniques. Numerical prediction tools are now a viable supplement to the very costly experimental measurements. Nowadays, CFD has become a fully recognized tool for the analysis of many complex fluid-flow problems. The physical phenomena around a rotor flow field can be captured more realistically by modeling the nature of the problem via using appropriate numerical methods. The blade motion, elastic response and rotor trim effects are one of the most significant factors that influence the quality of predictions of rotor dynamics analysis. Briefly, all the significant aspects of the problem should be properly included into the simulation model. However, the implementation of these dynamic motions into the simulations is quite difficult. Although many of the problems related to the application of numerical techniques in

which encountered in predicting the rotor flow fields have been overcome, there are still many aspects open to improvement. For instance, simulation of unsteady rotor-fuselage aerodynamic interaction requires the use of advanced CFD techniques. In addition, the accuracy of the numerical simulations is closely related to a variety of many other independent variables, such as the spatial and temporal resolution, numerical schemes and turbulence models. One of the significant items for accurate performance predictions of helicopters is the effective modeling of highly three-dimensional unsteady vortical rotor wake structures and tip vortices. CFD wake predictions can be poorly obtained with an improper or insufficient grid. Therefore, the grid independent results should be achieved primarily. This can be realized by the use of time-dependent solution based grid refinement techniques, such as the AMR method. Moreover, a reliability analysis should be performed for the validation of numerical schemes and turbulence models.

It is aimed to gain a better understanding of the flow field around helicopters by revealing the effects of all the significant parameters determining the accuracy of the predictions. From this point of view, the principal objective of this research project is to improve the performance predictions of helicopters by developing a methodology that is capable of sufficiently resolving the rotor wake field. In this context, unsteady compressible flow analyses around a scaled helicopter model have been performed by taking into account the dynamic blade motions compatible with the relevant flight conditions.

In contrast to numerous sliding mesh and/or overset grid applications in rotorcraft CFD, the single grid dynamic mesh approach is not common, due to difficulties in advancing the solution as the grid stretching becomes excessive, leading to unphysical solutions. The mentioned difficulty has been accomplished by the help of the dynamic mesh techniques available in the code. Thus, the present study introduces an affordable methodology to handle the complex interactional rotor-fuselage aerodynamics problem. The outstanding properties of the present methodology are as follows:

- i) A commercially available CFD solver FLUENT accessible by everyone. Majority of the complex interactional rotor aerodynamics analysis is accomplished by specialized institutional codes such as those of NASA, JAXA or EU.

- ii) The blade pitch and flap rigid body motions are introduced into FLUENT via the UDF code. The UDF is written to invoke azimuthal variations of the flap and pitch motions of the blades as a first order Fourier series.
- iii) Single unstructured meshes within predefined grid blocks. Almost all existing literature uses sliding mesh or overset mesh techniques to account for the rotor blade motion in forward flight.
- iv) A non-overset dynamic mesh motion method that applies volume mesh deformation and cell re-meshing within a priori organized block mesh structure to accommodate the rigid blade motion. Moving deforming grids are only needed within the deformable grid block.
- v) RANS based unsteady viscous compressible flow analysis. Most of the published works in open literature consider Euler and/or wake prediction techniques.
- vi) An accurate engineering solution approach: Relatively coarse, easy-to-prepare grids lead to acceptable computation times with modest computational power.

1.2 Literature Review

The first successful helicopter flight was conducted in the early twentieth century. From that day forward, many problems related to the rotary-wing aircraft design have been resolved and significant progress has been made. Today, helicopters have become indispensable parts of the civil and military aviation by successfully performing many different and challenging tasks due to their superior flight skills such as being able to hover and not needing a runway to land and take-off. Moreover, high maneuverability capabilities make them ideal and popular due to their providing superior traveling performance in any tough flight operations. These special features allow helicopters to be used in urban transportation and in isolated areas where fixed-wing aircraft cannot perform. Helicopters are mainly used in the fields of transportation, fire extinguishing, high building construction, search and rescue, aerial observation and military applications. Although many of the problems encountered throughout the history of helicopter were solved, it is still needed to conduct research in various areas to improve their performance: forward flight speed limits and high noise levels. Nowadays, there are many projects being carried out by NASA, Clean Sky Organization and other

significant helicopter manufacturers to improve and expand the field of use of helicopters. The Green Rotorcraft ITD is a section of European Clean Sky project, which aims to eliminate the undesirable effects of helicopters on environment by reducing the greenhouse gas emissions and noise footprints throughout the whole mission spectrum. To achieve these objectives, projects are organized along many aspects such as developing new power plants, innovative rotor blades and new aircraft configurations [1, 2]. Meanwhile, some interesting studies are carried out to enable helicopters to be used even outside the Earth's atmosphere. For instance, Jet Propulsion Laboratory at NASA is working on Mars Helicopter Project. The main point of the project is to find a design that produces sufficient amount of lift in the low-density atmosphere of Mars [3].

Examples of the most important high-speed helicopter development projects in design or prototype stage can be given as Sikorsky X2 in America, Eurocopter X3 in Europe, Kamov Ka92 in Russia and AVIC K800 in China. Eurocopter X3 prototype has been successful in tests by reaching the forward flight speed of 255 knots, which is the currently achieved high-speed flight record in this area.

Unsteady flow structure and the aerodynamic forces on the helicopter rotor blades and fuselage can be determined by accurate modeling of flow field with the implementation of advanced CFD techniques, which contribute significantly to the design of helicopters to meet the mission requirements. The helicopter industry demands for the improved blade design in order to enhance performance: with increased forward flight speeds, reduced noise and vibration. The performance, the vibration problems and the operating characteristics of the helicopter are strongly influenced by the generated wake of its rotor. Unsteady and highly three-dimensional rotor wake structure remains near the vehicle for almost all of its flight conditions. Moreover, the interactions of rotor wake with fuselage and other helicopter components should be taken into account for more realistic predictions.

The approaches found in literature to solve the challenging flow fields around the helicopters are generally based on the effective modeling of rotor wake using a variety of CFD techniques [4-7]. These methods range from the simplest to the more complex and time wise expensive ones. The momentum and blade element theories are the simplest methods of analyzing rotor blades. Lifting line/surface, prescribed wake, free-wake, panel/vortex and actuator disc methods can be given as examples of simplified

methods, which were frequently used in the previous studies to model the rotor wake [8-16]. These approaches are computationally inexpensive and have been used extensively in the past for the helicopter design. However, because of the assumptions made in these methods, the tip-vortex formation, interaction between other vortices and wall surfaces cannot be captured precisely. A comparison between panel method and a thin-layer Navier-Stokes method has been made in [17]. According to the authors, both methods are in good agreement with the experimental measurements but the panel method cannot easily model the viscous flow features and separation patterns.

The free wake method is a technique to capture the rotor wake. GENCAS is a multi-purposed parallelized CFD solver depends on hybrid three-dimensional compressible Navier-Stokes/free wake method [18, 19]. This method includes third order MUSCL, fifth and seventh order WENO for cell interface reconstruction, ROE's FDS scheme for the inviscid flux computation, second order central difference for viscous flux, and first order or second order implicit scheme for time marching with Newton sub-iterations [20, 21]. The code uses a two-equation Kinetic Eddy Simulation (KES) turbulence model to estimate the eddy viscosity [22]. The computation of traditional Lagrangian free-wake methods are inexpensive. However, interactions with other vortices and wall surfaces generate a complicated flow field. Thus, the vortex elements in the wake may become distorted and tangled due to this severe flow structure. In such cases, the free-wake methods become less accurate [13].

Actuator disc methods are used widely to simplify the rotor model for analytical computation (e.g. momentum theory) or simple numerical computation (e.g. blade element theory). Actuator disc model can also be used in the CFD simulations including Euler or RANS based numerical methods to represent the main rotor [11, 15, 16]. Improvements have been achieved with the implementation of new numerical schemes into the simplified methods, recently. As a result, a better prediction for the span wise and chord wise variation of the circulation can be obtained, and thus the unrealistic induced velocities can be eliminated. The mentioned simplified approaches have been used extensively in the past for the helicopter design. However, today these methods still constitute a basis for assessing the performance of the basic helicopter, since they provide reasonable computing times with acceptable accuracy [18, 19, 23-27].

The computationally demanding large-scale viscous flow simulations of rotors in forward flight began with the evolution of high-speed computers. Nowadays, CFD solvers, including commercial ones, are being increasingly used as a principal tool to investigate the rotor-fuselage interactional aerodynamics [28-37]. These Navier-Stokes codes, to some extent, can simulate the details of tip-vortex formation and their evolution. However, the accuracy of the results is determined by the turbulence models used for the numerical calculation of turbulent flows. The current weakness of numerical methods is the uncertainty at turbulence modeling. Up until now, the analyses of interactional helicopter aerodynamics have been carried out using URANS, DES and LES. DES and LES analyses provide much more realistic flow field predictions both in space and time, however, requirement for an excessive amount of mesh elements makes these models still computationally very expensive for most of the engineering applications. Figure 1.1 shows the 3D nature of the vortex wake of the UH-60 helicopter rotor, in which the time-dependent tip vortices could be captured in detail by using DES hybrid turbulence model. On the other hand, the solution of the RANS equations is a conventional approach to flow simulations. All the turbulent motions are modeled in the RANS approach. This provides significant savings in computational resources and makes the model appealing for practical applications. One major difficulty is the accurate calculation of the rotor wake. Computed wakes diffuse too rapidly due to the grid resolution and numerical dissipation. Therefore, accurate prediction of the rotor wake structure becomes a challenging problem [38]. The authors of [38] also assert that the azimuth angle increment is an important parameter that a second order accurate time stepping scheme should be applied for accurate prediction of BVI air loads. Furthermore, examined studies indicated that determination of a proper time step size is crucial to predict unsteady solutions accurately [39, 40]. The wake also has a significant effect on the noise generated. These vortex features may remain close to rotor blades. Even in some cases, the tip vortex of the preceding blade can interact with the subsequent blade. Interaction between the rotor blades and the tip vortices is known as blade-vortex interaction (BVI). BVI can become very strong due to the flight condition. BVI is the most basic source of helicopter rotor noise. It is necessary to predict and understand the physical mechanism of BVI phenomena in order to overcome BVI problems [41-48].

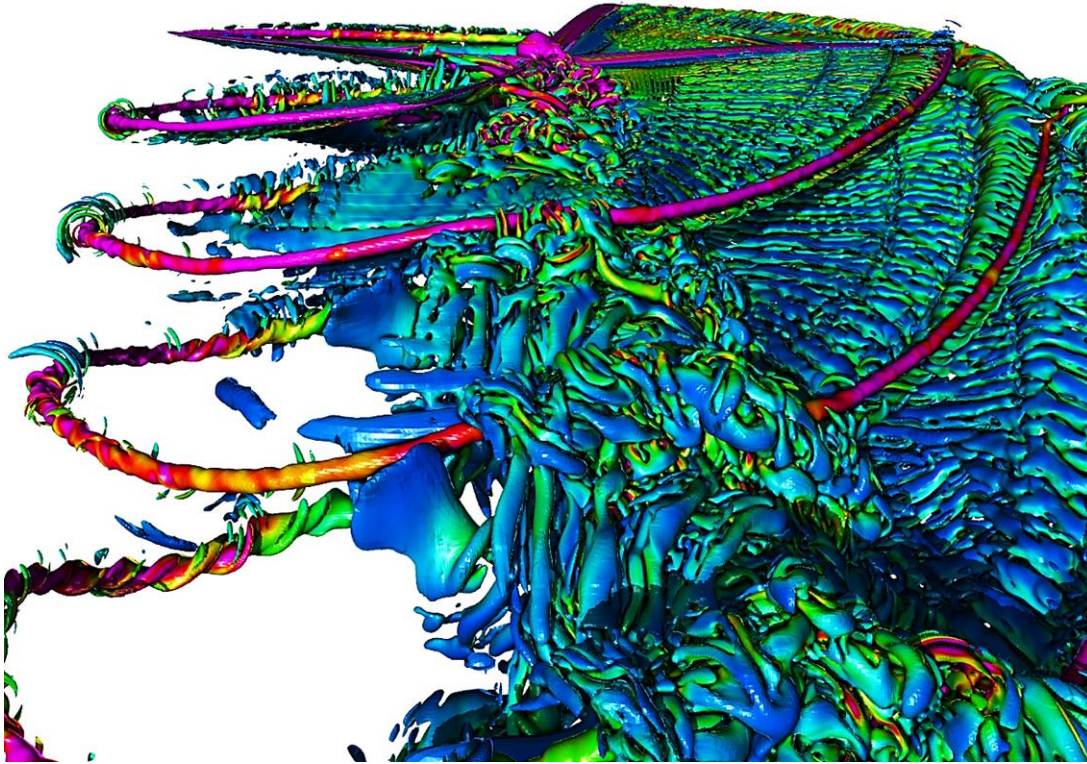


Figure 1.1 : DES analysis of the UH-60 helicopter rotor, [49].

Researchers are working on a variety of methods to capture the tip vortex accurately by preventing numerical diffusion. Improving the grid resolution and/or increasing the order of the spatial and temporal discretization form a basis to overcome numerical diffusion toward a better flow prediction. Refining the grid is a possibility at the preprocessing stage to enhance the spatial accuracy. The grid resolution can also be increased automatically during the computation by the application of Adaptive Mesh Refinement (AMR) technique in order to improve the accuracy of a solution [50-54]. As shown in Figure 1.2, the vortex wake can be effectively resolved by the use of solution-based AMR technique. The AMR technique provides remarkable details of the wake field such as the turbulent worm structures, wake shear layer entrainments and roll-up of the tip vortices. These turbulent flow structures can now be predictable by using high-end computing systems. In addition, the prediction of vortex core size and growth with wake age can be greatly improved by the use of AMR. Today, the AMR technique is being implemented by many flow solvers in order to simulate the rotor wake structure effectively. For example, HELIOS is a powerful flow solver that provides the AMR technique [55-57]. The application of the AMR can be performed using both a structured hexahedral mesh and an unstructured tetrahedral mesh.

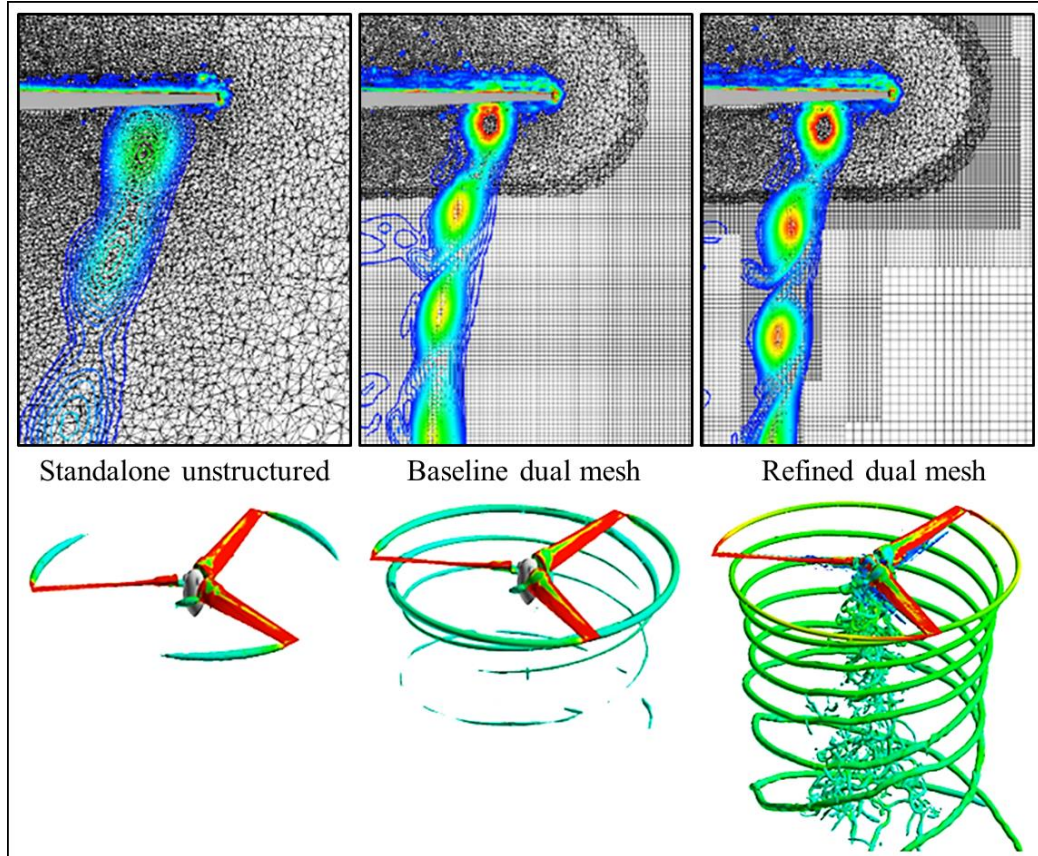


Figure 1.2 : Effect of the AMR technique on the wake predictions, [51].

Various spatial discretization schemes have been developed to overcome the numerical diffusion. High order accurate Weighted-Essentially-Non-Oscillatory (WENO) schemes are frequently used for the solutions of hyperbolic Partial Differential Equations (PDEs). Use of these schemes is very suitable, particularly when strong discontinuities like shock waves are present in the flow field. This numerical scheme provides high order spatial accuracy at smooth regions while preserving the discontinuities. The first WENO scheme was introduced in 1994 [58]. Since then, variations of WENO scheme have been proposed. A comparison between the Mapped Weighted-Essentially-Non-Oscillatory (WENO-M) scheme and the central difference scheme has been provided to investigate the effect of spatial discretization on the results, [59]. According to the results, a slight improvement in sectional normal force was obtained using WENO-M scheme but the computation time was increased by 73%. In a prior numerical study, it is stated that an improved fifth-order WENO-Z scheme can capture tip vortices much better than the Monotonic Upstream-Centered Scheme for Conservation Laws (MUSCL) scheme and yields a lower numerical dissipation, [60]. In another numerical study, a viscous flow solver on adaptive unstructured meshes is used for the flow fields around the HART II rotor.

Experimentally determined blade motion was simulated by using an overset mesh and a deforming mesh technique. To capture the rotor wake effectively a solution-adaptive mesh refinement technique was also used. The authors stated that the strength of the tip vortex was better preserved when the mesh refinement was used [38].

The blade motion, elastic response and rotor trim effects should be included properly in the CFD analysis to capture the physical phenomena more realistically. Frequently seen modeling problems in rotor simulations are related mostly to these arbitrary relative motions of the blades. The implementation of these dynamic motions into the simulations is quite difficult. For the solution of the problem, the sliding mesh, dynamic mesh, overset grid methods and Fluid Structure Interaction (FSI) techniques are commonly used. In the sliding mesh technique, two or more cell zones (e.g. for coaxial rotors) are used to model the blade motion when the motion of the cell zones is relative to each other along the mesh interface. Recent sliding mesh applications carried out especially for the rotor simulations can be found in [61-64]. Arbitrary Lagrangian-Eulerian (ALE) formulation introduced first in 1974 is one of the most used techniques for the simulation of moving boundary problems [65]. In ALE formulation, the dynamic mesh is used either by the application of mesh deformation or re-meshing methods [66, 67]. The rotor analyses including dynamic motions of the blades can be quite challenging due to the existence of large displacements and rotations which may lead to distorted mesh elements. A variety of mesh deformation techniques are available in order to maintain mesh quality and validity. The mesh deformation can be handled by using the spring analogy [68-70], solving the linear elasticity equation [71] or radial basis function (RBF) interpolation algorithms [72-74]. In some cases, the cell zone encounters an excessive anisotropic stretching or compression as a result of the very large displacement of moving boundary where inadmissible mesh elements cannot be eliminated by the grid deformation techniques any further. In such situations, re-meshing is required to sustain the motion [75-77]. The Chimera or overset grid approach can be given as an alternative to previously-mentioned methods in which the complex geometry is decomposed into a system of geometrically simple overlapping grids [78-87]. It is useful to give examples of the codes developed for the rotor field analysis. For instance, the rFlow3D is a rotor flow solver based on overlapped grid approach and depends on the modified SLAU scheme. This locally preconditioned numerical scheme enables the solver to calculate realistic

drag coefficient values both at low speeds and at transonic speeds. It is stated that the code ensures reliable results [31]. Moreover, ElsA, FLOWer, ROSITA and HELIOS can be given as examples of the powerful, multi-functioned codes based on the overset grid methodology. These codes are designed specifically for rotorcraft analyses [55-57]. The arbitrary relative motions of the blades can be easily modeled using overset grid technique. The grid quality remains unchanged during the motion of the bodies. This enables the relative motion of the bodies without re-meshing. Despite its many advantages, the method also has some drawbacks. In the overset grid method, the solution is exchanged from one grid to another (between donor-receiver pairs) at each time-step. Non-physical spurious oscillations of the pressure at discontinuous grid interfaces can arise as a result of interpolation errors. Therefore, order of the interpolation for the computation of spatial and temporal fluxes should be increased to make the numerical scheme conservative [88]. However, implementing higher order of accuracy may be computationally prohibitive. Parallelization and load balancing are also rather challenging in overset grid applications [89].

In addition to rigid blade motion, aero-elastic blade motion can be accurately included into the simulation by coupling the Computational Fluid Dynamics (CFD) and Computational Structural Dynamics (CSD) techniques [90-98]. When compared with prescribed rigid body motions, the use of CFD/CSD techniques produces more realistic representation of deformed shapes caused by aerodynamic loads. However, the technique is known as the most computationally demanding one. The FUN3D URANS solver for unstructured grids has been modified to allow prediction of trimmed rotorcraft air-loads. Moreover, aero-elastic deformation of the rotor blades and the trim of the rotorcraft can be simulated using a specialized CSD code, CAMRAD II. For instance, in a numerical study in which the CAMRAD II code is used, the effect of grid resolution and temporal accuracy is examined. According to the output of the study, the resulting air-loads and structural deformations were in good agreement with experimental measurements [99].

The parameters such as sweep, taper and airfoil section, which primarily identify the aerodynamic and aeroacoustics characteristics of the blade, should be examined for further improvements in blade design [47]. For instance, SU² is an open-source integrated computational environment for multi-physics simulation and design. This code includes design optimization property, which is highly beneficial for enhancing

the blade performance [100]. The code is robust and efficient in terms of memory and compute time, while ensuring high computing accuracy for large-scale optimization with complex geometries.

In the present study, the dynamic mesh approach is applied to carry out unsteady compressible flow analyses around a scaled helicopter model, the so called Rotor-Body-Interaction (ROBIN) geometry [101]. Particular emphasis is given to rotor fuselage interactional effects by performing RANS/URANS computations for the ROBIN fuselage/rotor configuration in hover and forward flight conditions. The standard use of techniques for the rotor simulations generally depends on the sliding meshes or overset grid applications. It is noteworthy to mention that the proposed methodology differs from the common methods found in literature. In this study, helicopter interactional aerodynamics problem has been solved using a combination of mesh deformation and cell re-meshing methods. Beforehand, the isolated fuselage and the isolated rotor configurations are analyzed to examine the individual effects of each component on the flow. Then, the rotor-fuselage interaction problem is analyzed. The time-dependent rotor analyses are simulated at three different advance ratios. The computational domain is modeled by unstructured hybrid mesh elements. Temporal discretization depends on the first-order implicit formulation in which the Discrete Geometric Conservation Law (DGCL) is being satisfied. Second order upwind and second order accurate central differencing schemes are used for the discretization of convective and diffusive terms, respectively. The isolated fuselage analyses are based on steady RANS computations. Unsteady Reynolds-Averaged Navier-Stokes (URANS) simulations are carried out for the cases including rotor blades. The Realizable k - ϵ turbulence model is found to perform best for the predictions [102]. The accuracy of the present numerical predictions has been demonstrated by the comparison with the experiments and other CFD results found in literature [17, 30, 31, 101, 103, 104]. As consistent with both the experimental and other numerical results, it is observed that the effect of rotor wake on the fuselage is gradually reduced by the increase in advance ratio since the wake bends downstream and flows above the body at higher forward flight speeds.

2. ROTOR AERODYNAMICS

A helicopter is a kind of rotorcraft whose lift is derived from the aerodynamic forces acting on its rotors. A helicopter may have one or more rotors generally turning about a vertical axis. The rotor of a helicopter may have formed by two or more blades. And the structure of the blades, from the root to the tip, are composed of airfoils which can be same or different type along the span wise direction. Therefore, a helicopter is often described as a rotary-wing aircraft since its rotor consists of rotating airfoils (blades). A helicopter is a very talented aircraft that can perform several maneuvers during its flight, which a typical airplane cannot. For instance, a helicopter can take off and land vertically. Moreover, it is capable of moving in any direction, or remaining stationary in the air (hovering). The required forces and moments in order to control the helicopter in flight can be obtained by tilting the orientation of the rotor disk. For instance, the rotor disk should be tilted fore and aft in order to provide a pitch control. Moreover, tilting the rotor disk left and right would give a roll control to the helicopter. The use of single main lifting rotor generates a moment-imbalance, which causes the rotation of the helicopter around its vertical axis. Therefore, helicopters that have a single main lifting rotor need a tail rotor that provides anti-torque in order to maintain the yaw control. Helicopters with coaxial counter-rotating main rotors do not need a tail rotor for the yaw control. The need of a propulsive force to overcome the vehicle drag can be obtained by tilting the rotor disk progressively forward. The helicopter will then accelerate into forward flight [105]. The advance ratio given by equation (2.1) is a non-dimensional number and characterizes the forward flight.

$$\mu = U_{\infty}/\Omega R \quad (2.1)$$

In above equation, U_{∞} is the forward flight speed, Ω is the angular speed of the rotor, and R is the rotor radius. The advance ratio (μ) generally takes values lower than 0.4 due to the design constraints [106]. The local angle of attack and local dynamic pressure determines the lifting capability of the relevant section of a rotating blade. Azimuth angle (ψ) is used to define the blade position. As shown in Figure 2.1, the zero azimuth angle is generally demonstrated by the blade pointing downstream

direction. Some distinctive flow features can characterize the hovering flight. For instance, the velocity along the blade changes linearly in radial direction. The velocity is zero at the origin where the rotational axis passes. Then, it increases linearly along the span wise direction and reaches to a maximum value at the blade tip. In addition to that, the velocity variation along the blade is azimuthally axisymmetric. However, in forward flight, the blades encounter an asymmetric velocity field with respect to the longitudinal axis since a component of the free stream adds to the rotational velocity on the advancing blade side and subtracts from the rotational velocity on the retreating blade side. The blade may meet supercritical and/or transonic flow regimes because of the reached maximum velocities at the blade tips on the advancing side. Particularly, at high forward flight speeds, the compressibility effects may become more dominant and strong shock waves may occur.

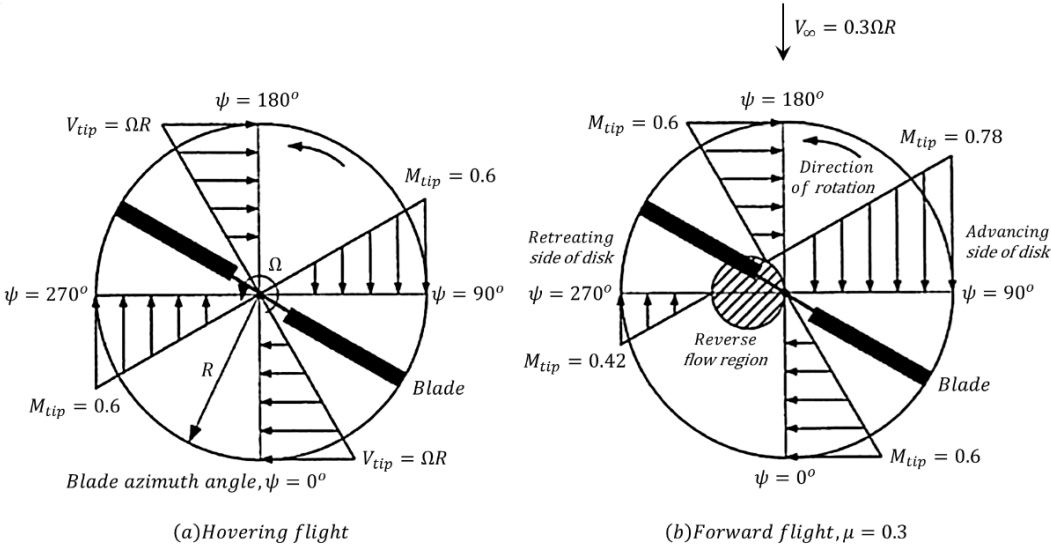


Figure 2.1 : Incident velocities occurred in hover and forward flight, [105].

Figure 2.2 gives a schematic view of the flow structure of a helicopter in forward flight. In case of the occurrence of shock induced flow separation and wave drag formation, driving the rotor becomes even more difficult due to the requirement for more power. The dynamic pressure and local velocities at the retreating blade are relatively low compared to advancing side of the disk. Therefore, the retreating blade requires to operate at a higher angle of attack in order to maintain same total lift produced by each blade. Otherwise, the helicopter will tend to roll due to the moment imbalance existing between the advancing and retreating sides of the rotor disk. The so-called cyclic pitch control is used as a balancing mechanism to remove this moment imbalance, which adjusts the angle of attack of the blades periodically throughout each blade rotation.

However, achieving very large angle of attack values may result in dangerously severe blade stall. This type of stall known as dynamic stall. Subsequently, the propulsion capability of the rotor and overall lifting will be reduced. Moreover, such a situation inhibits a further increase in forward flight speed [105].

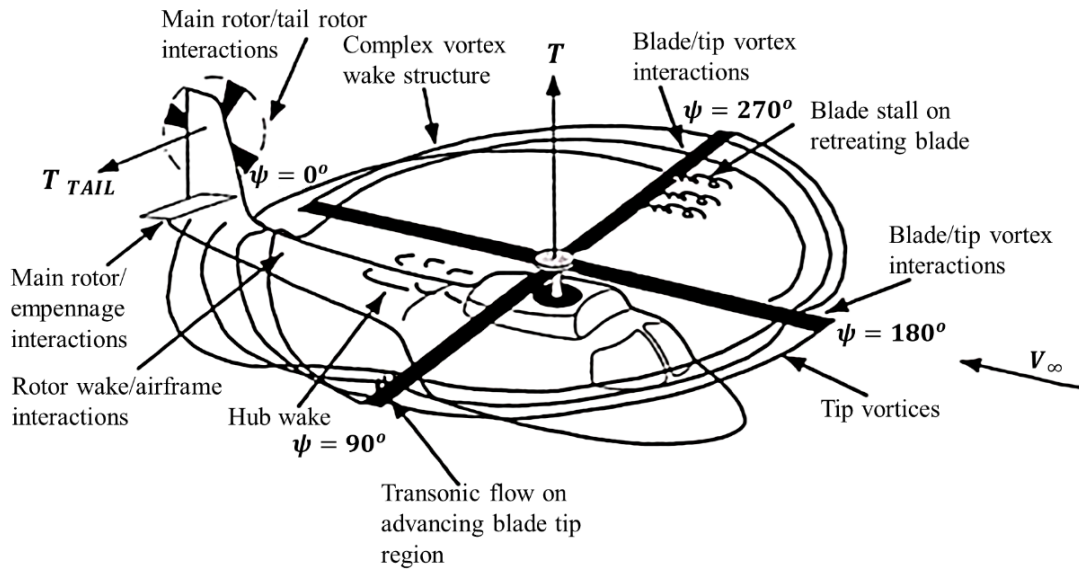


Figure 2.2 : Flow structure around a helicopter in forward flight, [105].

The velocity near the advancing blade side becomes larger as the rotor blade moves in the flight direction. As a result, the angle of attack needs not to be large to achieve sufficient lift since the lift is proportional to the velocity squared. On the other hand, the relative velocity around the retreating blade side is being smaller as the blade moves in a direction opposite to the direction of flight. The rotor needs to be trimmed to balance the forces and moments. Therefore, to overcome the moment balancing problems, the angle of attack of the retreating blade should somehow be adjusted to become larger in order to achieve the same total lift generated by the advancing blade. This can be done by using cyclic pitch mechanism, which enables the control of the angle of attack of the blades during the rotation. Moreover, the collective pitch feature of helicopters can be given as another example to the control mechanisms. This control mechanism provides a simultaneous increase in the angle of attack of each of the blades to achieve a higher lift. The helicopter will begin to rise and move into vertical flight as the collective pitch increases. Considering an isolated rotor in hover, theoretically, trim and flap controls are not required to balance forces. However, mostly due to the presence of the fuselage and possible flow disparities make the use of these controls necessary [106].

The hinging system can be given as one of the most preferred connection mechanisms. This type of connection provides trim capability. It is also beneficial to relieve the aero-elastic stress. The pitch and flap motion of the rotor blades should be permitted to satisfy trim requirements. Moreover, the rotor blades should be able to get into or out of the rotor plane during the flap motion. Figure 2.3 shows a sketch of a simple hinging mechanism.

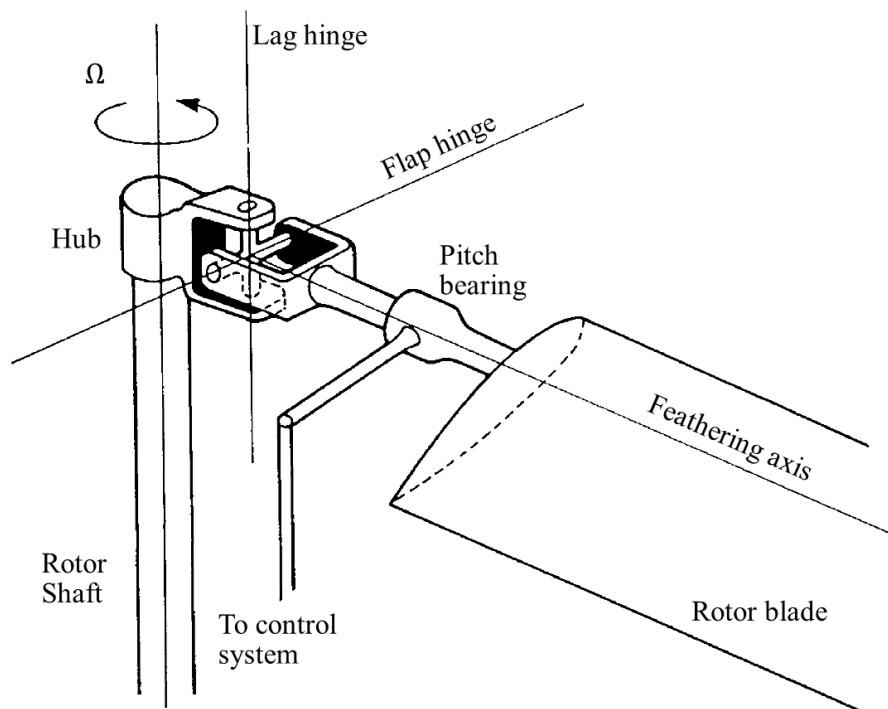


Figure 2.3 : View of a fully articulated rotor hinge system, [106].

The lead-lag and flapping hinges can be given as the two types of hinging mechanisms. The hinging mechanism is called as fully articulated if the both types of hinges are present in the system. The lead-lag hinge allows fore and aft motion of the blade within the rotor-disk plane. The blades are allowed to move freely out of the rotor-disk plane by the flapping hinge. The blades no longer trace out a single planar disk during the flapping motion. An alternative plane definition, namely tip-path plane, is used to describe such situations. The trajectory of the blade tips draws the boundary of the tip-path plane. The large span-to-chord ratio of the rotor blades makes them to have a slender structure. Therefore, the main reason for allowing the blades to flap is to prevent a possible structural failure due to the severe stresses conducted to the hub. However, both types of hinges can be eliminated if the stress levels have been kept to a minimum by using aero-elastically soft blades. This type of mechanisms are called as hinge-less systems [106].

The numerical performance prediction of the helicopters is generally based on the effective modeling of rotor wake using variety of CFD techniques. Various methods on the subject of rotor aerodynamics have been encountered during the literature survey carried out. These methods range from the simplest to the more complex and time wise expensive ones. Blade-element momentum theory, lifting line, panel and vortex methods, actuator disc methods and the Navier-Stokes solvers are the frequently used ones. The momentum and blade element theories are the simplest methods of analyzing rotor blades. Lifting line/surface, prescribed wake, free-wake, panel/vortex and actuator disc methods may be given as examples of other simplified methods, which have been used widely in the past for the solution of problems in rotor aerodynamics. These approaches are computationally inexpensive, and thus have been used extensively for the helicopter design. However, due to the assumptions made in these simplified methods, the tip-vortex formation, interaction between other vortices and wall surfaces cannot be captured precisely. In sub-section 2.1 some of the simplified approaches are briefly discussed.

The computationally demanding large-scale viscous flow simulations of rotors in forward flight began with the evolution of high-speed computers. The Navier-Stokes solvers are capable of simulating the details of tip-vortex formation and their evolution. Up until now, URANS, DES and LES turbulence models have been used for the analyses of interactional helicopter aerodynamics. DES and LES analyses provide much more realistic flow field predictions in both space and time; however, requirement for excessive amount of mesh elements and short time-steps makes these models still computationally very expensive for most of the engineering applications

2.1 Simplified methods

One of the simplest methods for performance calculations of rotor blades is known as Blade-Element Momentum (BEM) method, [107]. This method gives satisfactory results and it is cheap in computation, [108]. In the BEM method, the flow field is represented by control volumes in order to be able to perform computations. Momentum balance and energy conservation are applied in each control volume. This method does not account for wake expansion, whereas the induced velocity in the rotor plane is assumed to be one-half of the induced velocity in the ultimate wake, [109]. The blade is considered as a combination of independent elements (cross-

sections/airfoils) with which the overall blade characteristics and flow field predictions can then be obtained. The airfoil data, which are going to be used as an input in the method to obtain the aerodynamic forces on each blade element, are gathered from wind tunnel measurements. These wind-tunnel airfoil data, before being an input to the computations, are processed and corrected for three-dimensional effects. The predictions obtained at each section along the blade span are then integrated to obtain the overall performance characteristics of the blade, [110]. The rated power, power coefficient, mean free-stream speed, number of blades are the input parameters. Rotor diameter, chord and twist distributions are the outputs of the method. This method does not account for tip losses and turbulence effects. It is necessary to apply, at least, the following two corrections in order to get better results. The assumption of an infinite number of blades is corrected by Prandtl's tip loss factor. Glauert's correction is applied for such situations when the axial interference factor is greater than 0.3. Although it is being a cheap and reliable method, there are some limitations for some kind of situations such as the dynamic inflow, yaw misalignment, tip loss and heavily loaded rotors, [111].

For a detailed information of a flow around a 3D structure, inviscid aerodynamic models have been developed. In these simplified approaches, the viscous effects are neglected. There have been some studies on viscous-inviscid interaction techniques. According to Hansen et al. [112], these techniques have not yet reached the desired level of accuracy to become engineering tools.

In panel methods, the flow is assumed to be inviscid and incompressible. The flow field around the blades can be simulated with the help of elaborately distributed sources and dipoles. Source distributions are used to shape the solid boundaries. Dipoles, which are responsible for the creation of circulation, are included in the flow field to simulate lift, [111, 112].

In vortex models, lifting lines or surfaces represent the rotor blades and the flow structures in the wake, [113]. The lift force is created as the flow passes the blades. Then, the vortex strength on the blades can be obtained from the predicted lift. If the strength and position of the vortices is known, then the induced velocity $w(x)$ can be found using the Biot-Savart induction law;

$$w(x) = -\frac{1}{4\pi} \int \frac{(x - x')\omega'}{|x - x'|^3} dV \quad (2.2)$$

In equation (2.2), x is the location where the potential is computed and ω is the vorticity. The integration is taken over the region designated by V , where the vorticity is non-zero and x' is the point of integration. The calculation of circulation is similar to the BEM method and depends on the use of airfoil data. In this method, the induced velocity, the blade velocity, and the undisturbed free-stream velocity are considered to determine the inflow. The relationship between the bound circulation (Γ) and the lift coefficient (C_L) can be given by equation (2.3),

$$L = \rho U_{rel} \Gamma = \frac{1}{2} \rho U_{rel}^2 c C_L \quad \rightarrow \quad \Gamma = \frac{1}{2} U_{rel} c C_L \quad (2.3)$$

where L is the lift force, ρ is the density of the fluid, U_{rel} is the relative velocity seen by the blade section, and c is the local chord length.

Moreover, rotor performance can be evaluated by using actuator disc models. These techniques were frequently used in the past. In these models, the actual rotor geometry is not used. In an alternative way, a permeable disc is modeled to simulate the effect of the blade surface forces. There are many different applications of the actuator disc model. For instance, the actuator disc model can be combined with a blade-element analysis. The result of this approach is the classical Blade-Element Momentum Technique proposed by Glauert. In addition to that, the actuator disc method can be combined with the Euler and/or Navier-Stokes equations. As in a usual CFD computation, the governing equations can be solved by a second order accurate finite difference/volume scheme. The assumption made in the approach depends on the numerical integration of the evenly distributed surface forces along the actuator disc in the azimuthal direction. Therefore, the effect of an individual blade cannot be simulated. This can be given as the lack of the approach [111]. Sorensen and Shen [107] published an extended 3D actuator disc model to overcome the existent limitation. The body forces are distributed radially along each of the rotor blades by the proposed technique. The local angle of attack of the blades are computed iteratively to determine the airfoil characteristics and rotor loading. The influence of the tip vortices and the wake patterns on the inflow calculation can be determined.

2.2 Navier-Stokes solvers

The first studies on aircraft wings and helicopter rotor configurations with CFD using potential flow solvers have been studied in the late seventies and early eighties. The progress to unsteady Euler solvers was seen through the 80's. The first applications for helicopter rotor analyses including viscous effects were seen in the late eighties and early nineties. However, in the open literature, the first full Navier-Stokes computations of rotor aerodynamics were published in the late nineties, [114]. The physics for vorticity generation and its convection into the wake can be solved by the Navier-Stokes equations. Many multi-purpose flow solvers as given in Table 2.1 are available in the market. These codes are capable of performing incompressible or compressible flow analysis, inviscid or viscous turbulent flow analysis, and steady/unsteady flow analysis with moving meshes.

Table 2.1 : An overview for the multi-purpose flow solvers.

Company or Institution	Flow Solver
BOEING	HELIOS
DLR	FLOWer, TAU
EU	elsA, FASTFLO, HBM
FOI	EDGE
JAXA	rflow3D
NASA	FUN3D, NSU3D, OVERFLOW, USM3Dns
STANFORD	SU2

Performance variables of the rotor can be determined accurately by the prediction of the viscous drag acting on the blade. The direct numerical simulation of the Navier-Stokes equations is not affordable for most of the industrial flow problems due to the requirement for an intensive amount of computational power. Therefore, turbulence models are used for the numerical calculation of turbulent flows. Today, thanks to the evolution of high-speed computers, the computationally demanding large-scale viscous flow simulations of rotors can be solved. However, majority of the complex interactional rotor aerodynamics analysis is accomplished by specialized institutional codes such as those of National Aeronautics and Space Administration (NASA), Japan Aerospace Exploration Agency (JAXA) or European Union (EU). Therefore, a commercially available CFD solver, FLUENT, which is accessible by everyone, is used in the present study.

3. MATHEMATICAL FORMULATION

3.1 Navier-Stokes Equations

The three dimensional (3D) unsteady compressible viscous Navier-Stokes equations are the governing equations for fluid motion. The continuity equation is,

$$\frac{d\rho}{dt} + \frac{\partial}{\partial x_j}(\rho u_j) = 0 \quad (3.1)$$

The momentum equation can be written as,

$$\frac{\partial}{\partial t}(\rho u_i) + \frac{\partial}{\partial x_j}(\rho u_i u_j) = -\frac{\partial p}{\partial x_i} + \frac{\partial \hat{\tau}_{ij}}{\partial x_j} + \vec{F} \quad (3.2)$$

The energy equation can be written as,

$$\frac{\partial}{\partial t}(\rho e) + \frac{\partial}{\partial x_j}(\rho e u_j) = -\frac{\partial p u_j}{\partial x_j} + \frac{\partial}{\partial x_j}(u_i \hat{\tau}_{ij} - q_j) \quad (3.3)$$

where ρ is the density, u_j denotes the components of the velocity, p is the static pressure, e is the total energy, and $\hat{\tau}_{ij}$ is the stress tensor including both molecular and Reynolds stresses.

$$\hat{\tau}_{ij} = 2\mu \left(S_{ij} - \frac{S_{kk}\delta_{ij}}{3} \right) + \tau_{ij} \quad (3.4)$$

$$\tau_{ij} = 2\mu_t \left(S_{ij} - \frac{S_{kk}\delta_{ij}}{3} \right) - 2\rho k \frac{\delta_{ij}}{3} \quad (3.5)$$

$$S_{ij} = \frac{1}{2} \left(\frac{\partial u_i}{\partial x_j} + \frac{\partial u_j}{\partial x_i} \right) - 2\rho k \frac{\delta_{ij}}{3} \quad (3.6)$$

$$q_j = -\left(\frac{\gamma}{\gamma - 1} \right) \left(\frac{\mu}{Pr} + \frac{\mu_T}{Pr_T} \right) \frac{\partial T}{\partial x_j} \quad (3.7)$$

where μ is the dynamic (molecular) viscosity, μ_t is the turbulent dynamic viscosity, δ_{ij} is the Kronecker delta function, S_{ij} is the mean strain-rate tensor, q_j is the rate of total heat flux, γ is the ratio of the specific heats, Pr is the Prandtl number, Pr_T is the turbulent Prandtl number, and T is the static temperature.

In order to close the equations, the perfect gas equation of state is employed into the equations.

$$p = \rho(\gamma - 1) \left[e - \frac{1}{2} u_i u_i \right] \quad (3.8)$$

3.2 ALE Navier-Stokes Equations

The Navier-Stokes equations are written in the Arbitrary Lagrangian-Eulerian (ALE) form for the simulations of moving boundary problems.

ALE continuity equation is,

$$\frac{\partial \rho}{\partial t} + \nabla \cdot u - \vec{u}_g \cdot \nabla \rho = 0 \quad (3.9)$$

ALE momentum equation can be written as,

$$\frac{\partial(\rho u)}{\partial t} + \rho(u - \vec{u}_g) \cdot \nabla u = -\nabla p + \nabla \cdot \mu_m \left(\nabla u + u \nabla - \frac{2}{3} (\nabla \cdot u) \mathbf{I} \right) + \rho g \quad (3.10)$$

ALE energy equation is,

$$\begin{aligned} & \frac{\partial(\rho e)}{\partial t} + \rho(u - \vec{u}_g) \cdot \nabla e \\ & = \nabla \cdot (k \nabla T) + \nabla \cdot \left(\left[-p \mathbf{I} + \mu_m \left(\nabla u + u \nabla - \frac{2}{3} (\nabla \cdot u) \mathbf{I} \right) \right] \cdot u \right) \\ & + \rho g \cdot u \end{aligned} \quad (3.11)$$

where ρ is the density, u is the velocity, \vec{u}_g is the grid velocity, p is the static pressure, μ_m is the molecular viscosity, \mathbf{I} is the unit tensor, e is the specific internal energy, k is the thermal conductivity, and g is the gravity vector. In this study, the gravitational force was not taken into account. Once again, the perfect gas equation of state is employed into the equations to close the equation sets.

4. NUMERICAL METHOD

Many engineering problems related to fluid flow can be solved with the help of the fluid dynamics techniques. These techniques are being applied by solving the governing equations of fluid flow, which are derived from the basic physical laws. Generally, the equations to be solved are in the form of highly nonlinear partial differential equations. This brings an additional complexity to the solution of the fluid flow problem. Except for some very simple flow cases, analytical solutions of these equations do not exist. Therefore, physicists, mathematicians and engineers seek other ways of handling these equations [115]. Computational Fluid Dynamics (CFD) is the utilization of computers in order to provide information of a fluid under any condition. CFD with its outstanding features gives an insight into flow patterns by providing high resolution in both space and time. The solution searched for any disturbance object, no matter how its size, can be obtained by CFD simulations. However, it is not always possible to adjust the laboratory facilities for experiments. CFD packages are now a viable supplement to the very costly experimental measurements. Therefore, CFD may also be used to improve the understanding of complex physical phenomena when conducting an experiment becomes difficult. It includes many disciplines such as mathematics, physics, computer technology and engineering. Simulation parameters of a fluid flow should be determined carefully in order to gain results that are more reliable. Obtaining reliable results depends on the type of the problem, software and the user's knowledge and abilities. Nowadays, there exist many commercial CFD software packages. However, a comprehensive fluid mechanics knowledge is required in order to utilize these codes properly. Beforehand, a methodology should have been determined for the solution of a flow problem. For instance, each step (e.g. physics of the problem, geometry modeling, mesh generation, suitable solution schemes etc.) should have been constructed accurately. Moreover, the requirements of the commercial code (boundary conditions, coefficients etc.) should be obtained. This can be done by means of experiments, as well as by prior numerical analyses [116]. There are many different stages while inquiring for the solution of a CFD problem. The phases described here are actually well-known regular procedures. The first and

possibly the most time consuming one is the geometry and grid generation stage. Following stage consists of a physical model selection, which is required to simulate and to model the turbulent flow phenomena. The difficulty exists in this stage is related mostly to the determination of the physical model to be used for the solution of a turbulent flow regime, since the results are strongly dependent on the chosen physical model. The turbulence model should provide accurate results by ensuring a remarkable reduction in the computation time. This can be achieved by utilizing the intelligently simplified modeling equations. After having determined the turbulence model, the modeling equations are solved by an iterative process with the proper set of numerical schemes. The final stage is the post-processing, which is necessary to examine the computed data [117]. Accuracy of the numerical simulations directly related to the well-represented geometry with a proper mesh resolution, used turbulence model and the numerical schemes. In this study, the rotor/fuselage flow interaction problem is solved with the help of a commercially available finite-volume Navier–Stokes CFD solver, FLUENT.

4.1 Finite Volume Approach

The finite volume method (FVM) is used widely in numerical studies. FVM is a very useful approach, as it provides the solution with a lower memory usage, especially for large-scale problems. In the finite volume method, the governing equations are in the conservative form, and the discretization ensures the conservation of fluxes through the discrete control volumes. Jameson and Mavriplis provided the first successful application of finite volume method on unstructured grids [118]. Jameson et al. [119] published the calculation of inviscid transonic flow over a complete aircraft on unstructured grid solver via using first order scheme in 1986. However, a high order scheme should be adopted to avoid numerical diffusion. For instance, Desideri and Dervieux [120] derived a third order accurate MUSCL discretization for unstructured grids based on a cell-vertex finite volume scheme.

In this study, the governing equations of Navier-Stokes are solved via control volume based technique [121-123]. The pressure-based and density-based solvers are the two numerical methods available in FLUENT. The pressure-based solver was developed for low-speed incompressible flows, whereas the density-based solver was created for

the high-speed compressible flow solutions. The density-based coupled solver is more preferable when there is a strong interdependence between the field variables.

In the pressure-based approach, a pressure correction equation is solved to obtain the pressure field. The Segregated and Coupled methods are the two types of pressure-based solution algorithms provided by FLUENT. The segregated pressure-based solver uses a decoupled solution algorithm where the governing equations are solved sequentially from one another. The coupled pressure-based algorithm solves a coupled system of equations involving the momentum equations and the pressure-based continuity equation, [123]. The solution convergence of the pressure-based coupled algorithm is better (faster) than the segregated pressure-based solver. However, the memory requirement increases by approximately two times that of the segregated algorithm for the solution of same number of grid points. In the pressure-based coupled solver, the spent time for the solution of each iteration becomes larger. Moreover, the pressure-based coupled solver is not available for multiphase flows.

In our case, the study is carried out for a scaled helicopter model under mildly compressible flow conditions where none of the shock formation exists in the flow field. Our aim is to demonstrate an engineering solution approach for the examined ROBIN test cases within acceptable accuracy and practical computation time. The segregated solver is robust and provides lower memory requirements. The segregated algorithm is valid and applicable for incompressible and mildly compressible flows. When flows with significant discontinuities present in it, use of density-based coupled or pressure-based coupled solvers will be a necessity. Nonetheless, there are publications, which state that the segregated algorithm can be used even for the supersonic flow regimes [124-126]. In this study, the segregated pressure-based solver and collocated cell-based grid arrangement have been used to carry out a practical solution approach. The gradients at the cell faces are computed by using Least Squares Cell-Based formulation.

4.2 Pressure-Velocity Coupling

The pressure gradient contributes to each of the three momentum equations. The pressure equation is a constitutive equation and it is hard to find an independent equation for pressure. Thus, the solution of Navier-Stokes equation becomes complicated. Pressure is used as a mapping parameter to satisfy the continuity

equation. For an incompressible flow, the pressure field should be generated by satisfying mass conservation. The pressure correction is achieved by solving the Poisson equation. Then, within this iterative process, new pressure and velocity fields can be predicted by using the pressure correction. FLUENT provides several approaches for pressure-velocity coupling. The user can choose the appropriate one among five algorithms provided. These are the segregated pressure-based SIMPLE, SIMPLEC, PISO and Fractional Step Method (FSM). These schemes are based on the predictor-corrector approach. In addition, the fifth algorithm provided for pressure-velocity coupling is the pressure-based COUPLED solver.

In sections 6.1 and 6.2, the performance of the pressure-based COUPLED solver is examined. Since the examined test cases do not include any discontinuities, no further benefit was observed by the use of Coupled solver, but the computation time was increased. However, if a strong-interdependence exists between the flow variables, Coupled solver would be much convenient for computations. In section 6.2.2 and after, in order to create a practical solution strategy for unsteady compressible flow analysis of rotor-fuselage interactional aerodynamics where the dynamic mesh approach is incorporated, the pressure-based segregated algorithm, which is a semi-implicit method for pressure-linked equations (SIMPLE) based on the predictor-corrector approach, is adopted for the pressure-velocity coupling. Some complex flow types may cause large gradients in the momentum source terms between control volumes, thus resulting with steep pressure profiles at the cell faces. For that reason, the most appropriate pressure interpolation scheme convenient with the flow regime, by which the interpolation errors can then be considerably reduced, should be employed to achieve an accurate computation. In this study, the pressure interpolation have been performed using a second order scheme for the compressible flow analysis.

Under-relaxation of equations are used in the pressure-based solver to control the update of computed variables at each iteration. Each equation have under-relaxation factors associated with them. These factors are used to stabilize numerical schemes by limiting the effect of the previous iteration over the present one. Under-relaxation values can be changed to obtain faster convergence or to prevent divergence. The change in relaxation values may cause a change in the number of iterations. However, the results are independent of relaxation values. The under-relaxation factors are kept as their default values with which no convergence problems are encountered.

4.3 Spatial Discretization

Staggered grid approach and collocated arrangement are frequently used in the pressure based solvers. Staggered grids use different control volumes for each of the different flow variables. On the other hand, collocated arrangement needs only one volume for storing all the flow variables. Especially, in three dimensional space, the staggered grid approach becomes computationally prohibitive, which forms the major disadvantage of the approach. FLUENT provides two types of approaches to locate primitive variables in a given grid. The first one is the collocated node based arrangement, where all of the primitive variables (e.g. pressure and velocities) are both stored at the vertices of a mesh element. The second one is the collocated cell based arrangement, whereby pressure and velocity are both stored at cell centers. No matter which of the two approaches is employed, the field variables must be interpolated to each face of the control volume in order to perform the flux computation. The cell-based approach yields a faster computation than the node based arrangement. Nonetheless, the use of collocated grid system may give rise to numerical oscillations in the solution. These oscillations are tried to be eliminated by using artificial damping terms or interpolation schemes. In this study, the behavior of the cell-based and node-based approaches is examined for isolated fuselage configuration in Section 6.1.2.2. The cell-based arrangement is used to reduce the computational effort while performing the dynamic mesh simulations found in Sections 6.2.2 and 6.3.

In order to calculate the velocity derivatives and diffusive fluxes, the gradients of solution variables are required. The gradients across the cell faces can be computed by a variety of methods available in FLUENT. The Green-Gauss Cell-Based, Green-Gauss Node-Based and the Least Squares Cell-Based methods are provided by the code for the computation of the gradients. The least computationally demanding one is the Green-Gauss Cell-Based method. However, when using this method, the numerical solution may have false diffusion, especially when the flow field is dominated by convection. The grid may be aligned with the free-stream direction to minimize false diffusion. Moreover, the grid resolution and/or the order of the discretization scheme may be increased in order to reduce the false diffusion errors. In addition, the Green-Gauss Node-Based provides a minimized false diffusion. Furthermore, the computation of the gradients using node-based formulations is known to be more stable and accurate, especially for unstructured meshes. However,

this method is the most computationally intensive one among the three methods mentioned here. What is fascinating is that the accuracy of the Least Squares Cell-Based formulation is comparable to node-based gradients, while being less computationally intensive [123].

Another significant topic affecting the accuracy of the numerical computations is the grid resolution. Improving the grid resolution and/or increasing the order of the spatial discretization form a basis to overcome numerical diffusion toward a better flow prediction. Refining the grid is a possibility at the preprocessing stage to enhance the spatial accuracy. The grid resolution can also be increased automatically during the computation by the application of the adaptive mesh refinement (AMR) technique to improve the accuracy of a solution. The utilization of the AMR technique for the high-fidelity analysis of the wake features will provide a better capture for the roll-up of the tip vortices and thus, more realistic flow field predictions. It is believed that the computation time may be reduced with a careful set of refining-coarsening levels. The effect of the technique on the computation time may be examined in a future study. In this study, the volume mesh refinement was not done by using a solution-based adaption feature like Adaptive Mesh Refinement (AMR) technique. However, the possible wake regions, where a finer grid is generated at the preprocess stage, were determined by the help of previous numerical predictions, which ensure already visualized wake patterns for the test cases examined. The pre-adaptation is performed at a moderate level by considering computational effort. Prior numerical studies found in literature have been considered as reference to determine suitable grid sizes. These used grid metrics are consistent with the use of standard wall function approach, which enabled the number of mesh elements to be kept at an acceptable level.

Moreover, the second order upwind and third order MUSCL are examined as spatial discretization schemes for the momentum equation and the transport equation of turbulence parameters (k - ϵ).

4.4 Temporal Discretization

The solution of an unsteady problem varies with time for a particular position. The governing equations are discretized in both space and time in the transient simulations. The spatial discretization is done similarly as in the steady state analysis. In the finite

volume method, the integral of the transient term is evaluated to perform the temporal discretization.

Both explicit and implicit time marching algorithms are available in the density-based coupled solver. The point-implicit Gauss Seidel, symmetric block Gauss-Seidel and ILU methods can be used for implicit time advancement. For explicit time marching, a multi-step Runge-Kutta time integration method is used. The use of explicit approach would be much convenient for cases where the characteristic time scale of the flow is on the same order as the acoustic time scale.

Dynamic mesh simulations currently work only with first-order time advancement in the solver. Hence, temporal discretization depends on the first-order implicit formulation for the time accurate computations. The possibility for enhancing the temporal accuracy may be sought by making FLUENT second-order accurate in time for the moving boundary problems via embedding a UDF code, in a future study.

In addition, determination of a proper time step size is of great importance for the temporal accuracy of unsteady computations. The order of magnitude of an appropriate time step size can be estimated by the ratio between typical cell size and characteristic flow velocity. Furthermore, there are other important issues to be considered while setting a time-step size. The followings are very important and should be taken into consideration for accurate simulations:

- Time-step should be small enough to resolve time dependent features and turbulent quantities.
- Time step size can be chosen according to a known period of fluctuations by which the unsteady characteristics of the flow can be resolved.
- The amount of blade motion is determined by the defined time-step size as an input. FLUENT emphasizes that “the amount of displacement in one time step should not be more than half the cell size adjacent to the moving boundary”.
- Improper time step size can adversely affect the accuracy and stability of the numerical scheme.
- The CFL condition ($CFL \leq 1$) should be satisfied if shock waves exist in the flow field.

A sensitivity study on the effect of azimuth angle increment was performed with increments of 1.0, 0.2, and 0.1 degrees for HART II computations in a prior numerical study [38]. According to their results, BVI peaks could not be captured in the solution obtained by using 1-degree increment. On the other hand, the results for 0.2 and 0.1 degree increments are in good agreement with experiments and the results of both time-steps are also consistent with each other. In HART II tests, the blade tip Mach number value is a little bit higher than ROBIN test cases. The impact of the time-step size becomes even more dominant particularly, for both phase and magnitude predictions when the flow field is transonic or supersonic. In such flow regimes, a relatively small time-step value may be required in order to capture the blade passing effect. In another numerical study, the CFD-FASTRAN flow solver has been used to evaluate the performance of the code for the ROBIN test cases [40]. The authors stated that the time step size was chosen small enough to make the computation stable. The stable results have been achieved by using a 0.1-degree increment in the azimuth direction. Moreover, in another numerical study, the solution was advanced with a time step equivalent to 1-degree blade movement for the same ROBIN test cases by using a specialized solver, FUN3D, [30, 37]. These prior studies show that using 1-degree as time stepping can propose reliable results.

In Figure 4.1 (a), a total of 1-degree blade movement is represented by quarter-degree turns. Considering the given references' results, it can be concluded that the selection of the time-step value corresponding to 1 degree of the blade movement can provide sufficient accuracy for the computation of flow physics, particularly because of the properly captured time dependent geometrical changes of the blades in space and thus, their effects on the flow field. This has been resulted in this way mostly because of the negligible variations in flap and pitch motions occurring within the selected 1 degree azimuthal increment, as shown in Figure 4.1 (a). Moreover, although a high enough time-step size (corresponding to 1-degree blade movement) has been used by the FUN3D code, the results obtained have been well correlated with experimental measurements, because of its robust implicit solution methods. Relatively large time step sizes can be assigned without any losses in the accuracy of a solution, in which the high order implicit numerical schemes are used in both space and time, as in FUN3D code. However, the question 'how large' can be answered by considering the above listed significant items, which form the fundamentals for the time step size

selection. Generally, for the moving boundary simulations, the time dependent geometrical changes should be represented properly (this should be the major concern) with a carefully determined time step size.

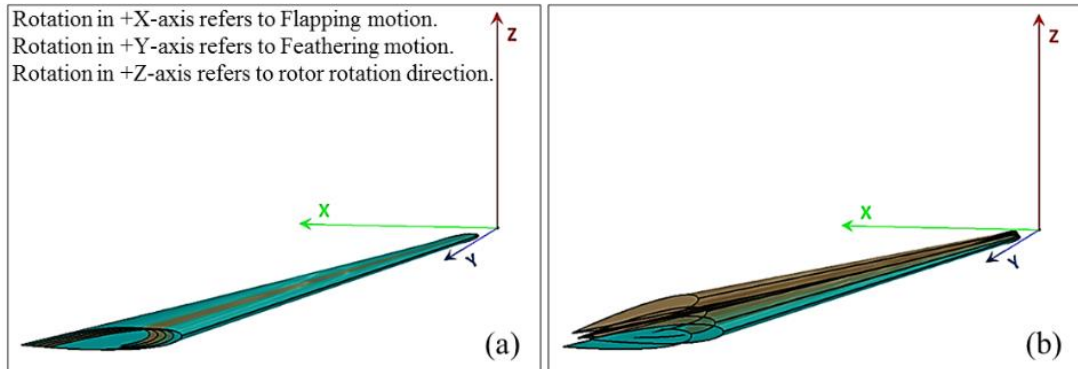


Figure 4.1 : Change in the blade's position: (a) actual, (b) imaginary.

Figure 4.1 (b) represents an arbitrarily generated imaginary situation and is not related with examined test cases. For instance, in such a situation depicted by Figure 4.1 (b), where enormous variations occurring in flap and pitch motions during the selected time step size, the results may not be obtained accurately even by the FUN3D code, as the change in the blade position is not represented properly in space. These variations will be lost because of the large jump exists in the selection of the time-step. In one hand, as shown in Figure 4.1 (a), the geometrical changes within the 1-degree movement in azimuth direction are negligible. On the other hand, as shown in Figure 4.1 (b), even for the same time step size, the changes are at a significant level, which can cause remarkable differences on the results. Briefly, which makes the selection of time step size important is that the circumstances happening during this time interval. Moreover, none of the solvers could produce reliable results if the time dependent features (here; they are the changes in blade's positions with time) are not properly captured or represented, no matter how robust or fully coupled implicit schemes are being used by the codes.

Furthermore, acceptable time step size is a code dependent parameter. Thus, even for the same time step size, the obtained results produced by the two different solvers may differ from one to another. The discrepancies are mostly because of the differences found in the numerical schemes used by the codes. The only way to alleviate these discrepancies is to carry out a time-step sensitivity study. Therefore, a sensitivity study is carried out using 1.0, 0.5, and 0.25° blade motions as time stepping in the azimuth direction. The analysis was performed for rotor only case ($\mu=0.231$). Figure 4.2 shows

the obtained results for each of the four blades when using different time-step increments. According to the figure, the prediction of thrust coefficient was not affected much for the examined test case, but slight differences have been observed due to the change in time-step selection.

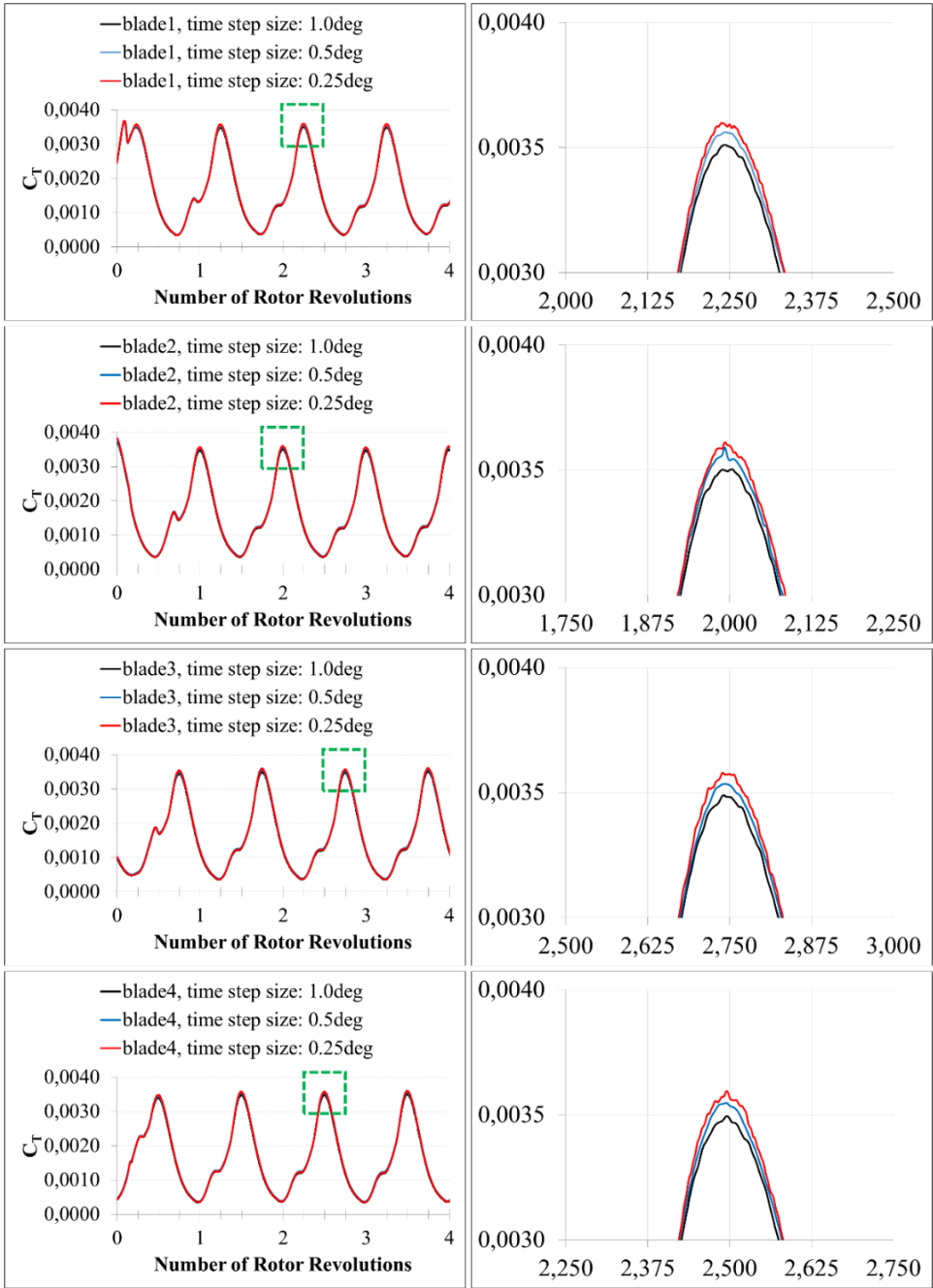


Figure 4.2 : Time-step sensitivity study for rotor only case ($\mu=0.231$).

The accuracy of phase predictions remained the same. The minor discrepancies are found in the prediction of magnitudes. The decrease in the time step increment had made the prediction of thrust coefficient converged to a higher value where the peaks found. The relative error found between the results of 1.0 and 0.5° time-steps is up to

1%, whereas it is far below 1% when the results of 0.5 and 0.25° are compared. It is evaluated that the results of 0.25° blade motion in the azimuth direction has given similar results to those of 0.5°. Therefore, in the present study, the solution is advanced with a time step equivalent to 0.5° blade motion in the azimuth direction, to both satisfy FLUENT's minimum time-step requirements while also preserving the efficiency of the computations.

Another important parameter influencing the accuracy of a solution is the solution convergence. In this study, a particular attention has been given for the convergence level of the solution obtained at each sub-iteration. Allowing five fixed sub-iterations for each time step to carry out a practical engineering approach yielded a reduction of the residual of two to three orders of magnitude. An acceptable convergence at each time-step has been achieved without having any stability problems during the computations. The root mean square (RMS) values are obtained below 10^{-3} for the continuity, 10^{-7} for the momentum and 10^{-10} for the energy equations (Figure 4.3).

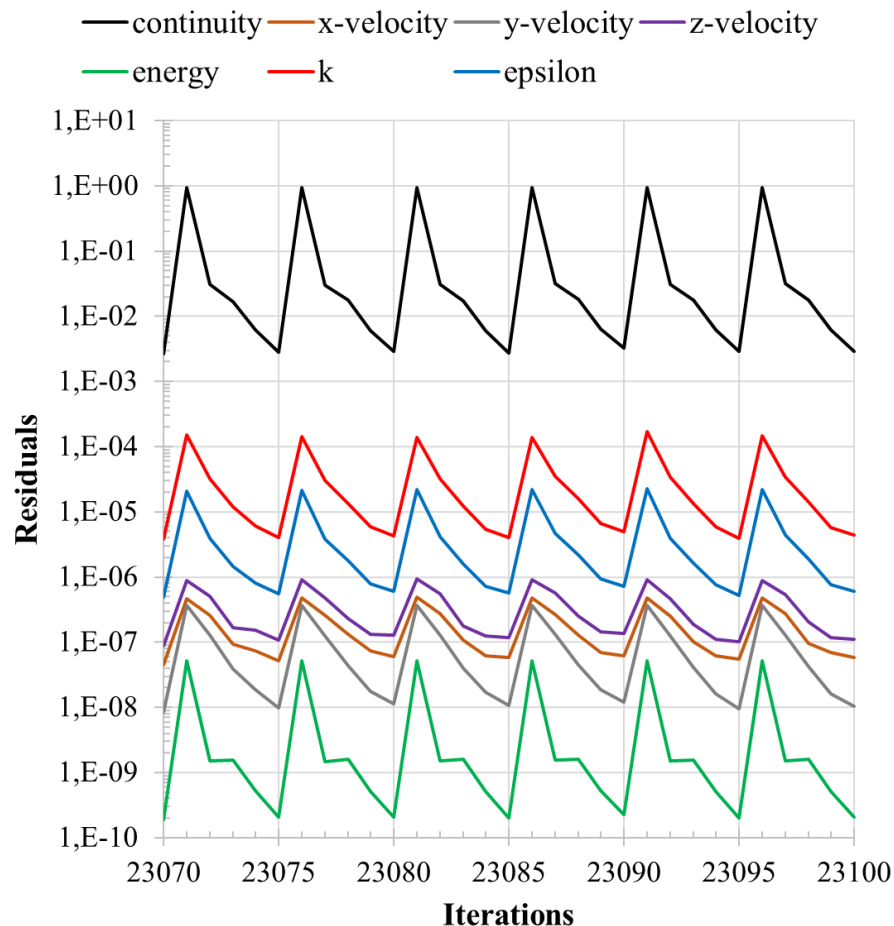


Figure 4.3 : Convergence history for rotor only case ($\mu=0.231$).

The number of sub-iteration can be increased to obtain a well-converged solution. This could also be done with the predefined convergence criteria for each of the equations to achieve a desired convergence level. Examining the effect of convergence level is left as a future study to investigate the behavior of the FLUENT software. Therefore, one should consider that a converged solution is not necessarily a correct one. For transient calculations, a converged solution can only demonstrate the results obtained with the chosen time step resolution. How the results would be like if a smaller time step had selected? If the same or very similar results are obtained with smaller step sizes then, it can be concluded that the chosen time step size is acceptable. Briefly, to perform accurate unsteady simulations, both the chosen time-step size and the achieved convergence level at each time-step should satisfy the requirements of the examined flow condition. There needs to be one thing in order to talk about the accuracy and precision of a solution. The results should be consistent with the measured data. After all, an accurate and precise solution could be obtained.

4.5 Boundary and Initial Conditions

To represent the physical model, the flow variables on the boundaries are specified as the boundary conditions. The solution accuracy depends on the appropriateness of the chosen physical models and the specified boundary conditions. Therefore, the boundary conditions should be considered according to physical processes in the boundary region. Nonphysical effects can be seen on the region of interest because of the use of inappropriate boundary conditions. For that purpose, generally, at the beginning of the CFD computations, experiments are performed to simulate the relevant flow problem with which the initial and boundary conditions of the problem can be obtained. The initial and boundary conditions determined by the experiments are being used as the inputs of the CFD code. Then, the results of the CFD code should be correlated with the experimental measurements. The CFD code becomes reliable when a satisfactory correlation between numerical and experimental results has been obtained.

The first-type boundary condition is the Dirichlet boundary condition where this condition specifies the value of the function itself on the boundary. The second-type boundary condition is the Neumann boundary condition, which specifies the value of the normal derivative of the function on the boundary. The Robin, Mixed and the

Cauchy boundary conditions can be given as examples of other types of boundary conditions, which involve a combination of Dirichlet and Neumann boundary conditions, but with some slight differences in application. For instance, the Robin boundary condition specifies a linear combination of values of a function and the values of its derivative on the boundary. In a mixed boundary value problem, the solution should satisfy a Dirichlet boundary condition for a part of the boundary, and the solution at the remained part of the boundary should satisfy a Neumann boundary condition. A Cauchy boundary condition specifies both the Dirichlet and Neumann boundary conditions for a same boundary where the solution should satisfy both the specified conditions at the same time [127].

The boundary conditions should be assigned according to the used formulation for the governing equations. The governing equations can be written in a conservative or non-conservative form. The implementation of the boundary conditions can be very difficult, especially when conservative formulations are used. For compressible flow computations, particularly when significant discontinuities such as shock waves are present in the flow field, the use of conservative variables may provide advantages over the primitive variable formulations. A better accuracy may be obtained using conservative formulations, however; storage requirements for the field variables may become quite extensive. In this study, the momentum and the energy are being computed from the initially defined primitive variables such as the velocity (U_0), density (ρ_0), pressure (P_0), and temperature (T_0). The undisturbed free stream condition has been assigned as an initial condition for the time-dependent compressible viscous flow simulations.

A pre-consideration should be done before assigning boundary conditions to the walls. Wall boundaries may be either stationary or moving. At a fixed-wall, no-slip conditions are specified while carrying out a viscous flow simulation, where the flow velocity should vanish on the wall surfaces ($\vec{u} = 0$). Regarding the Euler equations, where an inviscid flow assumption has been made, thus free-slip condition is specified to the walls, which allows the presence of tangential velocities, whereas the normal velocity should vanish ($\vec{u}_n = 0$). For a moving (translational or rotational) wall, the flow velocity on the wall surfaces should be the same as the wall velocity. Moreover, wall boundaries can be either isothermal or adiabatic. The temperature is assigned to the walls ($T = T_{wall}$) when specifying isothermal boundary conditions. For adiabatic

boundary conditions, the normal heat flux, ($\vec{\nabla}T \cdot \vec{n} = 0$), should be assigned as zero. Here, T_{wall} is the wall temperature, and \vec{n} is the unit vector in the direction normal to the wall surface. Furthermore, for turbulent flow simulations, wall roughness can be specified on the solid surface to investigate the effect of wall roughness on the turbulent flow characteristics.

Symmetry boundary conditions are frequently used in CFD computations when the physical geometry of interest have a plane of mirror symmetry. This type of boundary condition helps to reduce computational expense. Symmetry BC implies that the normal velocity ($\vec{u}_n = 0$) and normal gradients of all variables ($\vec{\nabla}\phi \cdot \vec{n} = 0$) are zero at the symmetry plane. In addition, symmetry BC can also be used to model an inviscid wall.

Periodic boundary conditions are used when the flow pattern and other flow variables have a periodically repeating behavior. The field variables are mapped from one side to the other between periodic pairs, $\phi(x_1) = \phi(x_2)$. Computational effort can be reduced significantly depending on the periodicity angle. For instance, for a four-bladed rotor simulation, only the quarter portion of the flow field can be modeled as the computational domain. Thereby, computational costs may reduce to one fourth of the whole configuration. The application of this boundary type can be found in Section 6.2. The interested reader may refer to FLUENT's theory manual [123] for further information on other types of boundary conditions.

Moreover, the determination of the flow domain size is another important parameter, which directly influences the accuracy of the solutions. Choosing an inappropriate domain size is one of the most common errors made at the beginning of the computations. The flow domain size can be determined based on the dimensions of the wind tunnel where the experiments are conducted. In case of using actual wind tunnel dimensions, the tunnel walls and the adjacent region should be represented with a proper grid resolution in order to predict the blockage ratio accurately. Therefore, modeling the actual wind tunnel would bring additional computational effort due to the increased number of grid points in the near-wall region. In this study, the aerodynamic interference effects between the main rotor and fuselage are primarily focused on. In addition, it is aimed to perform an external flow simulation because of a particular reason and thus, the actual tunnel dimensions were not used. It is intended to analyze the interference effects not only in the rotor near field in which the flow is

highly viscous and possibly compressible, but also in the entire wake region, to observe and investigate the tip vortex formation and their evolution. Considering an external flow simulation, inadequate choice of flow domain, especially the outlet boundary, can significantly affect solution's accuracy. Therefore, the size of the flow field was determined as large as possible. The domain boundaries are formed by a cylindrical shape and cover a region that is of 15 vehicle lengths to the upstream and radial directions. The domain extends 30 vehicle lengths (or approximately 35 rotor radii) to the downstream direction.

For compressible flows, free-stream condition at infinity can be modeled by the use of pressure-far-field boundary condition with specified free-stream Mach number and static conditions. Pressure-far-field BC uses Riemann invariants to determine the flow variables at the boundaries. In our simulation, the density is calculated using the ideal-gas law and the rest of the outer boundaries are placed far enough from the geometry. Therefore, pressure far-field boundary condition is applicable. In this work, however, Pressure Inlet and Pressure Outlet boundary conditions are assigned for all the outer boundaries of the computational domain. FLUENT, do not use Riemann invariants for the Pressure Inlet/Outlet boundary conditions. However, they are suitable for both incompressible and compressible flow calculations. In FLUENT, for external flow computations, pressure inlet boundary conditions can also be assigned to define a 'free' boundary, which allows the fluid in and out of the boundary face. In compressible flows, the total pressure, static pressure, and velocity of an ideal gas can be obtained from the isentropic relations to assign at a pressure inlet boundary. At a pressure outlet boundary, the static pressure can be specified if the flow is subsonic. This condition is convenient when the free-stream Mach number for the examined test cases is considered. At the inlet, the total pressure, total temperature and flow angle are specified, and at the exit, a fixed static pressure is specified. Upper half of the cylindrical boundary is defined as a Pressure Inlet where all the specifications assigned for the Inlet boundary were kept the same. The lower half of the cylindrical boundary is defined as the Pressure Outlet with a specified fixed static pressure. Medium turbulence level is assigned at inlet sections by defining the turbulent intensity as 5% and five for the viscosity ratio. Wall boundaries are assumed to be adiabatic and viscous (no-slip).

4.6 Methods for Modeling Rotating Bodies

FLUENT presents choices for the flow around a stationary or a moving/rotating object by solving the equations of fluid flow. Moving reference frame, sliding mesh and dynamic mesh techniques can be used to simulate flow over moving/rotating bodies. The moving reference frame (MRF) is one of the most preferred CFD modeling technique to simulate rotating bodies. It is a relatively simple and robust technique; however, it works in a steady-state manner. MRF provides a weak interaction between the rotating reference frame and the surrounding stationary volumes. However, moving mesh techniques, which provide strong interactions between the rotating zone and the surrounding stationary volumes, can be used for the solution of moving boundary problems. Sliding and dynamic mesh techniques available in FLUENT can be given as the examples of moving mesh techniques. Moving mesh technique is based on the unsteady numerical solution procedure where the grid velocities are assigned to the mesh elements representing the moving/rotating bodies. Moving mesh technique also provides a better solution accuracy compared to MRF approach. However, the computation time takes much longer than that of a solution obtained by MRF approach.

4.6.1 Moving reference frame

Many problems require the equations to be solved in a moving reference frame. A rotating blade of a rotor is such a case. For the application of this technique, the fluid domain should be generated within a moving reference frame definition. Single or multi reference frames can be created according to the complexity of the problem. For instance, if more than one rotor is to be analyzed, then a multiple reference frame definition is needed. In this approach, the actual rotating wall boundaries are assumed to be stationary. For implementing the effect of rotation, the non-wall boundaries (cylindrical, spherical) are assumed to be the surfaces of revolution. A constant speed of rotation is assigned to the fluid volume. Knowing its limitations, for most of the engineering problems involving rotational parts, MRF technique is preferred due to its robustness and simplicity. The moving reference frame (MRF) and mixing plane (MP) models are models that are applied to steady-state cases, thus neglecting unsteady interactions. Therefore, the blade passing effect, which is an inherently unsteady event, cannot be obtained by the MRF approach.

4.6.2 Sliding mesh technique

The sliding mesh model does not neglect unsteady interactions. The relative motion of stationary and rotating components can be handled by the sliding mesh technique. The application of the sliding mesh technique is very similar to that of MRF where the rotating and stationary domains have to be created once again. However, this time, the volume meshes representing the rotating domain actually rotates. The sliding mesh model is an accurate method for simulating unsteady flows in multiple moving reference frames. Nevertheless, the sliding mesh technique is more computationally demanding compared to moving reference frame approach [123]. In the sliding mesh technique, two or more cell zones (e.g. for coaxial rotors) are used to model the blade motion when the motion of the cell zones is relative to each other along the mesh interface. Node alignment along the mesh interface is not required.

4.6.3 Dynamic mesh technique

Another moving mesh capability available in FLUENT is the dynamic mesh technique. The dynamic mesh technique is possibly the most general one to simulate flows involving moving and deforming cell zones. The mesh motion can be assigned to a fluid volume that surrounds the rotating body to provide the rigid mesh motion of this rotating domain. Moreover, the mesh motion can be assigned to particular mesh elements such as the blades or any other rotating parts to enable the motion within a deforming mesh by taking the advantage of re-meshing facility. The integral form of the conservation equation for a general scalar (ϕ), on an arbitrary moving control volume can be written as in equation (4.1), [123]. In the equation, ρ is the fluid density, \vec{u} is the flow velocity vector, \vec{u}_g is the grid velocity of the moving mesh, Γ is the diffusion coefficient, and S_ϕ is the source term of the scalar (ϕ). ∂V denotes the boundary of the control volume. The time derivative term can be written by using a first-order backward difference formula, which is given by equation (4.2),

$$\frac{d}{dt} \int_V \rho \phi dV + \int_{\partial V} \rho \phi (\vec{u} - \vec{u}_g) \cdot d\vec{A} = \int_{\partial V} \Gamma \nabla \phi \cdot d\vec{A} + \int_V S_\phi dV \quad (4.1)$$

$$\frac{d}{dt} \int_V \rho \phi dV = \frac{(\rho \phi V)^{n+1} - (\rho \phi V)^n}{\Delta t} \quad (4.2)$$

The volume at $n + 1^{th}$ time level is computed from,

$$V^{n+1} = V^n + \frac{dV}{dt} \Delta t \quad (4.3)$$

where dV/dt is the volume time derivative of the control volume and its computation is given by equation (4.4) in which the mesh conservation law is being satisfied.

$$\frac{dV}{dt} = \int_{\partial V} \vec{u}_g \cdot d\vec{A} = \sum_j^{n_f} \vec{u}_{g,j} \cdot \vec{A}_j \quad \text{and} \quad \vec{u}_{g,j} \cdot \vec{A}_j = \frac{\delta V_j}{\Delta t} \quad (4.4)$$

n_f denotes the number of faces on the control volume and \vec{A}_j is the face area vector. δV_j is the volume swept out by the control volume face j over the time step Δt .

The Geometric Conservation Law (GCL) states that the volume time derivative of the control volume must be equal to the summation of the volumes swept out by the control volume faces over the time step Δt , which is shown in equation 4.4. The compressible ALE continuity equation can be written as

$$\frac{d}{dt} \int_V \rho dV + \int_{\partial V} \mathbf{n} \cdot (\vec{u} - \vec{u}_g) \rho d\vec{A} = 0 \quad (4.5)$$

For $\rho = 1$, and $\nabla \cdot \mathbf{u} = 0$, the continuity equation takes the following form, which is the mathematical description of the GCL.

$$\frac{d}{dt} \int_V dV - \int_{\partial V} \mathbf{n} \cdot \vec{u}_g d\vec{A} = 0 \quad (4.6)$$

The first term of above equation denotes the volume time derivative of the control volume and the second term is the volume swept out by each control volume face. Spurious numerical oscillations may occur if the numerical algorithm do not obey the GCL. However, a numerical scheme always provide a constant solution being independent of the mesh motion, when the GCL is satisfied at the discrete level. The volume time derivative can be found by using a first-order backward difference formula, which is applied in equation 4.3. Now, the first term of equation 4.6 can be rewritten as

$$\frac{dV}{dt} = \frac{V^{n+1} - V^n}{\Delta t} \quad (4.7)$$

The second term of equation 4.6 can be rewritten as

$$\int_{\partial V} \vec{u}_g \cdot d\vec{A} = \sum_j^{n_f} \vec{u}_{g,j} \cdot \vec{A}_j \quad (4.8)$$

The velocity is the change in position within a time interval. The displacements of the face centroids between two subsequent time levels can be used to estimate the grid velocity. Since \vec{u}_g is the grid velocity, it can be written as follows:

$$\vec{u}_g = \frac{x_C^{n+1} - x_C^n}{\Delta t} \quad (4.9)$$

where x_C^n and x_C^{n+1} are the geometric centroids of the control volume faces at time levels n and n+1, respectively. Embedding equation 4.9 into 4.8 yields,

$$\sum_j^{n_f} \left[\frac{x_C^{n+1} - x_C^n}{\Delta t} \right] \frac{A_j^{n+1} + A_j^n}{2} \quad (4.10)$$

where A_j^n and A_j^{n+1} are the face area vectors at time levels n and n+1, respectively. In the light of the equations of 4.7 and 4.10, the equation 4.6 can be written as follows:

$$\frac{V^{n+1} - V^n}{\Delta t} - \sum_j^{n_f} \left[\frac{x_C^{n+1} - x_C^n}{\Delta t} \right] \frac{A_j^{n+1} + A_j^n}{2} = 0 \quad (4.11)$$

A user defined function (UDF) is needed to assign the prescribed body motion to the relevant mesh elements. The UDF is written to invoke azimuthal variations of the flap and pitch motions of the blades as a first order Fourier series. The spring based smoothing method is often used in the present dynamic mesh approach. In this method, the number and the connectivity of the mesh nodes do not change during the motion. Unless the cell zone encounters an excessive anisotropic stretching or compression, the sustainability of the mesh motion can be provided by the spring based smoothing. Otherwise, the cell quality can deteriorate and negative volumes can occur. The solver invokes re-meshing methods to prevent this problem. At this time, the connectivity of

the mesh elements are no longer the same since the volume mesh is updated. Data from the previous mesh is interpolated onto the newly generated mesh with a zero-order remapping algorithm. Several re-meshing methods are available in FLUENT; including local face re-meshing, local cell re-meshing and zone re-meshing. The solver marks cells that violate the skewness or size criteria and locally re-meshes the marked cells. The cell zone re-meshing is used if local re-meshing is not able to reduce the maximum cell skewness sufficiently.

In the spring-based smoothing method, the spring stiffness can be controlled with an appropriate selection of the spring constant factor. Spring constant factor takes values between zero and one. Assigning a value of zero results in more influence on the motion of the interior nodes away from the moving boundary. On the other hand, the displacements at the boundary nodes will be at a maximum when it takes value of one. If the simulation model contains deforming boundary zones, the boundary node relaxation factor can be included into an iterative equation where the positions are updated using a Jacobi sweep on all interior nodes. A value of zero for the boundary node relaxation factor inhibits deforming boundary nodes from moving, whereas a value of one means that no under-relaxation is imposed, which fully permits the motion of the nodes on the deforming boundaries. The solution of the iterative equation can be controlled using the values of Convergence Tolerance and Number of Iterations. The iterative process continues until one of these two criteria are met.

In the present study, the dynamic mesh approach is applied to carry out unsteady compressible flow analyses around a scaled helicopter model, the so called ROBIN geometry. The present study introduces an affordable methodology to handle the complex interactional rotor-fuselage aerodynamics problem. However, further improvements may be possible on the application of the technique. In the current case setup, the solver searches for the volume mesh element quality according to a predefined threshold value at each time-step while the application of the dynamic mesh technique. The invoke of re-meshing algorithm can be delayed by finding a logical time interval in which the utilization of the spring analogy is sufficient and when re-meshing is unnecessary. With such an approach, as a result of the reduced checks, a significant reduction in computation time may be achieved, which results in a further improvement of the present methodology.

5. TURBULENCE

5.1 Introduction

Analytical and semi-analytical solutions for simple flow cases have been already known by the early 50's. However, analytical solutions do not exist for most of the flow cases, especially for the complex ones. Therefore, the solution of complex flow problems is established numerically through a variety of computational methods. The direct numerical solution of the Navier-Stokes equations is one of the best ways for a better understanding of the physical flow phenomena. The turbulent motion of fluids with all its aspects can be represented by the Navier-Stokes equations, since all the essential forces such as pressure, inertial, viscous, surface tension, gravitational forces and other external forces acting on the fluid particle are entirely included. It is worth noting that, the Navier-Stokes equations involve nonlinear partial differential equations, which are in a highly coupled form. Solving a huge nonlinear system of equations for large-scale problems, particularly when dealing with complex industrial flow applications, may pose an insurmountable barrier to accessing the solutions, since even with today's most advanced computing facilities the computational cost of DNS is very high, and is said to be infeasible. Therefore, fully realistic flow field predictions may be achieved with further advancements in computer-related technologies. Due to limitations in computing power, researchers seek other ways to propose affordable solutions for how to overcome the difficulties exist in solving the complex turbulent flow problems. In fact, almost all real engineering problems are turbulent. Turbulence modeling is, therefore, of crucial importance to propose turbulent statistical solutions to the challenging engineering applications, while considerably cutting down the computational costs.

Today, several turbulence models ranging from the simplest to the more sophisticated ones are available thanks to the many studies done in the turbulence research field. Turbulence models can be categorized in several types according to the level of approximation made. The first level approximation, which can be referred to as the advanced models, is the Large Eddy Simulation (LES) model where the Navier-Stokes

equations are spatially averaged through filtering operations in which the turbulent structures at grid-scale (large eddies) are directly resolved and the sub-grid scale turbulent structures (small eddies) are modeled via using sub-grid scale models. Detached Eddy Simulation, which can be given in this category, is a hybrid technique where the entire boundary layer region is modeled by eddy viscosity models and the outer fully turbulent part of the flow field is directly resolved. Another example of the advanced models can be given as the Reynolds Stress Models (RSM), also known as the Reynolds Stress Transport (RST) models, where individual Reynolds stresses are directly computed by solving additional six differential transport equations. Each of the individual Reynolds stresses are solved for the closure of the momentum equation where this method of closure is also called as the second-order moment closure. Moreover, advanced models can be expanded to include the nonlinear eddy viscosity models (NLEVM). In these models, more than one term are taken into account from the Taylor series expansion of the eddy terms to relate the mean turbulence field to the mean velocity field using a nonlinear function. For instance, algebraic Reynolds stress models (ARSM) are in this group. On the other hand, the linear eddy viscosity models (LEVM) can be categorized in a group in which the level of approximation is reached to a maximum. These models depend on the Boussinesq hypothesis where Reynolds stresses are modeled using an expression for the turbulent (eddy) viscosity. The computation of the turbulent viscosity differs for each of the turbulence models. This group can be further classified according to the number of the differential equations (e.g. zero equation (algebraic) models, one equation models, two equation models and so on) to be solved. A decrease in the number of equations yields the simpler forms of modeling. The level of complexity for the turbulence models listed here is in decreasing order. The decrease in the complexity level provides a remarkable reduction in the computational effort.

Turbulence models are embedded into the popular commercial CFD codes in order to be able to perform the analysis of extremely turbulent flow fields in a cost-effective way. As a result of that achievement, simpler models can now be used for the prediction of large-scale turbulent flows around complex geometries, since the accurate prediction of the mean turbulent flow quantities are sufficient for practical design and engineering applications. However, there are still many ambiguities in turbulence modeling, and thus no universal turbulence model exists yet. Different

turbulence models may produce different solutions. Therefore, a comprehensive understanding of physical flow phenomena is required in both derivation and application of these turbulence models. The flow variables to be evaluated can be drastically affected by the flow regime (e.g. turbulent flow); therefore, turbulence models need to be developed for particular flow conditions [117, 128-130]. Moreover, the turbulence model should be selected based on the flow regime to be examined, since each flow field has its own specific characteristics. The uncertainty mentioned here can be reduced to a minimum level by the utilization of advanced numerical techniques and sophisticated turbulence models. These advanced models may also assure realistic and detailed flow field predictions. However, the computational power requirement may still be at an excessive level. In this regard, a turbulence model can only be considered as a good one when the acceptable accuracy level within a moderate computational time is being provided.

Up until now, flow fields around rotating bodies have been simulated by using a variety of turbulence models such as RANS/URANS, DES and LES [131-135]. Due to their high accuracy, the use of DES and LES techniques became very important in many engineering applications, for example the aerospace industry. However, these techniques have not become very widespread in use because of the requirement for excessive amount of computing resources. Despite the availability of high-speed computing facilities, these techniques still cannot be treated as practical solution approaches [136-138]. On the other hand, the solution of the Reynolds-Averaged Navier-Stokes (RANS) equations is a conventional approach to flow simulations, since all the turbulent motions are modeled. This provides significant savings in computational resources and makes the model appealing for practical applications.

5.2 Typical Features of Turbulence

The turbulence is always three dimensional and rotational. Moreover, turbulent flows are chaotic, random, highly irregular, diffusive and dissipative, which therefore yields a rapid change in the flow variables in both space and time. Due to that feature, turbulence problems are generally examined statistically rather than deterministically. Furthermore, vortex stretching is a typical feature of turbulent flows and does not exist in two dimension. Vortex stretching causes the production of the Reynolds stresses, which then results in velocity fluctuations, and therefore responsible for the energy

transfer between all wavelengths. Vortex structures proceed towards to the primary flow direction for a fairly long time, and therefore they are not local. The larger flow structures gradually transforms into smaller structures until their kinetic energy can be converted into heat. Viscous shear stresses are responsible for converting the kinetic energy into internal energy. This process occurs really quick and results in rapid dissipation of turbulence. Therefore, energy source should be permanent to sustain turbulent flow, [128, 139].

5.3 Turbulent Length Scales

A wide range of time and length scales exist in the flow field characterizes turbulent flows. The physical quantity, which is used to describe the size of the large eddies comprising the great amount of kinetic energy is called as the integral length scale, ℓ . The size of the largest eddies is determined by the domain boundaries of the flow field. The effect of viscous dissipation determines the size of the smallest eddies. The interaction between large scales results in loss of the kinetic energy, which causes the formation of smaller scales. In other words, the kinetic energy is transferred from the largest scale to smaller scales through the cascade process, [140-142]. The prediction of the effects of cascading process can be very tough due to the existence of many different length scales in the flow field. Therefore, in order to perform an accurate viscous flow simulation, the turbulence model should capture the influence of each length scale properly. However, determining the contribution of each length scale forms the main difficulty of turbulence modeling. The Taylor macroscale is an intermediate turbulent length scale, which falls in between the large eddies and the small eddies. Above the Taylor macroscale, the viscous effects are not strong and thus, the motions of these larger length scales are generally referred to as the integral range. Viscous stresses at the smallest scales are increased as the frictional forces increase. After reaching the smallest eddy dimension, or below Taylor macroscale, the kinetic energy of the eddy is dissipated into internal energy by the viscous shear stresses. Therefore, these scales are also called as the dissipative scales or Kolmogorov scales. The viscosity and dissipation have a significant effect on the determination of the energy cascading process. Thus, these quantities can be related with the length scales of the flow field. The turbulent velocity scale (u_η), the Kolmogorov length scale (η),

and the time scale (τ) can be written in terms of the kinematic viscosity (ν) and dissipation (ε), [139]. These relationships are given in equation (5.1).

$$u_\eta = (\nu\varepsilon)^{1/4}, \quad \eta = (\nu^3/\varepsilon)^{1/4}, \quad \tau = (\nu/\varepsilon)^{1/2} \quad (5.1)$$

5.4 Direct Numerical Simulation (DNS)

A complex flow field involves a wide range of spatial scales, from the smallest dissipative scales, up to the integral length scales. Direct Numerical Simulation (DNS) provides all the detailed and statistical information of the flow field without a need for further approximation for the solution of the governing equations, since the Navier-Stokes equations are solved directly for a particular geometry in which the whole spectrum of turbulent scales are being resolved. Therefore, DNS can be regarded as a numerical experiment, which allows a way to get a better insight into the physics of turbulence phenomenon. All the instantaneous flow variables can be analyzed and any physical quantity or the relationship between quantities can be gathered with a high-level of accuracy by the utilization of DNS. Sometimes this may not be operationally feasible and/or possible with experimental measurements, since locating numerous pressure probes in many different places of the flow field may lead to disturbances, which are actually irrelevant from the desired data to be retrieved. Therefore, DNS is a very powerful tool to investigate the turbulent flow characteristics and provides for improvements to the turbulence modeling. However, DNS becomes computationally prohibitive for most of the industrial engineering problems, especially when the Reynolds number gets larger. The required computational cost for DNS is proportional to the third power of the turbulent Reynolds number. Consequently, the disadvantage of DNS is that it requires extremely fine meshes and short time-steps; which therefore yields huge computational costs, even today's largest supercomputers may not be suffice to handle it, and thus it can only be applied to flows with low Reynolds numbers and simple geometries. Currently, DNS is not available in FLUENT.

5.5 Large Eddy Simulation (LES)

LES is a technique that falls between DNS and RANS in terms of the computational cost required. In LES, the resolved spectrum only involves the large eddies. Moreover, the small eddies are modeled via using a variety of sub-grid scale (SGS) models. Large

eddies are responsible for the transportation of momentum, mass, energy, and other passive scalars. Large turbulent scales are more flow-dependent. The geometry, initial and boundary conditions of the flow problem characterizes the large eddies where anisotropic turbulence eddy fluctuations are mostly present in the flow field. However, small eddies are less dependent on the geometry and tend to be more isotropic compared to large scales. This feature of the small eddies makes them more universal, which allows their modeling by using turbulence models. In order to remove sub-grid fluctuations from resolving, the filtering functions are being applied in LES model. The sub-grid scale stresses are unknown, and require modeling. Smagorinsky-Lilly, Wall-Adapting Local Eddy-Viscosity (WALE), Algebraic Wall-Modeled Large Eddy Simulation (WMLES) and the Kinetic Energy Transport (KET) are the available sub-grid scale models in FLUENT, [123]. Incorporating the SGS models makes the LES model computationally affordable compared to DNS. Moreover, using a wall-modeled LES reduces considerably the computing costs, as compared to a full wall-resolved LES. In wall-modeled LES models, coarser mesh and larger time-step sizes can be assigned, since only the large eddies is being resolved. However, it is noteworthy to mention that any kind of LES models still require considerably finer meshes than those used for RANS calculations. Moreover, LES calculations require an adequately long flow-time solution to obtain stable statistics of the predicted flow field. Therefore, LES computations are run generally orders of magnitudes higher than that required for steady RANS calculations. As a result, there is a need for more memory (RAM) and CPU power in order to carry out a LES simulation. To summarize, high-performance computing (HPC) is a necessity for LES, especially for industrial engineering applications involving very high Reynolds numbers such as unsteady rotor-fuselage interactional aerodynamics problems.

5.6 Detached Eddy Simulation (DES)

Detached Eddy Simulation (DES) is a hybrid technique used for the prediction of highly separated turbulent flows at high Reynolds numbers. In this method, the entire boundary layer is computed by RANS modeling and the remained part of the computational domain is resolved with a LES treatment. DES technique can be properly applied with lesser grid points than are there in LES meshes. This feature of DES makes it computationally more affordable when compared to LES [143].

Nowadays, in most of the LES studies, the near wall region is modeled by complex wall models [144] or modeled using different analysis techniques (hybrid RANS / LES) [145]. The most widely used technique in industrial applications is the DES method developed by Spalart [146].

In DES analyses, RANS based turbulence models (S-A, k-w, k- ϵ , etc.) are employed to model the small-scale turbulent fluctuations in the near-wall region of the boundary layer, whereas the computations of large turbulent structures are similar to LES. FLUENT provides three different DES models to the user,

- Spalart-Allmaras based DES model
- Realizable k- ϵ based DES model
- SST k-w based DES model

The sub-grid stress term found in the momentum equation is responsible for the energy transfer between the modeled small-scales and the resolved large-scales. It is useful to keep in mind that sub-grid stress dissipation effects can occur in two ways during the energy cascade process, depending on whether the energy transfer is from the grid-scale to sub-grid scale or vice versa. Actually, this interaction is predominantly from larger to smaller scales and is referred to as the forward scattering. In the viscosity-affected regions, the pressure and velocity fluctuations are at remarkably high frequencies. In LES, sub-grid scale models are used to filter the small-scale turbulent fluctuations where the dissipation effects are dominant. Moreover, the use of appropriate SGS models is of center significance, especially for the accurate calculation of the resolved vorticity field, since the dissipation effects may also affect the larger turbulent scales (low-wave numbers) through a backward scattering process [147, 148]. Therefore, the most critical point in DES analyses is the determination of the transition from RANS to LES (Figure 5.1).

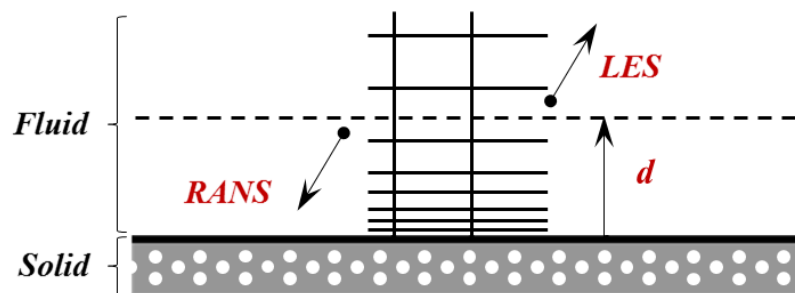


Figure 5.1 : A schematic view of the transition region in DES Method.

Spalart–Allmaras turbulence model has been developed for subsonic flow around airfoils, boundary layer flows, etc. [146]. Spalart, who introduced the use of this eddy viscosity model, carried out the first DES application found in literature. In this model, turbulent eddy viscosity is obtained by solving a transport equation. In the S-A based DES formulations, the distance to the nearest wall, d , is obtained as follows;

$$d = \min(d, C_{DES}\Delta) \quad \text{and} \quad \Delta = \max(\Delta_x, \Delta_y, \Delta_z) \quad (5.2)$$

DES calibration constant (C_{DES}) depends on an empirical derivation and has a value of 0.65. Δ , is the maximum local length of the mesh element generated on the wall surfaces. The transition from RANS to LES is ensured when the maximum local grid spacing (Δ) is less than the distance to the nearest wall, d .

During the computation, early transition to LES formulation can occur due to the uncertainty at the boundary layer region. Activation of LES formulation inside the boundary layer is an undesired situation because of the presence of small-scale structures. Delayed-DES (DDES) formulation can be enabled by the user to avoid early transition to LES mode;

$$\tilde{d} = d - f_d \max(0, d - C_{DES}\Delta) \quad \text{and} \quad f_d = 1 - \tanh((8r_d)^3) \quad (5.3)$$

Several studies in the literature showed that the vortex structures, detachment and reattachment regions in the complex unsteady flows could be more accurately predicted by DES method [149-151]. Briefly, the boundary layer and flow separation must be computed accurately in order to obtain precise force (drag, lift, etc.) calculation within a small amount of error. It is obvious that a considerably fine mesh resolution is still needed for a proper implementation of the DES method.

5.7 Reynolds Averaged Navier-Stokes (RANS) Models

The RANS based turbulence models have been widely used to investigate the turbulence flow field, and thus become a useful tool in many engineering applications due to their compact modeling, ease of use, comparable accuracy, and relatively inexpensive computational costs. Here, the derivation of the RANS equations are not shown explicitly; however, the idea behind the approach is discussed in brief. The

continuity equation, or the equation for conservation of mass, can be written in the most general form using Cartesian tensor notation:

$$\frac{\partial \rho}{\partial t} + \frac{\partial}{\partial x_i} (\rho u_i) = S_m \quad (5.4)$$

where S_m represents the mass source generated due to a phase change in the flow solution (i.e. vaporization of liquid droplets). Moreover, S_m may also be used to represent for any other sources. For a continuous phase, the continuity equation reads

$$\frac{\partial \rho}{\partial t} + \frac{\partial}{\partial x_i} (\rho u_i) = 0 \quad (5.5)$$

For incompressible flows, since density (ρ) is assumed to be constant, the continuity equation implies that the divergence of velocity field is zero everywhere. In other words, the local volume dilation rate is zero.

$$\frac{\partial u_i}{\partial x_i} = 0 \quad (5.6)$$

The equation for conservation of momentum for a compressible Newtonian fluid can be written in the most general form using vector notation:

$$\frac{\partial}{\partial t} (\rho \vec{u}) + \nabla (\rho \vec{u} \vec{u}) = -\nabla p + \nabla \cdot \left(\mu_m (\nabla \vec{u} + (\nabla \vec{u})^T) - \frac{2}{3} \mu_m (\nabla \cdot \vec{u}) \mathbf{I} \right) + \vec{F} \quad (5.7)$$

where ρ is the fluid density, \vec{u} is the fluid velocity, p is the fluid pressure, μ_m is the fluid dynamic (molecular) viscosity, \mathbf{I} is the unit tensor. The first two terms in the left hand side of the equation are the inertial forces: where the leftmost one is the instantaneous acceleration and the second one is the convection term. The first term on the right hand side represents the pressure gradients, and the second term denotes the divergence of viscous dissipation. Finally, the last term (\vec{F}) is the force vector including the gravitational body force and external body forces. The momentum equation can be written using tensor notation:

$$\frac{\partial}{\partial t} (\rho u_i) + \frac{\partial}{\partial x_j} (\rho u_i u_j) = -\frac{\partial p}{\partial x_i} + \frac{\partial}{\partial x_j} \left(\mu_m \left(\frac{\partial u_i}{\partial x_j} + \frac{\partial u_j}{\partial x_i} - \frac{2}{3} \delta_{ij} \frac{\partial u_k}{\partial x_k} \right) \right) + \vec{F} \quad (5.8)$$

where δ_{ij} is the Kronecker delta function (0 if $i \neq j$, 1 if $i = j$). The governing equations of compressible flow can be simplified for adiabatic incompressible flow, since the assumptions made imply that the density is independent of both pressure and temperature, and thus it can be considered as a constant in both space and time. Moreover, the viscous forces can be further simplified by incorporating the continuity equation (5.6) into the momentum equation (5.8), where the dilatation term vanishes because the divergence of the velocity is equal to zero ($\nabla \cdot \vec{u} = \partial u_k / \partial x_k = 0$). Furthermore, neglecting the external body forces, the conservation of momentum equation now reduces to

$$\rho \left(\frac{\partial u_i}{\partial t} + \frac{\partial (u_i u_j)}{\partial x_j} \right) = - \frac{\partial p}{\partial x_i} + \frac{\partial}{\partial x_j} \left(\mu_m \left(\frac{\partial u_i}{\partial x_j} + \frac{\partial u_j}{\partial x_i} \right) \right) \quad (5.9)$$

where $i = 1, 2, 3$ and summation is assumed over $j = 1, 2, 3$. Here, u_i is the instantaneous velocity component in the x_i direction, p is the instantaneous pressure. The instantaneous velocity and pressure are decomposed into the mean and fluctuating components to obtain the mean continuity and the Reynolds-averaged Navier-Stokes (RANS) equations.

$$u_i = \bar{u}_i + u'_i \quad \text{and} \quad p = \bar{p} + p' \quad (5.10)$$

Substituting equation (5.10) into equation (5.6) and (5.9), and averaging leads to

$$\frac{\partial \bar{u}_i}{\partial x_i} = 0 \quad (5.11)$$

$$\rho \left(\frac{\partial \bar{u}_i}{\partial t} + \frac{\partial (\bar{u}_i \bar{u}_j)}{\partial x_j} \right) = - \frac{\partial \bar{p}}{\partial x_i} + \frac{\partial}{\partial x_j} \left(\mu_m \left(\frac{\partial \bar{u}_i}{\partial x_j} + \frac{\partial \bar{u}_j}{\partial x_i} \right) \right) + \frac{\partial \tau_{ij}}{\partial x_j} \quad (5.12)$$

Reynolds decomposition and averaging produces additional variables, which appear in the numerator of the last term in equation (5.12). Most methods of analysis result in more unknowns (here, Reynolds stress tensor, τ_{ij}) than equations and this situation is known as turbulence closure problem. These Reynolds stresses must be modeled in order to close the equation. However, it is hard to find available relations for the Reynolds stress tensor, which is a symmetric tensor with six independent unknown turbulent stress terms given by equation (5.13). Normal stresses are placed in

the diagonal of the matrix, whereas the shear stresses appear in the symmetric lower and upper triangular portions. Constitutive relations can be found for viscous stresses. It may be inquired whether the similar deductions can be made for the Reynolds stress. However, there is a huge distinction between Reynolds stress and viscous stress. Viscous stress can be thought as the property of a fluid. Thus, the constitutive relations can be determined by separate experiments. Once these relations are obtained, several flow simulations for this particular fluid can be performed. On the other hand, Reynolds stress can only be the property of the flow itself, and not of the fluid. Reynolds stress may vary for different type of flows and thus, constitutive relations cannot be written [117].

$$\overline{u'_i u'_j} = \begin{bmatrix} \overline{u'^2} & \overline{u'v'} & \overline{u'w'} \\ \overline{v'u'} & \overline{v'^2} & \overline{v'w'} \\ \overline{w'u'} & \overline{w'v'} & \overline{w'^2} \end{bmatrix} \quad (5.13)$$

In the RANS based turbulence modeling, many approaches are based upon the Boussinesq hypothesis, which defines the Reynolds stresses in terms of the known averaged quantities through the eddy viscosity concept. By this way, all the turbulent motions can be modeled, which, therefore, ensures reduced computational effort. In this approximation, the eddy viscosity is assumed to be an isotropic scalar quantity, which is considered as the disadvantage of the model. For a Newtonian fluid, Boussinesq hypothesis [152] relates the Reynolds stresses to the gradients of the mean velocity field through a simple relationship given below

$$\tau_{ij} = -\rho \overline{u'_i u'_j} = 2\mu_t S_{ij} - \frac{2}{3}\mu_t \frac{\partial \bar{u}_k}{\partial x_k} \delta_{ij} - \frac{2}{3}\rho k \delta_{ij} \quad (5.14)$$

$$S_{ij} = \frac{1}{2} \left(\frac{\partial \bar{u}_i}{\partial x_j} + \frac{\partial \bar{u}_j}{\partial x_i} \right) \quad (5.15)$$

In above equations, μ_t is the turbulent dynamic viscosity, S_{ij} is the mean strain-rate tensor where \bar{u}_i is the mean velocity component in the x_i direction. For isentropic incompressible flows, the Reynolds stress tensor loses its trace and reduces to

$$\tau_{ij} = 2\mu_t S_{ij} \quad (5.16)$$

The final set of RANS momentum equations for an adiabatic incompressible flow in the tensor notation form are as follows,

$$\frac{\partial \bar{u}_i}{\partial t} + \frac{\partial (\bar{u}_i \bar{u}_j)}{\partial x_j} = -\frac{1}{\rho} \frac{\partial \bar{p}}{\partial x_i} + \frac{\partial}{\partial x_j} \left[(\nu + \nu_t) \frac{\partial \bar{u}_i}{\partial x_j} \right] \quad (5.17)$$

where $\nu = \mu_m / \rho$ and $\nu_t = \mu_t / \rho$.

The RANS approach provides significant savings in computational resources compared to DES, LES and DNS formulations, while ensuring reliable flow field predictions through mean turbulent quantities, which is sufficient for practical design purposes. The present numerical simulations were carried out using RANS based turbulence models, which allow one to use relatively coarse meshes. This feature is very suitable for the methodology presented here, since re-meshing, currently, can only be performed by using a single CPU. Thereby, an affordable methodology has been introduced to handle the complex interactional rotor-fuselage aerodynamics problem.

5.7.1 Zero equation (Algebraic) models

In eddy viscosity models, an expression is needed for the turbulent viscosity. The dimension of turbulent viscosity is same as kinematic viscosity, which is equivalent to $[\text{m}^2/\text{s}]$. A dimensional analysis would produce the relationship between the turbulent viscosity and other turbulent parameters. For instance, in order to find a same dimension with the turbulent kinematic viscosity (ν_t), it is logical to use the turbulent velocity and turbulent length scales, which are the most effective parameters of diffusive transport [139].

$$\nu_t \propto u l_m \quad (5.18)$$

In above expression, turbulent velocity scale (u) and turbulent length scale (l_m) constitute the characteristic for the large turbulent scales. Algebraic turbulence model uses the velocity gradient as a velocity scale and some kind of physical length scale as the length scale. For instance, the following equation can be written for boundary layer flows,

$$\nu_t = l_m^2 |\partial U / \partial y| \quad (5.19)$$

Above equation is known as the mixing length model where y demonstrates the coordinate normal to the wall and l_m is the mixing length. The underlying problem of the model is that l_m is an unknown and there may be some difficulties in determining a proper one [139]. Van Driest has published a viscous damping correction for the mixing-length model in 1956 [153]. Cebeci and Smith published a modified version of the eddy viscosity/mixing-length concept for the prediction of attached boundary layers in 1974 [154]. Moreover, Baldwin-Lomax model is an algebraic model and has been used widely in aerodynamics [155].

5.7.2 One equation models

In one-equation models, one transport equation is solved usually for the turbulent kinetic energy, whereas the unknown turbulent length scale is determined using an algebraic expression [156, 157]. The length scale can be taken as a ratio between the boundary layer thickness and the width of a wake. Prandtl's one-equation model, Baldwin-Barth model, Spalart-Allmaras model, Rahman-Agarwal-Siikonen model can be given as the examples of the most popular one-equation models [130]. A general expression for an algebraic length scale cannot be written for most of the flow types. This situation forms the main disadvantage of this type of models. Nevertheless, some studies have been found for the computation of the turbulent length scale in a more general way [158, 159]. Menter [159] showed that a two-equation model (standard k - ϵ) can be transformed into a one-equation model based on only two assumptions. The author stated that the diffusion coefficients in the transport equations for k and ϵ are the same, thereby a reduction in the number of coefficients can be obtained. The second assumption depends on the Bradshaw's relation [160], which is exact for equilibrium flows, where the production and dissipation of the kinetic energy are equivalent to each other.

5.7.3 Two equation models

In this section, the formulations of extensively used two-equation eddy viscosity models have been discussed briefly. For instance, in section 6.1.2.3, four widely used turbulence models are tested to assess the accuracy and suitability of the models for calculating the drag forces acting on an isolated fuselage geometry. The interested reader may find further information on other available turbulence models from the FLUENT's theory manual [123].

5.7.3.1 The realizable k-ε model

The Realizable k-ε (RKE) turbulence model is consistent with the physics of turbulent flows while satisfying certain mathematical constraints on the Reynolds stresses. This model is called as “Realizable”, since it ensures the positivity of normal stresses and Schwarz inequality for shear stresses. An alternative formulation for the turbulent viscosity is used in the Realizable k-ε model, which differs from the standard k-ε (SKE) model. Another difference is that the Realizable k-ε model uses a modified transport equation for the dissipation rate, which has been derived from the mean-square vorticity fluctuation. Realizable k-ε model is capable of providing more accurate results than the other types of k-ε models, especially when finding solutions for flows involving rotation, recirculation, and separated boundary layers under strong adverse pressure gradients. In the Realizable k-ε model, the modeled transport equations for turbulent kinetic energy (k) and turbulent dissipation rate (ε) can be given as [123],

$$\frac{\partial}{\partial t}(\rho k) + \frac{\partial}{\partial x_j}(\rho k u_j) = \frac{\partial}{\partial x_j} \left[\left(\mu_m + \frac{\mu_t}{\sigma_k} \right) \frac{\partial k}{\partial x_j} \right] + G_k + G_b - \rho \varepsilon - Y_M + S_k \quad (5.20)$$

$$\begin{aligned} \frac{\partial}{\partial t}(\rho \varepsilon) + \frac{\partial}{\partial x_j}(\rho \varepsilon u_j) \\ = \frac{\partial}{\partial x_j} \left[\left(\mu_m + \frac{\mu_t}{\sigma_\varepsilon} \right) \frac{\partial \varepsilon}{\partial x_j} \right] + \rho C_1 S_\varepsilon - \rho C_2 \frac{\varepsilon^2}{k + \sqrt{\nu \varepsilon}} \\ + C_{1\varepsilon} \frac{\varepsilon}{k} C_{3\varepsilon} G_b + S_\varepsilon \end{aligned} \quad (5.21)$$

In above equations,

$$C_1 = \max[0.43, (\eta/\eta + 5)], \quad \eta = S(k/\varepsilon), \quad S = (2S_{ij}S_{ij})^{1/2} \quad (5.22)$$

The generation of turbulence kinetic energy due to the mean velocity gradients is represented by G_k . Moreover, G_b represents the generation of turbulence kinetic energy due to buoyancy. The contribution of the fluctuating dilatation to the overall dissipation rate is represented by Y_M . S_k , and S_ε are source terms. C_2 , and $C_{1\varepsilon}$ are constants. $C_{3\varepsilon}$ is used to determine the effect of the buoyancy and is calculated according to the following relation: $C_{3\varepsilon} = \tanh |v/u|$. The turbulent Prandtl numbers for k and ε are represented by σ_k , and σ_ε , respectively. S is the modulus of the mean

rate-of-strain tensor. The model constants are; $C_{1\varepsilon} = 1.44$, $C_2 = 1.9$, $\sigma_k = 1.0$, and $\sigma_\varepsilon = 1.2$. The turbulent viscosity is $\nu_t = C_\mu k^2/\varepsilon$. Here, C_μ is not a constant. C_μ is a function of the mean strain and rotation rates, the angular velocity of the system rotation, and the turbulence fields [123].

$$C_\mu = \frac{1}{A_0 + A_S \frac{kU^*}{\varepsilon}} \quad \text{with } \left\{ \begin{array}{l} A_0 = 4.04 \\ A_S = \sqrt{6} \cos \phi \end{array} \right\} \quad \text{and } \phi = \frac{1}{3} \cos^{-1}(\sqrt{6}W) \quad (5.23)$$

$$W = \frac{S_{ij}S_{jk}S_{ki}}{\tilde{S}^3} \quad \text{where } \tilde{S} = \sqrt{S_{ij}S_{ij}} \quad \text{and } S_{ij} = \frac{1}{2} \left(\frac{\partial u_j}{\partial x_i} + \frac{\partial u_i}{\partial x_j} \right) \quad (5.24)$$

$$U^* \equiv (S_{ij}S_{ij} + \tilde{\Omega}_{ij}\tilde{\Omega}_{ij})^{1/2} \quad (5.25)$$

$$\tilde{\Omega}_{ij} = \Omega_{ij} - 2\varepsilon_{ijk}\omega_k \quad \text{and } \Omega_{ij} = \bar{\Omega}_{ij} - \varepsilon_{ijk}\omega_k \quad (5.26)$$

5.7.3.2 The renormalization group (RNG) k-ε model

The RNG model takes its name from a mathematical technique called “renormalization group” methods. The equation of the dissipation rate in the RNG k-ε model has an additional term, which improves the accuracy for swirling flows. Moreover, the turbulent Prandtl numbers are represented by an analytical formula while they were constants in the standard k-ε model. Furthermore, the effective viscosity calculation in the RNG model depends on an analytical formula, which provides more reliable results for low-Reynolds number effects in case of considering an appropriate treatment of the near-wall region. Briefly, RNG k-ε model provides better results than the standard k-ε model, particularly for complex shear flows, and flows with high strain rates, swirl, and separation. In the RNG k-ε model, the modeled transport equations for k and ε can be given as [123],

$$\frac{\partial(\rho k)}{\partial t} + \frac{\partial(\rho k u_i)}{\partial x_i} = \frac{\partial}{\partial x_j} \left[\alpha_k \mu_{eff} \frac{\partial k}{\partial x_j} \right] + G_k + G_b - \rho \varepsilon - Y_M + S_k \quad (5.27)$$

$$\begin{aligned} \frac{\partial(\rho \varepsilon)}{\partial t} + \frac{\partial(\rho \varepsilon u_i)}{\partial x_i} \\ = \frac{\partial}{\partial x_j} \left[\alpha_\varepsilon \mu_{eff} \frac{\partial \varepsilon}{\partial x_j} \right] + C_{1\varepsilon} \frac{\varepsilon}{k} (G_k + C_{3\varepsilon} G_b) - C_{2\varepsilon} \rho \frac{\varepsilon^2}{k} - R_\varepsilon + S_\varepsilon \end{aligned} \quad (5.28)$$

The RNG k- ε model uses the following differential equation for turbulent viscosity calculation. Equation (5.29) is integrated to obtain a better prediction for the effective turbulent transport at low Reynolds number and near-wall flows.

$$d\left(\frac{\rho^2 k}{\sqrt{\varepsilon \mu_m}}\right) = 1.72 \frac{\hat{v}}{\sqrt{\hat{v}^3 - 1 + C_v}} d\hat{v}, \quad \hat{v} = \frac{\mu_{eff}}{\mu_m}, \quad C_v \approx 100 \quad (5.29)$$

At high Reynolds number flows, FLUENT uses the following equation for turbulent viscosity, by default. Therefore, user should activate above equation to take advantage of the better accuracy when calculating a low Reynolds number flow simulation.

$$\mu_t = \rho C_\mu \frac{k^2}{\varepsilon}, \quad \text{with } C_\mu = 0.0845 \quad (5.30)$$

The inverse effective Prandtl numbers, $(\alpha_k, \alpha_\varepsilon)$, are computed by the following analytically derived formulation, which is given in equation (5.30). At high Reynolds number flows, the ratio of molecular viscosity to effective viscosity is negligible, $(\mu_m/\mu_{eff} \ll 1)$, which yields the equality of the inverse effective Prandtl numbers $\alpha_k = \alpha_\varepsilon \approx 1.3929$.

$$\left|\frac{\alpha - 1.3929}{\alpha_0 - 1.3929}\right|^{0.6321} \left|\frac{\alpha + 2.3929}{\alpha_0 + 2.3929}\right|^{0.3679} = \frac{\mu_m}{\mu_{eff}} \quad \text{and } \alpha_0 = 1.0 \quad (5.31)$$

The additional term found in the dissipation rate equation is given by,

$$R_\varepsilon = \frac{C_\mu \rho \eta^3 (1 - \eta/\eta_0) \varepsilon^2}{1 + \beta \eta^3} \frac{1}{k} \quad (5.32)$$

In above equation: $\eta \equiv Sk/\varepsilon$, $\eta_0 = 4.38$, and $\beta = 0.012$. The model constants are $C_{1\varepsilon} = 1.42$, and $C_{2\varepsilon} = 1.68$.

5.7.3.3 The shear-stress transport (SST) k- ω model

The SST k- ω model requires solution of two extra transport equations in order to achieve closure. In this turbulence model, the definition of the turbulent viscosity is modified to account for the transport of the principal turbulent shear stress. Other modifications made to the model are the addition of a cross-diffusion term in the ω

equation and a blending function, which is necessary for appropriate modeling in both the near-wall and far-field zones. Transport equations for the SST k- ω model are [123],

$$\frac{\partial}{\partial t}(\rho k) + \frac{\partial}{\partial x_i}(\rho k u_i) = \frac{\partial}{\partial x_j} \left(\Gamma_k \frac{\partial k}{\partial x_j} \right) + \tilde{G}_k - Y_k + S_k \quad (5.33)$$

$$\frac{\partial}{\partial t}(\rho \omega) + \frac{\partial}{\partial x_j}(\rho \omega u_j) = \frac{\partial}{\partial x_j} \left(\Gamma_\omega \frac{\partial \omega}{\partial x_j} \right) + G_\omega - Y_\omega + D_\omega + S_\omega \quad (5.34)$$

The effective diffusivities for the SST k- ω model are as follows,

$$\Gamma_k = \mu_m + \mu_t/\sigma_k \quad \text{and} \quad \Gamma_\omega = \mu_m + \mu_t/\sigma_\omega \quad (5.35)$$

where σ_k , and σ_ω are the turbulent Prandtl numbers. μ_t , is the turbulent dynamic viscosity and calculated as follows,

$$\mu_t = \frac{\rho k}{\omega} \frac{1}{\max \left[\frac{1}{\alpha^*}, \frac{\Omega F_2}{a_1 \omega} \right]} \quad \{a_1 = 0.31\} \quad (5.36)$$

$$\sigma_k = \frac{1}{F_1/\sigma_{k,1} + (1 - F_1)/\sigma_{k,2}} \quad (5.37)$$

$$\sigma_\omega = \frac{1}{F_1/\sigma_{\omega,1} + (1 - F_1)/\sigma_{\omega,2}} \quad (5.38)$$

$$\sigma_{k,1} = 1.176, \quad \sigma_{\omega,1} = 2.0, \quad \sigma_{k,2} = 1.0, \quad \text{and} \quad \sigma_{\omega,2} = 1.168 \quad (5.39)$$

$$\alpha^* = \alpha_\infty^* \left(\frac{\alpha_0^* + Re_t/R_k}{1 + Re_t/R_k} \right) \quad (5.40)$$

$$\Omega \equiv (2\Omega_{ij}\Omega_{ij})^{1/2} \quad (5.41)$$

Here, Ω is the modulus of the mean rate-of-rotation tensor, and Ω_{ij} is the mean rate-of-rotation tensor. F1 and F2 are the blending functions. F1 is the blending function designed to blend model constants between wall-affected region (subscript 1) and core turbulence region (subscript 2). It equals one in the wall-affected region and zero away from the walls. The blending function F1 is given by the following expression:

$$F_1 = \tanh(\phi_1^4) \quad (5.42)$$

$$\phi_1 = \min \left[\max \left(\frac{\sqrt{k}}{0.09\omega y}, \frac{500\mu_m}{\rho y^2 \omega} \right), \frac{4\rho k}{\sigma_{\omega,2} D_{\omega}^+ y^2} \right] \quad (5.43)$$

$$D_{\omega}^+ = \max \left[2\rho \frac{1}{\sigma_{\omega,2}} \frac{1}{\omega} \frac{\partial k}{\partial x_j} \frac{\partial \omega}{\partial x_j}, 10^{-10} \right] \quad (5.44)$$

where y , is the distance to the next surface and D_{ω}^+ is the positive portion of the cross-diffusion term. The blending function F_2 is defined as,

$$F_2 = \tanh(\phi_2^2) \quad (5.45)$$

$$\phi_2 = \max \left[2 \frac{\sqrt{k}}{0.09\omega y}, \frac{500\mu_m}{\rho y^2 \omega} \right] \quad (5.46)$$

The term \tilde{G}_k represents the production of turbulence kinetic energy, whereas G_k is defined in the same manner as in the standard k - ω model. The term G_{ω} represents the production of turbulence dissipation rate.

$$\tilde{G}_k = \min(G_k, 10\rho\beta^*k\omega) \quad \text{and} \quad G_{\omega} = \frac{\alpha}{\nu_t} \tilde{G}_k \quad (5.47)$$

In the standard k - ω model, α_{∞} is defined as a constant (0.52) but in this formulation it is evaluated as,

$$\alpha_{\infty} = F_1\alpha_{\infty,1} + (1 - F_1)\alpha_{\infty,2} \quad (5.48)$$

$$\alpha_{\infty,1} = \frac{\beta_1}{\beta_{\infty}^*} - \frac{\kappa^2}{\sigma_{\omega,1}\sqrt{\beta_{\infty}^*}} \quad \text{and} \quad \alpha_{\infty,2} = \frac{\beta_2}{\beta_{\infty}^*} - \frac{\kappa^2}{\sigma_{\omega,2}\sqrt{\beta_{\infty}^*}} \quad (5.49)$$

The dissipation of turbulence kinetic energy is defined as,

$$Y_k = \rho\beta^*k\omega \quad (5.50)$$

The dissipation of turbulence dissipation rate is defined as,

$$Y_{\omega} = \rho\beta\omega^2 \quad (5.51)$$

β , is not a constant and its formulation is given by,

$$\beta = F_1\beta_1 + (1 - F_1)\beta_2 \quad (5.52)$$

The model constants used in the equations are as follows,

$$\beta_\infty^* = 0.09, \quad \beta_1 = 0.075, \quad \beta_2 = 0.0828, \quad \kappa = 0.41 \quad (5.53)$$

5.7.4 Near wall behavior of RANS turbulence models

Determining the type of near wall modeling forms one of the major difficulties encountered in the simulation of wall bounded flows. Since the wall boundaries remarkably influence the turbulent flow, the near wall regions should be modeled precisely in order to achieve realistic predictions of the entire flow domain. The innermost layer, where the momentum and heat or mass transfer is highly determined by the molecular viscosity, is called as the "viscous sublayer". In this region, the viscous forces dominate the flow so that the flow is almost laminar. The outermost layer, where the turbulent viscosity supersedes the molecular viscosity, is called as the "fully-turbulent layer". The intermediate region, where the effects of molecular viscosity and turbulent viscosity are equally important, is called as the "buffer layer". Figure 5.2 shows a semi-log plot of the subdivisions of the near-wall region.

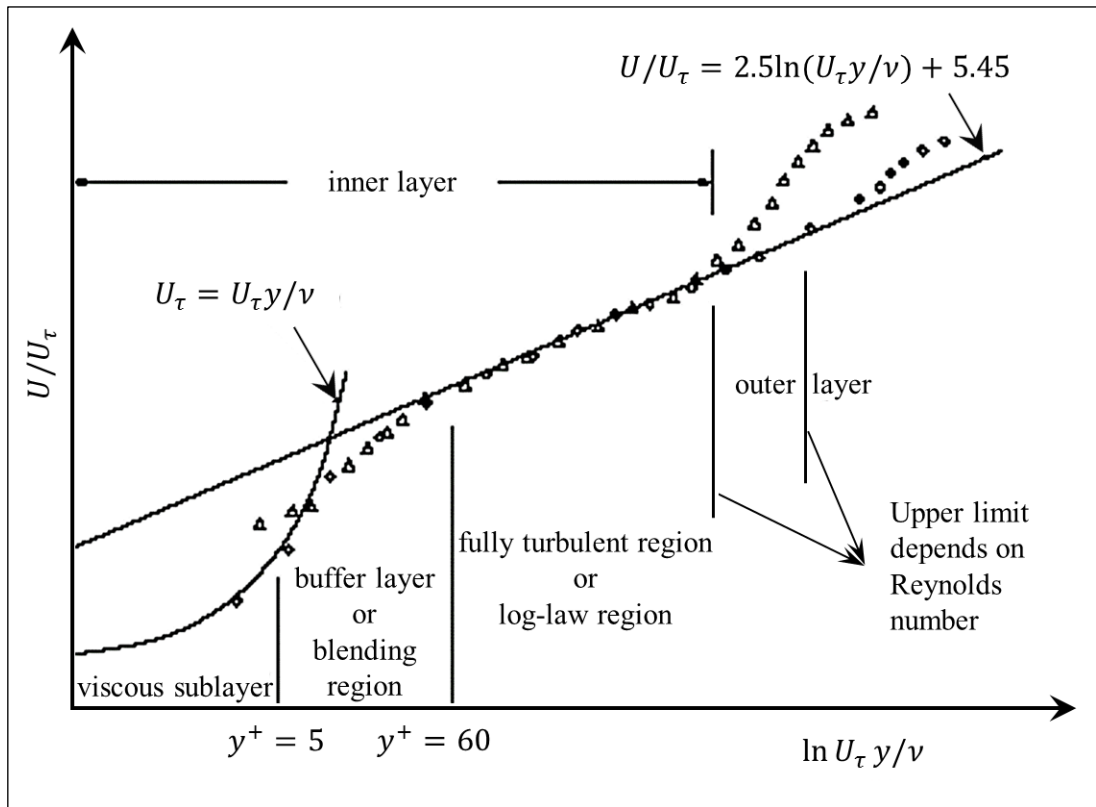


Figure 5.2 : Subdivisions of the near-wall region, [123].

There are traditionally two alternatives to modeling the near-wall region. In one approach, the viscosity-affected region all the way down to the viscous sublayer is represented with highly clustered meshes, since these modified turbulence models require very fine meshes on and around the walls. Using highly stretched cells in the direction normal to the wall within the near-wall region may help increase the accuracy. The viscous sub-layer length scale (non-dimensional wall distance) at the wall-adjacent cell should be on the order of $y^+=1$, when the laminar sublayer is intended to be resolved. In another approach, the viscosity-affected viscous sublayer and buffer layer is modeled rather than resolved. The viscosity-affected region between the wall and the fully-turbulent region is modeled using semi-empirical formulas called "wall functions", instead of resolving, resulting in flexibility in a reduction in grid resolution. In most high-Reynolds-number flows, the wall function approach considerably saves computational resources, because the viscosity-affected near-wall region does not need to be resolved, since at that region the solution variables change rapidly. Recalling that the wall function approach does not offer a sufficient simulation when the low-Reynolds-number effects are dominant in the flow field. In addition, standard wall function approach is not recommended in case of highly skewed 3D boundary layers and largely separated flows. Such situations require the use of first approach that are valid in the viscosity-affected region. However, the wall function approach is frequently preferred for high-Reynolds-number flows due to its distinctive features such as reasonable cost and accuracy. The use of standard wall functions is a practical option for the near-wall treatments for industrial flow simulations [123]. In this study, both approaches were tested and the results are discussed in the following chapters. However, as the computational effort is a major concern, and since the Reynolds number is high for rotor simulations, the use of standard wall functions is thought to be appropriate. Therefore, the analyses for the evaluation of the interference effects between rotor and fuselage have been carried out using standard wall functions based on the proposal of Launder and Spalding [161]. The near-wall region should be meshed depending on the requirements of the chosen near-wall model. For the proper use of standard wall functions, each wall-adjacent cell's centroid should be located within the log-law layer. In addition to that, excessive stretching should be avoided in the direction normal to the wall. Moreover, at least a few cells should be generated inside the boundary layer while using standard wall function approach.

6. RESULTS AND DISCUSSION

6.1 Isolated Fuselage Analyses

The investigated fuselage geometry is the well-known ROBIN geometry. Surface pressure characteristics of the fuselage have been obtained by numerical analysis to carry out a validation study. The experimental results from [101] and numerical results from [17, 103] are taken to validate the present CFD simulation of isolated fuselage configuration. The pressure coefficients of predefined measurement locations are obtained for the various angle of attack conditions for the comparison with both experimental and numerical results.

A numerical study have been carried out by [17] to compute surface pressures by using a panel method code (VSAERO) and a thin-layer Navier-Stokes code (CFL3D). The authors stated that the viscous flow features and separation patterns could not be easily modeled with the panel method. However, the two codes agree well ahead of the nacelle where separation is not expected.

In this section, the steady RANS analyses are carried out for the isolated fuselage configuration. At the beginning, the mesh dependency work is pursued to obtain a mesh independent result. For this purpose, the drag force generated due to the presence of the fuselage in the spare ambience is chosen as a variable to be investigated. The viscous and pressure components of the drag force are predicted whether to determine the most dominant one. Then, the mesh generation is performed by the increased resolution at the necessary regions. Furthermore, the effect of numerical schemes on the results is investigated. This is done by the examination of the spatial discretization schemes. The second order upwind and the third order MUSCL schemes are compared. In addition, the results of the cell-based and node-based solvers on the tetrahedral volume elements are studied. Moreover, the turbulence nature of the flow is simulated by using a variety of turbulence models that are available in the solver. A comprehensive numerical study has been conducted in order to find the best available numerical approach that achieves the most consistent results with both previously

performed experimental measurements and numerical studies. After determining the ideal configuration of the numerical approach for the examined problem, the drag and the lift predictions have been made at various angle of attack conditions.

6.1.1 The Robin geometry

The ROBIN fuselage has been extensively tested and used for CFD validation studies. ROBIN fuselage shape is formed using super-ellipse equations, which were developed by NASA. The details of the geometry can be found in given references [101, 104]. The fuselage geometry is formed by two parts: a pylon and a body. A code is written in MATLAB software to construct the fuselage geometry by means of these equations. The output of the code is the shape of the cross sections at related stations of the fuselage. The obtained cross sections are given in Figure 6.1. The number of cross sections is chosen for the best presentation of the geometry. The fuselage sections generated by the MATLAB code are imported into a Computer-Aided Design (CAD) tool, CATIA, to draw the surface of the fuselage.

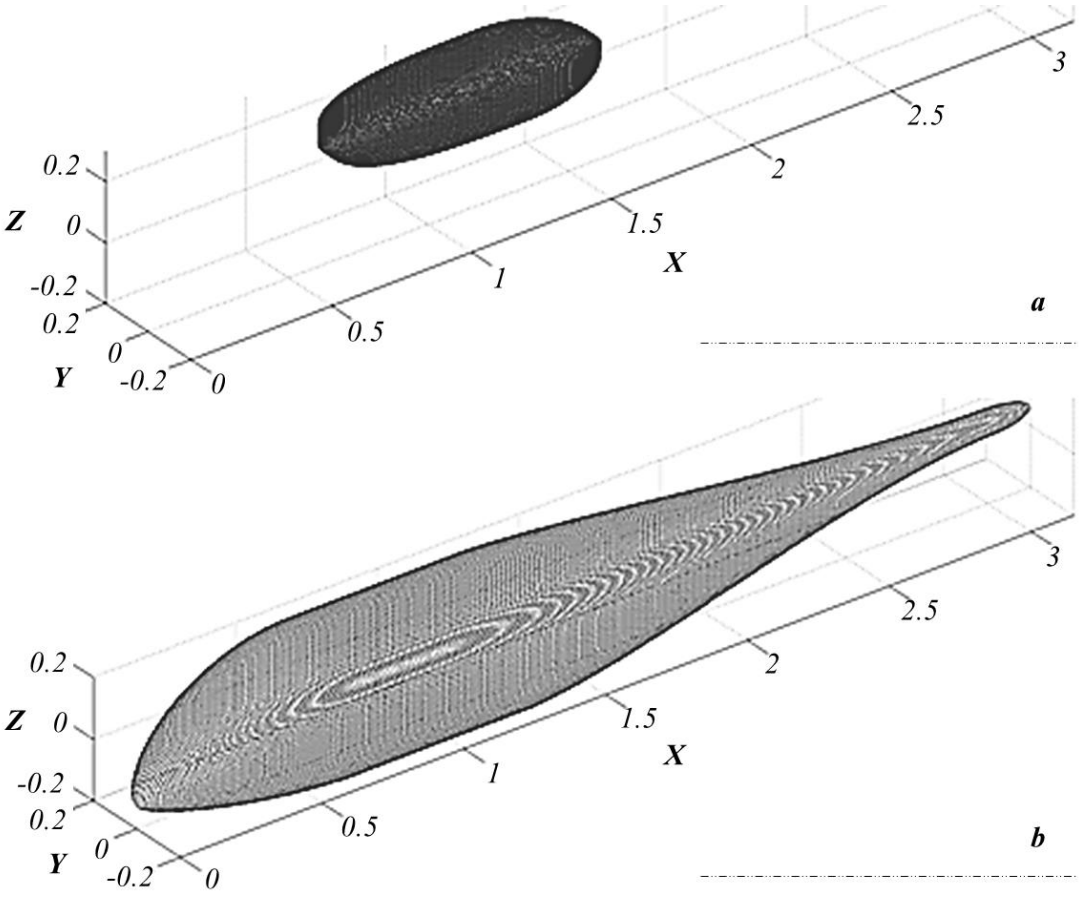


Figure 6.1 : Cross-sections of the (a) pylon and (b) body shapes.

6.1.2 Numerical solution procedure

The domain boundaries are formed by a cylindrical shape and covers a region that is of 15 vehicle lengths to the upstream and radial directions. The domain extends 30 vehicle lengths (or approximately 35 rotor radii) to the downstream direction.

The triangular grids can be generated by either the Delaunay triangulation or the advancing front technique. Highly stretched cells are required in the viscous regions. However, these grids do not naturally lend themselves to viscous flow computation. One of the approaches to represent the viscous region is to create a thin layer around a given geometry with a structured grid [115]. This method implemented and tested by the researchers [162, 163]. Determination of the grid's first height is of crucial importance, as it should be assigned properly in accordance with used turbulence model in order to get accurate results. The enhanced wall treatment is applied for the near-wall region to resolve the boundary layer and turbulence quantities more accurate. When the enhanced wall treatment is employed with the intention of resolving the laminar sublayer, y^+ at the wall-adjacent cell should be on the order of $y^+ = 1$ [123]. The grid's first height and boundary layer thickness are calculated using the following formula that depends on the basic boundary layer theory [123]. The length of the fuselage is used for the characteristic length, L .

$$\Delta y = L\Delta y^+ \sqrt{74} \text{Re}_L^{-13/14} \quad (6.1)$$

$$\delta = 0.035L \text{Re}_L^{-1/7} \quad (6.2)$$

The details of the medium mesh resolution are tabulated in Table 6.1.

Table 6.1 : Details of the medium mesh resolution.

<i>Surface Elements</i>		Element Type	Element Number / (min-max Element Length) [mm]
	<i>Pylon</i>		tria/quad
<i>Body</i>		tria/quad	107024 / (3-14.5)
	Total		143754 / (3-14.5)
<i>Volume Elements</i>	<i>Fluid Zone</i>	tetra/penta/hexa	11634782 / (3-5000)
	Total		11634782 / (3-5000)
<i>Boundary Layer</i>	<i>Element Type</i>		penta/hexa
	<i>Element Number</i>		3257600
	<i>Number of Layers</i>		25

The surface mesh, boundary layer and volume mesh structure close to geometry are shown in Figure 6.2. The distribution of the surface element lengths can be seen in Figure 6.3.

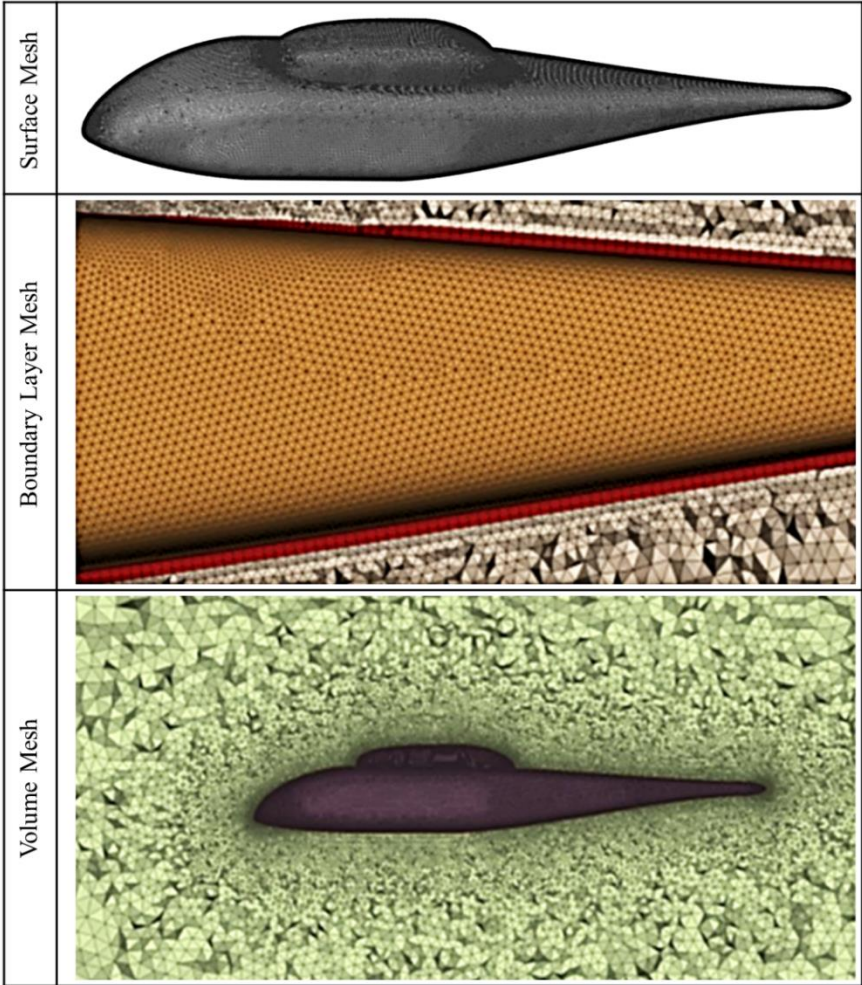


Figure 6.2 : Mesh details for the ROBIN fuselage.

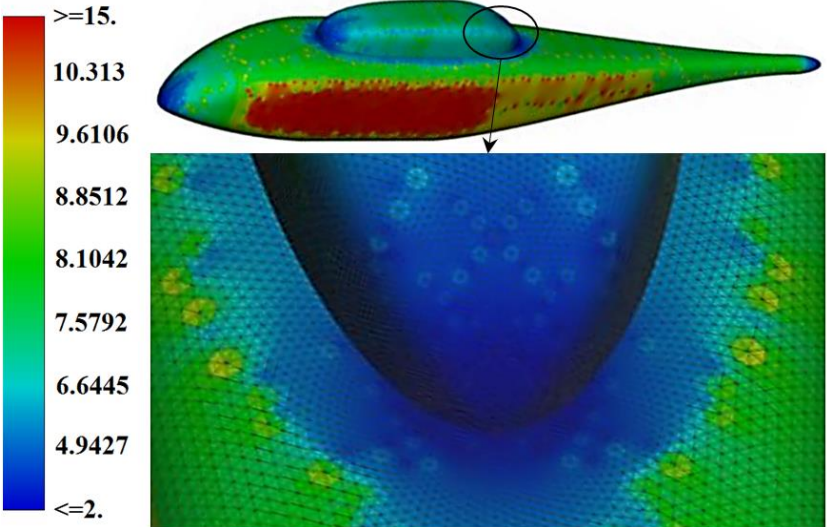


Figure 6.3 : Surface element length distribution [mm].

The surface and volume mesh elements are refined at the critical regions using the “size-box” feature of ANSA grid generator software. These size-boxes help to refine certain areas of surface and volume meshes without creating geometrical constructions for closed inner volumes [164]. The generated “size-boxes” and their influence on the element size distribution are shown in Figure 6.4.

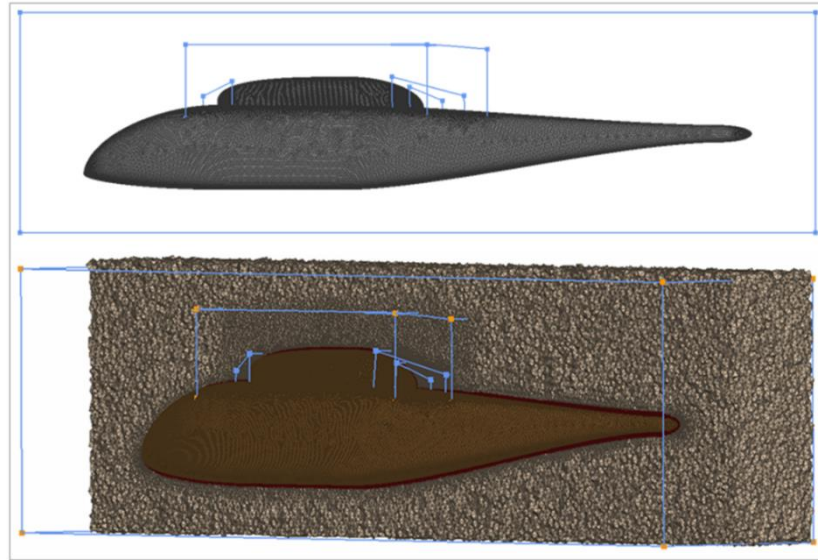


Figure 6.4 : Size-box usage.

Heise et al [16] stated that the grid independence was obtained after reducing the surface element length to 0.75% of fuselage length. Similar results for the grid independence were reported by Chaffin and Berry [165]. The surface element lengths determined in this study are consistent with those specified by other studies found in literature. The maximum surface element length is kept below 0.5% of the fuselage length.

6.1.2.1 Mesh dependency framework

The result of a blind analysis showed that the viscous effects constitute the great part of total drag force, nearly 78% of it. Hence, the accurate prediction of viscous drag has been the first subject of the present section. The effect of number of layers in the boundary layer region is studied to obtain the required boundary layer mesh specification. The task is to find the number of layers needed in the boundary layer region, which shall make the viscous force prediction independent from the boundary layer mesh resolution. The boundary layer mesh is generated by the combination of inner and additional outer layers. While surveying the number of layers a constant growth ratio, which is less than 1.2, is assigned for inner layers. The growth ratio is

not constant for the additional outer layers; it varies exponentially to a last aspect ratio, which is assigned as 0.6, of the relevant surface element length to provide the smooth junction between the boundary layer and the volume mesh. Moreover, orthogonality condition should be satisfied, particularly in the near body region. Special attention is given to obtain orthogonal mesh from the wall surface through the boundary layer region. In addition, the effect of grid stretching has been investigated for the viscous-affected region of the boundary layer to be properly resolved. The effect of number of layers on the prediction of viscous drag coefficient is presented in Figure 6.5. According to the results, the convergence is achieved at the layer number equivalent to 25. Therefore, the remaining analyses are carried out by using 25 layers.

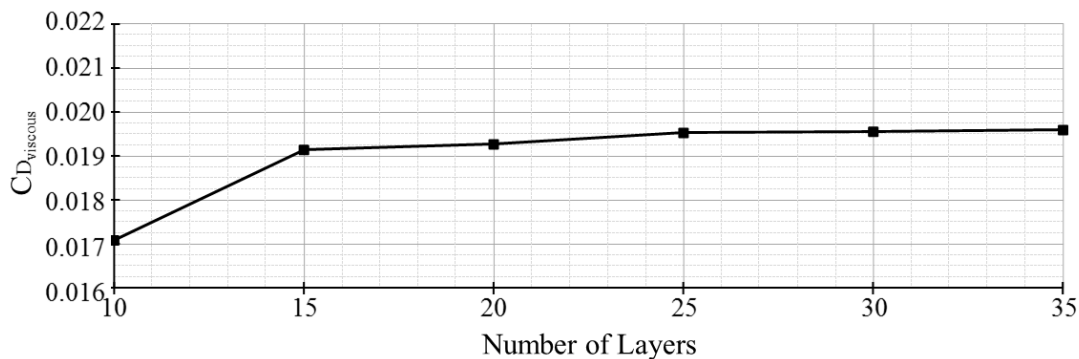


Figure 6.5 : Effect of the number of layers on the results.

Having determined the converged viscous drag, the subsequent study is to accurate prediction of pressure drag by establishing the necessary surface and volume mesh characteristics. Therefore, a systematic mesh dependency framework is taken into account. The mesh resolution specifications are given in Table 6.2.

Table 6.2 : Mesh resolution specifications.

	Coarse		Medium		Fine	
Edge/Corner Grid Spacing						
Min Element Length [mm]/ L%	16	0.51%	4	0.13%	2	0.06%
Max Element Length [mm]/ L%	24	0.76%	8	0.25%	8	0.25%
Growth Ratio	1.2		1.15		1.125	
Surface Mesh						
Min Element Length [mm]/ L%	16	0.51%	4	0.13%	2	0.06%
Max Element Length [mm]/ L%	48	1.52%	16	0.51%	16	0.51%
Growth Ratio	1.2		1.15		1.125	
Volume Mesh						
Growth Ratio	1.2		1.15		1.125	

Because the poor quality elements have unfavorable effect on the results, a particular attention is given during the mesh generation process. The maximum equiangle skewness of the triangular surface element is allowed to be 0.1. Distribution of the skewness values can be seen in Figure 6.6. The maximum skewness of the tetrahedral volume element is kept below 0.6 inside the computational domain.

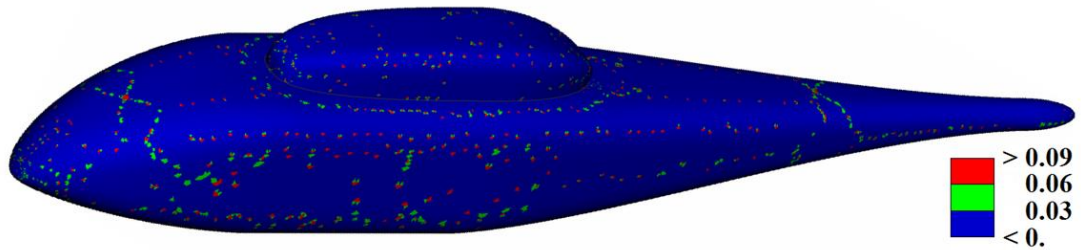


Figure 6.6 : Equiangle skewness of the surface elements.

The calculations are made at three different mesh resolutions. The grid refined at corners, possible stagnation and flow separation regions. Since the dominant part of the drag is due to the viscous effects and once it has been previously fixed by the determination of the required number of layers, the prediction of C_D is found almost the same for all three-mesh resolutions as can be seen in Figure 6.7. The medium mesh resolution is used for the following parametric studies.

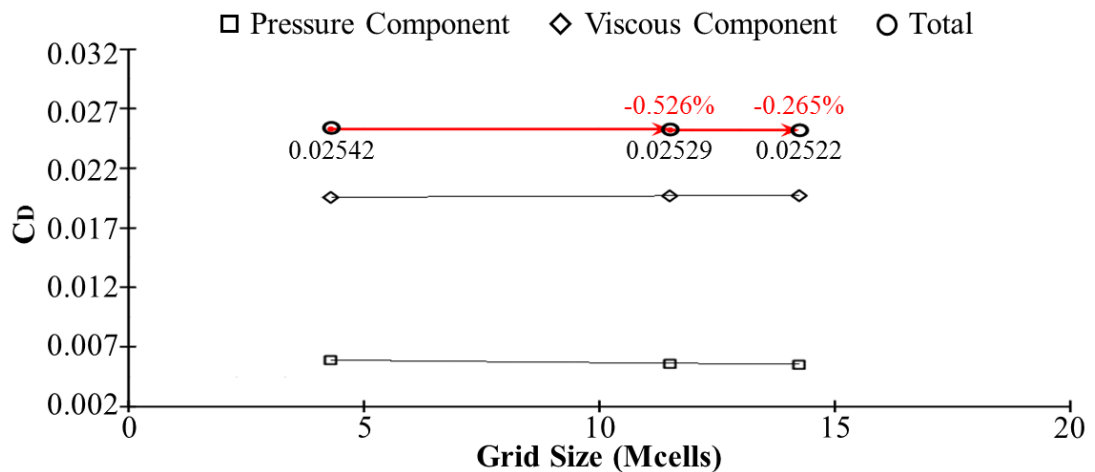


Figure 6.7 : Prediction of drag coefficient at different mesh resolutions.

6.1.2.2 Examination of spatial discretization schemes

In this sub-section, the effect of spatial discretization schemes is examined in order to get results that are more precise. For this purpose, the results of the second order upwind scheme and third order MUSCL scheme are compared. By using high order numerical schemes, the accuracy of the solutions can be improved significantly.

2nd order vs. 3rd order MUSCL discretization

Two types of approaches are studied to compare the effect of spatial discretization schemes on the drag coefficient prediction. The study is performed by using second order upwind and third order MUSCL discretization schemes for the discretization of the equations. The comparison of the results obtained by the discretization schemes is presented in Figure 6.8. The results show that there is not any significant change in C_D prediction due to the selected discretization schemes for the examined mesh resolutions. In other words, even the coarse mesh resolution is sufficient enough since the solution obtained by a high order scheme was not resulted in a remarkable change. It is obvious that a second order discretization can provide reliable results with the used mesh resolutions.

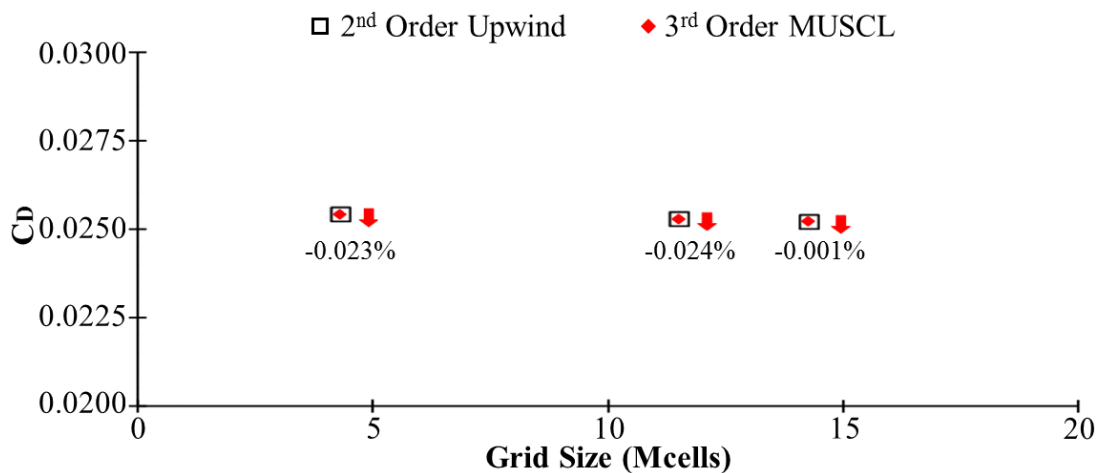


Figure 6.8 : Effect of the discretization schemes on the results.

Cell based vs. node based discretization

There are at least two choices as to where to locate the variables on a given grid. In the cell-based approach, the variables are stored at the centroid of the cells. On the other hand, in the node-based approach the variables are stored at the vertices of the grid. Particularly in 3D cases, the best choice between cell-based and node-based approach is still an open question. In the node-based scheme, the flux computation can be cast as loops over edges, whereas for the cell-based scheme they must loop over faces. The ratio of the number of faces to the number of edges is roughly two. From this point of view, the node-based schemes seem better than the cell-based schemes [115]. Therefore, the effect of cell-based and node-based discretization is also investigated in the present study. According to the FLUENT's theory guide [123], the node-based solver is more accurate than the cell-based approach especially, when the

computational domain is discretized by tetrahedral volume elements. The use of node-based solver leads to a lower C_D prediction when compared with the cell-based solutions. These C_D values are also close to the other CFD studies found in literature. As shown in Figure 6.9, the drag coefficient predictions of the node-based solver have been resulted in almost same amount of decrease for all three-mesh resolutions. Strictly speaking, the predictions are shifted down. The node-based solver requires more computing time but assures more reliable results.

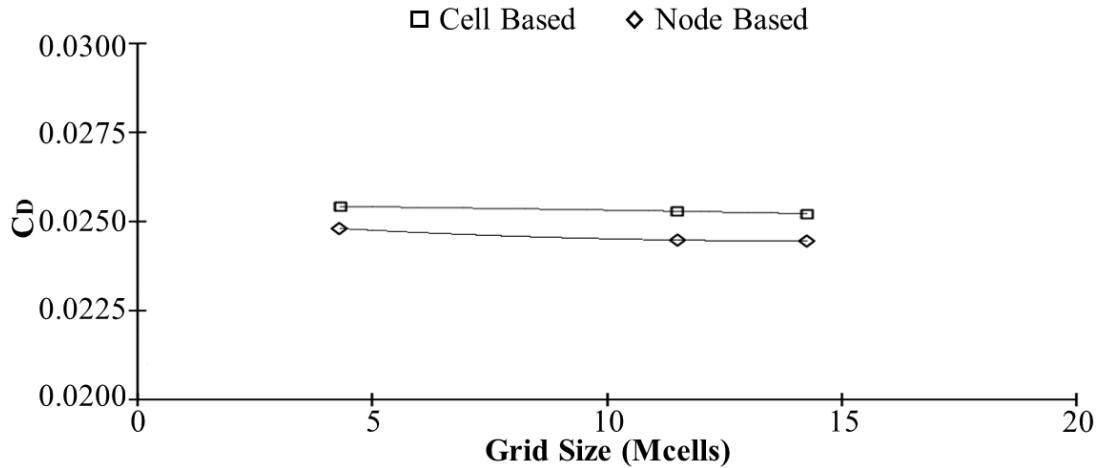


Figure 6.9 : Comparison of the Cell Based and Node Based discretizations.

6.1.2.3 The effect of turbulence models on the results

In the early days of N-S solver research, some algebraic model, namely, the Baldwin-Lomax (B-L) turbulence model has been used for implementation on unstructured grids [115]. In some applications, the B-L turbulence model is calculated on a reference grid and an interpolation with the values on the global unstructured grid has been made in [166] and [167]. With further development, the simple algebraic model gave place to more sophisticated turbulence models like the one-equation models of Baldwin-Barth [168] and Spalart-Allmaras [146] and the two equation models like $k-\epsilon$ and $k-\omega$.

In this section, the effect of turbulence models on C_D prediction are studied at zero angle of attack condition. The obtained results indicate that the predictions are in a good agreement with experiments for most of the cross-sections. The utilized turbulence models tend to be consistent in their prediction. However, it is observed that there are some slight differences in specific regions of the flow field. Therefore, detailed interpretation has been made for the results obtained by the examined turbulence models whether to clarify the cause of the observed differences. The

Realizable k- ϵ and SST k- ω models predicted the C_D lower than the results of Spalart-Allmaras and RNG k- ϵ models. Moreover, their results are also more convenient with the other CFD studies. A visual comparison has been made in Figure 6.10. According to the figure, the turbulence models produced very similar results ahead of the fuselage. Some discrepancies have been observed in the aft portions of the fuselage where $X/R > 1.0008$. The differences in calculation become obvious where the flow separation occurs. At those regions, for instance aft of the pylon (Figure 6.10 : $X/R = 1.162$ and $X/R = 1.345$), the C_p values in the vortex core regions are predicted differently by the turbulence models.

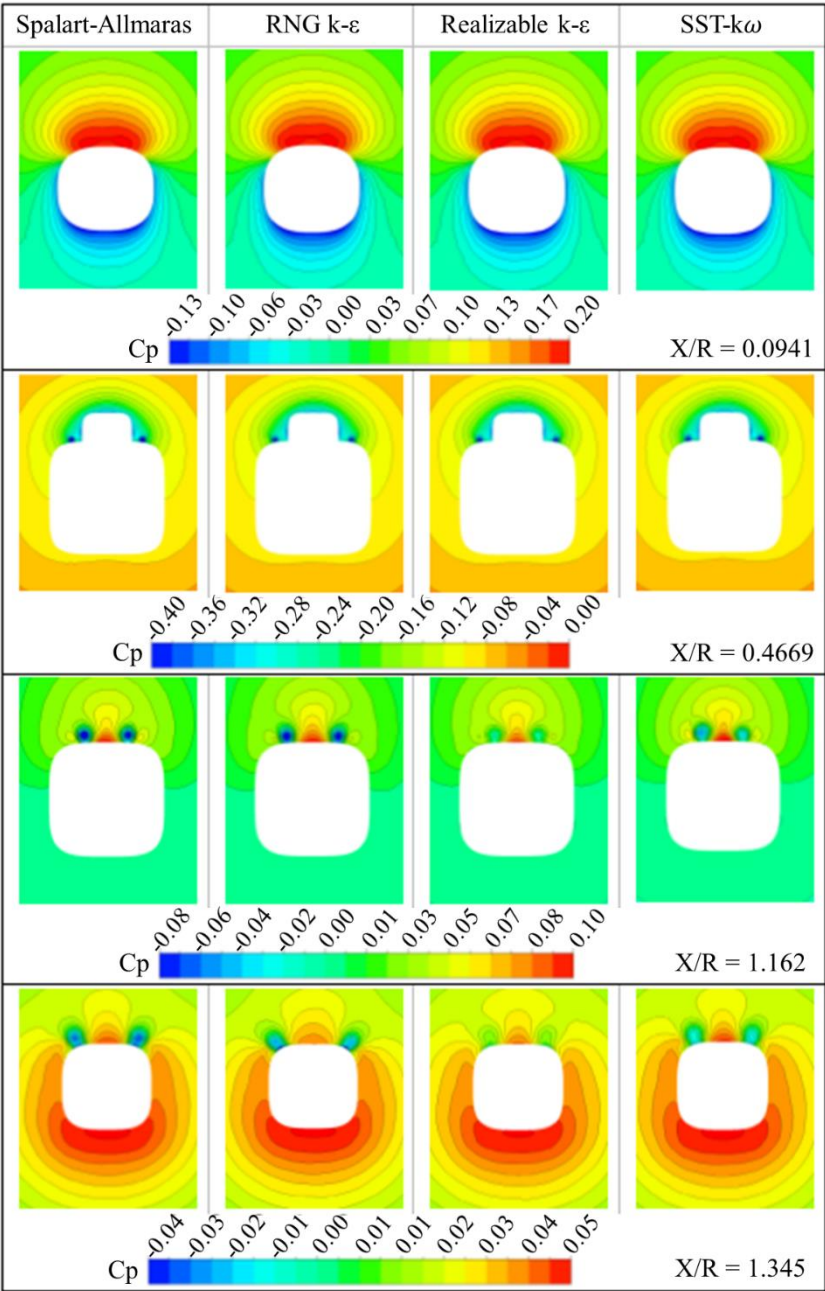


Figure 6.10 : Comparison of the turbulence models at selected sections.

6.1.3 Drag and lift predictions at various angles of attack

The predictions of drag and lift coefficients at various angles of attack have been made via using medium mesh resolution. Two types of turbulence models are chosen from a list of numerous options available in FLUENT and the obtained results are compared with the other CFD studies found in literature [103]. A better match is captured with the CFL3D predictions. The flow characteristics around the Robin fuselage and accuracy of the simulation approach is also examined by comparing the pressure coefficient values on the surface of the fuselage at different stations. The position of the sections can be seen in Figure 6.11. The non-dimensional values of these sections are given in Table 6.3. The C_p values of the specified cross-sections obtained from different angle of attack cases are given in Appendix A, where the figures also include the experimental and other CFD results found in literature. The obtained CFD results are well suited with the experimental data for most of the cross sections, but the results seem to be quite comparable between the present and prior numerical simulations.

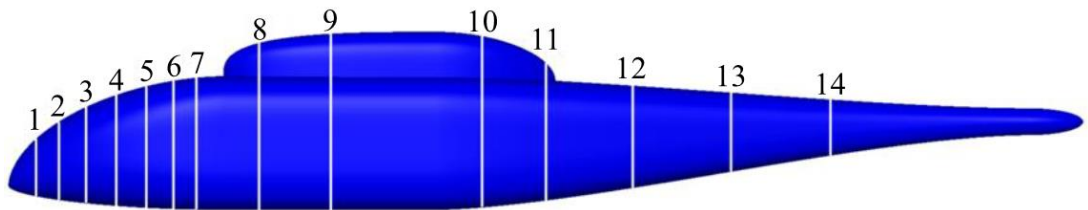


Figure 6.11 : Reference pressure sections of numerical solution.

Table 6.3 : Non-dimensional positions of the sections.

# Section	X/R	# Section	X/R
1	0.0517	8	0.4669
2	0.0941	9	0.6003
3	0.1450	10	0.8809
4	0.2007	11	1.0008
5	0.2563	12	1.1620
6	0.3074	13	1.3450
7	0.3497	14	1.5298

The prior numerical studies carried out by Tanabe et al. [31] and Chaffin and Berry [17] are examined to compare the pressure coefficients at the specified cross-sections. Table 6.4 provides the simulation parameters, where the first three rows are taken directly from these references.

Table 6.4 : Simulation details for the different angle of attack conditions.

Angles of Attack (α_f)	$-10^\circ, -8^\circ, -5^\circ, -3^\circ, 0^\circ, 5^\circ$
Reynolds Number	4.5E6
Mach Number	0.062
Inlet-Outlet static pressure value	1 atm
Turbulence Model	Realizable k- ϵ / SST kw
Near-Wall Region	Enhanced Wall Treatment
Pressure-Velocity Coupling	Coupled Algorithm
Spatial Discretization	3 rd order MUSCL

The calculated drag and lift coefficient values are given in Figure 6.12 and Figure 6.13, respectively. According to given figures, the results produced by the two types of turbulence models, which are examined in this study, are resulted in similar predictions to each other. Moreover, it is observed that a better agreement is obtained with the earlier predictions of CFL3D code.

The drag and lift coefficients are calculated using the following expressions,

$$C_D = 2D/\rho_\infty U_\infty^2 A \quad (6.3)$$

$$C_L = 2L/\rho_\infty U_\infty^2 A \quad (6.4)$$

where D is the drag force, L is the lift force, ρ_∞ is the density, U_∞ is the freestream velocity and A is the area.

The pressure coefficient on the fuselage surface is calculated using the traditional formulation, which is given by equation (6.5). However, the pressure coefficient on the rotor blades is calculated based on a modified expression, which is written in equation (6.6).

$$C_p = 2(P - P_\infty)/(\rho_\infty U_\infty^2) \quad (6.5)$$

$$C_p = (P - P_\infty)/(\rho_\infty U_{tip}^2) \quad (6.6)$$

The relationship between traditional and modified pressure coefficients is as follows

$$(2/\mu^2)(Modified C_p) = (Traditional C_p) \quad \text{where} \quad \mu = U_\infty/U_{tip} \quad (6.7)$$

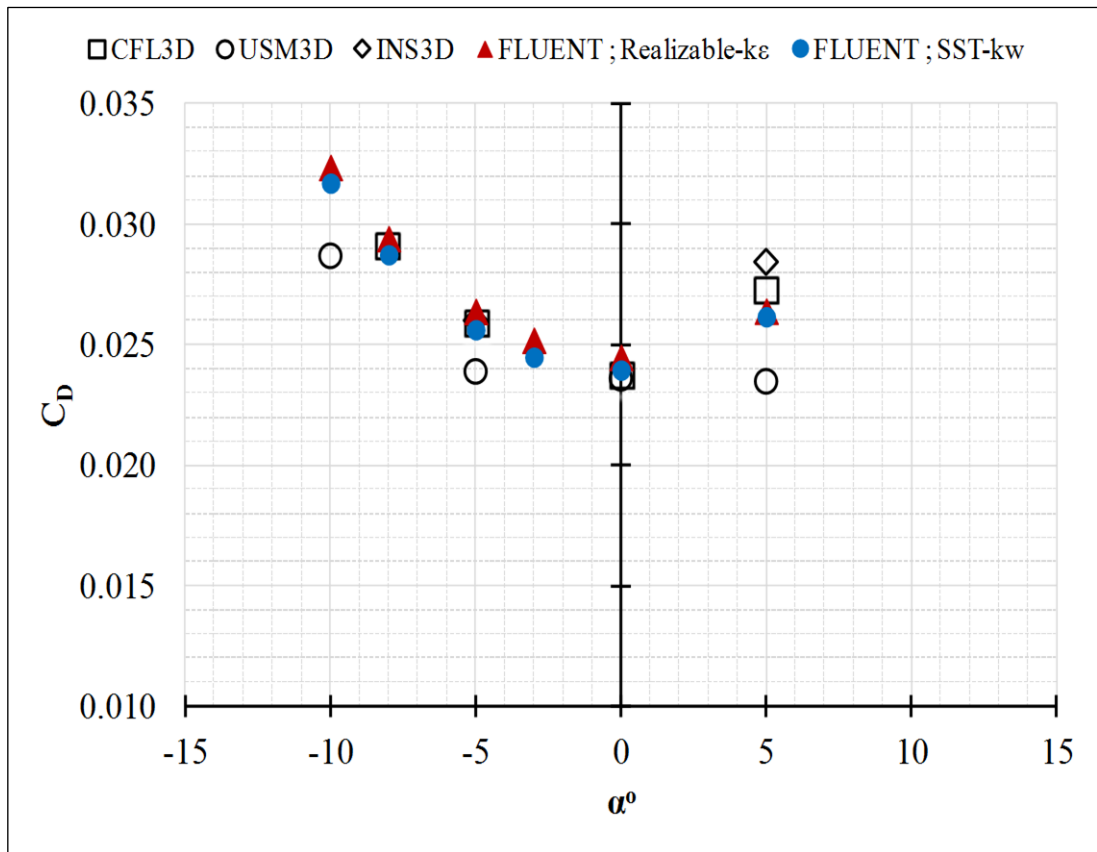


Figure 6.12 : Prediction of drag coefficients at different angles of attack.

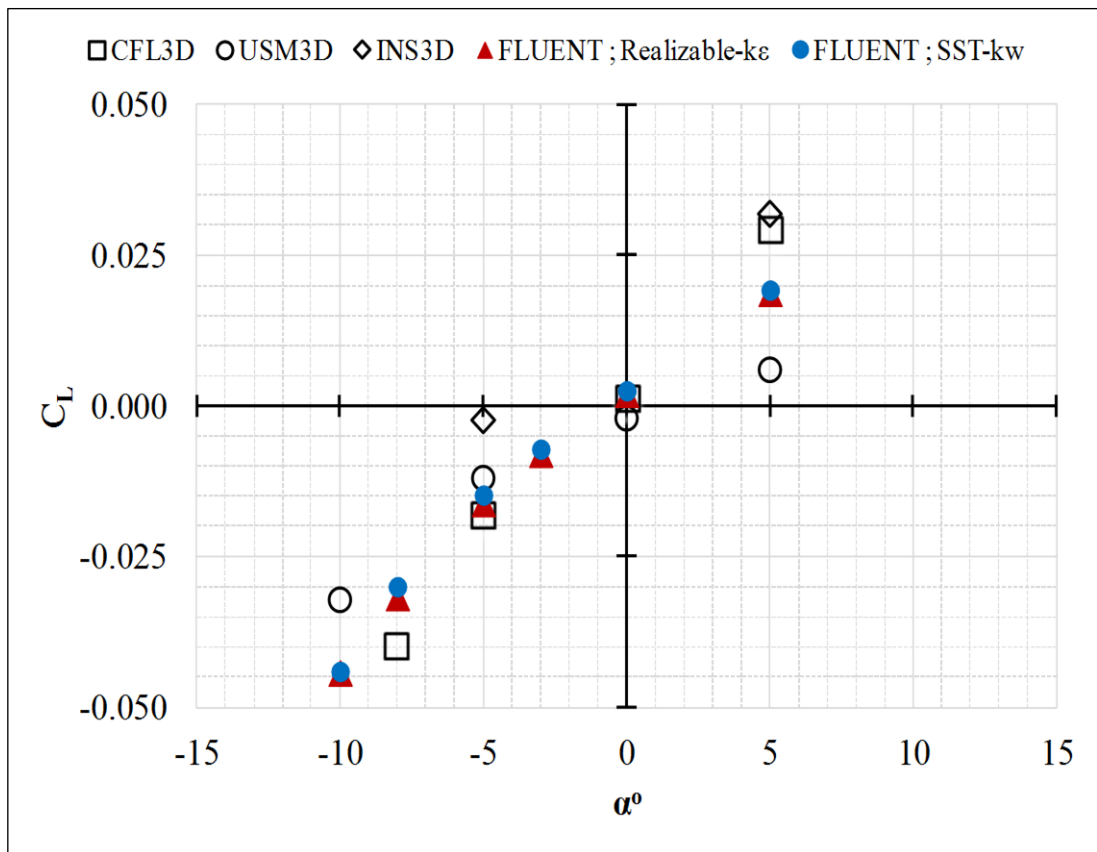


Figure 6.13 : Prediction of lift coefficients at different angles of attack.

Experimental data indicate a much larger pressure drop when the angle of attack values are 0° and 5° . Similar to other numerical predictions, the current results over-predict the C_p values ($-C_p$) around the aft and tail boom portion of the fuselage, particularly at angles of attack of 0° and 5° , (Figure A.3 and Figure A.4). The discrepancies seen at the aft parts of the fuselage are a result of the fuselage and the rotor hub strut being present in the experiments. It is intended to make comparisons with other numerical results found in the literature. Thus, the simulation geometry is constructed according to other numerical studies and the experimental conditions are not exactly modeled. The discrepancy between experimental and numerical results may have occurred as a result of neglecting these parts in the simulation model. This is also acknowledged by a prior numerical study [30]. When negative angles of attack are used the effect of the strut appears to diminish, (Figure A.1 and Figure A.2). Moreover, based on the experimental observations, it should be mentioned that the flow structure at the aft portion of the ROBIN fuselage at positive angles of attack are more complex than those obtained at negative angle of attack values, which may add to the discrepancies with the data. It is observed that the vortices generated at negative angle of attack conditions are more propagated through the sideways behind the pylon and proceeded towards the downwards without significantly impacting on the measurement points. The complex flow structure may require finer grids to resolve the associated changes therein.

The resulting streamlines on the fuselage surface are visualized in Figure 6.14, for fuselage angles of attack of 0° and -5° . The streamlines obtained from the analysis performed for 0° are more pointing downstream, whilst they are generally more directed toward the downwards for the -5° condition, as expected. The change observed for the surface streamlines actually compensates for the change in angle of attack values. For the same flow conditions, the results of reference studies [17, 31] are given in Figure 6.15. The existence of tightly curved streamlines corresponds to large pressure gradients and indicates vortex formation. The predictions of the panel method code (VSAERO) seem to be insufficient for the calculation of the streamline curvatures observed on the aft of the fuselage surface where flow separation can be expected due to the adverse pressure gradients. On the other hand, it is noteworthy that both the results of the present study and the prior CFL3D predictions are well consistent with each other in terms of the structure of the surface streamlines.

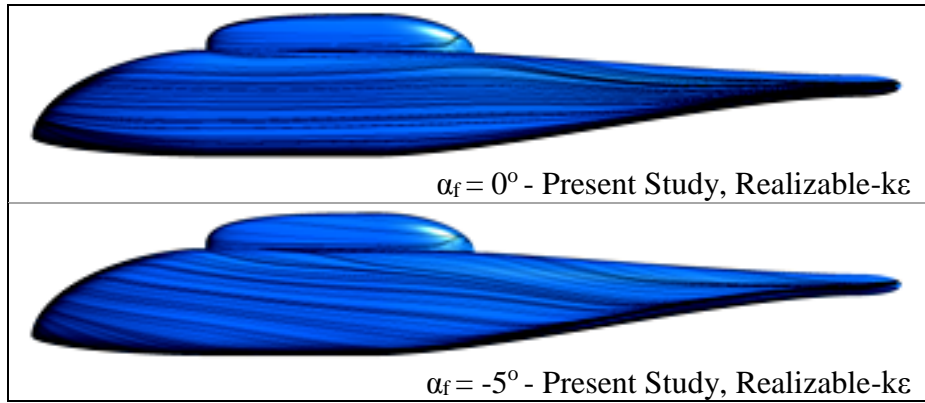


Figure 6.14 : Fuselage surface streamlines.

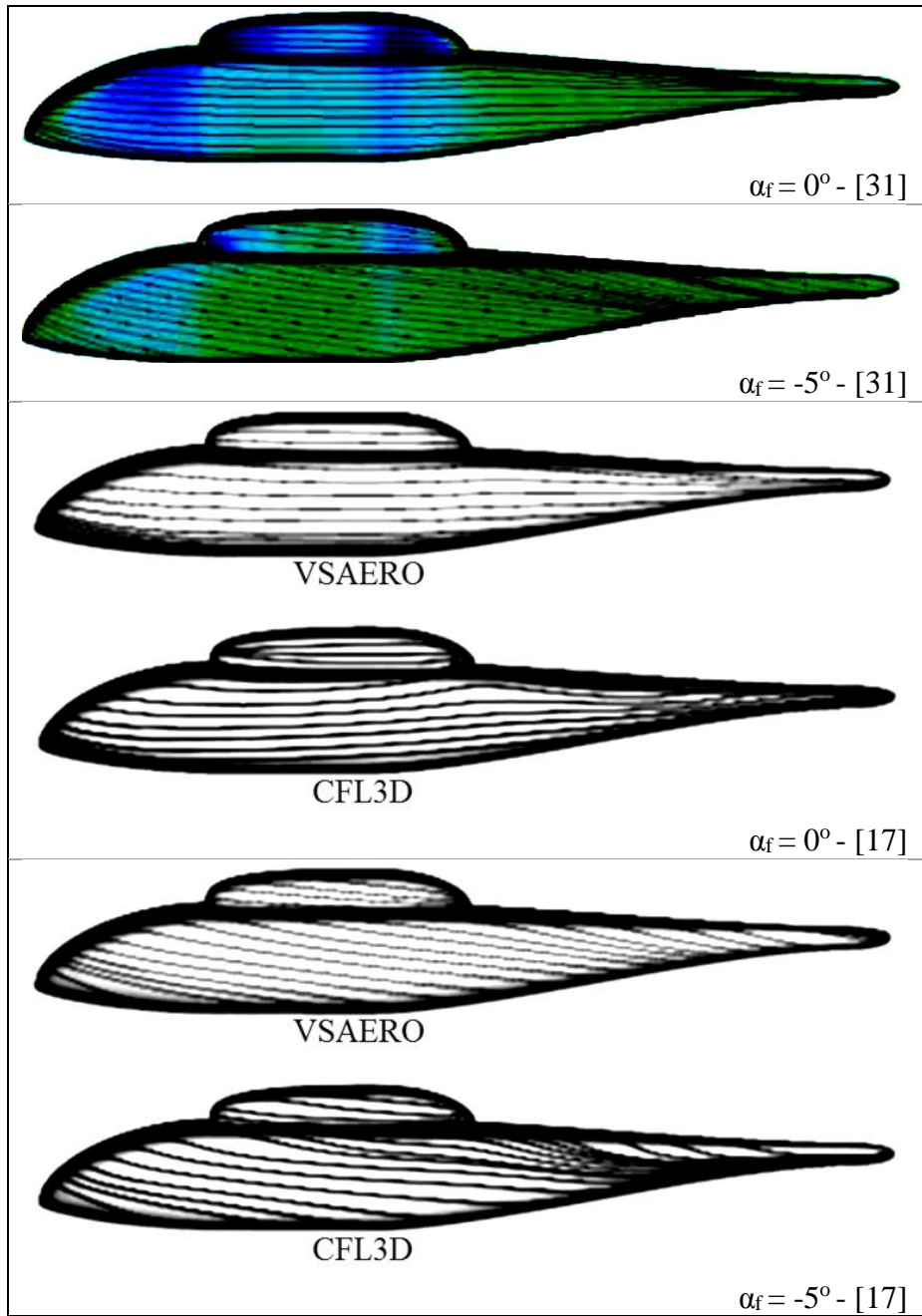


Figure 6.15 : Fuselage surface streamlines of reference studies.

For zero angle of attack, the contour plots of x-velocity and pressure coefficient distributions of the symmetry plane are given in Figure 6.16 and Figure 6.17, respectively. Figures indicate that the predictions obtained by the turbulence models are almost identical to each other in terms of both velocity and pressure fields.

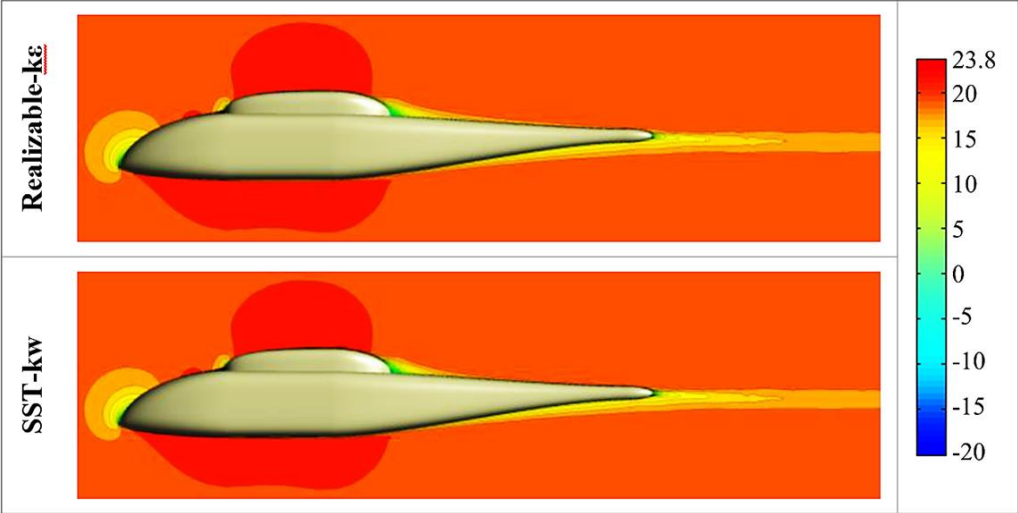


Figure 6.16 : X-velocity contours at symmetry plane, $\alpha_f = 0^\circ$.

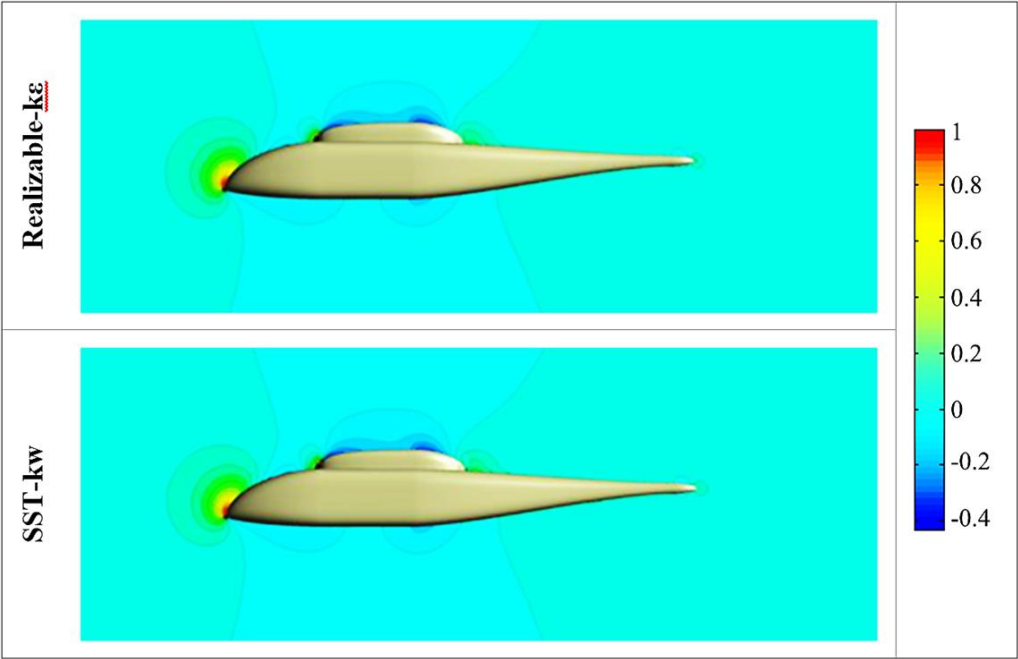


Figure 6.17 : The C_p contours at symmetry plane, $\alpha_f = 0^\circ$.

The flow characteristics obtained at zero angle of attack condition can be seen in Figure 6.18. According to the figure, the flow separation regions are predicted slightly smaller in size by the SST-kw turbulence model, which is therefore resulted in a lower drag prediction. Detailed representation of the flow patterns including the other angle of attack conditions are given in Appendix B.

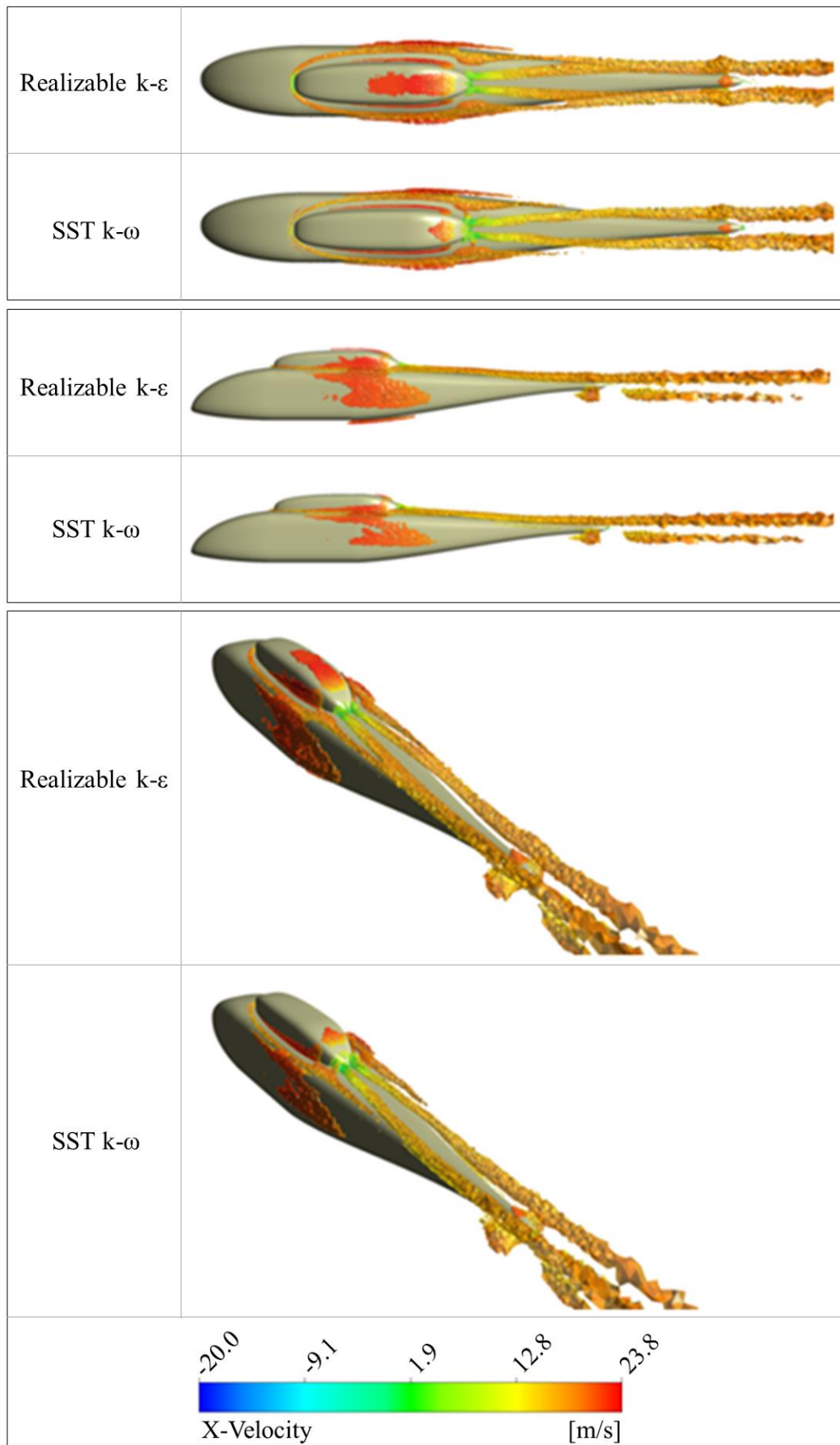


Figure 6.18 : Flow patterns obtained at $\alpha_f = 0^\circ$.

6.2 Isolated Rotor Analyses

6.2.1 Hover performance prediction of UH60-black hawk rotor

In this section, the hover performance prediction of UH60-Black Hawk rotor blade is obtained by steady RANS analysis. The rotation of the blades is modeled using moving reference frame approach. The computational grid is created with ANSA software. The entire flow domain is represented by structured hexahedral volume elements. A validation study is aimed to compare the results of CFD analysis via known performance data of the rotor. The determination of the most accurate numerical method for the flow phenomena around the helicopter rotors will maintain the reliability of the planned analyses. Although the rotor configuration has four blades in reality, only one blade is modeled due to the existence of periodicity, since the reduction of computational cost of CFD simulations is a major concern. A structured hexahedral grid with C-H-H topology is generated in the flow domain by paying considerable attention on capturing tip-vortex and wake structures to simulate flow phenomena over the rotor blades precisely. The Reynolds number based on blade chord length is approximately 1.36 million. The obtained CFD results are in a good agreement with experimental data. The more reliable performance prediction is based on the research in the area of grid adaptation and higher-order numerical schemes, as it is also stated in [169].

6.2.1.1 Geometry

UH60 Black Hawk rotor blade is used to numerically investigate the hover performance characteristics. Experiments were conducted for a four-bladed scaled-rotor model with a blade diameter of 9.4 ft. corresponding to a 1:5.73 scale of the actual geometry, [169]. The rotor solidity is given as 0.0825. This scaled model geometry constitutes a basis for the present CFD analysis. The blade has two types of airfoils through the span wise direction (Figure 6.19).

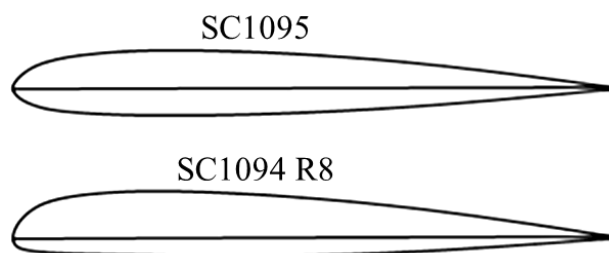


Figure 6.19 : Airfoils used in the blade geometry, [170].

Moreover, the information related to the blade geometric features were taken from other studies, [170]. The position of the airfoils are visually demonstrated in Figure 6.20, and their numerical expressions are tabulated in Table 6.5. Figure 6.21 illustrates the span wise twist angle distribution gathered from two different studies. In light of the information obtained through literature review, the 3D model of the blade geometry (Figure 6.22) has been generated using a CAD software, CATIA.

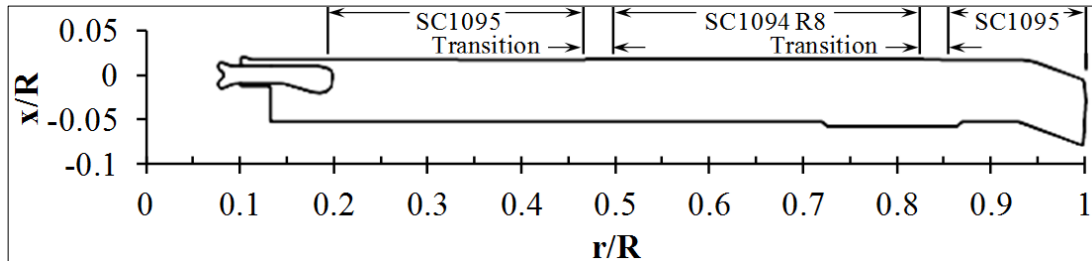


Figure 6.20 : Blade planform view and position of the airfoils, [170].

Table 6.5 : Section characteristics, [170].

Section Characteristic	Radial Location,in.	Chord,in.	Quarter
Root cutout	42.000	20.760	0.000
SC1095 (inner)	62.000	20.760	0.000
SC1095 (outer)	150.000	20.760	0.000
SC1094R8 (inner)	160.000	20.965	0.154
SC1094R8 (tab,inner)	236.910	22.317	-0.184
SC1094R8 (outer)	265.000	22.317	-0.184
SC1095 (inner)	275.000	22.112	-0.338
SC1095 (tab,outer)	277.860	22.112	-0.338
SC1095 (sweep,inner)	299.000	20.760	0.000
SC1095 (sweep,tip)	322.000	22.092	-12.562

^aRelative to SC1095 quarter chord, positive forward.

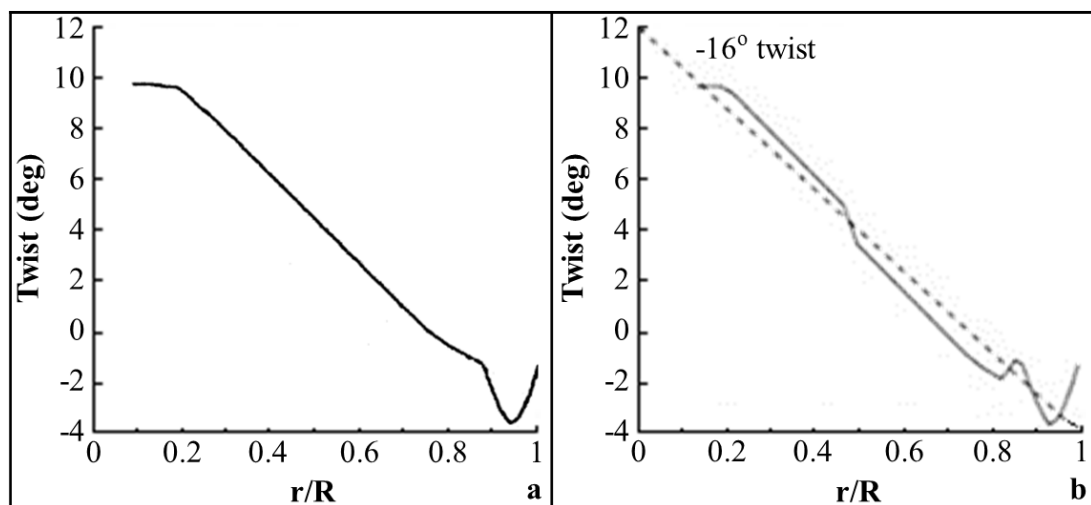


Figure 6.21 : Twist angle distributions used in: (a) [169] and (b) [170].



Figure 6.22 : UH60 Black Hawk blade geometry.

6.2.1.2 Computational mesh details

The entire flow domain is divided into four sub-blocks to generate structured grid around the rotor. C-topology is used along the free-stream direction. On the other hand, the grid structure has an H-topology on both the blade surface normal and span wise directions. The C-H-H topology captures the rotor wake better than O-O topology. However, the volume mesh elements, which are generated at far field, become considerably small while approaching to the rotation axis. This situation may negatively affect the stability of the numerical scheme. The mentioned problem has not been observed in the present analysis. Considerable attention is given to obey the orthogonality condition for the grids at near blade surface. Simulations are executed using only one main rotor blade. The effect of the other blades is handled through the periodic boundary condition in the azimuthal direction. Thereby, the use of 90° periodicity feature made the computation time reduced. Two different grid resolutions, namely, coarse (164x125x84) and fine (296x196x114), are used to obtain the results. The coarse and fine grids include approximately 1.7 and 6.6 million hexahedral volume elements, respectively. The grid stretching is not utilized only at the boundary layer development regions, but also exist all along the way of rotor wake and tip vortices. This grid structure is especially focused on the critical regions where sudden and significant changes occur in the flow properties. That kind of approach ensures reliable results leading to lower computational time, since the usage of minimal level of total number of elements. The hub is extended virtually through the entire flow domain and free-slip wall boundary condition is assigned to this surface in order to reduce the computation time. The z-axis (0,0,1) is being the rotation axis and the origin is located at (0,0,0). The top and bottom boundaries of the grid are five rotor radii above and ten rotor radii below the rotor disc, respectively. The information for the boundary conditions are provided in Figure 6.23.

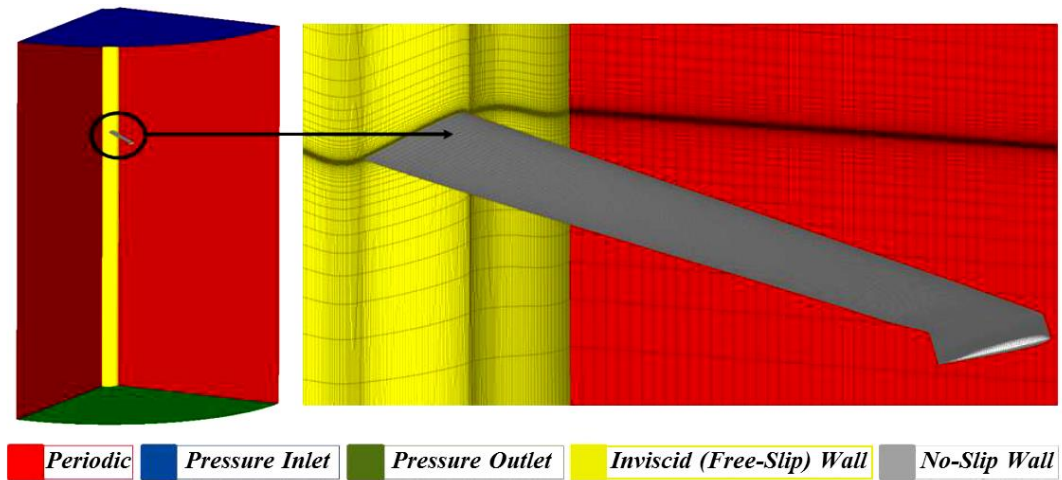


Figure 6.23 : View for the boundary conditions and grid structure.

In coarse mesh resolution, the minimum grid spacing at the blade tip is $0.008c$ and it is approximately $0.15c$ at the blade root. The grid distance to the nearest wall is $0.026c$. In fine mesh resolution, the minimum grid spacing at the blade tip and root are $0.005c$ and $0.1c$, respectively. The value of the grid first height is $0.00008c$ for the fine mesh resolution. The appropriate value of y^+ (determination of grid first height) for the employed turbulence model is of great importance on predicting the blade performance accurately. Figure 6.24(a) shows the grid structure on the blade surface and around the near-blade region. The grid stretching along the blade surface normal direction is performed to resolve the boundary layer precisely, Figure 6.24(b).

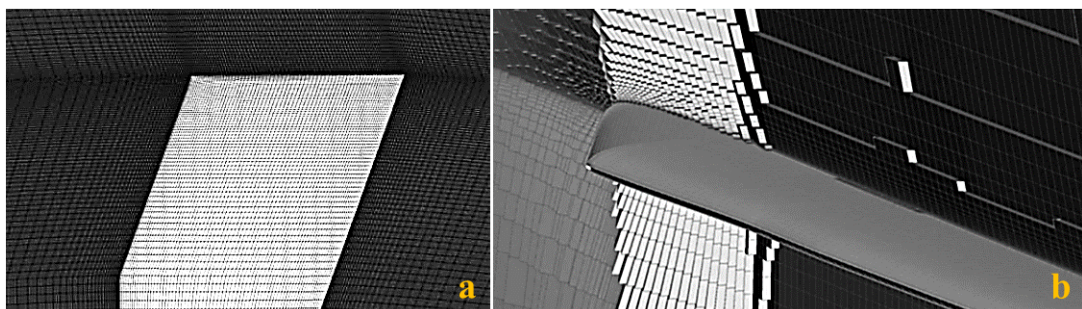


Figure 6.24 : (a) The surface grid structure, (b) the applied grid stretching.

6.2.1.3 Numerical methods

The rotor wake structure is three-dimensional and unsteady. Its accurate prediction of strength and position plays a significant role for the precise determination of the pressure distribution on rotor blades. The CFD analyses are performed for the hovering condition of the rotor at a prescribed rotational frequency by assuming a three-dimensional, steady, compressible, viscous flow. The moving reference frame approach is applied to represent the rotational motion of the blades. The experiments

are conducted for the tip Mach number equivalent to 0.628. The rotational frequency of the rotor is calculated as 1425rpm according to the given tip Mach number value. The Reynolds number based on blade chord length is approximately 1.36 million. The analyses have been conducted by the steady RANS computations. In the RANS approach, all the turbulent motions are modeled, which leads to a reduction of computational resources. Turbulence nature of the flow has been modeled using the SST- $k\omega$ and Realizable- $k\varepsilon$ with enhanced wall treatment option.

The ideal gas law relates the volume and pressure of a gas to the temperature of the gas. When the rotor blades operate at a relatively high rotational frequency, there may be change in the temperature of the flow field due to the high frictional rate occurred between the blade surface and the airflow. Possible changes in temperature would cause differences in both pressure and velocity fields. Therefore, the selection of the convenient pressure-velocity coupling scheme is of great importance for the accurate simulations of such kind of flow regimes. The pressure-velocity coupling is achieved through the Coupled scheme for the compressible flow analyses performed in this section. The equations are discretized based on the second order upwind scheme.

6.2.1.4 Results and discussion

The RMS (root mean square) values are obtained below 10^{-5} for the continuity, 10^{-7} for the momentum and 10^{-9} for the energy equations. Furthermore, a second check mechanism is performed pursuing the change in thrust and torque coefficients during the analysis in order to being sure that the convergence is achieved (Figure 6.25). In Table 6.6, the obtained results are compared with experiments.

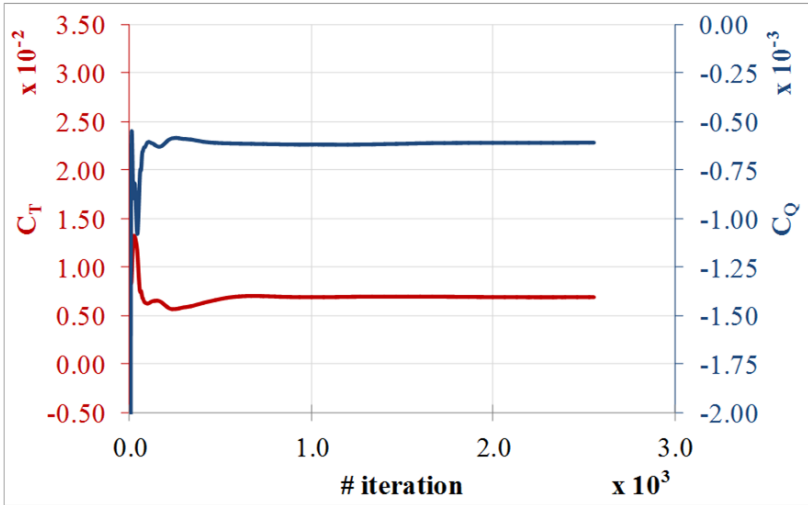


Figure 6.25 : Convergence of the thrust and torque coefficients.

Table 6.6 : Comparison of the CFD results with experimental data.

Turbulence Model / Grid Type	θ	CFD		EXP.	err%	CFD		EXP.	err%	CFD		EXP.	err%
		CT/ σ		CQ/ σ		FM							
SST - kw / Coarse (164x125x84)	10.7	0.0712	0.0884	0.0884	-19.4	0.0062	0.0073	0.0073	-15.3	0.624	0.731	0.731	-14.7
SST - kw / Fine (296x196x114)	10.7	0.0856	0.0884	0.0884	-3.2	0.0077	0.0073	0.0073	4.8	0.663	0.731	0.731	-9.4
	12	0.1008	0.1047	0.1047	-3.7	0.0097	0.0094	0.0094	3.0	0.673	0.729	0.729	-7.8
Realizable - k ϵ / Fine (296x196x114)	10.7	0.0858	0.0884	0.0884	-3.0	0.0079	0.0073	0.0073	7.6	0.650	0.731	0.731	-11.2

Figure 6.26 shows a comparison between the results of the present study and the results obtained by other numerical studies and measurements. The results obtained with the coarse grid are not well-suited with the experimental data. This situation can be explained by the inappropriate value of y^+ for the employed turbulence model, Figure 6.27(a). A finer grid is created to clarify whether the solution is independent of the grid resolution of the boundary layer. The y^+ distribution over the blade surface for the fine mesh resolution is given in Figure 6.27(b).

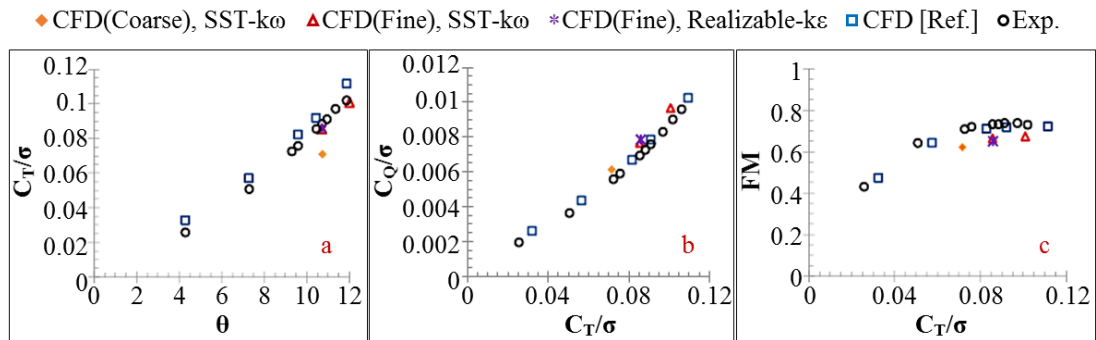


Figure 6.26 : (a) CT/σ vs. θ , (b) CQ/σ vs. CT/σ , (c) FM vs. CT/σ , [169].

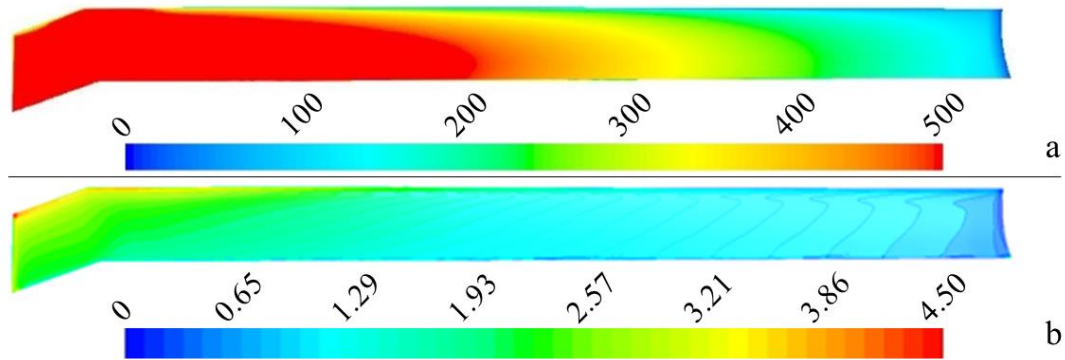


Figure 6.27 : The y^+ distribution over the blade : (a) coarse grid, (b) fine grid.

Shown in Figure 6.28(a) is the z-velocity distribution on the periodic boundaries. Only the negative values are presented to emphasize the induced flow regions. Figure 6.28(b) presents the vorticity distributions occurred on different r-z planes. This figure demonstrates the evolution of the tip vortices with increasing vortex age. As the vortex age increases, the blade tip vortices begin to lose their strength considerably and are exposed to a rapid change in shape, which resulted in enlargement due to loss in energy.

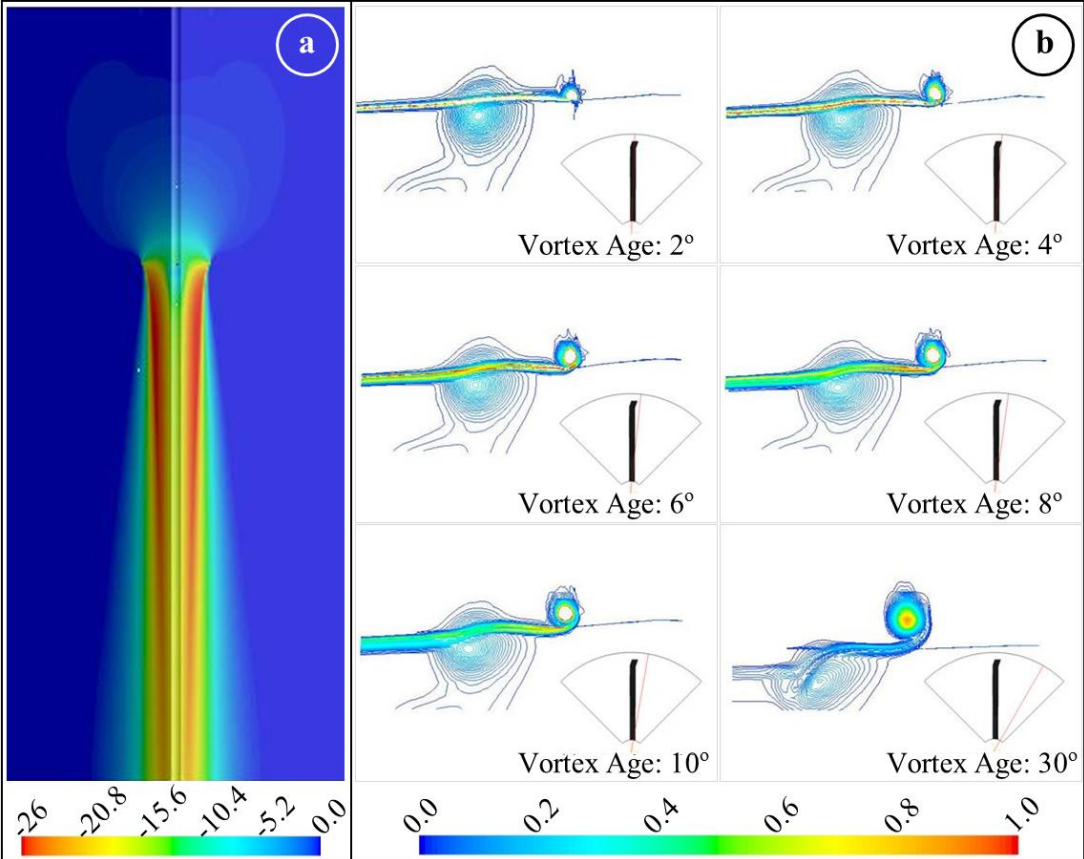


Figure 6.28 : (a) z-velocity distribution [m/s], (b) the vorticity distributions.

The pressure coefficient distributions are extracted from the selected cross sections of the blade. The results of SST- $k\omega$ and Realizable- $k\epsilon$ turbulence models are in a great consistency with each other. A slight difference has been observed for the predicted sectional pressure coefficients near the blade tips. Moreover, the results of fine grid simulations are in a good agreement with the experimental data, Figure 6.29. Although the most of the results are very well suited with measurements, some discrepancies have been observed. For instance, the C_p distribution at the root section ($r/R=0.225$) is to stay away from experiments. Somehow, the pressure distributions for both upper and lower blade surfaces are predicted inaccurate. The hub, which was not modeled in

the simulation, may be the reason of this circumstance. It seems probable that the blade geometry close to the hub might have some differences leading to a deviance in the results. Moreover, the C_p values along the 5% portion of the upper-front surface at sections ($r/R=0.965$) and ($r/R=0.99$) are predicted lower than the experimental results. In other words, the velocities at those regions are calculated higher than it should be. Wake et al [169] had encountered the similar problem in their studies.

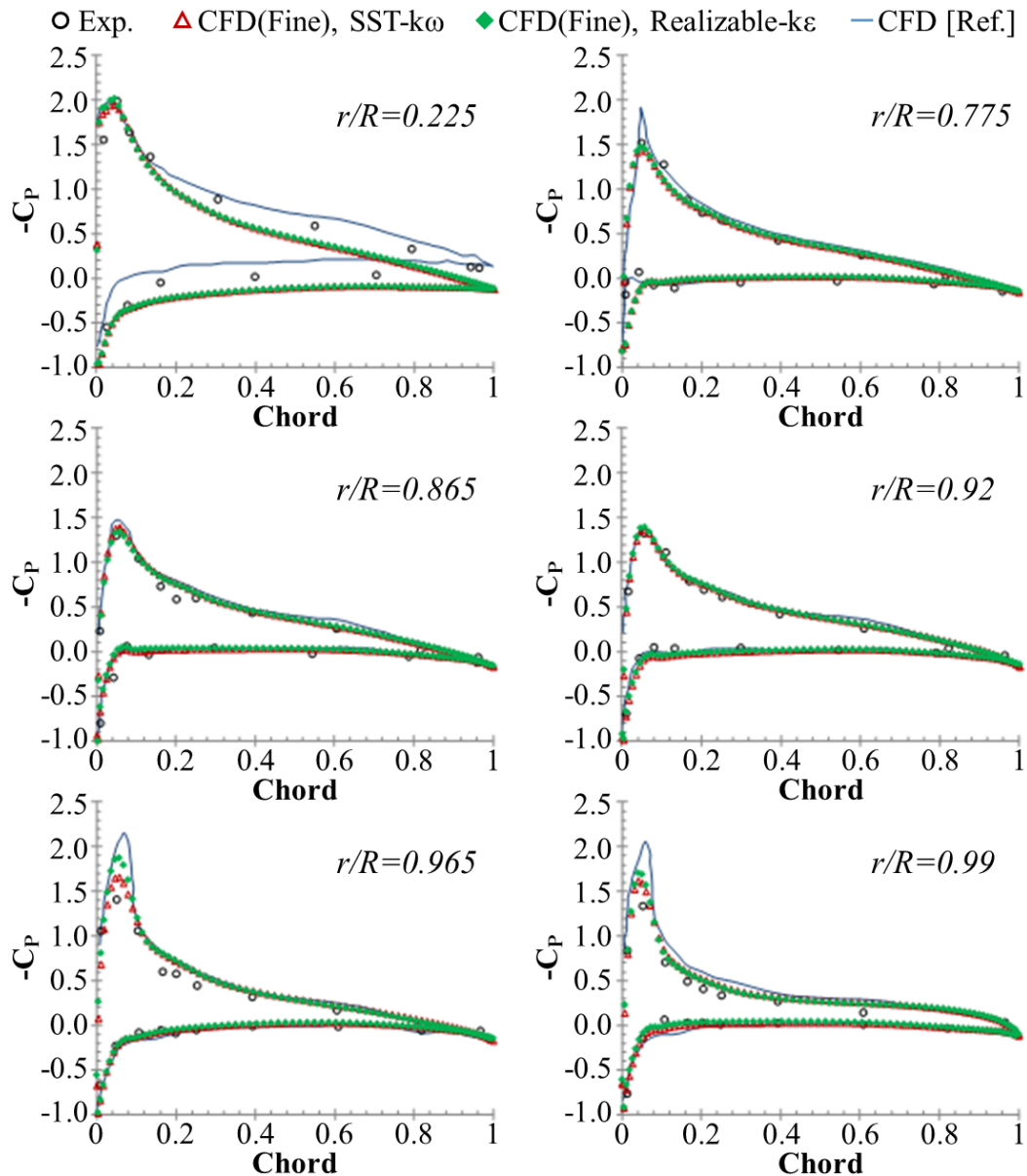


Figure 6.29 : Comparison of C_p distributions with [169].

As shown in Figure 6.30, the inflow ratio (the ratio of axial velocity to blade tip velocity) is compared with the results of the reference study. Only the negative values are visualized for emphasizing the wake region. Shown in Figure 6.31 is the comparison of axial velocity and tip vortex contours at an azimuth angle equivalent to

minus 35 degrees. A similar comparison of vorticity generated near the blade trailing edge is shown in Figure 6.32.

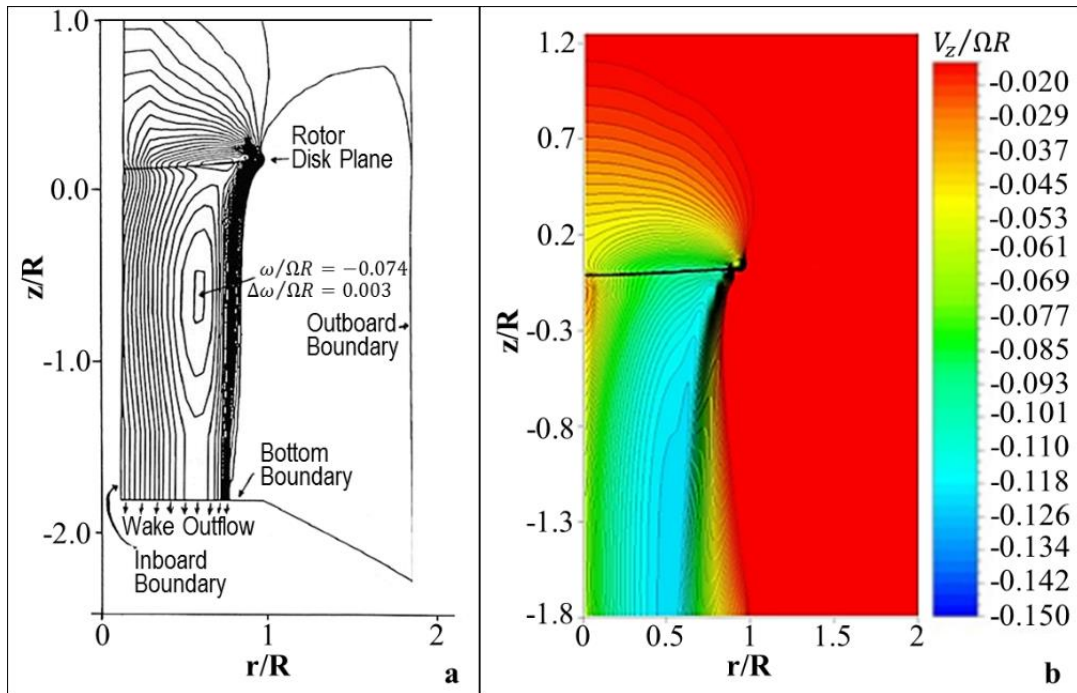


Figure 6.30 : Inflow ratio at $\psi = -10^\circ$: (a) [169], (b) present study.

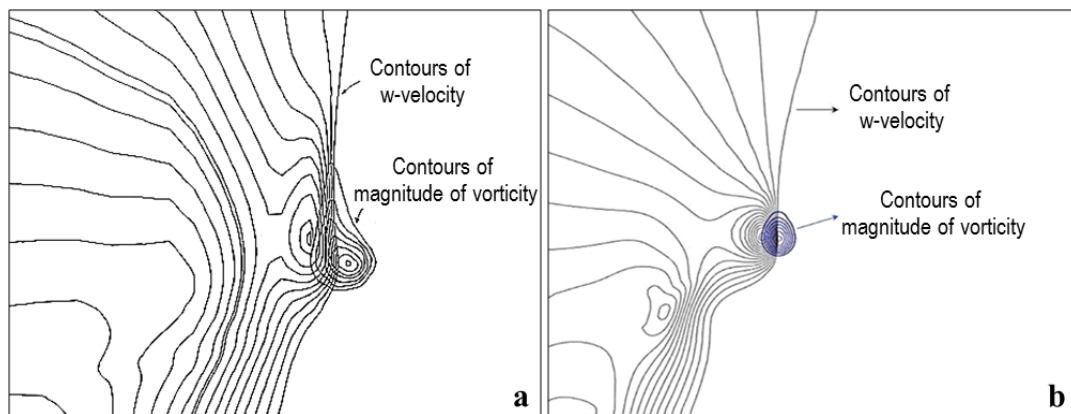


Figure 6.31 : Axial velocity and tip vortices: (a) [169], (b) present study.

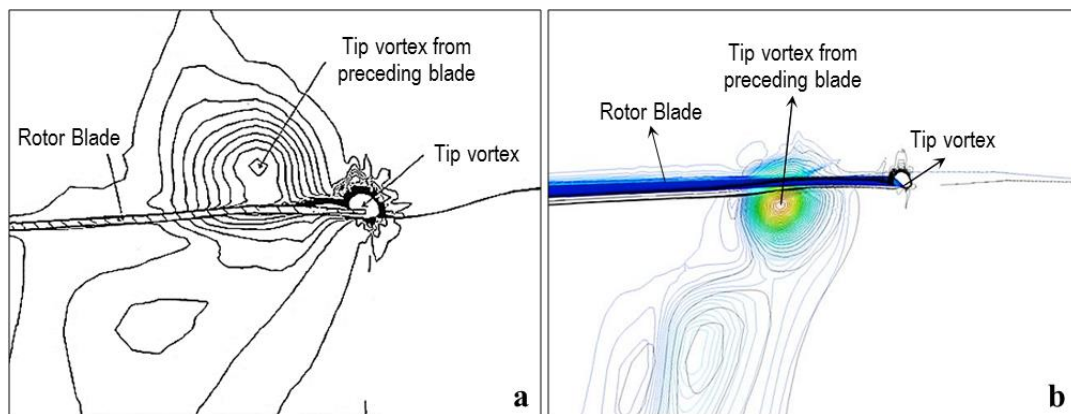


Figure 6.32 : Computed vorticity magnitudes: (a) [169], (b) present study.

Experiments show that the blade tip vortex passes by about $0.6c$ below the consequent blade. In the reference CFD study [169], the authors assert that the tip vortex passes above the consequent blade by about $0.4c$ for a coarse grid resolution ($191 \times 43 \times 55$) and $0.2c$ for a fine grid resolution ($201 \times 83 \times 55$). They indicate that the details of the tip-vortex flow could not be captured well due to diffusion, which causes the discrepancy with the experimental results. In the present study, the result of the fine mesh resolution ($296 \times 196 \times 114$) shows that the blade tip vortex passes by about $0.27c$ below the consequent blade (Figure 6.32.b, Figure 6.33 and Figure 6.34).

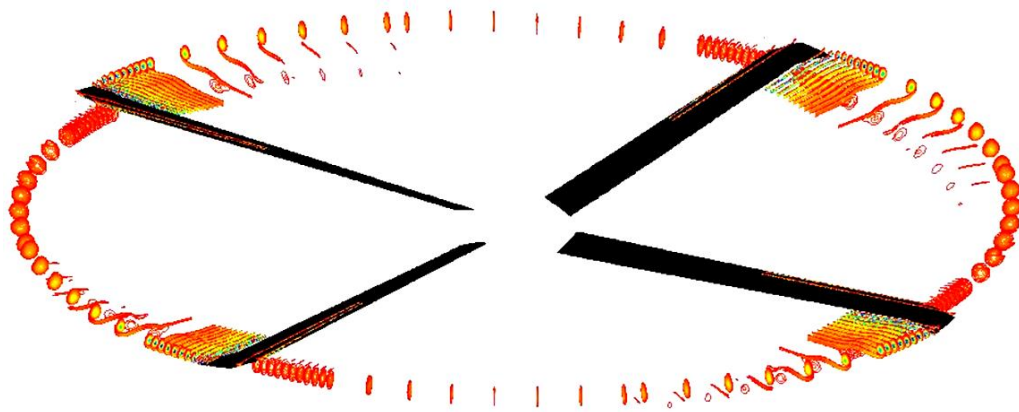


Figure 6.33 : The path of the blade tip vortex.

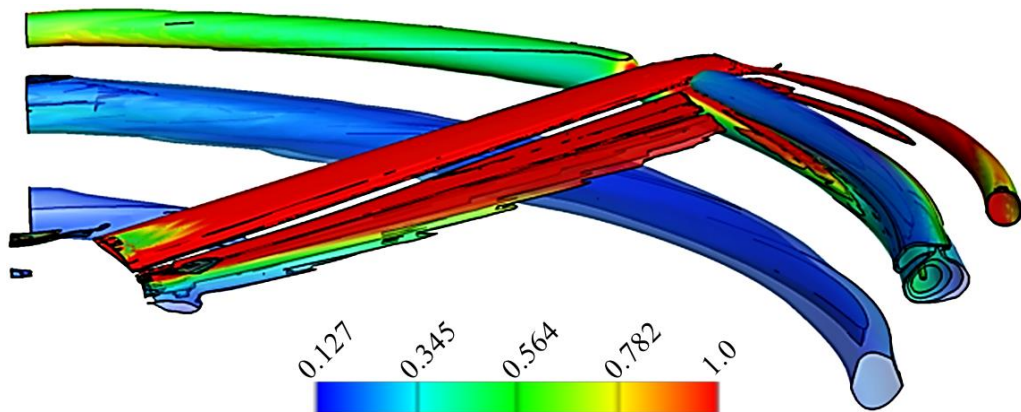


Figure 6.34 : Normalized vorticity contours of the blade tip vortex.

6.2.1.5 Concluding remarks

In this section, a validation study is carried out to obtain the hover performance characteristics of UH60 Black Hawk rotor blade by using moving reference frame approach. The output of this study also emphasizes the importance of using higher-order numerical schemes and improved grid resolution. The presented numerical methodology can be said reliable enough to simulate a helicopter rotor analysis in hover condition. The study in this section does not include the forward flight condition

where the blades encounter an asymmetric velocity field and unsteady effects become dominant. Therefore, it is highly recommended to review and examine the applied numerical procedure for the forward flight condition. However, it should be noted that although the used moving reference frame approach is able to predict the intrinsic steady-state behavior of hover condition, it is not very convenient for forward flight condition, especially when the unsteady flow field data is needed. Therefore, in Section 6.2.2, a more accurate numerical approach called "dynamic mesh technique" is introduced to evaluate the unsteady flow characteristics of forward flight condition. The application of the technique is presented and the obtained results are discussed in detail.

6.2.2 Four-bladed rotor analyses in forward flight

In this section, URANS analyses of four-bladed IRTS rotor have been carried out using dynamic mesh technique. The following subsections present the description of used geometry, the rotating blade motion, details of the computational mesh, and numerical modeling. The obtained results for the isolated rotor are provided in Section 6.2.2.6.

6.2.2.1 Geometry

The geometric features of the fuselage and the main rotor complementing the whole simulation model are given in Table 6.7. The features of the geometry is taken from the references [28, 31].

Table 6.7 : ROBIN IRTS geometric features

Fuselage	ROBIN
l (m)	1
Fuselage yaw	1.2° (the nose left)
Center Points, (x/l,y/l,z/l)	
Fuselage	(0.051,0,-0.322)
Rotor hub	(0,0,0)
Blade section	NACA0012
c (m)	0.06858
Rotor rotation	CCW from above
Linear twist	-8°
b	4
Planform	Rectangular
R (m)	0.860
σ	0.098

The four-bladed IRTS rotor (independent rotor test system) is drawn by CATIA to be placed over the fuselage, as shown in Figure 6.35. The model does not include a tail rotor.

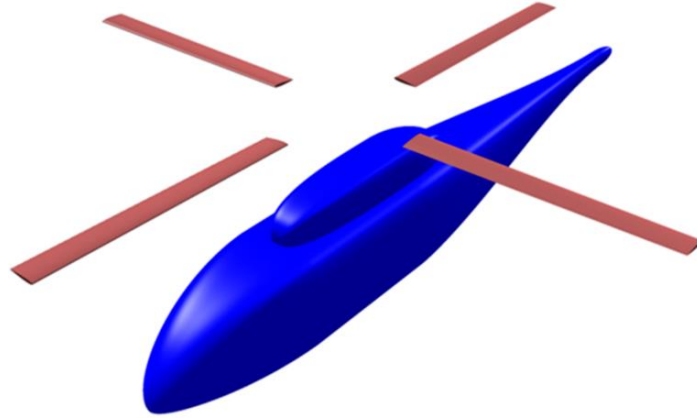


Figure 6.35 : Surface model of the ROBIN fuselage and its four-bladed rotor.

6.2.2.2 Rotating blade motion

Unlike the hover condition, the blades are exposed to asymmetric aerodynamic loads in forward flight. Therefore, the motion of the blades varies with the azimuth angle because of these air-loads. Fourier series can describe the periodic pitching and flapping motions of the blades as a function of blade azimuth [61, 105].

Pitch (Feathering):

$$\theta(\psi) = \theta_0 + \sum_{n=1}^{\infty} (\theta_{nc} \cos n\psi(t) + \theta_{ns} \sin n\psi(t)) \quad (6.8)$$

$$\theta(\psi) = \theta_0 + \theta_{1c} \cos\psi(t) + \theta_{1s} \sin\psi(t) + \theta_{2c} \cos 2\psi(t) + \theta_{2s} \sin 2\psi(t) + \dots \quad (6.9)$$

Flap:

$$\beta(\psi) = \beta_0 + \sum_{n=1}^{\infty} (\beta_{nc} \cos n\psi(t) + \beta_{ns} \sin n\psi(t)) \quad (6.10)$$

$$\beta(\psi) = \beta_0 + \beta_{1c} \cos\psi(t) + \beta_{1s} \sin\psi(t) + \beta_{2c} \cos 2\psi(t) + \beta_{2s} \sin 2\psi(t) + \dots \quad (6.11)$$

The pitch and flap of the blade vary at each time step by an increment in the rotational motion, where

$$\psi(t) = \Omega t \quad (6.12)$$

The subscript 1 in the equations denotes the first harmonics of the blade. The higher harmonics of the blade motion can be found by adding more terms. In practice, these are found to be very small and for rotor performance evaluation, it is considered acceptable engineering practice to neglect all harmonics above the first [105]. The motion of rotating bodies in terms of the fixed inertial frame can be expressed by Eulerian angles. In this study, Eulerian angles prescribe the blade motion using only the mean and first blade harmonics.

The experimental blade control variables associated with different flight conditions are given in Table 6.8. Tanabe et al. [31] stated that, when the blade control settings are defined as in experiments, the calculated thrust values are not met with the measured ones. Generally, as given in Table 6.9 and Table 6.10, these control settings are adjusted until the calculated thrust matches to that of the experiment, as performed in references [28, 82]. In the present study, the simulations are performed using parameters listed in Table 6.11.

Table 6.8 : Blade control variables obtained by experiments, [31].

μ	M_∞	α_s	θ_0	β_0	θ_{1c}	θ_{1s}
0.012	0.0064	0.0	11.8	1.5	-0.1	0.2
0.151	0.080	-3.0	10.3	1.5	-2.7	2.4
0.231	0.122	-3.0	10.4	1.5	-0.4	3.8

Table 6.9 : Blade control variables obtained by other simulations, [28].

μ	M_∞	α_s	θ_0	β_0	θ_{1c}	θ_{1s}
0.05	0.0064	0.0	6.8	1.5	-2.3	1.2
0.151	0.080	-3.0	6.3	1.5	-2.3	2.1
0.231	0.122	-3.0	6.3	1.5	-2.1	3.3

Table 6.10 : Blade control variables obtained by other simulations, [82].

μ	M_∞	α_s	θ_0	β_0	θ_{1c}	θ_{1s}
0.012	0.0064	0.0	8.8	1.5	-0.1	0.2
0.151	0.080	-3.0	6.64	1.5	-2.356	2.288
0.231	0.122	-3.0	6.523	1.5	-1.906	3.434

Table 6.11 : Flow conditions and blade control variables.

μ	M_∞	α_s	θ_0	β_0	θ_{1c}	θ_{1s}
0.012	0.0064	0.0	9.3	1.5	-0.1	0.2
0.151	0.080	-3.0	7.4	1.5	-2.3	2.1
0.231	0.122	-3.0	7.0	1.5	-2.1	3.3

In this study, the x-axis is on the retreating side of the rotor, the y-axis is pointing in the downstream (toward the helicopter tail) and the z-axis is vertical, pointing up. The rotor rotation is in the counter clockwise direction when viewed from above. The orientation of the blades is shown in Figure 6.37. The grid coordinates of the blades and capsule-like blocks are located based on their initial positions. The coordinates of the initial positions can be determined from the relevant azimuth angles such as 0° , 90° , 180° and 270° . The new grid coordinates during the simulation are always computed using the initial mesh. The blade position can be changed by transforming the position vector through successive matrix multiplications [61, 99]. Equation (6.13) represents the transformation matrix: T, which consists of the rotation matrices.

$$T = [R(\theta)][R(\beta)][R(\psi)] \quad (6.13)$$

Here, $R_y(\theta)$ is the rotation in y-axis and refers to feathering motion. $R_x(\beta)$ is the rotation in x-axis and refers to flapping motion of the blade. $R_z(\psi)$ is the rotation in z-axis which represents the azimuthal change.

$$R_y(\theta) = \begin{bmatrix} \cos\theta & 0 & -\sin\theta \\ 0 & 1 & 0 \\ \sin\theta & 0 & \cos\theta \end{bmatrix} \quad (6.14)$$

$$R_x(\beta) = \begin{bmatrix} 1 & 0 & 0 \\ 0 & \cos\beta & \sin\beta \\ 0 & -\sin\beta & \cos\beta \end{bmatrix} \quad (6.15)$$

$$R_z(\psi) = \begin{bmatrix} \cos\psi & \sin\psi & 0 \\ -\sin\psi & \cos\psi & 0 \\ 0 & 0 & 1 \end{bmatrix} \quad (6.16)$$

The new position of a given point can be determined by the application of the transformation matrix, which is given by equation (6.17).

$$\vec{x}_{new} = T\vec{x}_{old} \quad (6.17)$$

Application of the inverse transformation returns the newly generated point to its original position. In addition, the application of transformation matrix to an entire mesh provides the rigid mesh motion of whole domain. Furthermore, the transformation matrix may also be applied to particular mesh elements to enable the motion within a deforming mesh [99].

6.2.2.3 Practical difficulties and aspects open to improvement

In FLUENT, dynamic mesh simulations currently work only with first-order time advancement. A second-order time advancement algorithm for enhancing the temporal accuracy shall be resulted in more realistic flow field predictions. Moreover, distorted volume mesh elements may have been generated in the computational domain while using this solution technique. This can be stated as one of the most common problems in dynamic mesh applications. The mesh validity can be maintained for a while by the use of mesh smoothing methods. At the time when the smoothing methods cannot be sufficient due to the presence of inadmissible mesh elements, re-meshing of the flow field will be a necessity in order to sustain the motion. It is worthy to note that re-meshing process, currently, can only be realized by using single CPU, [123]. Therefore, the time step size, which actually determines the amount of blade motion, should be chosen with care for the effective use of smoothing methods. Otherwise, dynamic mesh approach will be resulted in frequent re-meshing, which would lead to a prohibitive computational cost.

6.2.2.4 Computational mesh details

The domain boundaries are formed by a cylindrical shape and cover a region that is of 15 vehicle lengths to the upstream and radial directions. The domain extends 30 vehicle lengths (or approximately 35 rotor radii) to the downstream direction.

The standard wall functions in FLUENT are based on the proposal of Launder and Spalding [161], and have been used widely for industrial flows. The logarithmic law for mean velocity is known to be valid for $30 < y^* < 300$. In FLUENT, the log-law is employed when $y^* > 11.225$. The laminar stress-strain relationship is being applied when the mesh is such that $y^* < 11.225$ at the wall-adjacent cells. Standard wall functions are available with $k-\varepsilon$ and Reynolds stress models (ANSYS FLUENT). Some consideration during the mesh generation is a necessity for successful computations of turbulent flows. For standard wall functions, each wall-adjacent cell's centroid should be located within the log-law layer. Thus, a suitable boundary layer meshing strategy is taken into consideration for the proper use of the standard wall function approach. The value of $0.01c$ as the grid's first height for this flow problem ensures that almost every wall-adjacent cell's centroid is located within the log-law layer. The minimum grid spacing is assigned as $0.015c$ at the blade tip and corners.

The maximum element length reaches to $0.1c$ on the blade surface. The boundary layer region of the blades is represented by six prismatic layers with a value of $0.01c$ as the grid first height. The assigned growth ratio for the boundary layers is less than 1.2. Figure 6.36 demonstrates the boundary layer mesh and the volume mesh inside the capsule-like block. The rest of the domain represented by tetrahedral volume elements.

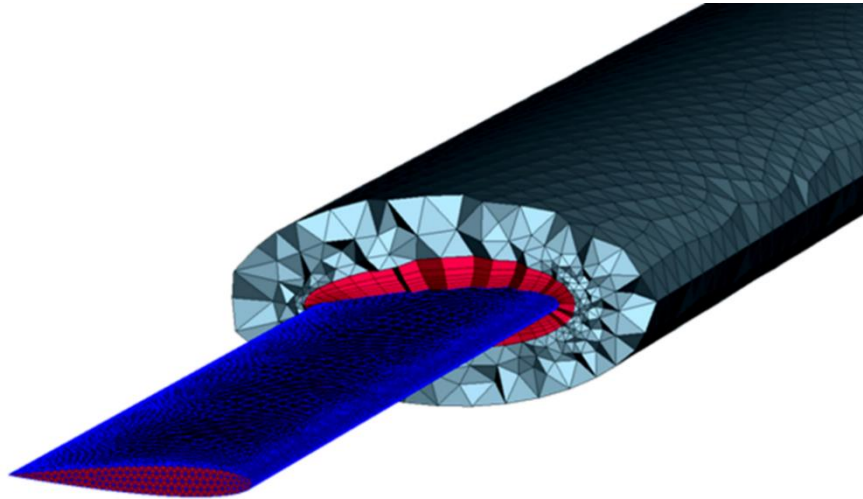


Figure 6.36 : Mesh details around the blade.

The computational grid consists of non-overlapping six blocks for the isolated rotor simulations. The boundaries between these blocks are not overset. The blocks were generated all at once using internal grid boundaries. The surface meshes on the block boundaries do exactly correspond with each other. The mesh used in this study is a traditional finite volume mesh involving unique connectivity information for all the generated volume mesh elements. The surface meshes on the block boundaries do not contain any hanging nodes. Each rotor blade is surrounded by its own capsule-like block. Each capsule-like block performs the same prescribed rigid body motion with the corresponding blade. The main reason to create capsule-like blocks around the blades is to preserve element quality at the near blade region. The capsule-like blocks are enclosed by a fifth block. Subtraction of capsule-like blocks from the fifth block defines a closed inner volume, named as sub-domain#5, in which the volume mesh elements are allowed to deform as the blades move. Inside the deformable block, the mesh validity has been maintained using the spring based smoothing and re-meshing methods. As the deformation gets larger, the mesh validity cannot be maintained by the spring based smoothing method, only. Therefore, re-meshing is required to accommodate the motion. The solver invokes re-meshing when the grid deformation is more than a pre-defined skewness value of 0.95. Thus, re-meshing is not carried out

at every time step, leading to reduced computational effort. When re-meshing is applied, the connectivity of the mesh elements within the deformable block is also updated. Moreover, the solution obtained at previous time-step is being interpolated onto the newly generated mesh. Finally, the sixth block formed by a cylindrical shape represents the outer stationary far field. A detailed representation of the blocks are given in Figure 6.37 (a). The size of the deformable block should be large enough to accommodate the motion of the blades. The boundary of the deformable block extends approximately one chord length away from the capsule-like blocks, everywhere, Figure 6.37 (a) and Figure 6.37 (b). The mesh for the deformable block and capsule-like blocks contains approximately two million tetrahedral volume elements. The total number of the volume mesh elements generated in the computational domain is about seven million.

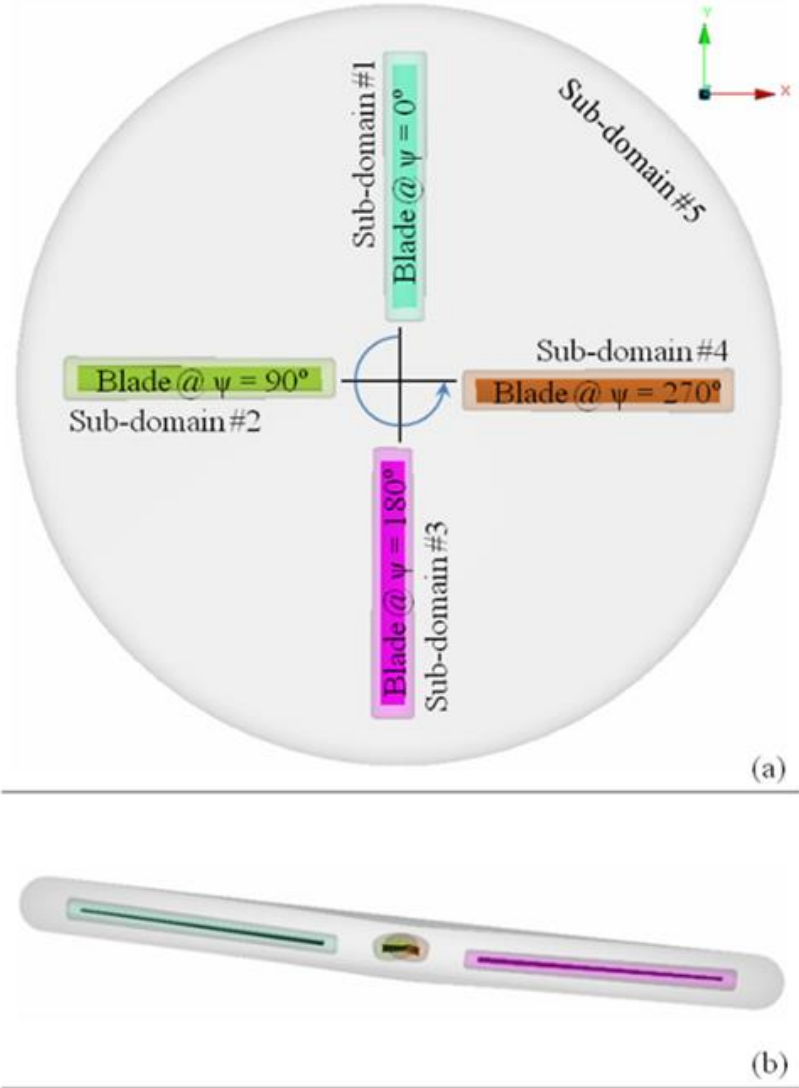


Figure 6.37 : Structure of the blocks: (a) top view, (b) side view.

Figure 6.38 shows the volume mesh inside the deformable block where a uniform element length was maintained, away from the capsule-like blocks. A very similar approach, particularly for the block structure has been used in [84]. Another similarity has been captured for the total cell count in the computational domain. The author states that the cell count for the complete helicopter is about seven million.

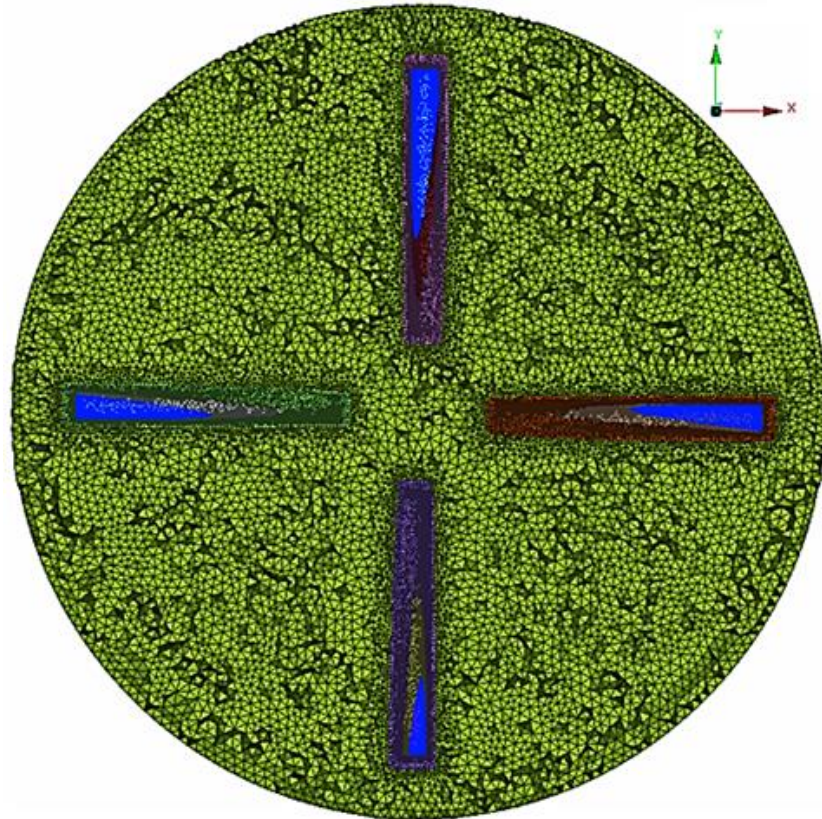


Figure 6.38 : Uniformly generated elements in the deforming block.

The generated volume meshes for different advance ratios are given in Figure 6.39 to Figure 6.41. The mesh is refined at possible wake regions at a moderate level by considering computational effort. The volume mesh refinement was not done by using a solution-based adaption feature like Adaptive Mesh Refinement (AMR) technique. However, this refinement can also be made by the use of AMR technique which is a more sophisticated approach to improve the accuracy of the wake predictions. AMR technique is available in the used solver and it provides grid refinement at regions where flow features have steep changes or large gradients. While refining the grid, FLUENT identifies these relevant regions through a predefined threshold value for the physical variable. FLUENT provides a wide variety of adaption functionalities. Some of them can be given as boundary adaption, gradient adaption, isovalue adaption, region adaption and yplus/ystar adaption.

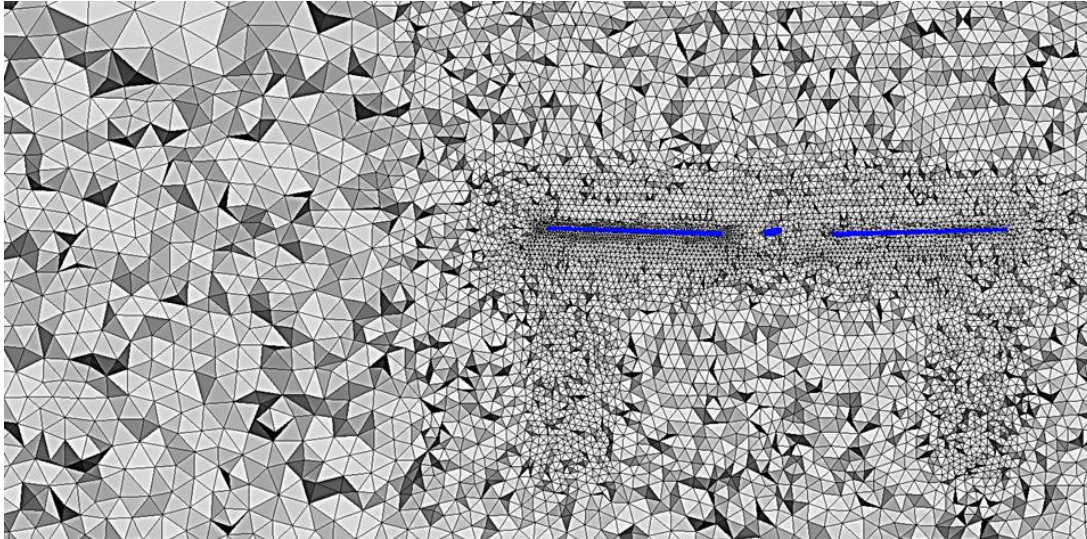


Figure 6.39 : View of the volume mesh for isolated rotor cases at $\mu = 0.012$.

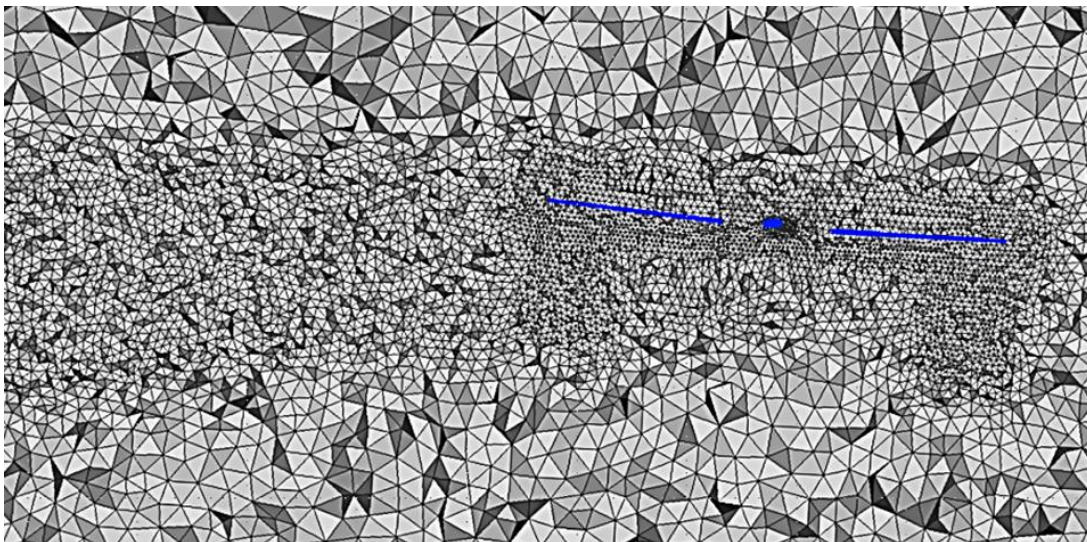


Figure 6.40 : View of the volume mesh for isolated rotor cases at $\mu = 0.151$.

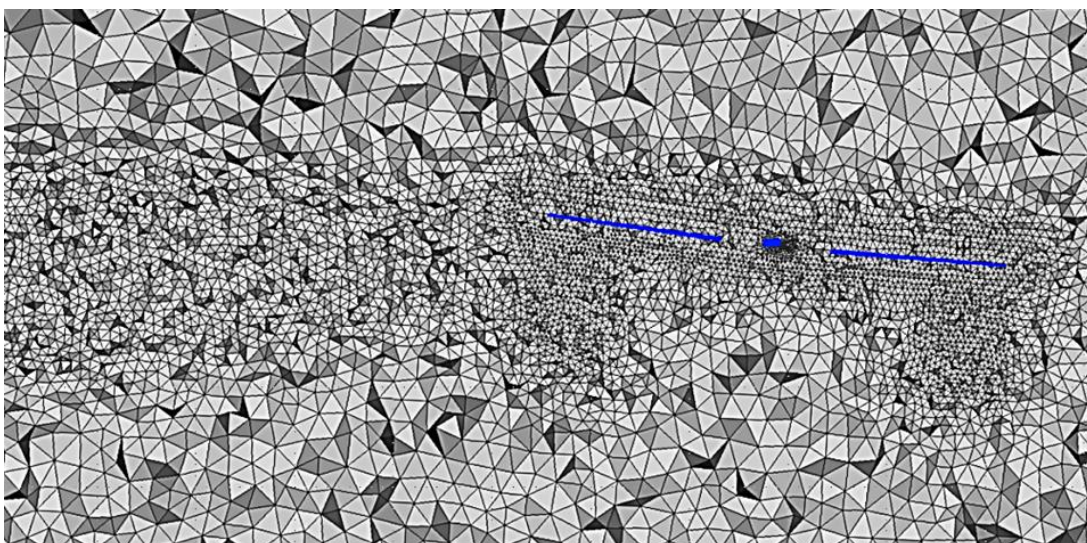


Figure 6.41 : View of the volume mesh for isolated rotor cases at $\mu = 0.231$.

The grid adaption criteria can be based either on the velocity or pressure gradient. Selecting the appropriate type of adaption for the specific application is the responsibility of the user. User should determine the most appropriate one considering the type of the flow to be simulated. For instance, wakes represent a total pressure deficit. Therefore, selecting the pressure gradient as a refinement criteria would be a better choice for the wake regions. On the other hand, jets are more characterized by their having relatively high velocity fields. In such kind of flows, the criteria can be based on the velocity gradients. However, user should be careful before performing an adaption. A reasonably well-converged solution should be obtained. By the use of AMR technique, a better capture for the roll-up of the tip vortices shall be provided. One could examine the impact of the technique on the computation time.

6.2.2.5 Numerical methods

The CFD analyses are carried out using a commercially available solver, ANSYS FLUENT v14.5. The solver used is based on the finite volume method for the RANS equations and several available turbulence models. The Realizable k- ϵ turbulence model developed by Shih et al. [171] is employed to model the turbulent nature of the flow. The standard wall function approach is applied for the near-wall region to estimate the boundary layer and turbulence quantities. Because the considered flow cases do not involve any discontinuities such as shock waves, the pressure-based segregated algorithm, which is a Semi-Implicit Method for Pressure-Linked Equations (SIMPLE) based on the predictor-corrector approach, is adopted for the pressure-velocity coupling, and a second-order scheme is employed for the pressure interpolation. Under-relaxation of equations are used in the pressure-based solver to control the update of computed variables at each iteration. Each equation have under-relaxation factors associated with them. These factors are used to stabilize numerical schemes by limiting the effect of the previous iteration over the present one. Under-relaxation values can be changed to obtain faster convergence or to prevent divergence. The change in relaxation values may cause a change in the number of iterations. However, the results are independent of relaxation values. The under-relaxation factors are kept as their default values with which no convergence problems are encountered. All flow variables are stored at the same nodes (cell-centered) and the gradients are computed by using a Least Squares Cell based formulation. The diffusive terms are discretized based on the second order accurate central differencing.

The convective terms of all transport equations are discretized using the second order upwind scheme. In FLUENT, the dynamic mesh simulations currently work only with first-order time advancement. Hence, temporal discretization depends on the first-order implicit formulation for the time accurate computations. The dynamic mesh algorithm together with the time advancement within the context of the segregated solver is presented as a flowchart in Figure 6.42.

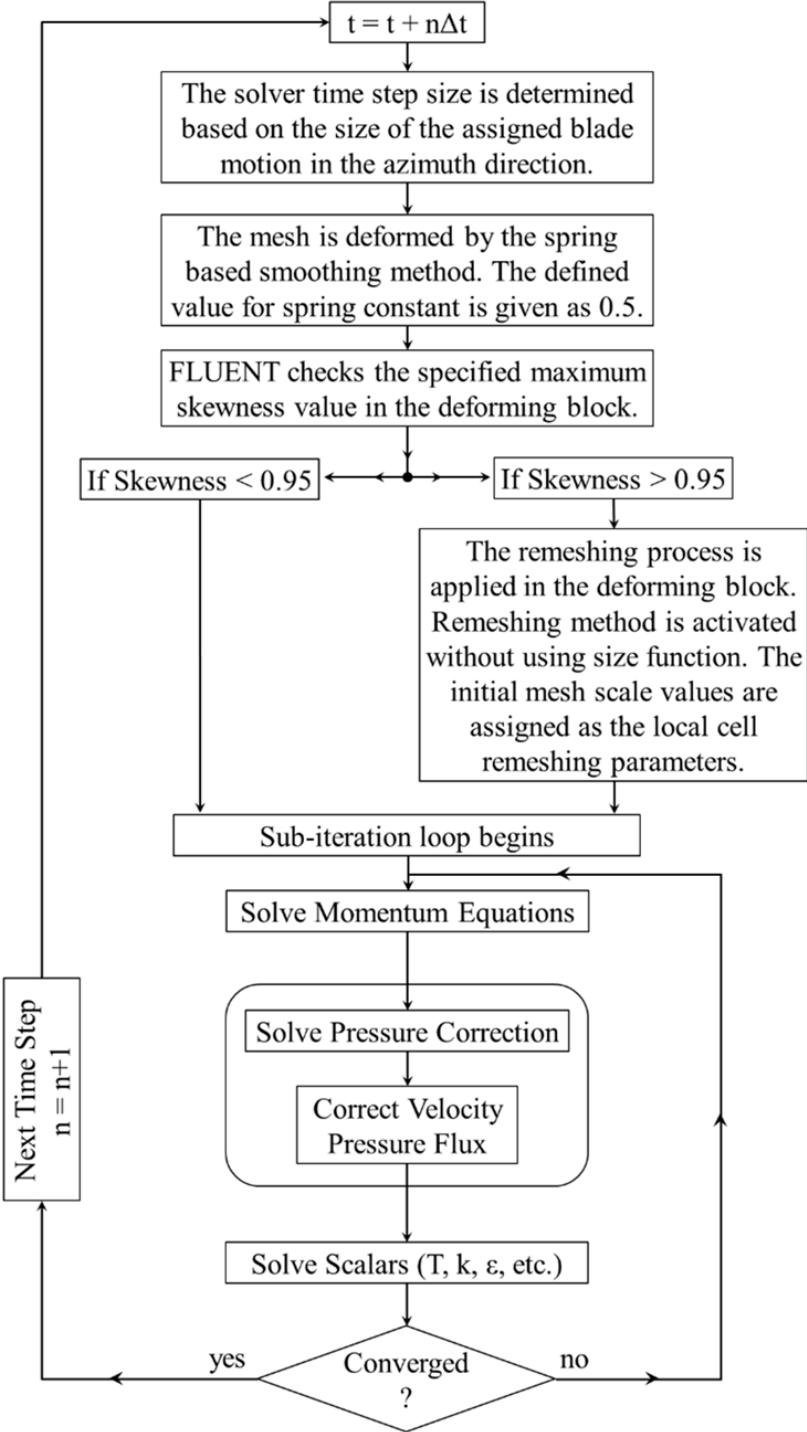


Figure 6.42 : Dynamic mesh and time advancement algorithms.

The free stream speed in the examined cases is quite low. However, the speed is quite high at the blade tips. Therefore, compressible flow analyses are carried out, as the blade tip regions involve local speeds corresponding to Mach numbers over $M=0.3$. The experimental data considered for comparisons is for a tip Mach number of 0.53 [104]. For such values above $M=0.3$, the compressibility effects are becoming more influential and must be considered for accurate solutions. The air is modeled as an ideal gas, and the viscosity change depends on the three coefficient method of Sutherland law [172].

The isolated fuselage analyses are based on steady RANS computations. The steady state solutions are obtained under 1000 iterations. On the other hand, URANS simulations are carried out for the cases including rotor blades. The spring based smoothing and re-meshing techniques are incorporated inside the deformable block to accommodate the prescribed blade motion. Determination of a proper time step size is of great importance for the accuracy of unsteady computations [38, 40]. Time-steps should be small enough to resolve time dependent features and turbulent quantities. Moreover, when using mesh smoothing methods, there is a significant relationship between the mesh element size and the time-step size in accommodating the prescribed blade motion successfully. The solver time step size is determined based on the size of the assigned blade motion in the azimuth direction, as FLUENT emphasizes that “the amount of displacement in one time step should not be more than half the cell size adjacent to the moving boundary”. This condition automatically brings a constraint on the selection of time-step size. Choosing a larger time step will lead to ineffective smoothing, resulting in frequent re-meshing. Moreover, a solution convergence may not be achieved at all, with much larger time steps. However, the time step size shall be taken as large as possible, to reduce the computation time. Thus, the best way to determine the optimum time-step size is to perform a sensitivity study, to make the results independent of the size of the blade azimuthal movement. In the literature [30, 37] numerical predictions using a specialized code, namely FUN3D, indicate that use of 1 degree blade movement in azimuth direction has resulted in reasonable phase and magnitude predictions for the same ROBIN test cases. Therefore, in the present study, the solution is advanced with a time step equivalent to 0.5 degree blade motion in the azimuth direction, to both satisfy FLUENT's minimum time step requirements while also preserving the efficiency of the computations. Indeed, a sensitivity study carried

out with a time step equivalent to 0.25 degree blade motion in the azimuth direction has given similar results to those of 0.5 degrees.

The time-dependent simulations start from an undisturbed free stream condition. The rotational frequency of the rotor is given as 2000rpm [104]. The Reynolds number based on blade chord length is approximately 0.845 million. Five main rotor revolutions have been performed using a constant azimuthal step size that corresponds to half degree of blade movement. At an advance ratio of 0.012 (very low), even after five rotor revolutions, the wake has not reached a steady state. For this test condition, eight full revolutions of the rotor are simulated to obtain a time periodic numerical solution by ensuring a sufficient rotor wake formation. For the advance ratios of 0.151 and 0.231, the calculated thrust values have reached a steady state after 1.5-2 rotor revolutions.

All calculations are carried out on a 12 core parallel machine with 2 x 2.60 GHz Intel Xeon E5-2630 processors. The platform uses a 64-bit Win-7 operating system and a total of 64 GB of RAM. The mesh partitioning is done using the “METIS” algorithm [173]. The elapsed wall-clock time for the steady analysis is approximately 1 hour and it is about 17 hours for a solution of one rotor revolution with 720 time-steps, in transient analysis. Allowing five fixed sub-iterations for each time step yielded a reduction of the residual of 2–3 orders of magnitude. The computational parameters are given in Table 6.12.

Table 6.12 : Computational parameters.

Parameter	Value
Azimuthal step, ψ^o	0.5
Time step size (s), Δt	4.167E-05
# of time-steps per revolution	720
# of sub-iterations at each time step	5
# of main rotor revolutions	5
# of processors	12
Type of processor	Xeon 5610
Steady Analyses;	
<i>CPU-time for 1000 iterations (h)</i>	<i>13.17</i>
<i>Wall-clock time (h)</i>	<i>1</i>
Unsteady Analyses;	
<i>CPU-time per revolution (h)</i>	<i>194.6</i>
<i>Wall-clock time (h)</i>	<i>17</i>

6.2.2.6 Results and discussion

Having validated the fuselage only configuration, the rotor only configuration in forward flight is considered. The blades encounter an asymmetric velocity field, and the unsteady effects become dominant under forward flight conditions. The relative motion between the blades and the outer stationary flow region is modeled using the dynamic mesh approach. The numerical solutions are obtained by the URANS analyses. The pitch motion of the blades varies according to the blade control variables given in Table 6.11, whereas the flap motion of the blades obeys the so-called Modane law ($\beta_{1s} = 0$, and $\beta_{1c} = -\theta_{1s}$), Figure 6.43 to Figure 6.45. The deviation in pitch and flap angles becomes larger as the advance ratio increases.

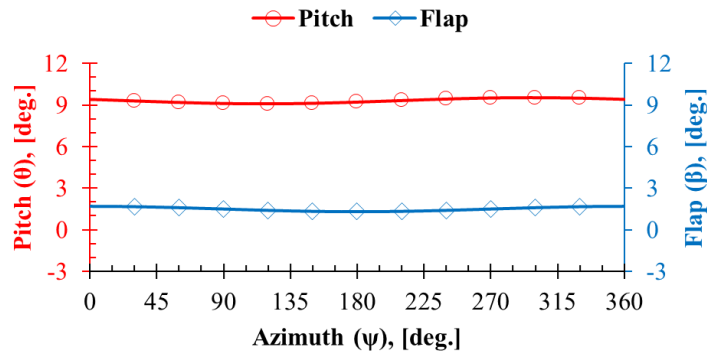


Figure 6.43 : Change in pitch and flap angles with azimuth for $\mu = 0.012$.

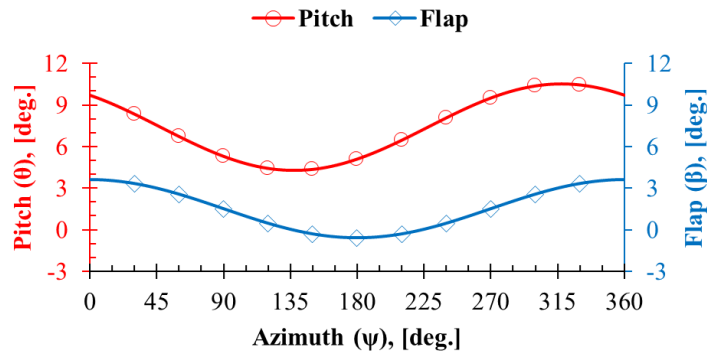


Figure 6.44 : Change in pitch and flap angles with azimuth for $\mu = 0.151$.

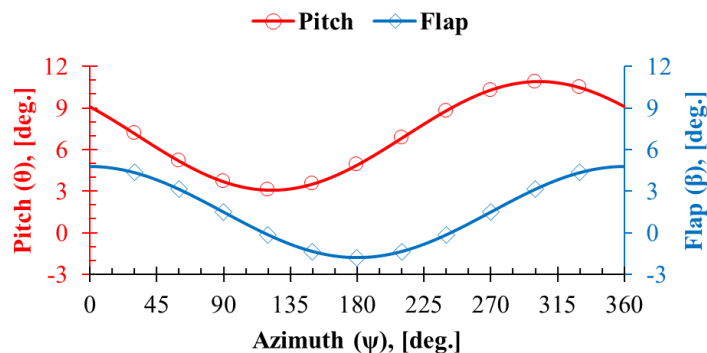


Figure 6.45 : Change in pitch and flap angles with azimuth for $\mu = 0.231$.

The maximum changes in blade pitch and flap angles become larger as the advance ratio increases. A comparison of the blade positions at different advance ratios is presented in Figure 6.46, where also shown are the direction of flight and the initial positions of the blades according to their azimuthal locations. The initial position of blade-1 is located at $\psi = 0^\circ$ and pointing downstream direction. In the figure, the blades with dotted pattern show the un-deformed case. The ones with striped pattern represent the deformed shapes because of the change in the advance ratio. Figure 6.46(a) shows that the amount of blade deformation is very small for a very small advance ratio of 0.012, which is a near hovering condition. The small flap and pitch changes in the blade motion during an entire revolution, while operating at relatively low freestream speeds, yields nearly a symmetrical flow field with respect to longitudinal axis, resembling very much the hover condition. As depicted in Figure 6.46(b) and Figure 6.46(c), the blade movement becomes more evident by the increased advance ratio. Figure 6.47 demonstrates altogether the comparison of the blade movements for all three test cases.

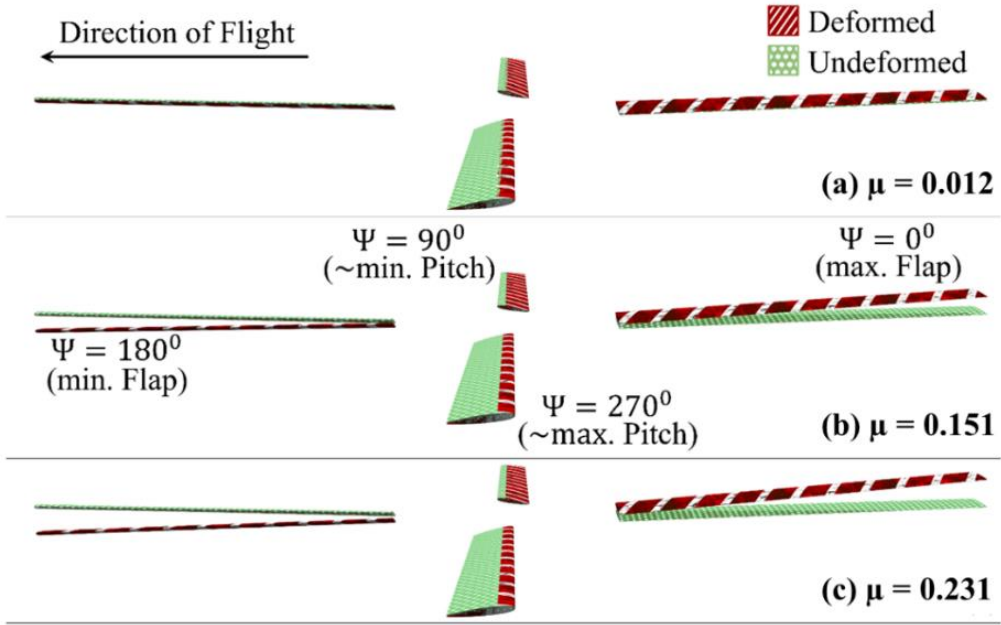


Figure 6.46 : Positions of deformed and undeformed blades.

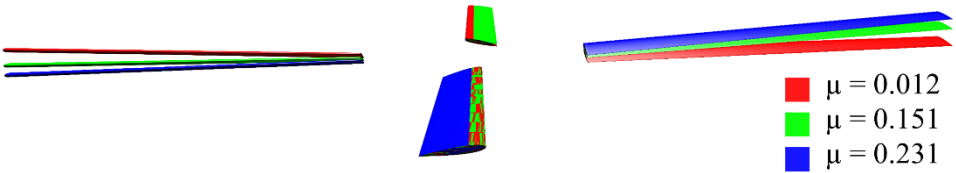


Figure 6.47 : Comparison of the blade positions at different advance ratios.

In Figure 6.48, the instantaneous time histories of blade thrust coefficients for the examined three advanced ratios are plotted for individual rotor blades. As the advance ratio is increased from 0.012 to 0.231, the amplitude of thrust variation is also increased, whereas the change in the average thrust coefficient is not significant. The increase in the amplitude is analogous to the increased blade deformation.

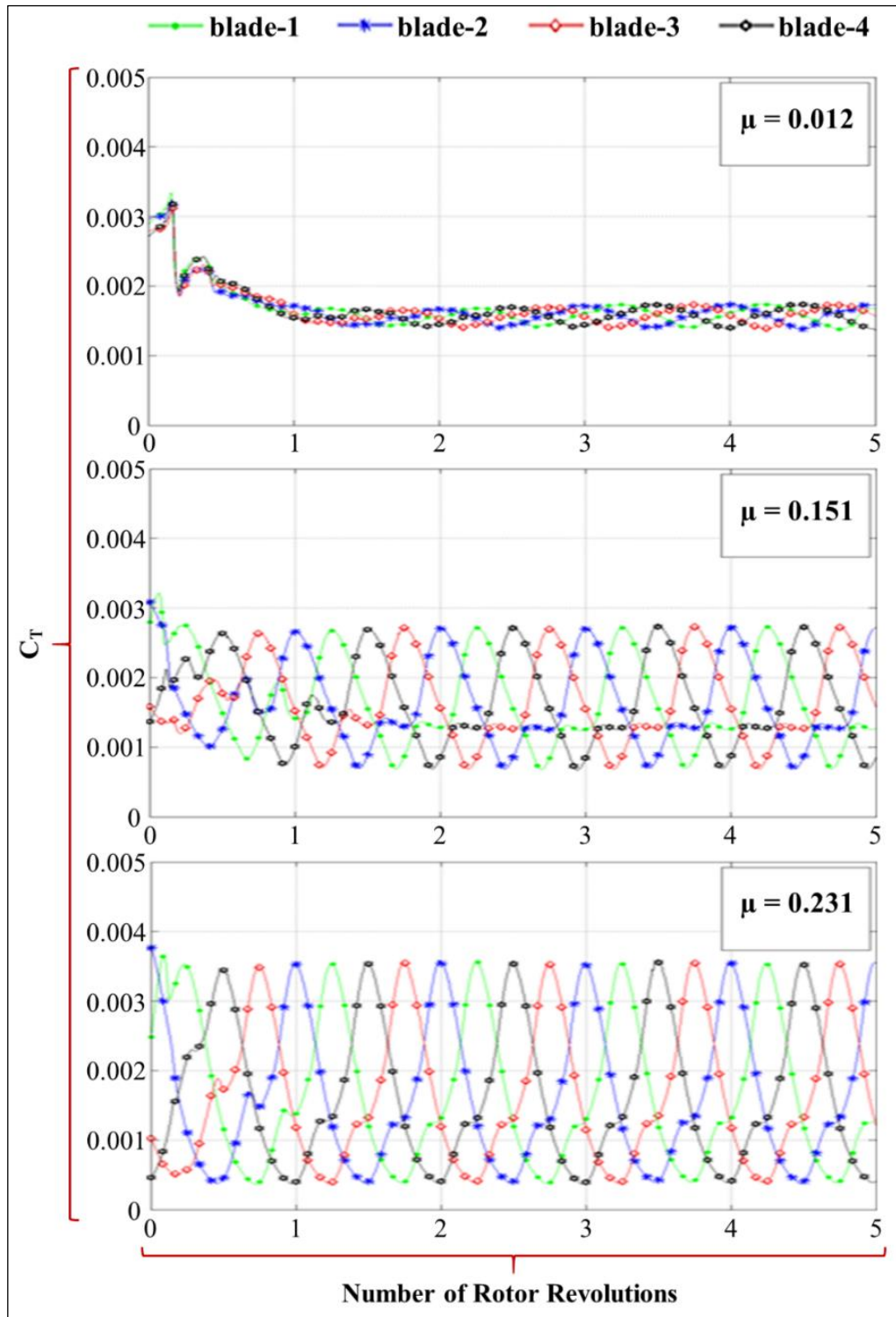


Figure 6.48 : Instantaneous thrust coefficients for individual rotor blades.

The instantaneous time-histories of blade thrust coefficients for five rotor revolutions are presented in Figure 6.48. After initial two rotor revolutions, the four blades follow the same periodic time pattern. Blade-1, which is initially located at $\psi = 0^\circ$, produces the largest thrust coefficient after covering a distance of approximately 90° in azimuthal direction. The blade is now on the advancing side and experiences the largest relative velocity. Thus, the blade is under the largest aerodynamic load (advancing side). The lowest value occurs at the blade rotational angle of $\psi = 270^\circ$ where the blade experiences the smallest relative velocity (retreating side). The thrust coefficients calculated for the three advanced ratios for the isolated rotor case are listed in Table 6.13.

Table 6.13 : Predicted thrust coefficients for the isolated rotor configuration.

μ	M_∞	α_s	C_T, exp	C_T, CFD
0.012	0.0064	0	0.00627	0.00639
0.151	0.080	-3	0.00644	0.00643
0.231	0.122	-3	0.00645	0.00646

The cross sectional blade pressure coefficient distributions, at a radial position of 75% rotor radius, are compared for the three advance ratios considered, Figure 6.49. Figure 6.49(a) indicates that the blades produce almost same sectional thrust distribution, independent of the azimuth value, at the very low advance ratio of 0.012. A negligible pressure difference observed between the azimuth locations of $\psi = 90^\circ$, and $\psi = 270^\circ$, once more shows the presence of symmetrical flow feature with respect to longitudinal axis.

As can be seen by the comparison of Figure 6.49(b) and Figure 6.49(c), for the advance ratio of 0.231, the pressure values along the 4% portion of the upper-front surface of the blade located at $\psi = 90^\circ$ are predicted lower than those found for $\mu=0.151$ case. In other words, the velocities at that part of the section are calculated higher by the increase in advance ratio. Moreover, the stagnation pressure became larger on the lower surface and therefore, at that section of the blade a greater pressure difference is predicted between upper and lower surfaces. Further investigating of Figure 6.49(b) and Figure 6.49(c) indicates that the lowest pressure difference between upper and lower surfaces is found at $\psi = 270^\circ$ for $\mu=0.231$. The obtained results emphasize a rise in the level of asymmetry with respect to longitudinal axis by the increased advance ratio. Briefly, as the advance ratio is increased, the advancing side pressure

difference is increased, whereas retreating side one is decreased further, for the advance ratios of 0.151 and 0.231, respectively. Consequently, the greater sectional thrust is obtained for $\mu=0.231$ case at $\psi = 90^\circ$. These interpretations can also be gathered from the overall individual blade thrust coefficients that were given in Figure 6.48.

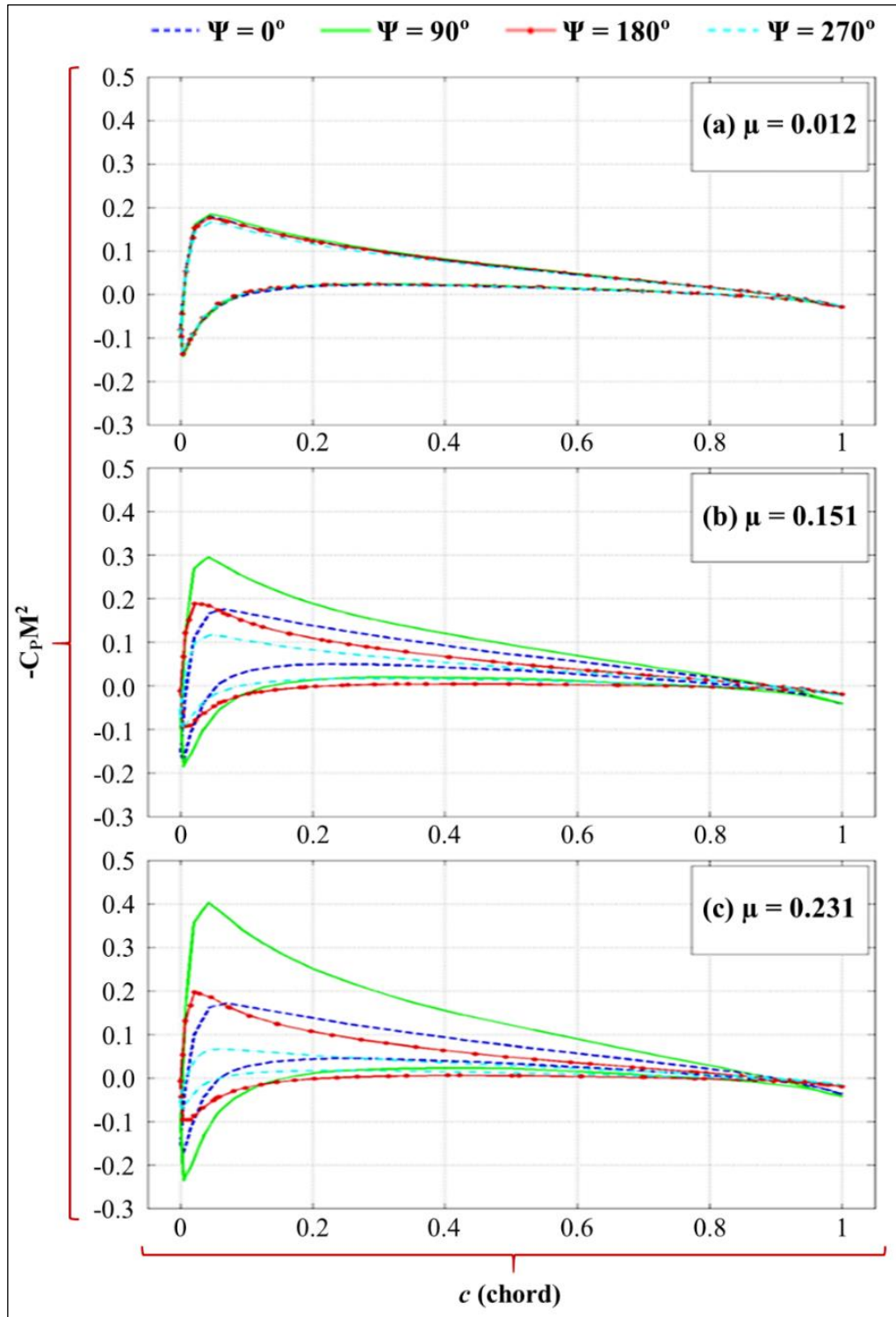


Figure 6.49 : Comparison of $-C_p M_{r=0.75R}^2$.

6.3 Rotor and Fuselage Analyses

In this section, the interference effects between rotor and fuselage are analyzed. Computations are carried out for the previously defined three advance ratios. For the validation of rotor and fuselage configuration, the experimental results from [104] and numerical results from [31] are used. The predefined measurement points indicated in Figure 6.50 are chosen to compare the unsteady and averaged pressure coefficients. The results, in terms of pressure coefficient (C_p) distributions, are also compared with the isolated rotor case to investigate the effect of the fuselage on the rotor flow field and vice versa. Moreover, the effect of rotor wake on the fuselage is studied by analyzing of recorded transient pressure data at measurement points.

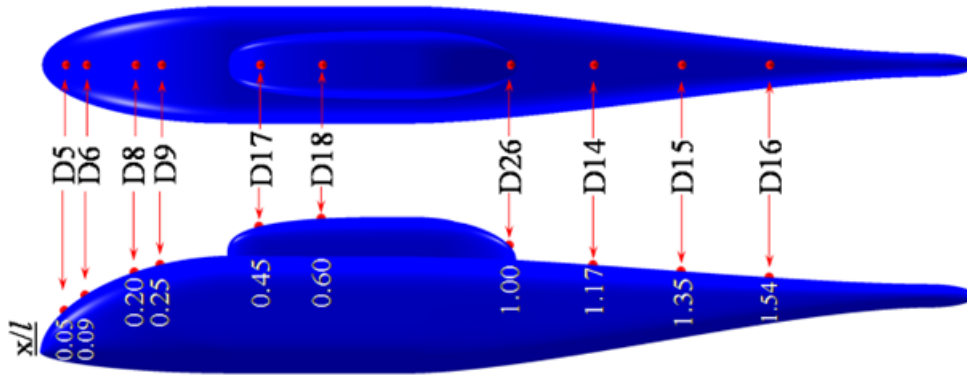


Figure 6.50 : Locations of the static pressure orifices.

6.3.1 Computational mesh details

The computational grids for the rotor and fuselage configurations have almost the same properties with the isolated rotor conditions where described in detail at previous subsection 6.2.2.4. The only difference is the existence of the fuselage in the flow domain, inside block 6.

The grid independence studies for the ROBIN fuselage carried out by [165] and [16] indicate similar results. Heise et al. (2007) state that the grid independence was obtained after reducing the surface element length to 0.75% of the fuselage length [16]. These studies have been considered as a reference to determine suitable grid sizes. In the present study, the maximum surface element length is kept below 0.5% of the fuselage length. Smaller element sizes are used on the surface of the vehicle at stagnation and possible flow separation regions and where a proper representation of geometry is needed, such as curved ones. The rest of the domain is represented by tetrahedral volume elements. Because the poor quality elements have unfavorable

effect on the results, a particular attention has been given to the unstructured mesh generation process. The skewness of a mesh element is an indicator of mesh quality. Highly skewed cells can decrease accuracy and stability of the solution. A skewness value of zero holds for the ideal mesh element and a skewness of one shows highly skewed element, which may lead to convergence difficulties. The maximum equiangle skewness of the triangular surface element is allowed to be 0.1 and the maximum skewness of the tetrahedral volume element is kept below 0.6 inside the computational domain. The generated boundary layer mesh for the fuselage is shown in Figure 6.51.

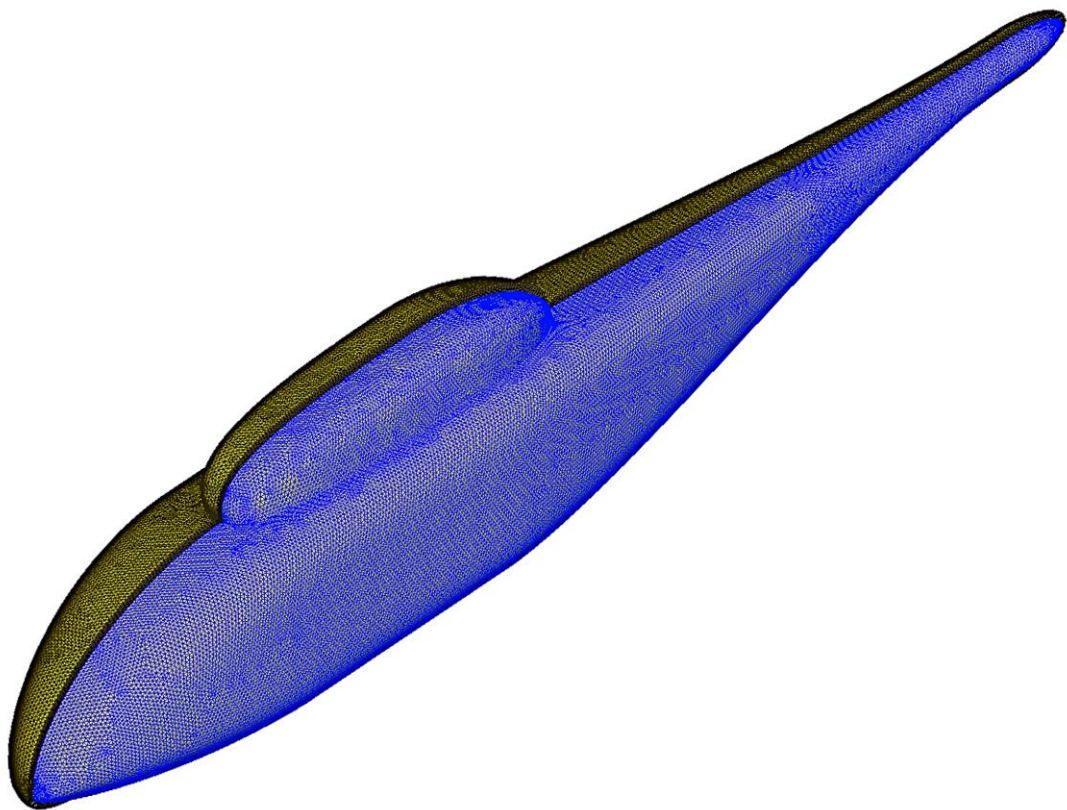


Figure 6.51 : Boundary layer mesh around fuselage.

The generated volume meshes for the three different flight conditions, namely; $\mu=0.012$, $\mu=0.151$ and $\mu=0.231$, are presented in Figure 6.52 (a, b and c), respectively. In the preprocess stage, the mesh refinement was done in the possible wake regions at a moderate level by considering the computational effort. The refinement was not performed with a solution-based mesh adaptation feature. The possible wake regions, where a finer grid is generated a priori, were determined by the help of prior numerical predictions, which ensure already visualized wake patterns for the test cases examined in this study.

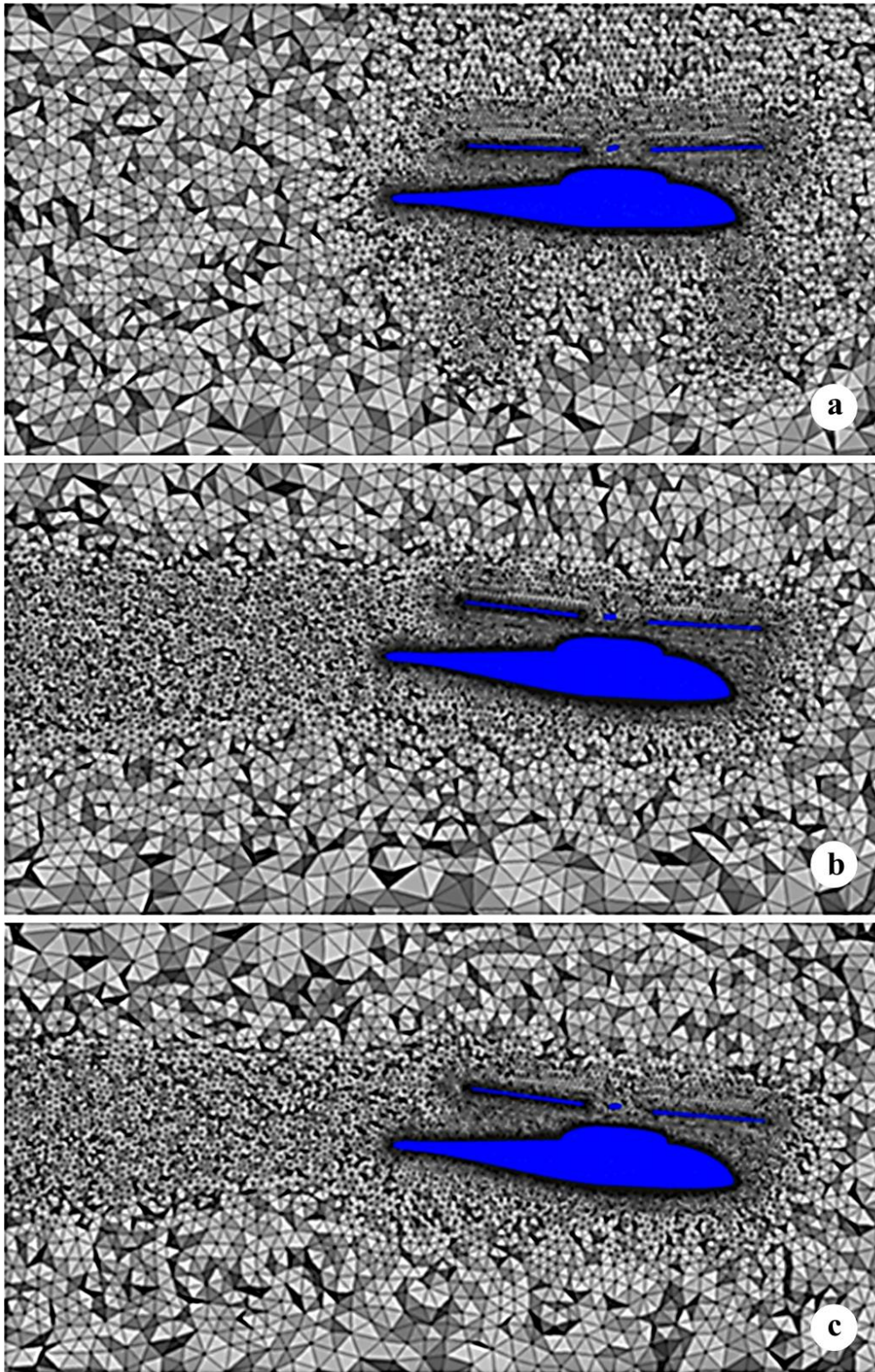


Figure 6.52 : Volume mesh views: (a) $\mu=0.012$, (b) $\mu=0.151$, (c) $\mu=0.231$.

6.3.2 Numerical methods

The used numerical algorithms are identical with isolated rotor configurations. All the simulation details are the same as described previously in Section 6.2.2.5.

6.3.3 Results and discussion

For the cases considered, the effect of the fuselage on rotor blades' pressure distributions at a section of 75% blade radius is found to be negligible. However, a comparison is made to deduce the behavior. The effect will be more significant at radial cross-sections closer to the hub (radial position below 60% radius) where the distance between rotor and fuselage becomes closer. The rotor blades are mostly effected by the presence of the fuselage, especially at azimuthal positions of $\psi = 0^\circ$, and $\psi = 180^\circ$. Figure 6.53 indicates that the rotor blades at $\psi = 0^\circ$, and $\psi = 180^\circ$ are under an up-wash effect due to presence of fuselage that results in greater sectional thrust prediction. According to Figure 6.54 and Figure 6.55, a negligible downwash induced by the fuselage is observed for $\mu = 0.151$ and $\mu = 0.231$ at azimuthal position of $\psi = 0^\circ$. On the other hand, a favorable effect on rotor blades has been captured at $\psi = 180^\circ$ for these two cases. For $\mu = 0.231$ case, increase in the blade loading has become even more distinct because the blade passes closer to the body. Similar results have been obtained by [29, 35] for different rotor and fuselage configurations available in the EU project GOAHEAD.

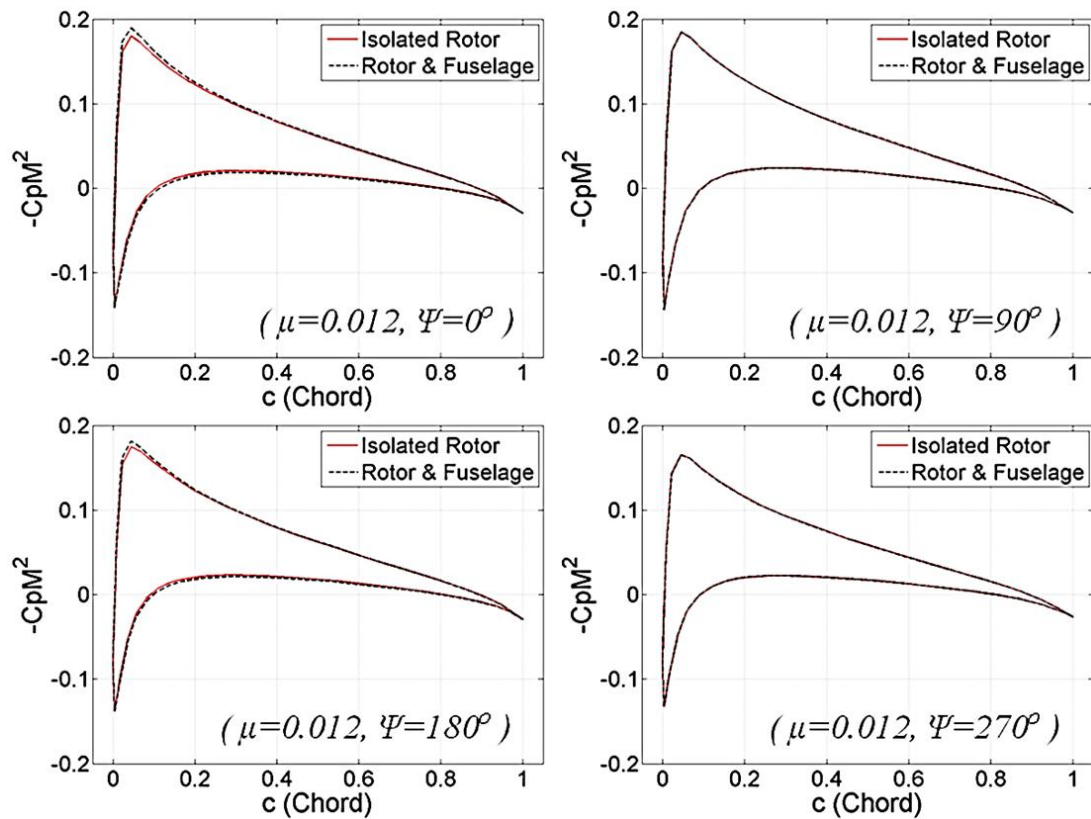


Figure 6.53 : Comparison of $-C_p M_{r=0.75R}^2$ at $\mu=0.012$.

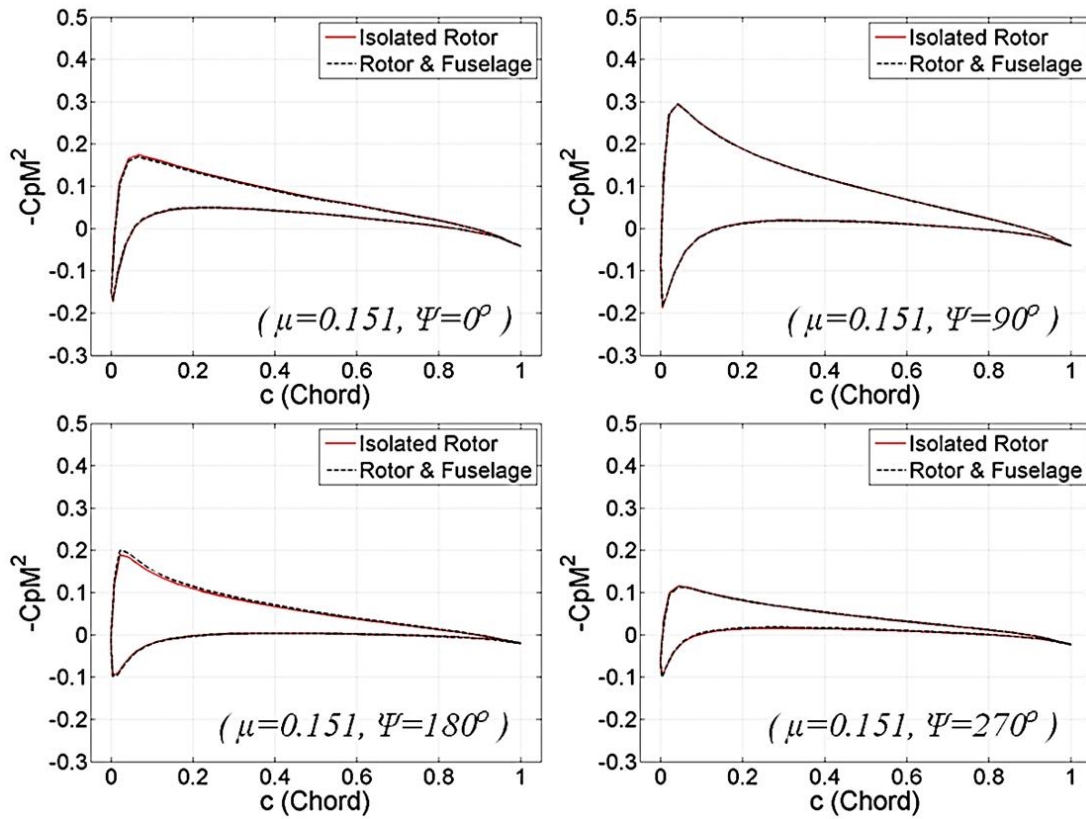


Figure 6.54 : Comparison of $-C_p M^2_{\Gamma=0.75R}$ at $\mu=0.151$.

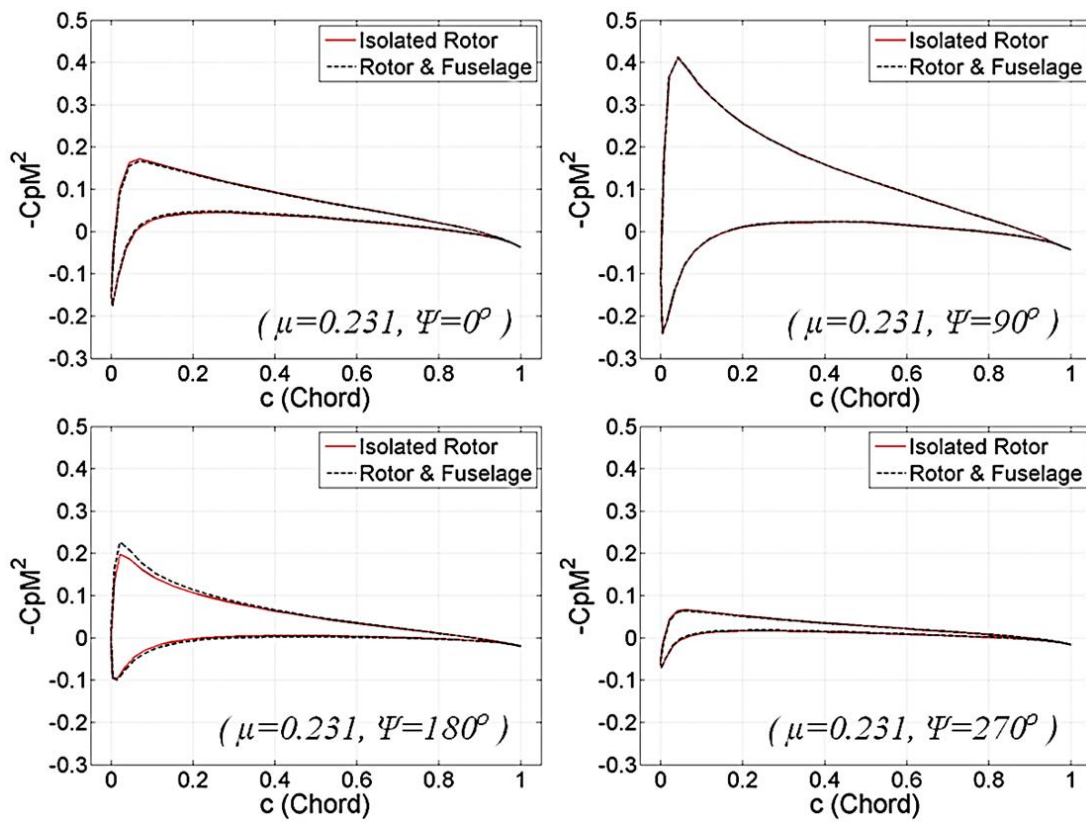


Figure 6.55 : Comparison of $-C_p M^2_{\Gamma=0.75R}$ at $\mu=0.231$.

The purpose was to develop a methodology by which rotorcraft intake aerodynamics, the wake region and the effect of the rotor wake on the body can be evaluated. The wake angle and downwash have to be predicted correctly for the accurate pressure distribution around the fuselage. In a numerical study, it is indicated that the pressure distribution of the fuselage significantly affected by the load distribution of the rotor disk, [174].

The pressure fluctuations for one entire rotor revolution are plotted between Figure C.1 and Figure C.3 for each of the designated fuselage points (Figure 6.50) for the three advance ratios, respectively, to analyze the effect of the rotor blades on the body, in comparison with data [104] and other computations [31]. To facilitate the comparison of the unsteady data, the experimental data were shifted by a phase of 28 degrees to account for the experimental phase lag, [23, 31, 104]. A periodic change was observed in the time-dependent pressure data by the rotational motion of the rotor (4 peaks, 1 per blade, during one revolution). The dynamic behavior of the blades under different operating conditions determines the amplitude of the pressure distribution obtained on the body. The results of the present study are compared with the results of experimental and numerical studies found in the literature. The current predictions, in line with other numerical predictions, follow the variations present in the experimental data [104]. Acceptable agreement with the experimental data is obtained, though noticeable differences are detected, especially on the aft part of the fuselage, at higher advance ratios. However, the obtained results are in a close agreement with the numerical study presented by [31]. The rotor flow solver, rFlow3D, used by the authors is based on the overlapped grid approach and depends on the solution of Euler equations with the modified Simple Low-dissipative Advection Upstream Splitting Method (SLAU) scheme. This locally preconditioned numerical scheme enables the solver to calculate realistic drag coefficient values, both at low speeds and at transonic speeds. The authors assert that the code ensures reliable results.

Moreover, the present results are also compared with previously published RANS based computations of [30], Figure 6.56. This figure shows the variation of modified pressure coefficient with azimuth location for $\mu=0.151$ and $C_T=0.0064$ at selected locations on the top centerline of the fuselage. Both the phase and magnitude predictions are in good agreement. At sections $x/R=0.2$ and $x/R=1.18$, the magnitude predictions agree well with the Vorticity Transport Method (VTM) results,

demonstrating that the vortex structures are well captured. At section $x/R=1.56$, both the compression and suction peaks are under-predicted as a result of the coarse grid and numerical dissipation. Nevertheless, given the significant reduction in computational costs, the results are very promising and suggest future potential of the proposed methodology in using adaptive grid refinement.

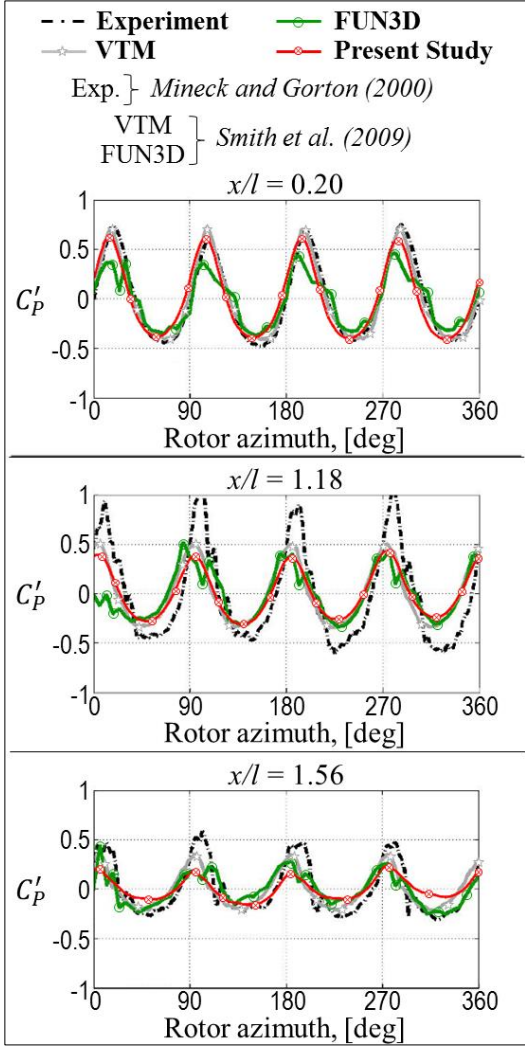


Figure 6.56 : Comparison of C_p fluctuations with other RANS results, [30].

The comparisons of surface pressure fluctuations are made after reaching a periodic time solution (after five rotor revs). Generally, the magnitude of the amplitudes were over-predicted in some of the locations on the front part and under-predicted at the aft of the fuselage. The rotor wake at the lowest advance ratio ($\mu=0.012$) moves downward and collides with most part of the fuselage, whereas at higher advance ratios, the wake impinges only the rear part of the tail (Figure 6.59 a to c). According to Figure C.1, at D8 ($x/L=0.201$) and D9 ($x/L=0.256$), the suction peaks agree well with experiment, whereas the predicted compression peaks are higher. The largest deviation with data

is observed at D26 measurement point located on the rear surface of the pylon. At D26 ($x/L=1.00$), the pressure peaks have a phase shift of approximately 25 degrees from the experiment for all three test cases. However, all numerical predictions are consistent with each other [31]. Same behavior is also presented in [30]. As can be seen in Figure C.2 and Figure C.3, the pressure fluctuations are generally in agreement with the experiment for the front half of the body, both in terms of phase and amplitude. For the aft of the body especially, at D14 ($x/L=1.18$) and D15 ($x/L=1.368$) where the rotor wake affects it, the agreement worsens in terms of the magnitude of the amplitudes. Additional comparisons for the averaged C_p values at each pressure orifice are made with both the experimental and numerical results. Figure 6.57 shows that a fair agreement has been captured except at $x/L=1.00$. The cause of this difference is considered as the existence of complex flow field on the aft of the fuselage caused by flow separation and blade root vortices. According to the figure, the C_p values begin to decrease as the advance ratio increases. This indicates that the effect of the rotor on the fuselage is being reduced gradually, as the advance ratio increases.

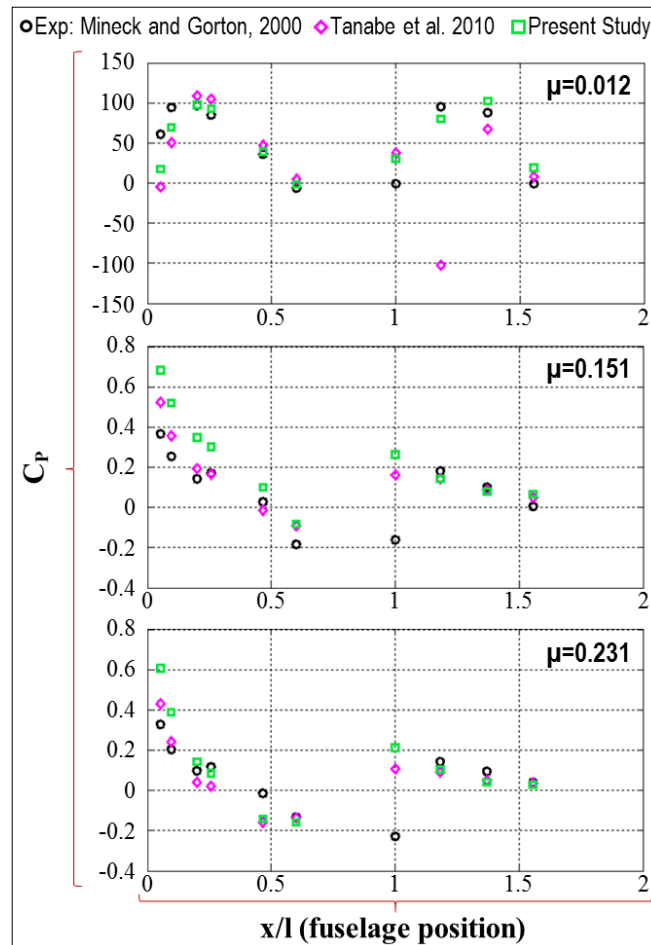


Figure 6.57 : Comparison of averaged periodical C_p values.

There are many vortex identification techniques based on local analysis of the velocity gradient tensor. For instance, the Q-criterion and λ_2 criterion are used widely to demonstrate the vortex structures. The Q-criterion determines vortices in the flow regions by calculating the positive second invariant of velocity gradient tensor, which indicates that the vorticity magnitude is greater than the magnitude of rate of strain. The secondary condition for the Q-criterion is that the pressure in the eddy region should be less than the ambient pressure. Jeong and Hussain (1995) asserted that $Q > 0$ does not guarantee the existence of a pressure minimum inside the region identified by it [175]. The λ_2 criterion is formulated as a result of the requirements when a local pressure minimum in a plane fails to identify vortices under strong unsteady and viscous effects. By definition, the $\lambda_2 < 0$ condition holds for every point inside the vortex core. The main difference between Q and λ_2 criteria is that the λ_2 criterion looks for the excess rotation rate relative to the strain rate magnitude only on a specific plane, whereas the Q criterion looks for this excess in all directions [175, 176]. Q-criteria do not distinguish the difference between rotation and vorticity for rotating bodies. Both the Q and λ_2 criteria hold for incompressible flows only. For example, the pressure Hessian concept defined for the λ_2 criterion is not applicable for the case of compressible flows because of the additional terms such as non-vanishing density gradient and divergence of velocity [177]. Compressibility effect in vortex identification is examined in [178]. According to this study, only the Δ -criterion and the λ_{ci} criterion are directly extendable to compressible flows.

The wake structures are visualized by iso-surfaces of λ_2 criterion and vorticity magnitude to depict the rotor-fuselage interactional features in the flow field for different forward flight conditions. These figures demonstrate a very good, qualitative agreement when compared with the other numerical results found in literature [28, 31], particularly for the predictions of shape and size of the tip vortex and their evolution to form coherent vortex structures. The strength and position of the vortex wake structure are of crucial importance for the rotor performance evaluation. More accurate and reliable predictions may be obtained by using higher order numerical schemes both in spatial and temporal coordinates. Figure 6.58 shows the computed vorticity distributions for the analyzed test cases, when viewed from the front of the complete helicopter model. In forward flight, the incident velocities at the retreating blade side are relatively low when compared to advancing side of the disk. Therefore, the rotor

loading becomes asymmetrical, resulting in different induced effects on each side of the model at forward flight conditions. According to the figure, as the advance ratio increases, the rise in the level of asymmetry becomes more distinct between advancing and retreating blade sides.

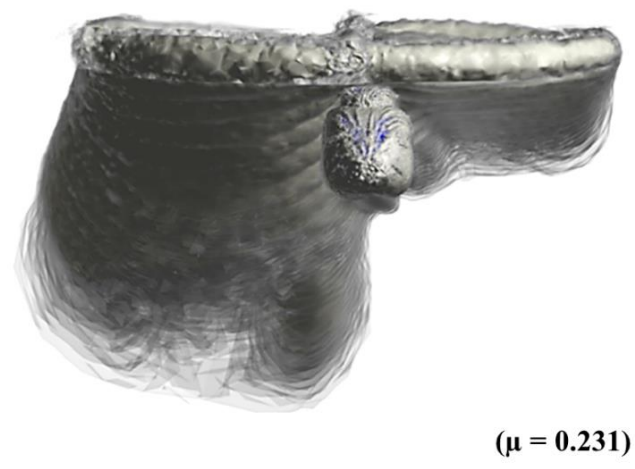
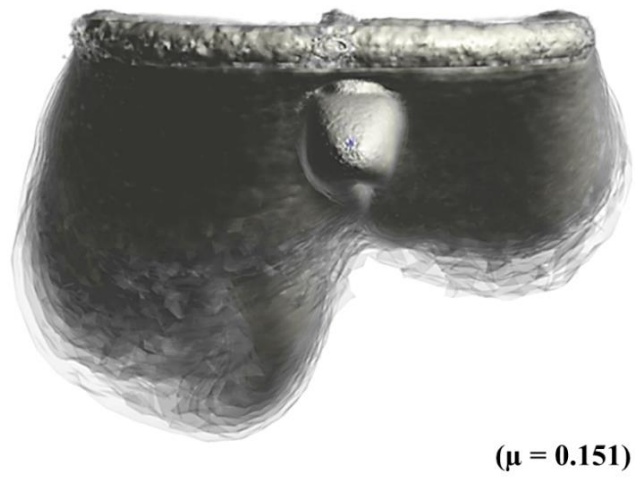
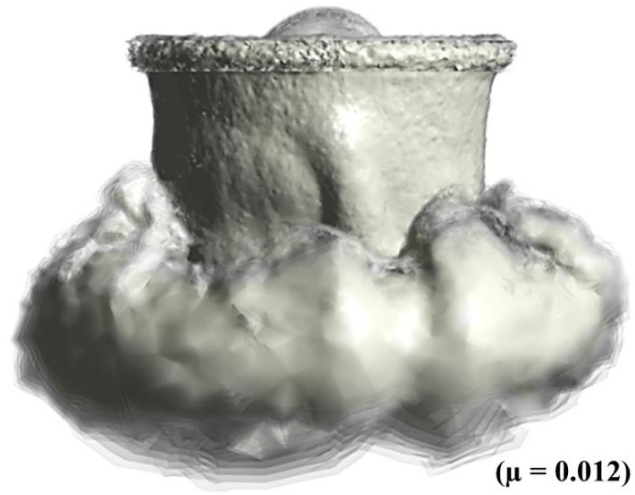


Figure 6.58 : Iso-surface plots of vorticity ranges between 10-50 (1/s).

Figure 6.59 depicts the rotor wake by the iso-surface plots of λ_2 criterion. Figure 6.59(a), which represents the advance ratio of 0.012, shows the wake deflected back very slightly, whereas the significant part of it moves in the downward direction. Thus, the fuselage is influenced mostly by the rotor wake at the lowest advance ratio.

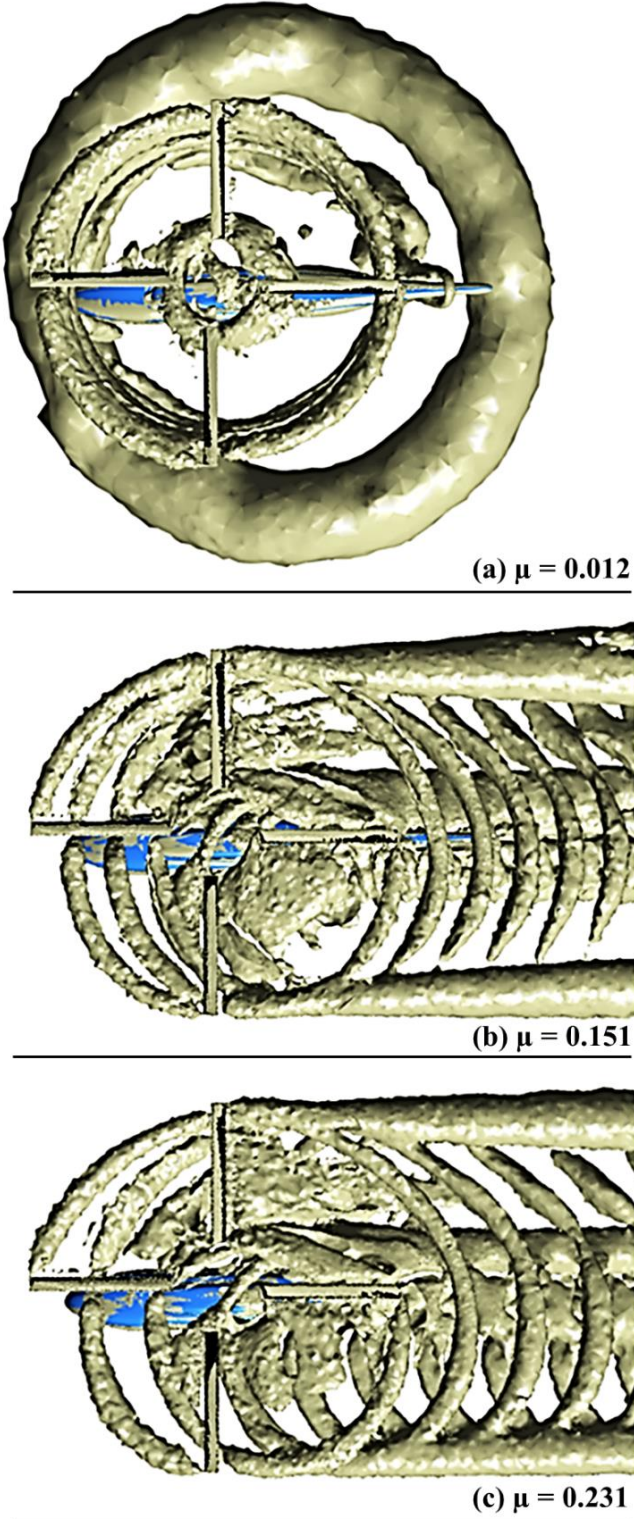


Figure 6.59 : Iso-surface plots of λ_2 -criterion.

At the higher advance ratios ($\mu=0.151$ and $\mu=0.231$), the calculations indicate that the wake is blown back by the free-stream and impinged on the tail of the fuselage. Furthermore, as shown by the comparison of Figure 6.59(b) and Figure 6.59(c), the distance between adjacent tip vortices becomes larger. The wake angle bends further toward the downstream. Therefore, the rotor-induced effect predicted is relatively small at higher advance ratios.

The average thrust coefficients (C_T) of the rotor and the vertical loads on the fuselage for the three cases are given in Table 6.14. The fuselage loads are calculated by the same formulation given for thrust coefficient. For $\mu=0.012$, the average C_T of the rotor itself is 6.49×10^{-3} , the download of the fuselage is -0.249×10^{-3} , and the total lift coefficient is 6.25×10^{-3} . The C_T is calculated as 6.39×10^{-3} from the isolated rotor configuration for the same test case (Table 6.13). The obtained thrust for the isolated rotor is lower than the rotor thrust with a fuselage by 1.67% but larger than the total lift value by 2.24%. The same comparison have been made by [31], who stated that the isolated rotor thrust is lower than the rotor thrust with a fuselage by 0.7%, but larger than the total lift value by 2%. As given in Table 6.14, the rotor effect on the fuselage becomes negligible at higher advance ratios.

Table 6.14 : Predicted thrust coefficients for the rotor-fuselage configuration.

μ	M_∞	α_s	$C_{T,rotor}$	$C_{L,fuselage}$	Total
0.012	0.0064	0	0.00649	-0.000249	0.00625
0.151	0.080	-3	0.00645	-0.0000409	0.00641
0.231	0.122	-3	0.00647	-0.0000404	0.00643

Surface flow visualization studies are performed to expose the effect of the rotor wake on the fuselage. The streaklines obtained from the isolated fuselage analyses are compared with the streaklines formed on the surface of the body under the rotor effect. At the lowest advance ratio (Figure 6.60), the streaklines are generally directed downward with nearly symmetrical distribution on the two sides of the model. At the two higher advance ratios (Figure 6.61 and Figure 6.62), the streaklines are generally directed downstream; however, some dissymmetry has been observed between starboard and port sides of the fuselage. The streaklines on the starboard side are directed more downward compared with the port side, as that part of the fuselage is under the effect of advancing blade. The streaklines on the port side point downstream because of the weaker induced effects of retreating blade.

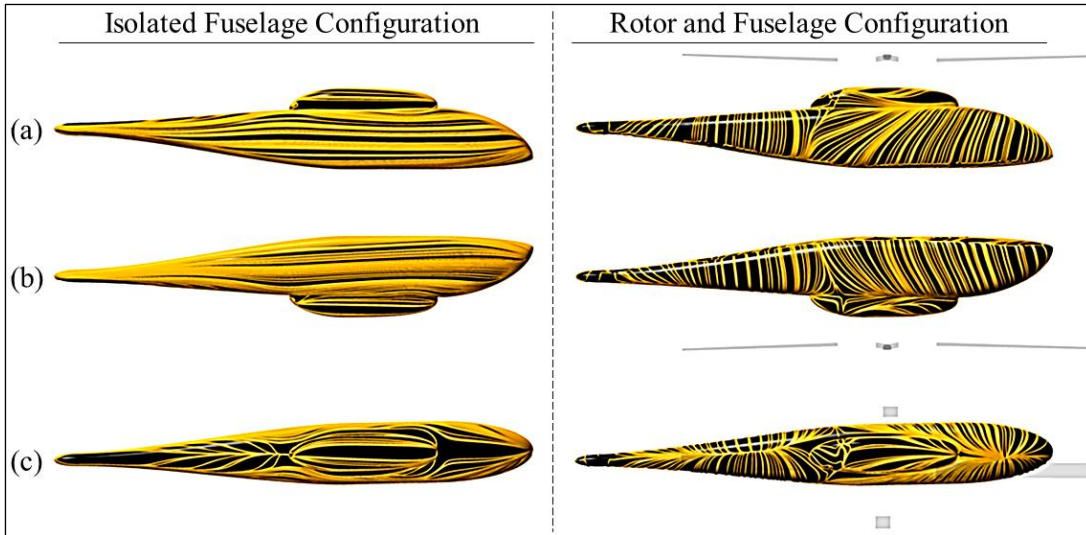


Figure 6.60 : Surface streaklines, $\mu=0.012$: (a) starboard, (b) port, (c) top views

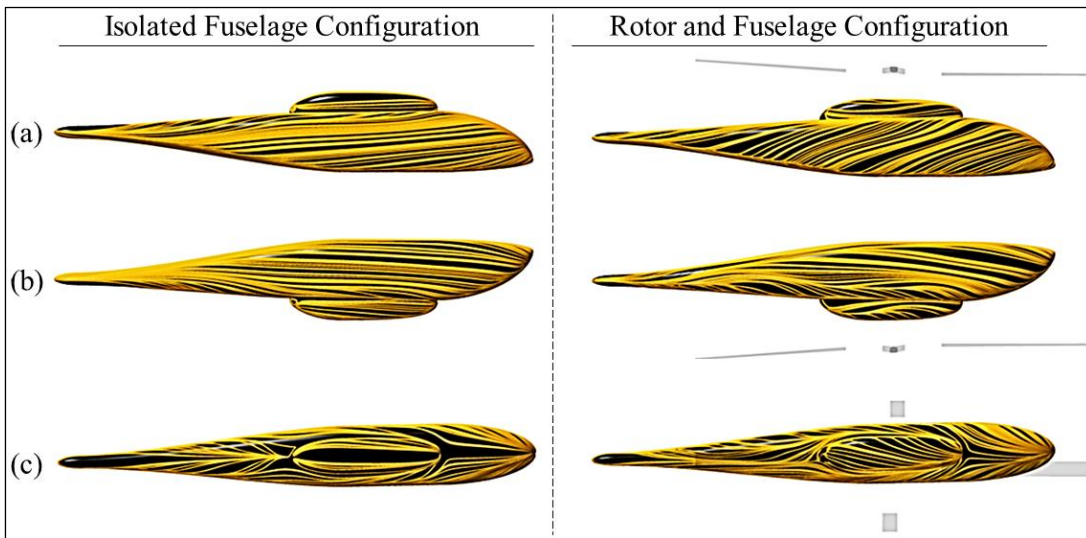


Figure 6.61 : Surface streaklines, $\mu=0.151$: (a) starboard, (b) port, (c) top views

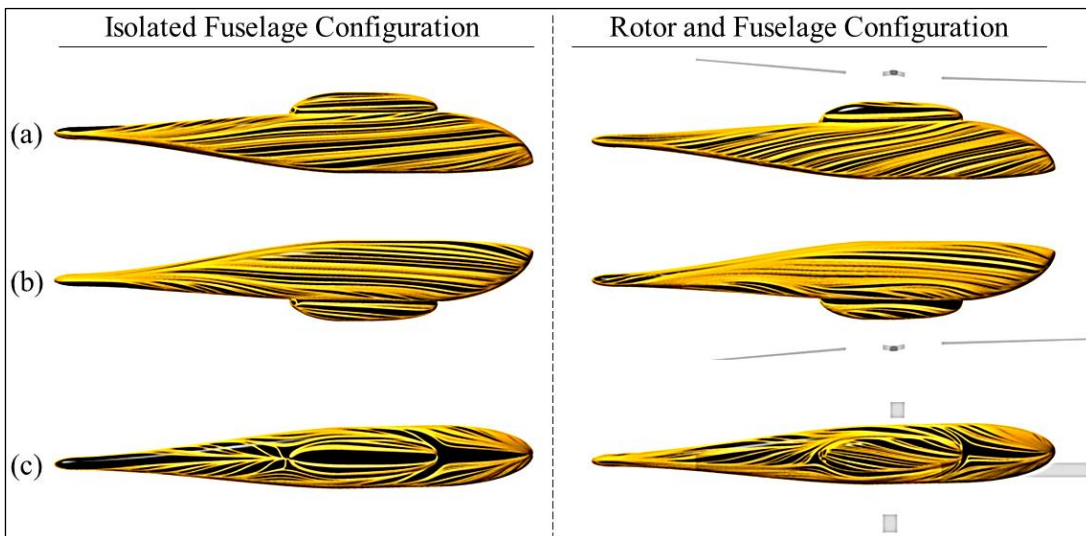


Figure 6.62 : Surface streaklines, $\mu=0.231$: (a) starboard, (b) port, (c) top views

7. CONCLUSION AND RECOMMENDATIONS

In the present work, numerical simulations of unsteady flow around helicopters are carried out to examine the aerodynamic interaction between the main rotor and the fuselage. A non-overset dynamic mesh approach is presented to analyze complex flows such as the rotor-fuselage interaction using the ROBIN configuration with the four-bladed IRTS rotor. In literature, majority of the complex interactional rotor aerodynamics analysis is accomplished by specialized institutional codes such as those of NASA, JAXA or EU. In this study, the unstructured Reynolds-averaged Navier-Stokes (RANS) solver of commercial CFD code FLUENT is used for the analyses. The reason for the selection of this code is that it is accessible by anyone, whereas the specialized institutional codes are for internal use and can only be used within the institution due to licensing legislations. Furthermore, most of the published works in open literature consider Euler or wake prediction techniques. This study considers the effects of viscosity by utilizing RANS based unsteady viscous compressible flow analysis. Moreover, almost all existing literature uses sliding mesh or overset mesh techniques to account for the rotor blade motion in forward flight. However, in this study, the applicability of single unstructured meshes within predefined grid blocks has been demonstrated. The prescribed flap and pitch rigid body motions of the blades are introduced into FLUENT via the UDF code to take into account the effect of the blade motion on the flow field and thus, on the performance of the helicopter. These periodic blade motions are modeled into the simulations by first-order Fourier series approximations through User Defined Function feature of the code. The UDF codes are needed for simulating moving boundary problems, since these motions cannot be directly represented with the existing code capabilities. The dynamic mesh technique that is readily available in the code provides the relative motion between the main rotor and the fuselage by taking advantage of volume mesh deformation and re-meshing methods. While using the dynamic mesh technique, the prescribed blade motion may result in undesirable grid qualities leading to unphysical solutions. This problematic issue is alleviated by carefully selected dynamic grid parameters needed within the spring based smoothing and re-meshing methods. The use of moving deforming grids

are only required inside the predefined deformable grid block. In the current case setup, the solver searches for the volume mesh element quality according to a predefined threshold value at each time-step while the application of the dynamic mesh technique. The invoke of re-meshing algorithm can be delayed by finding a logical time interval in which the utilization of the spring analogy is sufficient and when re-meshing is unnecessary. With such an approach, as a result of the reduced checks, a significant reduction in computation time may be achieved, which results in a further improvement of the present methodology.

The computational domain is modeled by unstructured hybrid mesh elements. The grid is pre-adapted to enhance the spatial accuracy of the solution. The volume mesh refinement was not done by using a solution-based adaption feature like Adaptive Mesh Refinement (AMR) technique. However, the possible wake regions, where a finer grid is generated at the preprocess stage, were determined by the help of previous numerical predictions, which ensure already visualized wake patterns for the test cases examined. The mesh refinement is performed at a moderate level by considering computational effort. Prior numerical studies found in literature have been considered as reference to determine suitable grid sizes. These used grid metrics are consistent with the use of standard wall function approach, which enabled the number of mesh elements to be kept at an acceptable level. The complete flow field grids involve total cell numbers below 8 million. The fascinating output of this study is that the presented single grid methodology has given similar successful results with much lower number of grid elements, thus resulting in much shorter computing times, using modest computational power.

In this study, the segregated pressure-based solver and collocated cell-based grid arrangement have been used to carry out a practical solution approach. The gradients at the cell faces are computed by using Least Squares Cell-Based formulation. The pressure-based segregated algorithm, which is a semi-implicit method for pressure-linked equations (SIMPLE) based on the predictor-corrector approach, is adopted for the pressure-velocity coupling. Some complex flow types may cause large gradients in the momentum source terms between control volumes, thus resulting with steep pressure profiles at the cell faces. For that reason, the most appropriate pressure interpolation scheme convenient with the flow regime, by which the interpolation errors can then be considerably reduced, should be employed to achieve an accurate

computation. In this study, the pressure interpolation have been performed using a second order scheme for the compressible flow analysis. The convective terms of all transport equations are discretized by the second order upwind scheme and the discretization of diffusive terms are based on the second order accurate central differencing scheme. The time advancement on the unsteady solution is performed by the first-order implicit formulation.

The accuracy of the present numerical predictions has been demonstrated by the comparison of obtained results with the experiments and other available numerical results found in literature. The present numerical approach can effectively capture rotor wake and reach periodic solutions within 1.5-2 rotor revolutions for higher advance ratios. Steady and unsteady pressure solutions and wake trajectories have been compared with experimental data and other numerical solutions. The present predictions correlate well with the measured unsteady pressure, which is given in [104], in terms of both phase and magnitude variations at most of the measurement locations. Discrepancies are observed particularly at the after body sections where the numerical grid is coarser as a result of the larger distance between the rotor blade and fuselage. It is observed that the rotor effect on the fuselage becomes negligible at higher advance ratios, because the wake bends further downstream and flows above the body. It is worthy to note that the accuracy of the numerical simulations is closely related to the spatial and temporal resolution, numerical schemes and turbulence models. Therefore, further validation would be beneficial by considering the effects of all of the significant parameters. However, for the unsteady rotor-fuselage interaction problem, the adequate level of reliability has been reached within a reasonable computational time and it is found satisfactory for practical engineering purposes. The present dynamic mesh algorithm with re-meshing is robust and efficient to deal with large mesh deformations and can provide well captured, near wake topology, which is beneficial for the physical interpretation of flow phenomena around helicopters. Achieved reduction in computational costs will allow for flexibility in the implementation of more sophisticated techniques such as the AMR for the higher-fidelity analysis of the wake features. The proposed methodology may still be kept as a practical solution approach, when the AMR technique is utilized with a careful set of refining / coarsening levels. In addition, the presented methodology may be applied on a full-scale helicopter geometry to create additional comparison data.

REFERENCES

- [1] **Healey, A.** (2009). Project Clean Sky - Europe Takes action. *Vertiflite*, 55 (1), pp. 42-46.
- [2] **Diodati, G., Ciminello, M., and Concilio, A.** (2011). Technological Solutions for realising an active gurney flap for green rotorcraft applications, based on piezoelectrics and electromagnets, in *Proceedings of the ASME 2011 Conference on Smart Materials, Adaptive Structures and Intelligent Systems*, Scottsdale, Arizona, USA.
- [3] **Aiken, E. W., Ormiston, R. A., and Young, L. A.** (2000). Future Directions in Rotorcraft Technology at Ames Research Center, in *American Helicopter Society 56th Annual Forum*, Virginia Beach, VA.
- [4] **McCroskey, W. J.** (1995). Vortex wakes of rotorcraft, In *33th Aerospace Sciences Meeting and Exhibit*, Reno, NV, January (pp. 9-12).
- [5] **Hariharan, N., and Sankar, L. N.** (2000). A Review of computational techniques for rotor wake modeling, In *38th AIAA Aerospace Sciences Meeting* (pp. 00-0114).
- [6] **Chen, Z., Jiang, X., Zhou, Z., Xiao, H., Huang, Y., Mou, B., Xiao, Z., Liu, G., and Wang, Y.** (2008). Progress in application of CFD techniques, *Science in China Series E: Technological Sciences*, 51 (7), pp. 827-841.
- [7] **Deng, X., Mao, M., Tu, G., Zhang, H., and Zhang, Y.** (2012). High-order and high accurate CFD methods and their applications for complex grid problems, *Communications in Computational Physics*, 11 (4), pp. 1081-1102.
- [8] **Weber, J.** (1974). Notes on the Approximate Solution of Lifting-Surface Theory Used in the R.A.E. Standard Method, *Reports and Memoranda*, R.A.E. Technical Report 73044 - A.R.C. 34 766, HM Stationery Office, London, UK.
- [9] **Young, C.** (1974). The prediction of helicopter rotor hover performance using a prescribed wake analysis, *Reports and Memoranda*, RAE Technical Report 74078 - ARC 35652, HM Stationery Office, London, UK.
- [10] **Isser, A., and Rosen, A.** (1989). Applying the lifting surface method to the blade tip of a hovering helicopter, *Computers and Mathematics with Applications*, 17 (11), pp. 1455-1466.
- [11] **Bettschart, N.** (1999). Rotor Fuselage Interaction: Euler and Navier-Stokes Computations with an Actuator Disk, in *Proceedings of the 55th Annual Forum of the American Helicopter Society*, Montreal, Canada, AHS, Washington, D.C., pp. 419-438.
- [12] **Mikkelsen, R.** (2003). *Actuator Disc Methods Applied to Wind Turbines*, (Doctoral dissertation), Technical University of Denmark.

- [13] **Wachspress, D. A., Quackenbush, T. R., and Boschitsch, A. H.** (2003). Rotorcraft Interactional Aerodynamics with Fast Vortex/Fast Panel Methods, *Journal of the American Helicopter Society*, 48 (4), pp. 223-235.
- [14] **Chuiton, F. L.** (2004). Actuator disc modelling for helicopter rotors, *Aerospace Science and Technology*, 8 (4), pp. 285–297.
- [15] **O’Brien, D. M., and Smith, M. J.** (2005). Analysis of Rotor-Fuselage Interactions Using Various Rotor Models, *43rd AIAA Aerospace Sciences Meeting and Exhibit, Reno, NV*, AIAA 2005-468, AIAA, Reston, VA.
- [16] **Heise, R., Meyer, C. J., and Backström, T. W.** (2007). CFD Simulation of Helicopter Flow Fields Using an Actuator Disk Main Rotor Model. *South African Institution of Mechanical Engineering, R and D Journal*, 23 (3), pp. 26-39.
- [17] **Chaffin, M. S., and Berry, J. D.** (1994). Navier-Stokes and Potential Theory Solutions for a Helicopter Fuselage and Comparison with Experiment. NASA TM 4566, NASA, Washington D.C.
- [18] **Min, B. Y., Sankar, L. N., Rajmohan, N., and Prasad, J. V. R.** (2008). Computational Investigation of the Effects of Gurney Flap on the Forward Flight Characteristics of Helicopter Rotors, *in 26th AIAA Applied Aerodynamics Conference*, Honolulu, Hawaii, August 18-21.
- [19] **Min, B. Y., Sankar, L. N., and Yu, Y. H.** (2009). Combined Lagrangean-Eulerian Approaches for Improved Prediction of Blade Vortex Interaction Phenomena, *in Second International Forum on Rotorcraft Multidisciplinary Technology*, Korea, October 19-20.
- [20] **Shu, C. W.** (1997). Essentially non-oscillatory and weighted essentially non-oscillatory schemes for hyperbolic conservation laws, NASA/CR-97-206253, Hampton.
- [21] **Shu, C. W.** (1999). High order ENO and WENO schemes for Computational Fluid Dynamics, *in High-Order Methods for Computational Physics*, Lecture Notes in Computational Science and Engineering, 9, pp. 439–582. Springer Verlag, New York.
- [22] **Fang, Y., and Menon, S.** (2006). A Two-Equation Subgrid Model for Large-Eddy Simulation of High Reynolds Number Flows, *44th AIAA Aerospace Sciences Meeting and Exhibit*, AIAA 2006-116, Reno, NV, January 9-12.
- [23] **Domenge, P. X. C., and Ilie, M.** (2012). Numerical study of helicopter blade–vortex mechanism of interaction using the potential flow theory, *Applied Mathematical Modelling*, 36, pp. 2841–2857.
- [24] **Jianfeng, T., and Haowen, W.** (2013). Panel/full-span free-wake coupled method for unsteady aerodynamics of helicopter rotor blade, *Chinese Journal of Aeronautics*, 26 (3), pp.535–543.
- [25] **Lynch, C. E., Prosser, D. T., and Smith, M. J.** (2014). An efficient actuating blade model for unsteady rotating system wake simulations, *Computers & Fluids*, 92, pp.138–150.

- [26] **Yang, H., Shen, W., Xu, H., Hong, Z., and Liu, C.** (2014). Prediction of the wind turbine performance by using BEM with airfoil data extracted from CFD, *Renewable Energy*, 70, pp. 107-115.
- [27] **Kim, T., Oh, S., and Yee, K.** (2015). Improved actuator surface method for wind turbine application, *Renewable Energy*, 76, pp. 16-26.
- [28] **Kenyon, A. R., and Brown, R. E.** (2009). Wake Dynamics and Rotor-Fuselage Aerodynamic Interactions, *Journal of the American Helicopter Society*, 54 (1), pp. 1-18.
- [29] **Steijl, R., and Barakos, G. N.** (2009). Computational study of helicopter rotor-fuselage aerodynamic interactions, *AIAA journal*, 47 (9), 2143-2157.
- [30] **Smith, M.J., Shenoy, R., Kenyon, A.R., Brown, R.E.** (2009). Vorticity-transport and unstructured RANS investigation of rotor-fuselage interactions, *35th European Rotorcraft Forum 2009*, Deutsche Gesellschaft fuer Luft und Raumfahrt (DGLR), Bonn, Germany, pp. 494-512.
- [31] **Tanabe, Y., Saito, S., and Otani, I.** (2010). Validation of Computational Results of Rotor/Fuselage Interaction Analysis Using rFlow3D Code, *JAXA Research and Development Report*, JAXA-RR-10-001E, Japan Aerospace Exploration Agency, Chofu, Tokyo, Japan.
- [32] **Zhao, J., He, C., Zhang, L., Zhao, H., and Hu, P.** (2011). Coupled Viscous Vortex Particle Method and Unstructured Computational Fluid Dynamics Solver for Rotorcraft Aerodynamic Interaction Analysis, *49th AIAA Aerospace Sciences Meeting including the New Horizons Forum and Aerospace Exposition, Orlando, Florida*, AIAA 2011-1121, AIAA, Reston, VA.
- [33] **De Gregorio, F.** (2012). Flow field characterization and interactional aerodynamics analysis of a complete helicopter, *Aerospace Science and Technology*, 19 (1), pp. 19-36.
- [34] **Antoniadis, A. F., Drikakis, D., Zhong, B., Barakos, G., Steijl, R., Biava, M., Vigevano, L., Broklehurst, A., Boelens, O., Dietz, M., Embacher, M., and Khier, W.** (2012). Assessment of CFD methods against experimental flow measurements for helicopter flows, *Aerospace Science and Technology*, 19 (1), pp. 86-100.
- [35] **Biava, M., and Vigevano, L.** (2012). Simulation of a complete helicopter: A CFD approach to the study of interference effects, *Aerospace Science and Technology*, 19 (1), pp. 37-49.
- [36] **Kyrkos, A., and Ekaterinaris, J. A.** (2012). Assessment of an unstructured mesh approach for CFD predictions of the NH90 fuselage rotor, *Aerospace Science and Technology*, 19 (1), pp. 77-85.
- [37] **Quon, E.W., Smith, M.J., Whitehouse, G. R., Wachspress, D.** (2012). Unsteady Reynolds-averaged Navier-Stokes-based hybrid methodologies for rotor-fuselage interaction, *Journal of Aircraft*, 49 (3), pp. 961-965.
- [38] **Sa, J. H., Kim, J. W., Park, S. H., Park, J. S., Jung, S. N., and Yu, Y. H.** (2009). KFLOW Results of Airloads on HART-II Rotor Blades with

Prescribed Blade Deformation, *International Journal of Aeronautical and Space Sciences*, 10 (2), pp. 52-62.

- [39] **Yu, D. O., Jung, M. S., Kwon, O. J., and Yu, Y. H.** (2009). Predicting Blade Loading and Wake Structure of the HART II Rotor using Adaptive Unstructured Meshes, in *Second International Forum on Rotorcraft Multidisciplinary Technology*, Korea.
- [40] **Zhang, S., Gentela, M., Fuchiwaki, T., and Xu, H.** (2009). CFD Developments for Unsteady Aerodynamics of Rotorcraft in Forward Flight with Realistic Motion Schedules, *19th AIAA Computational Fluid Dynamics, San Antonio, Texas*, AIAA 2009-4267, AIAA, Reston, VA.
- [41] **Yu, Y. H.** (2000). Rotor blade-vortex interaction noise, *Progress in Aerospace Sciences*, 36, pp. 97-115.
- [42] **Beaumier, P., and Delrieux, Y.** (2005). Description and validation of the ONERA computational method for the prediction of blade-vortex interaction noise, *Aerospace Science and Technology*, 9, pp. 31-43.
- [43] **Lim, J. W., and Strawn, R. C.** (2007). Prediction of HART II Rotor BVI Loading and Wake System Using CFD/CSD Loose Coupling, *45th AIAA Aerospace Sciences Meeting and Exhibit*, AIAA-2007-1281, Reno, NV.
- [44] **Yang, C., and Aoyama, T.** (2008). Effect of Computation Parameters on BVI Noise Prediction Using HART II Motion Data, *34th European Rotorcraft Forum*, Liverpool, England.
- [45] **Kelly, M. E., and Brown, R. E.** (2009). The effect of Blade Aerodynamic Modeling on the Prediction of High-Frequency Rotor Airloads, *AHS 65th Annual Forum*, Grapevine, TX.
- [46] **Gennaretti, M., Testa, C., and Bernardini, G.** (2013). An unsteady aerodynamic formulation for efficient rotor tonal noise prediction, *Journal of Sound and Vibration*, 332, pp. 6743-6754.
- [47] **Brocklehurst, A., and Barakos, G. N.** (2013). A review of helicopter rotor blade tip shapes, *Progress in Aerospace Sciences*, 56, pp. 35-74.
- [48] **Stephenson, J. H., Tinney, C. E., Greenwood, E., and Watts, M. E.** (2014). Time frequency analysis of sound from a maneuvering rotorcraft, *Journal of Sound and Vibration*, 333, pp. 5324-5339.
- [49] **Chaderjian, N. M.** A Breakthrough in Rotorcraft Prediction Accuracy Using Detached Eddy Simulation. Date retrieved 12.05.2016. Address: <https://www.nas.nasa.gov/SC12/demos/demo1.html>.
- [50] **Park, Y. M., Nam, H. J., and Kwon, O. J.** (2003). Simulation of Unsteady Rotor-Fuselage Interactions Using Unstructured Adaptive Meshes, *American Helicopter Society 59th Annual Forum*, 51 (2), pp. 141-149, Amer Helicopter Soc. Inc., Alexandria, VA.
- [51] **Wissink, A. M., Kamkar, S., Pulliam, T. H., Sitaraman, J., and Sankaran, V.** (2010). Cartesian adaptive mesh refinement for rotorcraft wake resolution, in *28th AIAA Applied Aerodynamics Conference*, AIAA 2010-4554, Chicago, Illinois.

- [52] **Sitaraman, J., Floros, M., Wissink, A., and Potsdam, M.** (2010). Parallel domain connectivity algorithm for unsteady flow computations using overlapping and adaptive grids, *Journal of Computational Physics*, 229 (12), pp. 4703-4723.
- [53] **Kamkar, S. J., Wissink, A. M., Sankaran, V., and Jameson, A.** (2012). Combined Feature-Driven Richardson-Based Adaptive Mesh Refinement for Unsteady Vortical Flows, *AIAA journal*, 50 (12), pp. 2834-2847.
- [54] **Biboulet, N., Gravouil, A., Dureisseix, D., Lubrecht, A. A., and Combescure, A.** (2013). An efficient linear elastic FEM solver using automatic local grid refinement and accuracy control, *Finite Elements in Analysis and Design*, 68, pp. 28–38.
- [55] **Sankaran, V., Sitaraman, J., Wissink, A., Datta, A., Jayaraman, B., Potsdam, M., Mavriplis, D., Yang, Z., O'Brien, D., Saberi, H., Cheng, R., Hariharan, N., and Strawn, R.** (2010). Application of the Helios Computational Platform to Rotorcraft Flow, in *48th AIAA Aerospace Sciences Meeting Including the New Horizons Forum and Aerospace Exposition, Orlando, Florida*, AIAA 2010-1230, AIAA, Reston, VA.
- [56] **Sitaraman, J., Potsdam, M., Jayaraman, B., Datta, A., Wissink, A., Mavriplis, D., and Saberi, H.** (2011). Rotor Loads Prediction Using Helios: A Multi-Solver Framework for Rotorcraft CFD/CSD Analysis, *49th AIAA Aerospace Sciences Meeting including the New Horizons Forum and Aerospace Exposition, Orlando, Florida*, AIAA 2011-1123, AIAA, Reston, VA.
- [57] **Abras, J. N., and Hariharan, N.** (2015). Comparison of CFD Hover Predictions on the S-76 Rotor, *53rd AIAA Aerospace Sciences Meeting, Kissimmee, Florida*, AIAA 2015-1711, AIAA SciTech, Reston, VA.
- [58] **Liu, X.-D., Osher, S., and Chan, T.** (1994). Weighted Essentially Non-oscillatory Schemes, *Journal of computational physics*, 115 (1), pp. 200-212.
- [59] **Lim, J. W., and Dimanlig, A. C.** (2009). An Investigation of the Fuselage Effect for HART II Using a CFD/CSD Coupled Analysis, *Second International Forum on Rotorcraft Multidisciplinary Technology, Seoul, Korea*, AHS International, Fairfax, VA.
- [60] **Xu, L., and Weng, P.** (2014). High order accurate and low dissipation method for unsteady compressible viscous flow computation on helicopter rotor in forward flight, *Journal of Computational Physics*, 258, pp. 470-488.
- [61] **Steijl, R., Barakos, G., and Badcock, K.** (2006). A framework for CFD analysis of helicopter rotors in hover and forward flight, *International journal for numerical methods in fluids*, 51 (8), pp. 819-847.
- [62] **Steijl, R., and Barakos, G.** (2008). Sliding mesh algorithm for CFD analysis of helicopter rotor–fuselage aerodynamics, *International journal for numerical methods in fluids*, 58 (5), pp. 527-549.

- [63] **Steijl, R., and Barakos, G. N.** (2012). CFD analysis of complete helicopter configurations – lessons learnt from the GOAHEAD project, *Aerospace Science and Technology*, 19 (1), pp. 58-71.
- [64] **Zhang, B., and Liang, C.** (2015). A simple, efficient, and high-order accurate curved sliding-mesh interface approach to spectral difference method on coupled rotating and stationary domains, *Journal of Computational Physics*, 295, pp. 147-160.
- [65] **Hirt, C. W., Amsden, A. A., and Cook, J. L.** (1974). An arbitrary Lagrangian-Eulerian computing method for all flow speeds, *Journal of Computational Physics*, 14 (3), pp. 227-253.
- [66] **Gülçat, Ü., Mısırhoğlu, A., and Aslan, A. R.** (2000). 3-D Viscous Flow Solutions over Bodies in Relative Motion, *International Journal of Computational Fluid Dynamics*, 14 (1), pp. 1-19.
- [67] **Sahin, M., and Mohseni, K.** (2009). An arbitrary Lagrangian–Eulerian formulation for the numerical simulation of flow patterns generated by the hydromedusa *Aequorea victoria*, *Journal of Computational Physics*, 228, pp. 4588–4605.
- [68] **Batina, J. T.** (1990). Unsteady Euler airfoil solutions using unstructured dynamic meshes, *AIAA journal*, 28 (8), pp. 1381-1388.
- [69] **Bottasso, C. L., Detomi, D., and Serra, R.** (2005). The ball-vertex method: a new simple spring analogy method for unstructured dynamic meshes, *Computer Methods in Applied Mechanics and Engineering*, 194 (39), pp. 4244-4264.
- [70] **Lin, T. J., Guan, Z. Q., Chang, J. H., and Lo, S. H.** (2014). Vertex-Ball Spring Smoothing: An efficient method for unstructured dynamic hybrid meshes, *Computers and Structures*, 136, pp. 24-33.
- [71] **Johnson, A. A., and Tezduyar, T. E.** (1994). Mesh update strategies in parallel finite element computations of flow problems with moving boundaries and interfaces, *Computer methods in applied mechanics and engineering*, 119 (1), pp. 73-94.
- [72] **De Boer, A., Van der Schoot, M. S., and Bijl, H.** (2007). Mesh deformation based on radial basis function interpolation, *Computers and structures*, 85 (11), pp. 784-795.
- [73] **Cordero-Gracia, M., Gómez, M., Ponsin, J., and Valero, E.** (2012). An interpolation tool for aerodynamic mesh deformation problems based on octree decomposition, *Aerospace Science and Technology*, 23 (1), pp. 93-107.
- [74] **Erzincanli, B., and Sahin, M.** (2013). An arbitrary Lagrangian–Eulerian formulation for solving moving boundary problems with large displacements and rotations, *Journal of Computational Physics*, 255, pp. 660-679.
- [75] **Johnson, A. A., and Tezduyar, T. E.** (1999). Advanced mesh generation and update methods for 3D flow simulations, *Computational Mechanics*, 23 (2), pp. 130-143.

- [76] **Rane, S., Kovacevic, A., Stosic, N., and Kethidi, M.** (2013). Grid deformation strategies for CFD analysis of screw compressors, *International Journal of Refrigeration*, 36 (7), pp. 1883-1893.
- [77] **Dapogny, C., Dobrzynski, C., and Frey, P.** (2014). Three-dimensional adaptive domain remeshing, implicit domain meshing, and applications to free and moving boundary problems, *Journal of Computational Physics*, 262, pp. 358-378.
- [78] **Ahmad, J., and Duque, E. P.** (1996). Helicopter Rotor Blade Computation in Unsteady Flows Using Moving Overset Grids, *Journal of Aircraft*, 33 (1), pp. 54-60.
- [79] **Djomehri, M. J., and Biswas, R.** (2003). Performance enhancement strategies for multi-block overset grid CFD applications, *Parallel Computing*, 29 (11), pp. 1791-1810.
- [80] **Pahlke, K., and Van Der Wall, B. G.** (2005). Chimera simulations of multibladed rotors in high-speed forward flight with weak fluid-structure-coupling, *Aerospace Science and Technology*, 9 (5), pp. 379-389.
- [81] **Dietz, M., Kramer, E., and Wagner, S.** (2006). Tip Vortex Conservation on a Main Rotor in Slow Descent Flight Using Vortex-Adapted Chimera Grids, AIAA Paper 2006-3478, AIAA, Reston, VA.
- [82] **Lee, B. S., Jung, M. S., Kwon, O. J., and Kang, H. J.** (2010). Numerical Simulation of Rotor-Fuselage Aerodynamic Interaction Using an Unstructured Overset Mesh Technique, *International Journal of Aeronautical and Space Sciences*, 11 (1), pp. 1-9.
- [83] **Shenoy, R., and Smith, M. J.** (2011). Unstructured Overset Grid Adaptation for Rotorcraft Aerodynamic Interactions, *American Helicopter Society 67th Annual Forum*, American Helicopter Society International, Alexandria, VA.
- [84] **Rodriguez, C.** (2012). *CFD Analysis on the Main-Rotor Blade of a Scale Helicopter Model using Overset Meshing*, (Masters' Degree Project), Stockholm, Sweden.
- [85] **Renaud, T., Costes, M., and Péron, S.** (2012). Computation of GOAHEAD configuration with Chimera assembly, *Aerospace Science and Technology*, 19 (1), pp. 50-57.
- [86] **Castillon, L., Billonnet, G., Riou, J., Péron, S., and Benoit, C.** (2014). A Technological Effect Modeling on Complex Turbomachinery Applications with an Overset Grid Numerical Method, *Journal of Turbomachinery*, 136 (10), 101005.
- [87] **Roget, B., and Sitaraman, J.** (2014). Robust and efficient overset grid assembly for partitioned unstructured meshes, *Journal of Computational Physics*, 260, pp. 1-24.
- [88] **Meakin, R. L.** (2000). Adaptive spatial partitioning and refinement for overset structured grids, *Computer methods in applied mechanics and engineering*, 189 (4), pp. 1077-1117.

- [89] **Zagaris, G., Campbell, M. T., Bodony, D. J., Shaffer, E., and Brandyberry, M. D.** (2010). A toolkit for parallel overset grid assembly targeting large-scale moving body aerodynamic simulations, *Proceedings of the 19th International Meshing Roundtable*, pp. 385-401, Springer Berlin Heidelberg.
- [90] **Bauchau, O. A. and Ahmad, J. U.** (1996). Advanced CFD and CSD methods for Multidisciplinary Applications in Rotorcraft Problems, *AIAA/NASA and ISSMO Symposium on Multidisciplinary Analysis and Optimization, Bellevue, WA*, pp. 1441-1451, AIAA, Reston, VA.
- [91] **Potsdam, M. A., Yeo, H., and Johnson, W.** (2006). Rotor Airloads Prediction Using Loose Aerodynamic/Structural Coupling, *Journal of Aircraft*, 43 (3), pp. 732-742, AIAA, Reston, VA.
- [92] **Friedmann, P. P.** (2004). Rotary-Wing Aeroelasticity: Current Status and Future Trends, *AIAA journal*, 42 (10), pp. 1953-1972.
- [93] **Lee, H.-K., Yoon, S.-H., Shin, S., and Kim, C.** (2008). Coupled CFD/CSD Analysis of a Hovering Rotor Using High Fidelity Unsteady Aerodynamics and a Geometrically Exact Rotor Blade Analysis, *34th European Rotorcraft Forum*, Royal Aeronautical Society, London, U.K.
- [94] **Guruswamy, G. P.** (2009). CFD- and CSD-based Aeroelastic Computations of Helicopter Rotor Blades using a Modular Approach, *39th AIAA Fluid Dynamics Conference, San Antonio, Texas*, AIAA 2009-4199, AIAA, Reston, VA.
- [95] **Shyy, W., Aono, H., Chimakurthi, S. K., Trizila, P., Kang, C. K., Cesnik, C. E., and Liu, H.** (2010). Recent progress in flapping wing aerodynamics and aeroelasticity, *Progress in Aerospace Sciences*, 46 (7), pp. 284-327.
- [96] **Bernardini, G., Serafini, J., Colella, M. M., and Gennaretti, M.** (2013). Analysis of a structural-aerodynamic fully-coupled formulation for aeroelastic response of rotorcraft, *Aerospace Science and Technology*, 29 (1), pp. 175-184.
- [97] **Shi, J., Xu, T., Schafer, S. R., and Chen, C.-L.** (2013). Adaptive Control of Shock Waves with a Passively Morphing Layer for Rotating Blades, *Journal of Aerospace Engineering*, 28 (2), 04014070.
- [98] **Mishra, A., Mani, K., Mavriplis, D., and Sitaraman, J.** (2015). Time dependent adjoint-based optimization for coupled fluid-structure problems, *Journal of Computational Physics*, 292, pp. 253-271.
- [99] **Biedron, R. T., and Lee-Rausch, E. M.** (2008). Rotor Airloads Prediction Using Unstructured Meshes and Loose CFD/CSD Coupling, *26th AIAA Applied Aerodynamics Conference, Honolulu, Hawaii*, AIAA 2008-7341, AIAA, Reston, VA.
- [100] **Palacios, F., Colonno, M. R., Aranake, A. C., Campos, A., R, C. S., Economon, T. D., and Alonso, J. J.** (2013). Stanford University Unstructured (SU2): An open-source integrated computational environment for multi-physics simulation and design, *51st AIAA*

- [101] **Freeman, C. E., and Mineck, R. E.** (1979). Fuselage Surface Pressure Measurements of a Helicopter Wind Tunnel Model with a 3.15 Meter Diameter Single Rotor, NASA TM 80051, NASA, Washington D.C.
- [102] **Açıkgöz, M. B., Anbarcı, K., Aslan, A. R.** (2014). Askı ve İleri Uçuş Şartlarında Helikopter Rotor-Gövde Akış Etkileşimi için HAD Analiz Yöntemi Geliştirilmesi, 3. *Ulusal Havacılıkta İleri Teknolojiler Konferansı (HİTEK 2014)*, 18-19 Haziran, Hava Harp Okulu, İstanbul, Türkiye.
- [103] **Mineck, R. E.** (1999). Application of an Unstructured Grid Navier-Stokes Solver to a Generic Helicopter Body, NASA/TM-209510, NASA, Washington D.C.
- [104] **Mineck, R. E., and Gorton, S. A.** (2000). Steady and Periodic Pressure Measurements on a Generic Helicopter Fuselage Model in the Presence of a Rotor, NASA/TM-2000-210286, NASA, Washington D.C.
- [105] **Leishman, J. G.** (2006). *Principles of Helicopter Aerodynamics, 2nd Ed.*, Cambridge University Press, New York.
- [106] **Conlisk, A. T.** (1997). Modern Helicopter Aerodynamics, *Annual Review of Fluid Mechanics*, 29, pp. 515-567.
- [107] **Sorensen, J. N., and Shen, W. Z.** (2002). Numerical modeling of wind turbine wakes, *Journal of Fluid Engineering*, 124 (2), 393-399.
- [108] **Ivanell, S., Sørensen, J. N., and Henningson, D.** (2007). Numerical Computations of Wind Turbine Wakes, In *Wind Energy*, (pp. 259-263). Springer Berlin Heidelberg.
- [109] **Lanzafame, R., and Messina, M.** (2012). BEM theory: How to take into account the radial flow inside of a 1-D numerical code, *Renewable energy*, 39 (1), pp. 440-446.
- [110] **Bai, C. J., Hsiao, F. B., Li, M. H., Huang, G. Y., and Chen, Y. J.** (2013). Design of 10 kW Horizontal-Axis Wind Turbine (HAWT) Blade and Aerodynamic Investigation Using Numerical Simulation, *Procedia Engineering*, 67, pp. 279-287.
- [111] **Carcangiu, C. E.** (2008). *CFD-RANS study of horizontal axis wind turbines*, (Doctoral Thesis), University of Cagliari, Department of Mechanical Engineering.
- [112] **Hansen, M. O. L., Sørensen, J. N., Voutsinas, S., Sørensen, N., and Madsen, H. A.** (2006). State of the art in wind turbine aerodynamics and aeroelasticity, *Progress in aerospace sciences*, 42 (4), pp. 285-330.
- [113] **Milne-Thomson, L.** (1966). *Theoretical aerodynamics*, Dover Publications, New York.
- [114] **Hansen, M. O. L.** (1997). Extraction of lift, drag and angle of attack from computed 3-D viscous flow around a rotating blade, In *Proceedings of EWEC 97*, (pp. 499-502). Dublin.

- [115] **Yao, Y.** (1996). *High order resolution and parallel implementation on unstructured grids*, (Doctoral dissertation), University of Glasgow, Department of Aerospace Engineering.
- [116] **Shaw, C.** (1992). *Using Computational Fluid Dynamics*, Hemel Hempstead, England: Prentice Hall.
- [117] **Wilcox, D.** (1994). *Turbulence Modelling for CFD*, DCW Industries, California, USA.
- [118] **Jameson, A., and Mavriplis, D.** (1986). Finite Volume Solution of the Two-Dimensional Euler Equation on Regular Triangular Meshes, *AIAA journal*, 24 (4), pp. 611-618.
- [119] **Jameson, A., Baker, T. J., and Weatherill, N. P.** (1986). Calculation of Inviscid Transonic Flow over a Complete Aircraft, *AIAA paper*, 86, 0103.
- [120] **Desideri, J. A., and Dervieux, A.** (1988). Compressible Flow Solvers Using Unstructured Grids, *VKI Lecture Series*, von Karman Institute for Fluid Dynamics, Belgium, pp. 1-115.
- [121] **Versteeg, H. K., and Malalasekera, W.** (1995). *An Introduction to Computational Fluid Dynamics: The Finite Volume Method*, Harlow: Longman Scientific & Technical, New York.
- [122] **Ferziger, J. H., and Peric, M.** (1999). *Computational Methods for Fluid Dynamics*, Springer-Verlag, Berlin.
- [123] **ANSYS FLUENT** (version 14.5) [Computer software - Theory Guide], Canonsburg, PA, ANSYS, Inc.
- [124] **Van Doormaal, J. P., Raithby, G. D., and McDonald, B. H.** (1986). The segregated approach to predicting viscous compressible fluid flows, *In ASME 1986 International Gas Turbine Conference and Exhibit*. American Society of Mechanical Engineers.
- [125] **Lien, F. S., and Leschziner, M. A.** (1993). A pressure-velocity solution strategy for compressible flow and its application to shock/boundary-layer interaction using second-moment turbulence closure, *Journal of fluids engineering*, 115 (4), pp. 717-725.
- [126] **Darwish, M., Asmar, D., and Moukalled, F.** (2004). A comparative assessment within a multigrid environment of segregated pressure-based algorithms for fluid flow at all speeds, *Numerical Heat Transfer, Part B: Fundamentals*, 45 (1), pp. 49-74.
- [127] **Url-1** <https://en.wikipedia.org/wiki/Boundary_value_problem>, date retrieved 10.06.2016.
- [128] **Bradshaw, P.** (2013). *An Introduction to Turbulence and Its Measurement: Thermodynamics and Fluid Mechanics Series*. Elsevier.
- [129] **Libby, P. A.** (1996). *An introduction to turbulence*. CRC Press.
- [130] **Url-2**, *CFD Online*, <http://www.cfd-online.com/Wiki/Turbulence_modeling>, date retrieved 25.06.2013.

- [131] **Do, T., Chen, L., and Tu, J.** (2010). Numerical study of turbulent trailing-edge flows with base cavity effects using URANS, *Journal of Fluids and Structures*, 26 (7), pp. 1155-1173.
- [132] **Wang, G., Duchaine, F., Papadogiannis, D., Duran, I., Moreau, S., and Gicquel, L. Y.** (2014). An overset grid method for large eddy simulation of turbomachinery stages, *Journal of Computational Physics*, 274, pp. 333-355.
- [133] **Pacciani, R., Marconcini, M., Arnone, A., and Bertini, F.** (2014). URANS Prediction of the Effects of Upstream Wakes on High-lift LP Turbine Cascades Using Transition-sensitive Turbulence Closures, *Energy Procedia*, 45, pp. 1097-1106.
- [134] **Ghasemian, M., and Nejat, A.** (2015). Aerodynamic noise prediction of a Horizontal Axis Wind Turbine using Improved Delayed Detached Eddy Simulation and acoustic analogy, *Energy Conversion and Management*, 99, pp. 210-220.
- [135] **Gourdain, N.** (2015). Prediction of the unsteady turbulent flow in an axial compressor stage. Part 1: Comparison of unsteady RANS and LES with experiments, *Computers & Fluids*, 106, pp. 119-129.
- [136] **Arakawa, C., Fleig, O., Iida, M., and Shimooka, M.** (2005). Numerical approach for noise reduction of wind turbine blade tip with Earth Simulator, *Journal of the Earth Simulator*, 2 (3), pp. 11-33.
- [137] **Sorensen, N. N., Johansen, J., and Conway, S.** (2004). *CFD computations of wind turbine blade loads during standstill operation, KNOW-BLADE Task 3.1* (Technical Report R-1465). Riso National Laboratory, Roskilde-DK.
- [138] **Iida, M., Shimooka, M., and Arakawa, C.** (2006). Basic study of winglet effects on aerodynamics and aeroacoustics using Large-Eddy Simulation, *In Proceedings of EWEC European Wind Energy Conference*, Athens.
- [139] **Davidson, L.** (1997). *An introduction to turbulence models* (Tech Rep 97/2). Dept of Thermo and Fluid Dynamics, Chalmers University of Technology, Göteborg, Sweden.
- [140] **Richardson, L. F.** (1922). *Weather Prediction by Numerical Process*, Cambridge University Press.
- [141] **Kolmogorov, A. N.** (1941). The local structure of turbulence in incompressible viscous fluids at very large Reynolds numbers, *Dokl. Nauk. SSSR*. 30, 301-305.
- [142] **Kolmogorov, A. N.** (1962). A refinement of previous hypotheses concerning the local structure of turbulence in a viscous incompressible fluid at high Reynolds numbers, *J. Fluid Mech.* 13, 82-85.
- [143] **Squires, K. D.** (2004). Detached eddy simulation: current status and perspectives', in: Friedrich, R., Geurts, B.J., Metais, O. (Eds.), *Direct and Large Eddy simulation*, 5, pp. 465-480, Kluwer, Dordrecht.

- [144] **Gungor, A. G., and Menon, S.** (2010). A new two-scale model for large eddy simulation of wall-bounded flows, *Progress in Aerospace Sciences*, 46, pp. 28-45.
- [145] **Wang, M., and Moin, P.** (1991). Dynamical wall modeling for large-eddy simulation of complex turbulent flows, *Physics of Fluids*, 14, pp. 2043-2051.
- [146] **Spalart, P. R., and Allmaras, S. R.** (1992). A one-equation turbulence model for aerodynamic flows, *AIAA Paper*, 1992-0439.
- [147] **Vreman, B., Geurts, B., and Kuerten, H.** (1997). Large-eddy simulation of the turbulent mixing layer, *Journal of Fluid Mechanics*, 339, 357-390.
- [148] **da Silva C. B., and Pereira, J. C.** (2004). The effect of subgrid-scale models on the vortices computed from large-eddy simulations, *Physics of Fluids*, 16 (12), 4506-4534.
- [149] **Spalart, P. R.** (2000). Strategies for turbulence modelling and simulations, *Int. J. Heat Fluid Flow*, 21, pp. 252–263.
- [150] **Strelets, M.** (2001). Detached eddy simulation of massively separated flows, *AIAA Paper 2001-0879*.
- [151] **Piomelli, U., Balaras, E., Pasinato, H., Squires, K. D., and Spalart, P. R.** (2003). The inner-outer layer interface in large-eddy simulations with wall-layer models, *Int. J. Heat Fluid Flow*, 24, pp. 538–550.
- [152] **Boussinesq, J.** (1877). Essai sur la theorie des eaux courantes, Memoires presentes par divers savants ` l'Acad. des Sci. Inst. Nat. France, *Tome XXIII*, (1).
- [153] **Van Driest, E. R.** (1956). On Turbulent Flow Near a Wall, *Journal of the Aeronautical Sciences*, 23, p. 1007.
- [154] **Cebeci, T., and Smith, A.** (1974). Analysis of Turbulent Boundary Layers, Academic Press.
- [155] **Baldwin, B., and Lomax, H.** (1978). Thin-layer approximation and algebraic model for separated turbulent flows, *AIAA 78-257*, Huntsville, AL.
- [156] **Bradshaw, P., Ferriss, D., and Atwell, N.** (1967). Calculation of boundary-layer development using the turbulent energy equation, *Journal of Fluid Mechanics*, 28, pp. 593-616.
- [157] **Wolfshtein, M.** (1969). The velocity and temperature distribution in one dimensional flow with turbulence augmentation and pressure gradient, *Int. J. Mass Heat Transfer*, 12, pp. 301-318.
- [158] **Davidson, L., and Olsson, E.** (1987). Calculation of some parabolic and elliptic flows using a new one equation turbulence model, *In 5th Int. Conf. on Numerical Methods in Laminar and Turbulent Flow* (pp. 411-422). Pineridge Press.
- [159] **Menter, F.** (1996). On the connection between one- and two-equation models of turbulence, *In Engineering Turbulence Modelling and Experiments*, 3, pp. 131-140, Elsevier.

- [160] **Bradshaw, P.** (1967). The turbulence structure of equilibrium boundary layers., *Journal of Fluid Mechanics*, 29, pp. 625-645.
- [161] **Lauder, B. E., and Spalding, D. B.** (1974). The numerical computation of turbulent flows, *Computer methods in applied mechanics and engineering*, 3 (2), 269-289.
- [162] **Weatherill, N. P., Hassan, O., Marcum, D. L., and Marchant, M. J.** (1994). Grid Generation by the Delauney Triangulation, Lecture Series 1994-02, VKI Jan.24-28.
- [163] **Holmes, D. G., and Connell, S. D.** (1989). Solution of the 2D Navier-Stokes Equations on Unstructured Adaptive Grids, *AIAA paper 89-1932-CP*.
- [164] **ANSA** (version 13) [Computer software - User Guide], GR-57500 Epanomi, Greece, BETA CAE Systems S. A.
- [165] **Chaffin, M. S., and Berry, J. D.** (1997). Helicopter fuselage aerodynamics under a rotor by Navier-Stokes simulation, *Journal of the American Helicopter Society*, 42 (3), pp. 235-43.
- [166] **Mavriplis, D. J.** (1990). Algebraic Turbulence Modelling for Unstructured and Adaptive Meshes, *AIAA paper 90-1653*.
- [167] **Kallinderis, Y.** (1992). Algebraic Turbulence Modelling for Adaptive Unstructured Meshes, *AIAA Journal*, 30 (3), pp. 631-639.
- [168] **Baldwin, B. S., and Barth, T. J.** (1991). A One-Equation Turbulence Transport Model for High Reynolds Wall-Bounded Flows, *AIAA paper 91-0610*.
- [169] **Wake, B. E., and Waeder, J. D.** (1994). Evaluation of a Navier-Stokes Analysis Method for Hover Performance Prediction, *AHS Aeromechanics Specialists Conference*, San Francisco, CA, Jan 19-21.
- [170] **Bousman, W. G.** (2003). Aerodynamic characteristics of SC1095 and SC1094 R8 airfoils, NASA/TP-212265, AFDD/TR-04-003.
- [171] **Shih, T. H., Liou, W. W., Shabbir, A., Yang, Z., and Zhu, J.** (1995). A New k- ϵ Eddy-Viscosity Model for High Reynolds Number Turbulent Flows - Model Development and Validation, *Computers and Fluids*, 24 (3), pp. 227-238.
- [172] **Sutherland, W.** (1893). The viscosity of gases and molecular force, *Philosophical Magazine*, 5 (36), pp. 507-531.
- [173] **Karypis, G., and Kumar, V.** (1997). METIS - A Software Package for Partitioning Unstructured Graphs, Partitioning Meshes, and Computing Fill-Reducing Orderings of Sparse Matrices, Version 3.0. Manual, *University of Minnesota and Army HPC Research Center*.
- [174] **Ruffin, S.M., O'Brien, D., Smith, M.J., Hariharan, N., Lee, J.D. and Sankar, L.** (2004). Comparison of rotor-airframe interaction utilizing overset and unstructured grid techniques, *42nd AIAA Aerospace Sciences Meeting and Exhibit*, Reno, NV.
- [175] **Jeong, J., and Hussain, F.** (1995). On the identification of a vortex, *Journal of Fluid Mechanics*, 285, pp. 69-94.

- [176] **Chakraborty, P., Balachandar, S., and Adrian R. J.** (2005). On the relationships between local vortex identification schemes, *Journal of Fluid Mechanics*, 535, pp. 189-214.
- [177] **Cucitore, R., Quadrio, M., and Baron, A.** (1999). On the Effectiveness and Limitations of Local Criteria for the Identification of a Vortex, *European Journal of Mechanics B/Fluids*, 18 (2), pp. 261–282.
- [178] **Kolář, V.** (2009). Compressibility Effect in Vortex Identification, *AIAA Journal*, 47 (2), pp. 473–475.

APPENDICES

APPENDIX A: Cp distributions of fuselage only cases.

APPENDIX B: The flow patterns obtained at different angles of attack.

APPENDIX C: Cp fluctuations obtained from rotor and fuselage configurations.

APPENDIX A

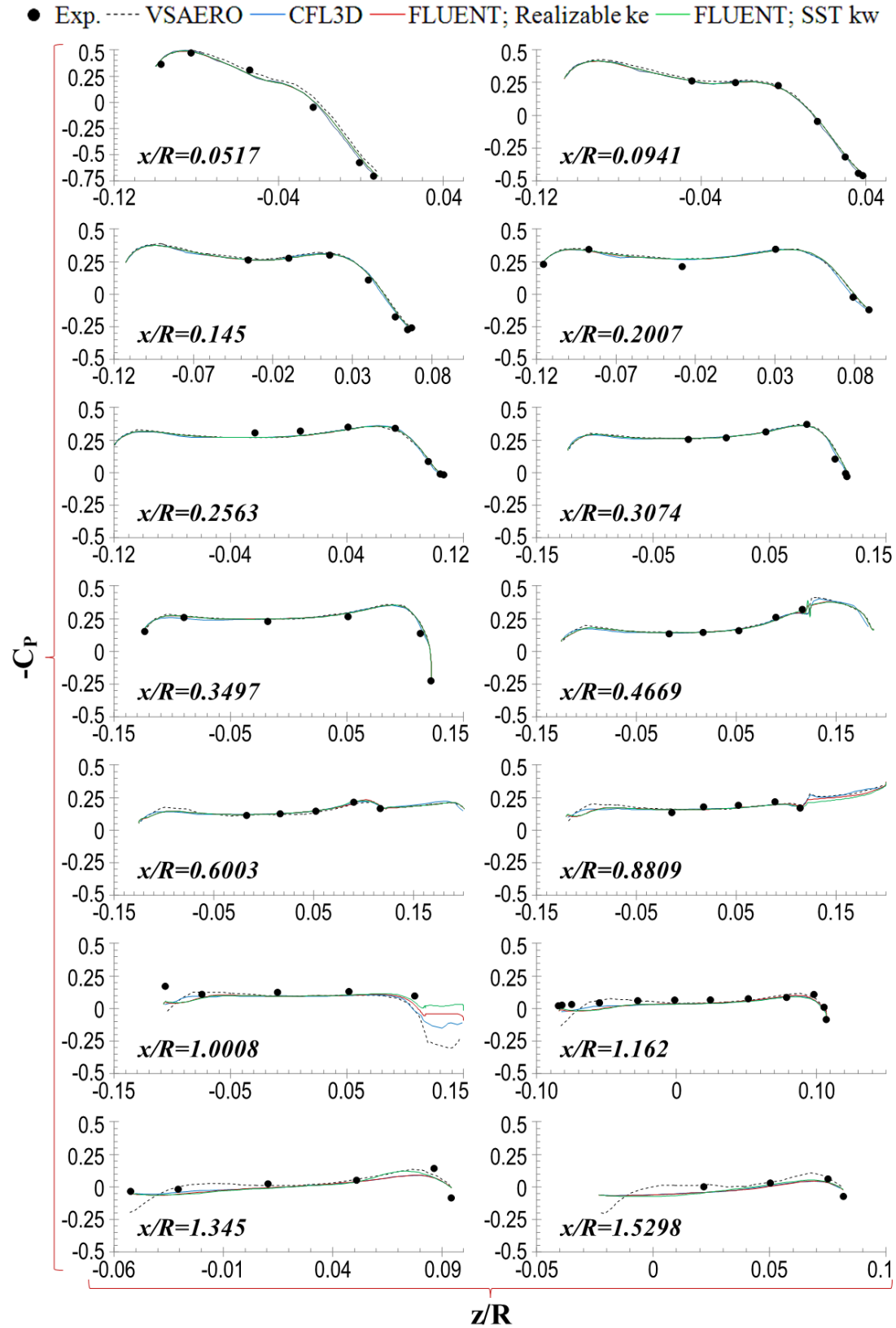


Figure A.1 : C_p distributions obtained at $\alpha_f = -10^\circ$.

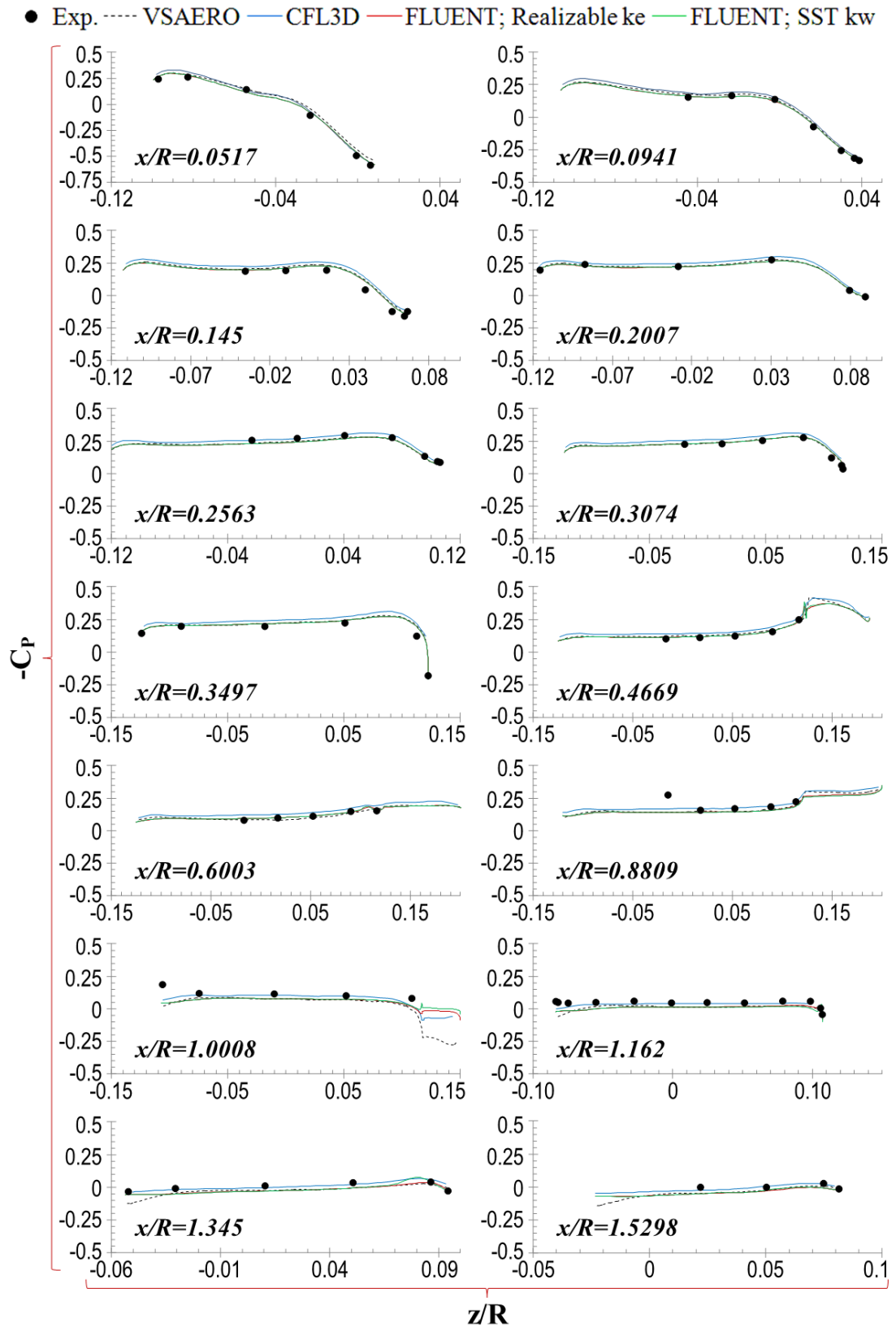


Figure A.2 : C_p distributions obtained at $\alpha_f = -5^\circ$.

● Exp. - - - VSAERO - - - CFL3D - - - FLUENT; Realizable ke - - - FLUENT; SST kw - - - FLUENT; RNG ke - - - FLUENT; Spalart Allmaras

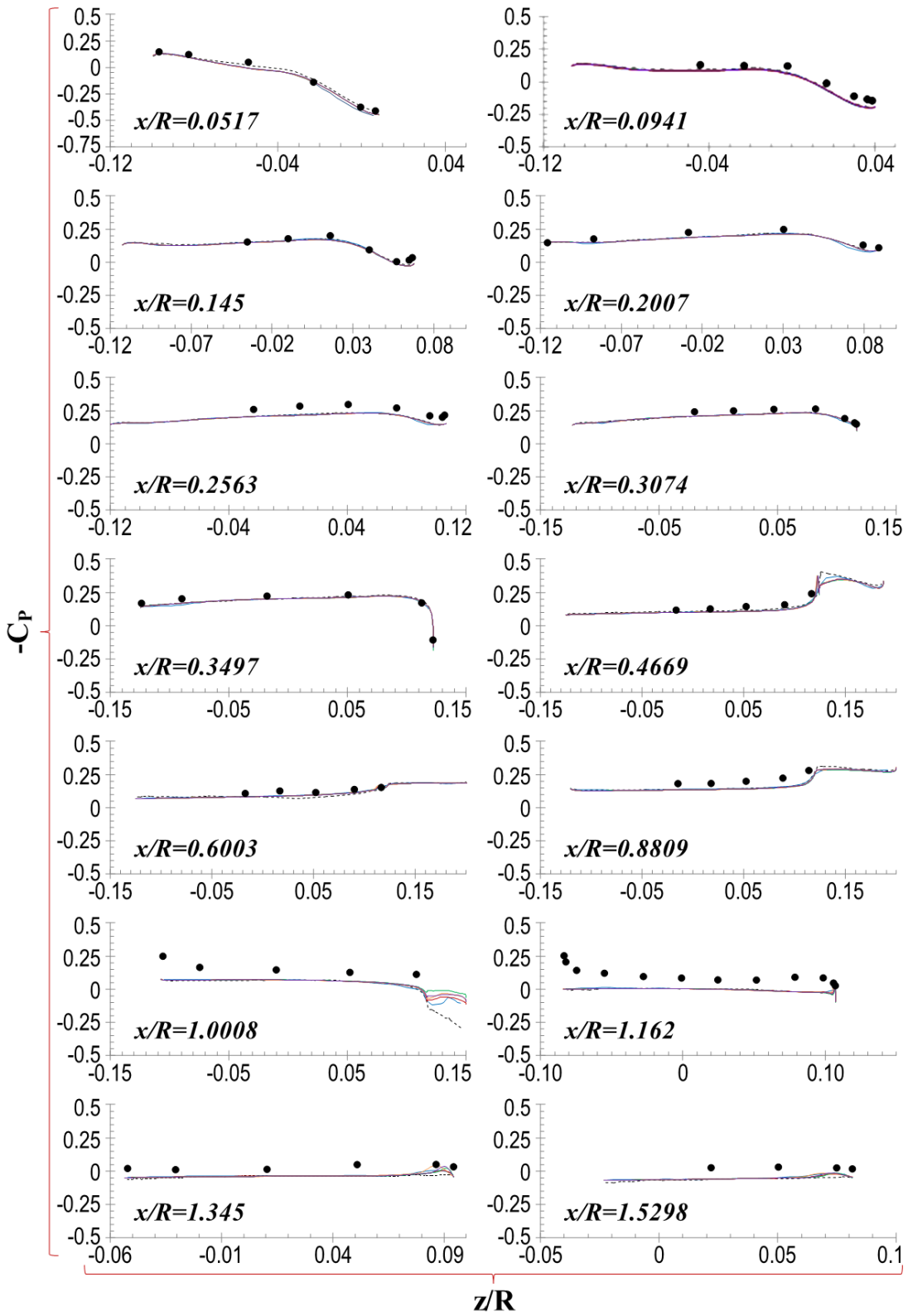


Figure A.3 : Cp distributions obtained at $\alpha_f = 0^\circ$.

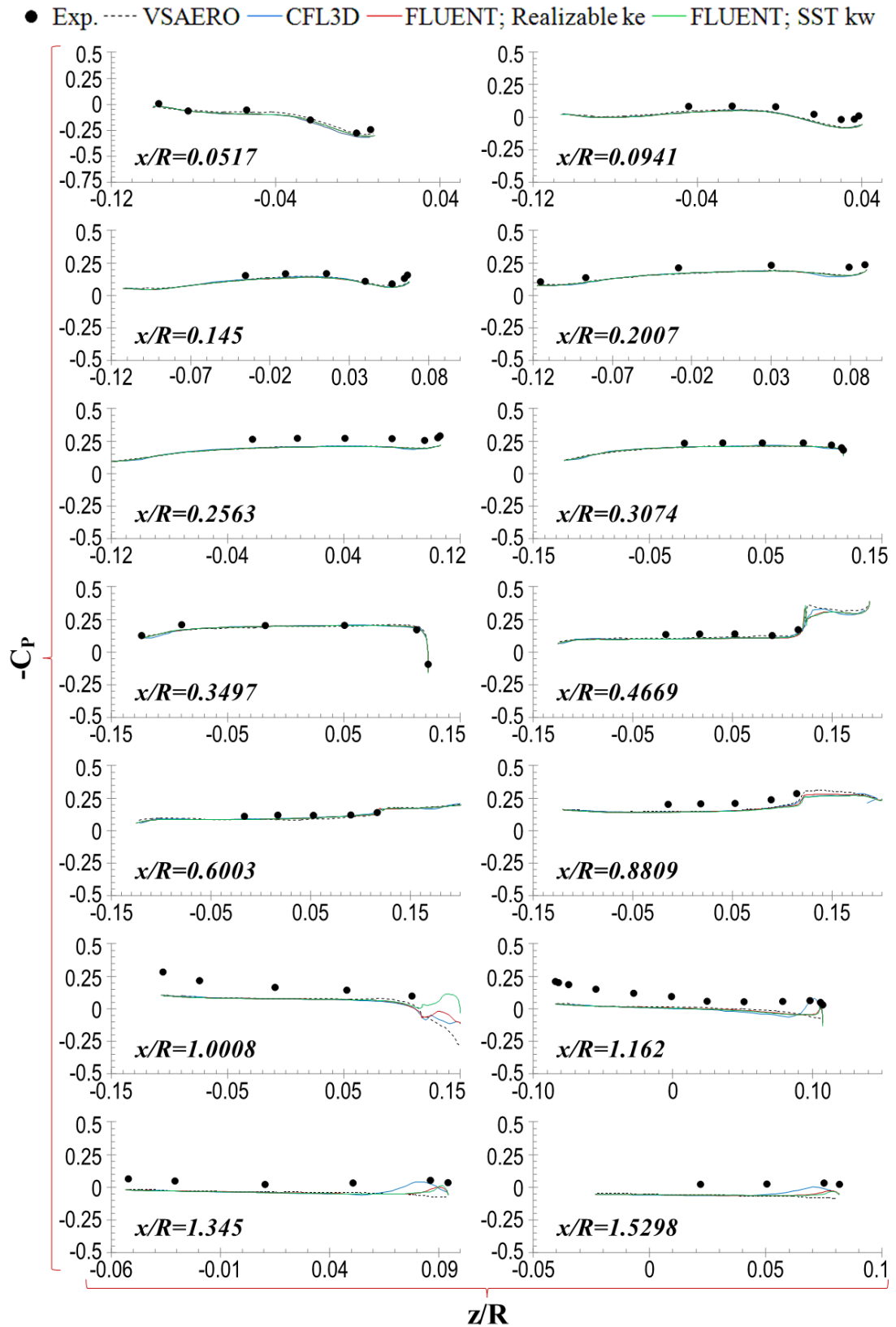


Figure A.4 : C_p distributions obtained at $\alpha_f = 5^\circ$.

APPENDIX B

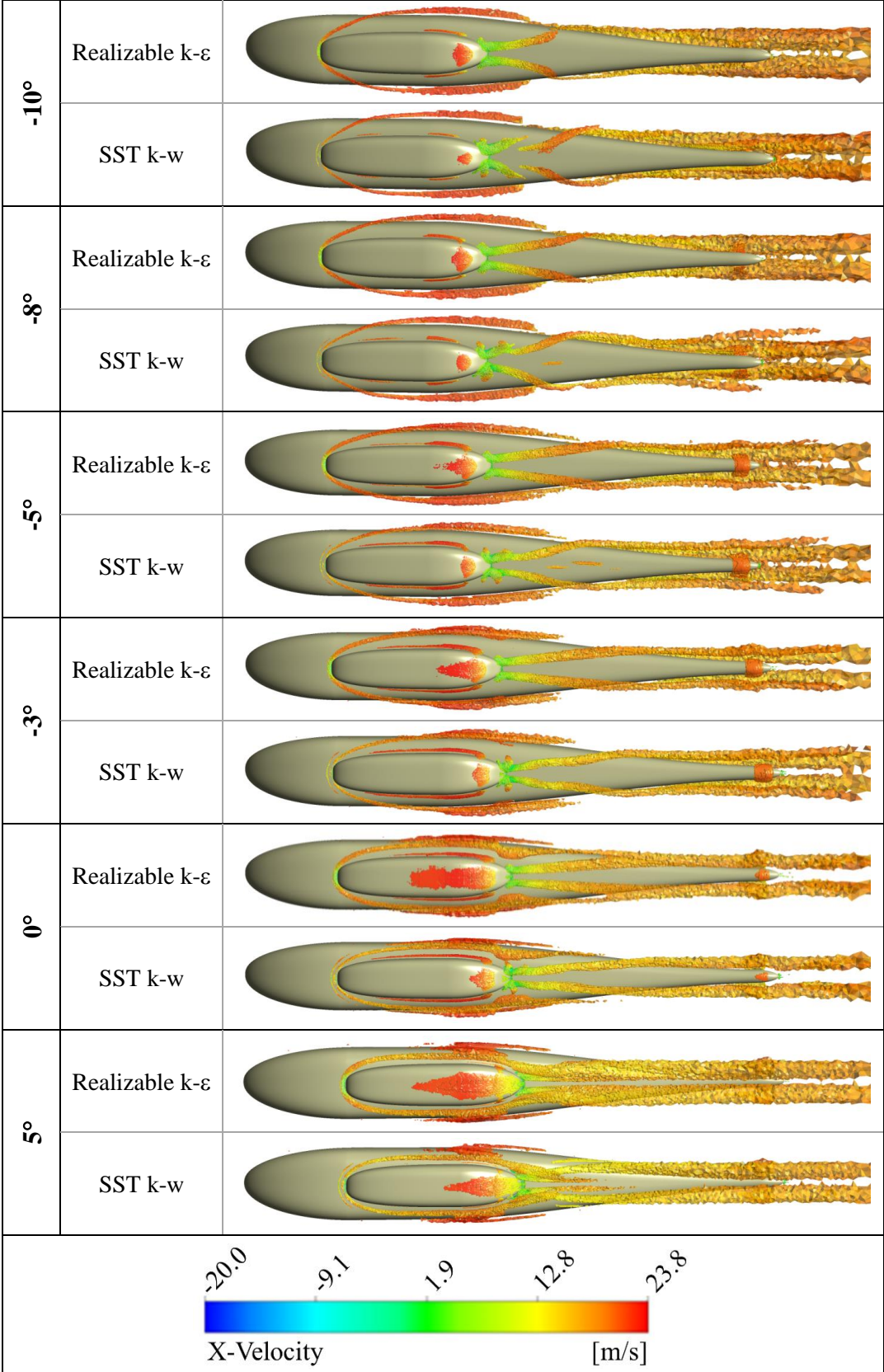


Figure B.1 : Flow patterns of different AoA conditions, top view.

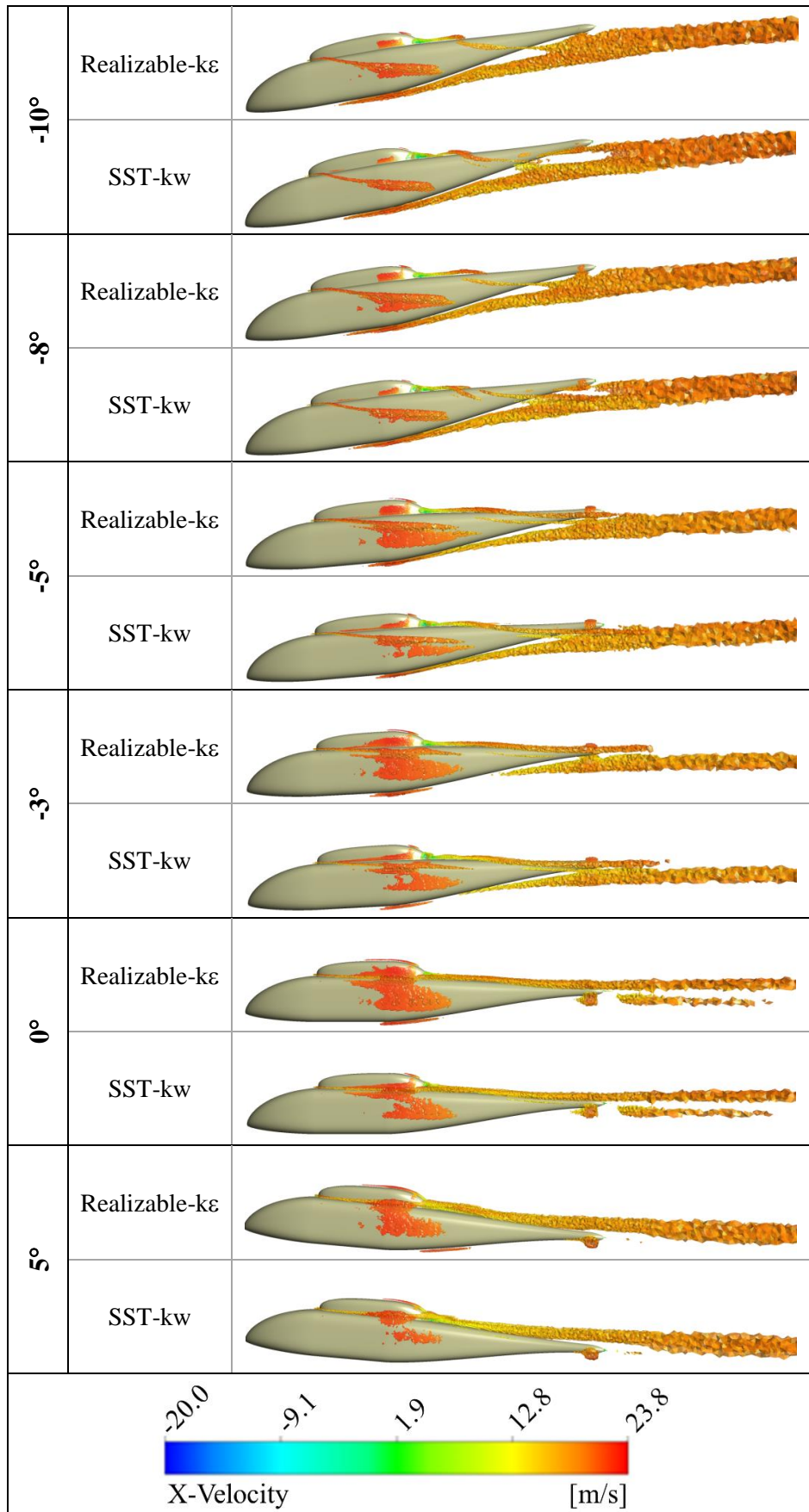


Figure B.2 : Flow patterns of different AoA conditions, side view.

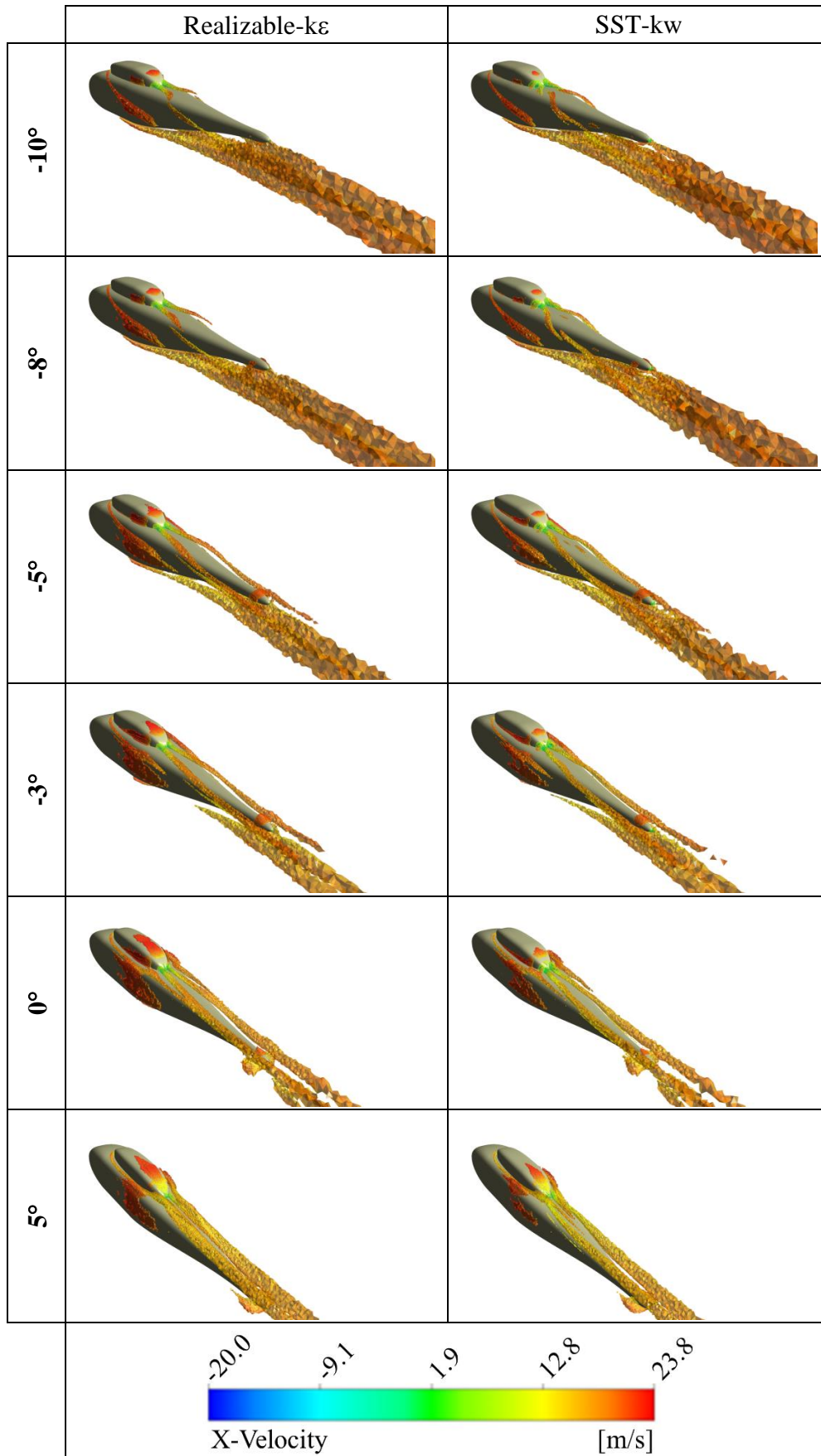


Figure B.3 : Flow patterns of different AoA conditions, isometric view.

APPENDIX C

○Exp: Mineck and Gorton, 2000 — Tanabe et al. 2010 — Present Study

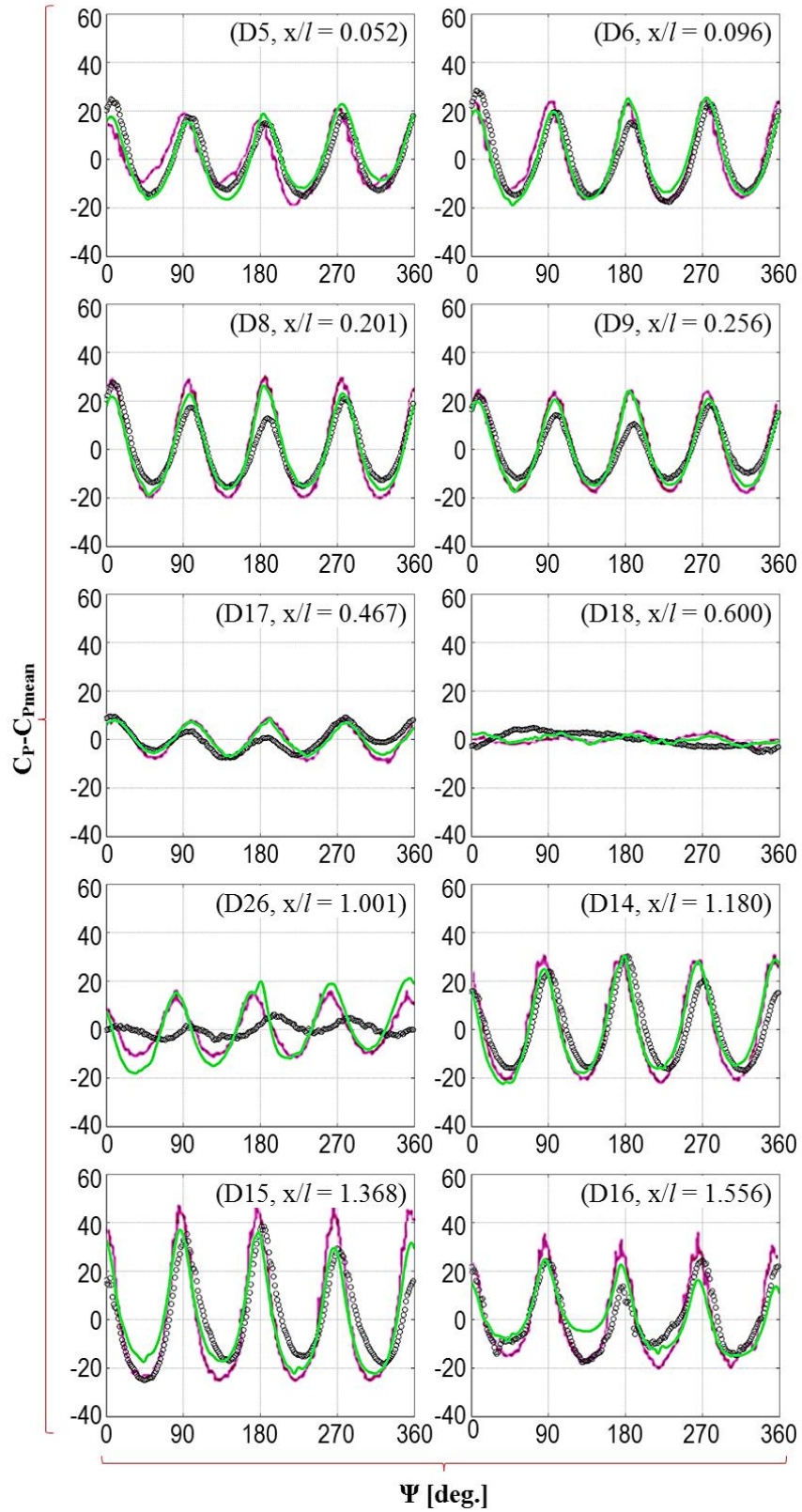


Figure C.1 : Comparison of C_p fluctuations ($\mu=0.012$).

oExp: Mineck and Gorton, 2000 — Tanabe et al. 2010 — Present Study

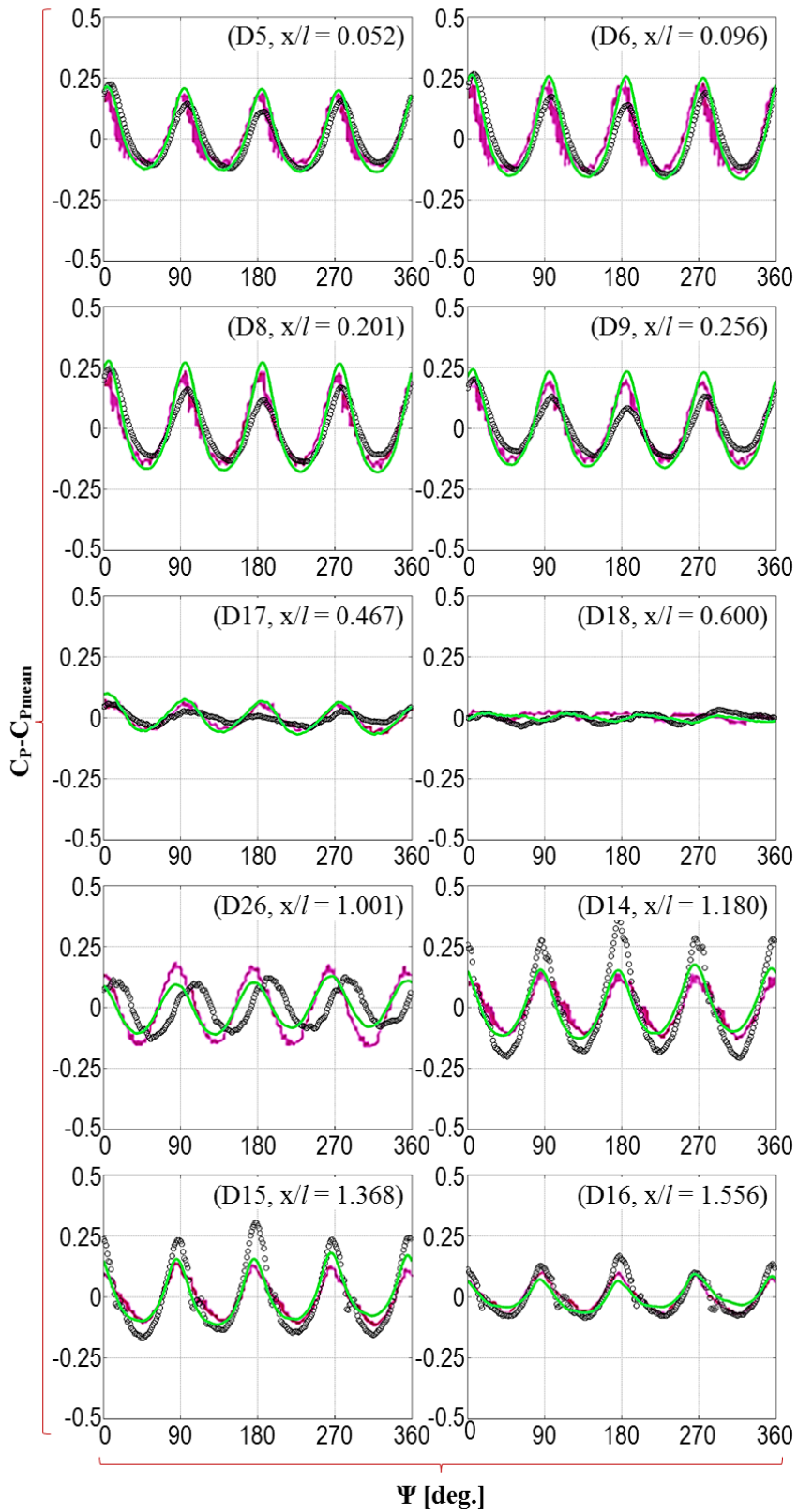


Figure C.2 : Comparison of C_p fluctuations ($\mu=0.151$).

oExp: Mineck and Gorton, 2000 — Tanabe et al. 2010 — Present Study

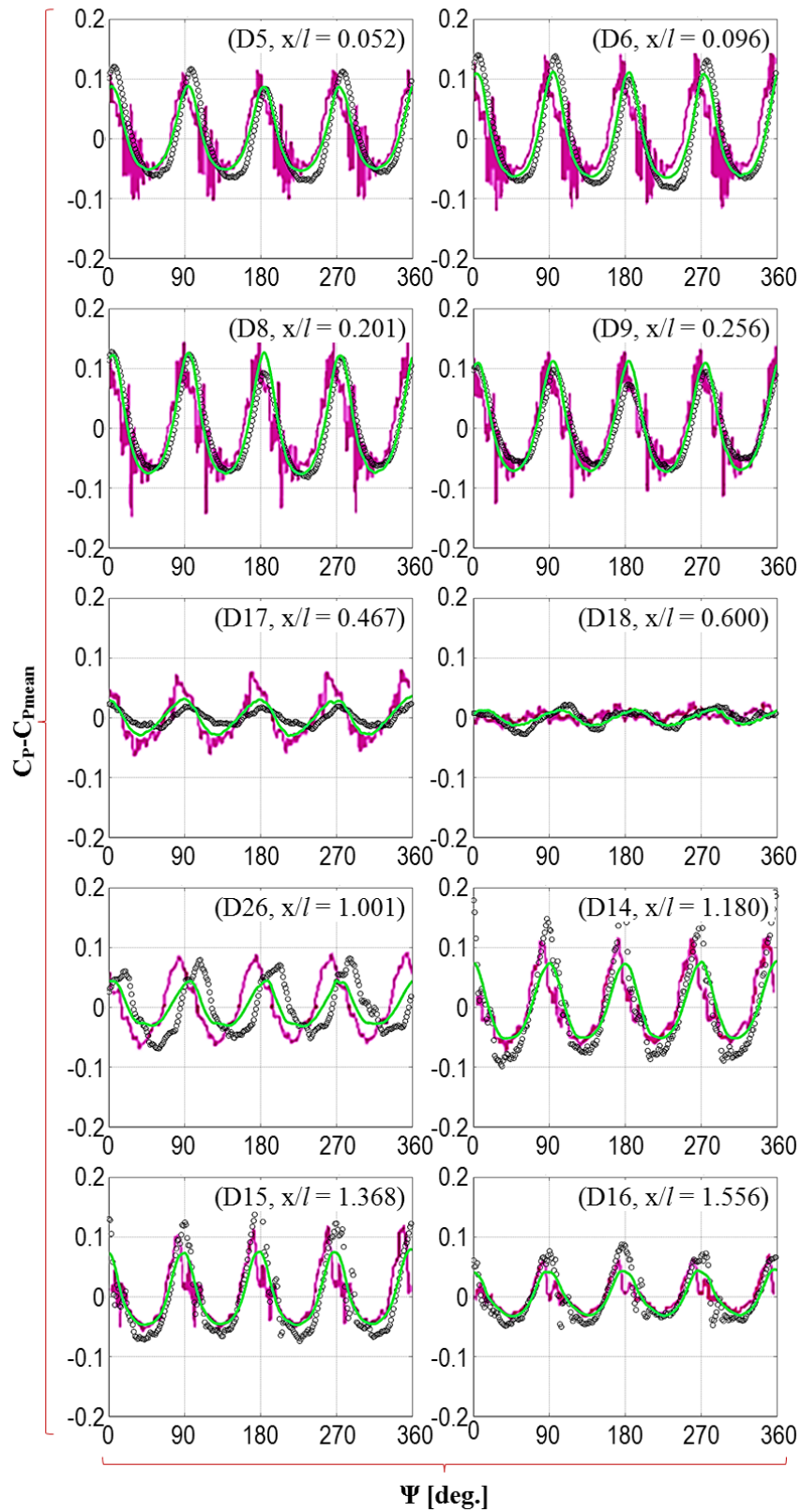


Figure C.3 : Comparison of C_p fluctuations ($\mu=0.231$).

CURRICULUM VITAE



Name Surname: Mustafa Berkay AÇIKGÖZ

Place and Date of Birth: İzmit – 09.05.1984

E-Mail: acikgozbe@itu.edu.tr, acikgozbe@gmail.com

EDUCATION:

B.Sc. : 2007, Istanbul Technical University, Faculty of Aeronautics and Astronautics, Aeronautical Engineering.

M.Sc. : 2009, Istanbul Technical University, Department of Aeronautics and Astronautics Engineering, Aeronautics and Astronautics Engineering.

PROFESSIONAL EXPERIENCE AND REWARDS:

Arçelik Inc., Research and Development Center, R&D Engineer, 2007-2009

AES-Aero Ltd., Design and Analysis Engineer, 2011-....

PUBLICATIONS, PRESENTATIONS AND PATENTS ON THE THESIS:

Acikgoz, M.B., Anbarci, K., Aslan, A.R., (2014): Askı ve İleri Uçuş Şartlarında Helikopter Rotor-Gövde Akış Etkileşimi için HAD Analiz Yöntemi Geliştirilmesi, 3. *Ulusal Havacılıkta İleri Teknolojiler Konferansı (HİTEK)*, 18-19 Haziran, Hava Harp Okulu, İstanbul, Türkiye.

Açikgöz, M.B., and Aslan A.R., (2016): Dynamic Mesh Analyses of Helicopter Rotor–Fuselage Flow Interaction in Forward Flight, *J. Aerosp. Eng.*, DOI: 10.1061/(ASCE)AS.1943-5525.0000641, 04016050.

OTHER PUBLICATIONS, PRESENTATIONS AND PATENTS:

- Nikbay, M., **Acikgoz, M.B.**, Kerpicci, H., (2009): Investigation of Airflow and Temperature Distribution in the Freezer Cabinet of a Domestic No-Frost Refrigerator, *Proceedings of the ASME 2009 Heat Transfer Summer Conference, HT2009*, July 19-23, 2009, San Francisco, California, USA. DOI: 10.1115/HT2009-88121.
- Acikgoz, M.B.**, Akay, B., Miguel, A.F., Aydin, M., (2011): Airborne Pathogens Transport in an Aircraft Cabin, *Defect and Diffusion Forum*, 312-315, pp.865-870, Trans Tech Publications, Switzerland, ISSN: 1662-9507, DOI: 10.4028/www.scientific.net/DDF.312-315.865.
- Anbarci, K., **Acikgoz, B.**, Aslan, R., Arslan, O., Icke, O., (2013): Development of an Aerodynamic Analysis Methodology for Tractor-Trailer Class Heavy Commercial Vehicles, *SAE Int. J. Commer. Veh.*, 6 (2): pp.441-452, DOI: 10.4271/2013-01-2413.
- A. Rüstem ASLAN, Kerem ANBARCI, **M. Berkay AÇIKGÖZ**, Omur ICKE, Ozgur ASLAN, Cenk DINC, (2014): Numerical Modelling and Prediction of the effect of Cooling Drag on the total Vehicle Drag, *Eighth International Conference on Computational Fluid Dynamics (ICCFD8)*, July 14-18, Chengdu, China.
- Icke, O., Dinc, C., **Acikgoz, M.B.**, Mestanli, S., Anbarci, K., Gungor, A.G., Aslan, A.R., (2015): DES Analyses and Drag Prediction of a Light Commercial Road Vehicle, *8th ICCHMT*, May 25-28, Istanbul, Türkiye.
- A. Rüstem ASLAN, Kerem ANBARCI, **M. Berkay AÇIKGÖZ**, Omur ICKE, Ozgur ASLAN, Cenk DINC, (2016): Numerical Modelling and Prediction of the effect of Cooling Drag on the total Vehicle Drag, *ACTA Aerodynamica Sinica*, 34 (02): pp.232-238, DOI: 10.7638/kqdlxxb-2016.0012.